Lifetime Assessment of Alloy 718 under the Influence of Gaseous Hydrogen

Zur Erlangung des akademischen Grades eines
DOKTORS DER INGENIEURWISSENSCHAFTEN (Dr.-Ing.)

von der KIT-Fakultät für Maschinenbau des
Karlsruher Instituts für Technologie (KIT)
angenommene

DISSERTATION

von

M.Sc. Fabien Ebling

Tag der mündlichen Prüfung:	02.11.2026
Hauptreferentin:	Prof. Dr. rer. nat. Astrid Pundt
Korreferent:	Prof. Dr.-Ing. Thomas Böllinghaus



This document is licensed under a Creative Commons
Attribution-Non Commercial 4.0 International License (CC BY-NC 4.0):
https://creativecommons.org/licenses/by-nc/4.0/deed.en

Abstract

The latest developments in the field of hydrogen as an energy carrier for a climate-neutral infrastructure make it necessary to get components ready for hydrogen application. However, it is known that particularly high-strength steels can be subject to severe degradation of the mechanical properties and reduced service lifetime due to hydrogen contact. For a reliable component design, the material properties must be determined under the relevant operating conditions, and the service lifetime of components must be calculated by models.

The nickel-based Alloy 718 is widely used in aero-engines, gas turbines, oil and gas industry and nuclear reactors due to its high strength, good corrosion and creep resistance at high temperature. However, the use of Alloy 718 in a hydrogen environment is challenging, as it is susceptible to hydrogen degradation. The extent to which this occurs is highly dependent on influencing factors such as hydrogen pressure, gas purity, temperature, material and surface conditions, mechanical load and time. There is still a lack of comprehensive understanding how these factors interact.

This work examines these influencing factors using hollow specimens in slow strain rate tensile tests and low cycle fatigue experiments. For comparison, hollow specimens exposed to internal hydrogen gas pressure and conventional specimens in a hydrogen autoclave are tested. As standardization for tensile testing of hollow specimens is still ongoing, results of this work are incorporated in the ISO/FDIS 7039. To examine the hydrogen influence over a wide temperature range, new test rigs are established that allow for cooling the hollow specimens down to -196 °C with liquid nitrogen and heating them up to 600 °C with induction heating. To gain a better understanding of the interactions between hydrogen and Alloy 718, the solubility, diffusion, and permeation of hydrogen in the metal lattice are investigated, and binding energies of hydrogen at defects are determined. Microstructural and fractographic investigations provide insights into the temperature-dependent damage mechanisms.

The increasing use of additive manufacturing raises new questions regarding the influence of hydrogen on the specific microstructure of additively manufactured materials, which exhibit anisotropic properties and defects. Therefore, additively manufactured Alloy 718 is investigated and compared to conventionally wrought alloy.

An established mechanism-based model employing the damage parameter Z_D according to Heitmann [1] is applied to describe the fatigue life in air. To account for the influence of hydrogen in the framework of the hydrogen-enhanced localized plasticity (HELP) theory, this parameter is extended to the newly developed hydrogen damage parameter $Z_{D,H}$. The model describes the micro crack growth from defects of approximately 20 µm to technical crack initiation of 1 mm in length. The influence of hydrogen on crack growth is represented based on physical relationships, allowing to account for the influencing factors such as temperature, hydrogen pressure, loading frequency, and mechanical load amplitude. The experimentally determined fatigue lives in the hydrogen pressure range $0 - 250\,bar$, temperature range $-100 - 600\,°C$, frequency range $0.001 - 1\,Hz$ and strain range $1.1 - 3$ % are successfully predicted by the model within a scatter band factor of 2 ($R^2 = 0.89$).

Kurzfassung

Die neuesten Entwicklungen im Bereich Wasserstoff als Energieträger für eine klimaneutrale Infrastruktur machen es notwendig Komponenten für den Einsatz mit Wasserstoff bereit zu machen. Es ist jedoch bekannt, dass insbesondere hochfeste Stähle einer erheblichen Verschlechterung der mechanischen Eigenschaften und einer verkürzten Lebensdauer aufgrund des Kontakts mit Wasserstoff unterliegen können. Für ein zuverlässiges Komponentendesign müssen die Materialeigenschaften unter den relevanten Betriebsbedingungen ermittelt werden und basierend auf diesen die Lebensdauer der Komponenten mit Modellen bestimmt werden.

Die nickelbasierte Legierung 718 wird aufgrund ihrer hohen Festigkeit, guten Korrosions- und Kriechbeständigkeit bei hohen Temperaturen in Flugtriebwerken, Gasturbinen, der Öl- und Gasindustrie sowie in Kernreaktoren weit verbreitet eingesetzt. Der Einsatz der Legierung 718 in einer Wasserstoffumgebung stellt jedoch eine Herausforderung dar, da sie anfällig für Wasserstoffschädigung ist. Das Ausmaß, in dem dies auftritt, hängt stark von Einflussfaktoren wie Wasserstoffdruck, Gasreinheit, Temperatur, Material- und Oberflächenbedingungen, mechanischer Belastung und Zeit ab. Es fehlt noch immer ein umfassendes Verständnis darüber, wie diese Faktoren zusammenwirken.

In dieser Arbeit werden diese Einflussfaktoren in langsamen Zugversuchen und niederzyklischen Ermüdungsversuchen an Hohlproben untersucht. Zum Vergleich werden Hohlproben mit Wasserstoffinnendruck sowie konventionelle Proben in einem Wasserstoffautoklaven geprüft. Da die Normung für Zugversuche an Hohlproben noch im Gange ist, fließen die Ergebnisse dieser Arbeit in die ISO/FDIS 7039 ein. Um einen großen Temperaturbereich zu untersuchen, werden neue Prüfstände aufgebaut, die es ermöglichen, die Hohlproben mit flüssigem Stickstoff auf bis zu -196 °C abzukühlen und sie mit einer Induktionsheizung auf bis zu 600 °C zu heizen. Um ein besseres Verständnis der Interaktionen zwischen Wasserstoff und der Legierung 718 zu erhalten, werden die Löslichkeit, Diffusion und Permeation von Wasserstoff im Metallgitter untersucht und die Bindungsenergien von Wasserstoff an Defekten bestimmt. Mikrostruktur- und fraktografische Untersuchungen geben Aufschluss über die temperaturabhängigen Schadensmechanismen.

Der zunehmende Einsatz der additiven Fertigung wirft neue Fragestellungen hinsichtlich des Einflusses von Wasserstoff auf die spezifische Mikrostruktur additiv gefertigter Werkstoffe auf, die anisotrope Eigenschaften und Defekte aufweisen. Daher wird in dieser Arbeit neben einer konventionell Knetlegierung auch eine additiv gefertigte Legierung 718 untersucht.

Ein etabliertes mechanismenbasiertes Modell unter Verwendung des Schädigungsparameters Z_D nach Heitmann [1] wird angewendet, um die Ermüdungslebensdauer in Luft zu beschreiben. Um den Einfluss von Wasserstoff im Rahmen der Theorie der wasserstoffinduzierten lokalisierten Plastizität (HELP) zu berücksichtigen, wird dieser Parameter zum neu entwickelten Wasserstoffschädigungsparameter $Z_{D,H}$ erweitert. Das Modell beschreibt das Kurzrisswachstum von der Initiierung mit einer Risslänge von etwa 20 µm bis zum technischen Anriss von 1 mm Länge. Der Einfluss von Wasserstoff auf das Risswachstum wird anhand physikalischer Zusammenhänge

dargestellt. Dadurch kann das Modell die Einflussfaktoren Temperatur, Wasserstoffdruck, Belastungsfrequenz und mechanische Lastschwingbreite abbilden. Die experimentell ermittelten Ermüdungslebensdauern im Wasserstoffdruckbereich von $0 - 250\ bar$, im Temperaturbereich von $-100 - 600\ °C$, im Frequenzbereich von $0{,}001 - 1\ Hz$ und im Dehnungsbereich von $1{,}1 - 3\ \%$ werden durch das Modell mit einem Streubandfaktor von 2 erfolgreich bestimmt ($R^2 = 0.89$).

Preface

This work was carried out during my employment as a research associate at the Fraunhofer Institute for Mechanics of Materials IWM. The financial support of the Federal Ministry for Economic Affairs and Energy (BMWE) within the Project AdHyBau (20M1904E) and AdHyBau2 (20M2202C) is gratefully acknowledged.

My special thanks go to Prof. Astrid Pundt for supervising this work and for the warm welcome within the Defects in Metals group at KIT. I would like to express my sincere thanks also to Dr. Stefan Wagner for his careful proofreading and valuable corrections. Furthermore, I would like to thank Prof. Thomas Böllinghaus for serving as second examiner and for reviewing this thesis.

I am grateful to Dr. Christoph Schweizer, who made it possible for me to conduct this work within the business unit Materials Assessment and Lifetime Concepts at Fraunhofer IWM.

Special thanks go to Dr. Frank Schweizer and Dr. Thorsten Michler for their continuous guidance and support, for granting me the time to focus on my thesis, and for enabling me to present my research at numerous conferences and events.

My sincere thanks go to my daily advisor, Dr. Ken Wackermann, who was always available for any questions and supported me in many ways. I would also like to express my special thanks to Heiner Augenstein for his support in developing the lifetime model and for being constantly available for technical discussions. I would like to thank Dr. Johannes Preußner especially for his support during the initial phase and in defining the research topic.

This work would not have been possible without the great support of the staff in the laboratory and metallography, as well as the bachelor's and master's students, to whom I would also like to express my sincere thanks. In particular, I would like to thank David Primus from the laboratory for his great support in conducting many technically challenging experiments with hollow specimens, and Sabine Oeser and Karin Hintz from the metallography for their invaluable assistance with the metallographic investigations. In addition, I wish to thank Dr. Steffen Schönborn from Fraunhofer LBF for carrying out the fatigue tests in the hydrogen autoclave. Thanks to all my colleagues for the great time and the positive working atmosphere!

Finally, I would like to thank my wife Tamara, who accompanied me through all the highs and lows during this work and was always patient and encouraging.

Table of contents

Abstract ... iii

Kurzfassung ... v

Preface ... vii

Table of contents ... ix

Abbreviations and Symbols ... xiii

1 Introduction ... 1

2 Fundamentals of alloy 718, fatigue crack growth and hydrogen effects ... 5

2.1 Alloy 718 ... 5
2.1.1 Microstructure and strengthening ... 6
2.1.2 Manufacturing process ... 7
2.1.3 Low cycle fatigue ... 8
2.2 Fundamentals of fracture mechanics ... 10
2.2.1 Linear elastic material behavior ... 11
2.2.2 Elastic-plastic material behavior ... 13
2.2.3 Fatigue crack growth ... 15
2.2.4 Lifetime prediction ... 17
2.2.5 Models for environmental effects ... 18
2.3 Fundamentals of hydrogen in metals ... 21
2.3.1 Behavior of non-ideal gases ... 21
2.3.2 Hydrogen permeability, solubility and diffusivity ... 22
2.3.3 Hydrogen traps ... 26
2.4 Hydrogen embrittlement ... 28
2.4.1 Hydrogen enhanced decohesion ... 29
2.4.2 Hydrogen enhanced localized plasticity ... 30
2.4.3 Hydrogen embrittlement of Alloy 718 ... 31

3 Methodology ... 37

3.1 Material ... 37
3.2 Hydrogen pre-charging ... 38
3.3 Carrier gas melt extraction ... 39
3.4 Thermal desorption spectroscopy ... 40
3.5 Gas permeation ... 40
3.6 Metallographic and fractographic examinations ... 41
3.7 Slow strain rate tensile testing ... 42
3.8 Fatigue testing ... 43
3.9 Specimen preparation ... 44
3.10 Mechanical test setups ... 46
3.10.1 High pressure hydrogen autoclave ... 46

3.10.2 Hollow specimen test setup 47
3.10.3 Heating and cooling setups 49

4 Microstructural investigations 52

4.1 Microstructure of Alloy 718 wrought and SLM 52
4.2 Roughness and microstructural changes after machining 53
4.3 Discussion 57

5 Investigation of the interactions between hydrogen and Alloy 718 59

5.1 Hydrogen charging and solubility 59
5.2 Hydrogen desorption experiments 61
5.3 Determination of hydrogen diffusion coefficient by gas permeation 62
5.4 Determination of activation energies 64
5.5 Discussion 65
5.5.1 Permeation, diffusion and solubility 65
5.5.2 Activation and binding energies 67

6 Mechanical experiments 71

6.1 Slow strain rate tensile tests 71
6.1.1 Qualification of hollow specimen testing on X60 pipeline steel 71
6.1.2 Comparison of conventional and hollow specimens of Alloy 718 in slow strain rate tensile tests 74
6.2 Discussion of slow strain rate tensile tests 80
6.2.1 Effect of strain rate 80
6.2.2 Effect of gas purity 81
6.2.3 Comparison of mechanical properties obtained from conventional and hollow specimens 81
6.2.4 Failure mechanisms 83
6.2.5 Multi axial stress in hollow specimens caused by internal pressure 84
6.2.6 Effect of additive manufacturing on hydrogen embrittlement of Alloy 718 85
6.3 Low cycle fatigue experiments 86
6.3.1 Pre-charged low cycle fatigue experiments 87
6.3.2 Comparison of conventional and hollow specimens in low cycle fatigue experiments 88
6.3.3 Effect of frequency 94
6.3.4 Effect of pressure 97
6.3.5 Effect of temperature 98
6.3.6 Additive manufactured Alloy 718 SLM 101
6.4 Discussion of low cycle fatigue experiments 104
6.4.1 In-situ vs. ex-situ 104
6.4.2 Comparability of conventional and hollow specimens 105
6.4.3 Crack growth in hollow and conventional specimens 107
6.4.4 Effect of frequency 108
6.4.5 Effect of pressure 109
6.4.6 Effect of temperature 110

6.4.7 Effect of additive manufacturing 110
6.4.8 Hydrogen embrittlement mechanisms 111

7 Mechanism-based lifetime model 115

7.1 Hydrogen assisted fatigue crack growth model 115
7.2 Investigation of the model behavior 119
7.3 Determination of the temperature-dependent material properties 122
7.4 Adaptation and validation of the model 124
7.5 Discussion of the crack growth model and the hydrogen damage parameter $Z_{D,H}$ 132

8 Global Discussion 135

8.1 Hollow specimens and comparison to conventional specimens 135
8.2 Effect of hydrogen on the damage behavior of Alloy 718 wrought 138
8.3 Ex-situ versus in-situ testing 141
8.4 Influence of additive manufacturing on hydrogen damage 142
8.5 Fatigue life prediction for hydrogen environments 143

9 Summary and conclusions 147

References 151

Figures 175

Tables 185

Publications 187

Statement on the use of AI tools 189

Abbreviations and Symbols

Abbreviation	Description
AFM	Abrasive flow machining (AFM)
AIDE	Adsorption-induced dislocation emission
AM	Additive manufacturing
BCC	Body-centered cubic
BCT	Body-centered tetragonal
BD	Building direction
BSE	Backscattered electron
CAD	Computer-aided design
CS	Conventional specimens
EBSD	Electron backscattered diffraction
ECM	Electrochemical machining
EDM	Electrical discharge machining
EDX	Energy dispersive X-ray spectroscopy
FCC	Face-centered cubic
HCF	High cycle fatigue
HE	Hydrogen embrittlement
HEDE	Hydrogen enhanced decohesion
HELP	Hydrogen enhanced localized plasticity
HESIV	Hydrogen enhanced strain induced vacancies
HID	Hydrogen induced decohesion
HIPT	Hydrogen induced phase transformation
HPT	Hydrogen pressure theory
HS	hollow specimens
HTHA	High temperature hydrogen attack
IGP	Ion getter pump
IPI	InProcess Instruments
KAM	Kernel average misorientation
LCF	Low cycle fatigue
LPBF	Laser powder bed fusion
QMS	Quadrupole mass spectrometer
SE	Secondary electron
SEM	Secondary electron microscopy
SLM	Selective laser melting
SLM	Selective laser melting
SSRT	Slow strain rate tensile
TDS	Thermal desorption spectroscopy
TMF	Thermomechanical fatigue
TMP	Turbomolecular pump
TTT	Time temperature transformation diagram
WAAM	Wire arc additive manufacturing

Symbol	Description
a	Crack length
a_0	Initial crack length
a_f	Final crack length
a_l	Activity of hydrogen in lattice
A_r	Reaction constant
a_t	Activity of hydrogen at trap
a_x	Fractional activity
b	Constant
b_g	Constant of Abel-Noble equation
C	Concentration
C_{f,O_2}	Final oxygen concentration
C_{i,O_2}	Initial oxygen concentration
$C_{l,max}$	Maximum lattice hydrogen concentration
C_{σ_h}	Stress dependent hydrogen concentration
$C_{initial}$	Initial hydrogen concentration
$CTOD$	Crack tip opening displacement
D	Diffusivity
$d_{N'}$	Geometrical function
D_0	Diffusion coefficient
da/dN	Growth per cycle
ds	Path increment
E	Young's modulus
e	Empirical order of reaction
$E_{l,d}$	Activation energy of lattice diffusion
$E_{t,a}$	Trap activation energy
$E_{t,b}$	Trap binding energy
E_S	Saddle point energy
erf	Error function
F	Fugacity
f	Frequency
g	Constant
h	Exponent
H_D	Diffusion formation enthalpy
H_m	Micro-hardness
H_P	Permeation formation enthalpy
H_S	Solution formation enthalpy
HEI	Hydrogen embrittlement index
HEI_{NTS}	Hydrogen embrittlement index of notched tensile strength
$I_{N'}$	Numerical constant
J	J-integral
J^{el}	Elastic part of the J-integral
J^{pl}	Plastic part of the J-integral
J_D	Diffusion flux
K	Stress intensity factor
k	Summation index
$K_{I(th)}$	Threshold stress intensity factor
K_I	Stress intensity factor
K_{IC}	Fracture toughness

K'	Equilibrium constant
L	Length
M, m	Material constants
N	Exponent
N'	Strain hardening exponent
n'	Cyclic hardening exponent
N_0	Cycles at crack initiation
N_f	Cycles at final crack length
n_j	Normal vector
P	Permeability
p	Pressure
$p_{H_{th}}$	Threshold hydrogen pressure
P_0	Permeation coefficient
p_H	Hydrogen pressure
p_{purge}	Total maximum pressure used for purging
p_{vent}	Total pressure to which the gas is released
R	Universal gas constant
r	Radius
r_b	Blunted notch root radius
r_{crit}	Critical radius of particles
r_X	Distance from crack tip
r_s	Sharp notch root radius
R_σ	Stress ratio
RA	Reduction of area
$R\varepsilon_f$	Relative elongation to failure
RRA	Relative reduction of area
S	Solubility
s	Striation width
S_0	Solution coefficient
T	Temperature
t	Time
t_{cyc}	Time of one load cycle
$T_{HE,max}$	Temperature of maximum hydrogen embrittlement
T_0	Initial temperature
T_{cr}	Critical temperature
T_p	Peak temperature
u	Deformation
u_i	Displacement vector
u_x	Displacement in x-direction
u_y	Displacement in y-direction
$\bar{V}_H$	Partial molar volume of hydrogen
V_m	Molar volume
w	Width
W'	Strain energy density
X	Point
x	Position
X_{cr}	Critical distance
X_{Dev}	Deviation of two iteration steps
x_p	Penetration depth

Y	Summary of crack-length-independent parameters
Z	Compressibility factor
z	Plastic zone size
Z_D	Damage parameter according to Heitmann
$Z_{D,H}$	Hydrogen damage parameter
$Z^*_{D,H}$	Modified hydrogen damage parameter
α	Proportionality factor of hydrogen enhanced crack growth
α^*	Modified proportionality factor of hydrogen enhanced crack growth
β, B	Proportionality factors of crack growth
Γ	Path surrounding the crack tip
γ'	Precipitation phase
γ''	Precipitation phase
δ	Precipitation phase
δ_{max}	Maximum crack opening
Δa	Crack propagation
Δa_{Air}	Crack propagation in air
Δa_H	Crack propagation in hydrogen
Δa_i	Crack propagation calculated in iteration step i
$\Delta CTOD$	Cyclic crack tip opening displacement
ΔK	Cyclic stress intensity factor
ΔK_{cr}	Critical stress intensity range
ΔK_{th}	Threshold stress intensity range
$\Delta\varepsilon$	Strain range
$\Delta\varepsilon_t$	Total strain range
$\Delta\sigma$	Stress range
$\Delta\sigma_{eff}$	Effective stress range
ε	Strain
$\dot{\varepsilon}$	Strain rate
ε^{el}	Elastic strain
ε^{pl}	Plastic strain
ε_f	Elongation to failure
ε^{pl}_{ij}	Plastic strain field at crack tip
ζ	Reacted fraction
$\bar{\theta}_d$	Average hydrogen occupation at dislocations
θ_d	Lattice occupancy
θ_t	Trap occupancy
θ_x	Fractional occupancy
σ	Stress
σ^*	Hydrogen-reduced cohesive stress
σ_{cy}	Cyclic yield stress
σ_{eq}	Equivalent stress
σ_{ij}	Singular stress field at crack tip
σ'_{ij}	Deviatoric stress tensor
σ_{NTS}	Notched tensile strength
σ_{op}	Crack opening stress
σ_{UTS}	Ultimate tensile stress
σ_{YS}	Yield strength
σ_{yy}	Tensile stress
υ	Poisson's ratio

φ	Angle of stress field ahead of the crack tip
λ	Angle of the crack front
Φ	Heating rate
χ, ψ	proportions of the total crack propagation
ω	Angular function

1 Introduction

Hydrogen is considered a promising climate-neutral energy carrier for storing renewable energy from sources such as wind or solar power. Through electrolysis, hydrogen can be produced from water and renewable energy. This can then be used in sectors such as mobility, heating, electricity, and the chemical industry to replace climate-damaging fossil fuels such as coal, oil, and gas. To achieve this transition to a climate-friendly hydrogen economy, high reliability and safety of components in contact with hydrogen are required.

As early as 1875, William H. Johnson discovered "That the tensile strain of steel is diminished by the occlusion of hydrogen, and that as the hydrogen is expelled (a process of long duration) the tensile strain rises, till eventually it exceeds the original strain before immersion in acid" [2]. This means that hydrogen solved in metal deteriorates its mechanical properties, but it does not damage the material itself, and the metal regains its original properties when the hydrogen has escaped. In the 1960s and 1970s, hydrogen embrittlement (HE) was intensively studied in the field of aerospace [3], and in recent decades, the topic has regained attention with regard to a hydrogen economy and the conversion of the existing natural gas network for hydrogen transport [4]. However, the mechanisms of hydrogen embrittlement are not yet fully understood and there is no model that can describe the processes comprehensively. There are therefore a multitude of theories on hydrogen embrittlement. Among the most popular are the hydrogen pressure theory, hydrogen induced phase transformation (HIPT), hydrogen-enhanced localized plasticity (HELP), and hydrogen enhanced decohesion (HEDE). Different mechanisms can occur depending on the material and operating conditions.

While hydrogen embrittlement usually does not affect the yield strength σ_{YS} of a material, it can significantly reduce its ductility, which can lead to sudden and catastrophic failure of components. To evaluate HE in tensile tests, the mechanical properties elongation to failure ε_f and reduction of area RA are compared with and without hydrogen in tensile tests. Since hydrogen can accumulate in stress fields of notches and lead to premature failure, the notched tensile strength σ_{NTS} is also an important parameter for evaluation of HE. Figure 1.1 shows the degree of hydrogen embrittlement as a ratio of RA or σ_{NTS} in hydrogen (RA_{H2}) and in helium (RA_{He}) atmospheres at 345 bar or 690 bar for various steel grades and non-ferrous alloys. Some alloys such as austenitic stainless steel 316 or alloy 286 show only a minor influence of hydrogen ($ratio \approx 1$) and would therefore be preferable for hydrogen applications. However, many applications require the use of materials which are susceptible to hydrogen embrittlement due to requirements such as high strength, low material costs or high operating temperature. For example, in the automotive industry, advanced high strength steels (AHSS) are used to reduce weight and increase crash safety. But during the manufacturing process and due to corrosion, hydrogen can be absorbed, leading to embrittlement [5]. Due to the lower material costs compared to stainless steels and good weldability, low carbon steels are mainly used for pipelines, which are currently being extensively tested for their compatibility with hydrogen to use the natural gas network for hydrogen transport [6]. Gas turbines are already being operated with hydrogen-natural gas mixtures and are expected

to switch to 100% hydrogen for decarbonization. Due to high temperature and mechanical requirements, nickel-based alloys are used [7]. In this study, nickel-based Alloy 718 is examined.

Beside gas turbines, Alloy 718 is utilized in various applications such as aerospace, nuclear reactors, oil and gas industry, cryogenic tanks, and many others [8,9], making it one of the most widely used nickel-based alloys in the past [10]. This is where the advantages of the alloy such as high strength, good creep resistance at high temperatures, corrosion resistance, weldability and good ductility at low temperatures come into play, making it almost indispensable in these applications [10,11]. However, as shown in Figure 1.1, Alloy 718 is susceptible to hydrogen embrittlement at room temperature and high hydrogen pressures (345 bar), and the degree of embrittlement also depends on the manufacturing process and heat treatment of the material. Therefore, it is essential to better understand the effects of hydrogen on Alloy 718 under service conditions raging from low to high pressure and temperature.

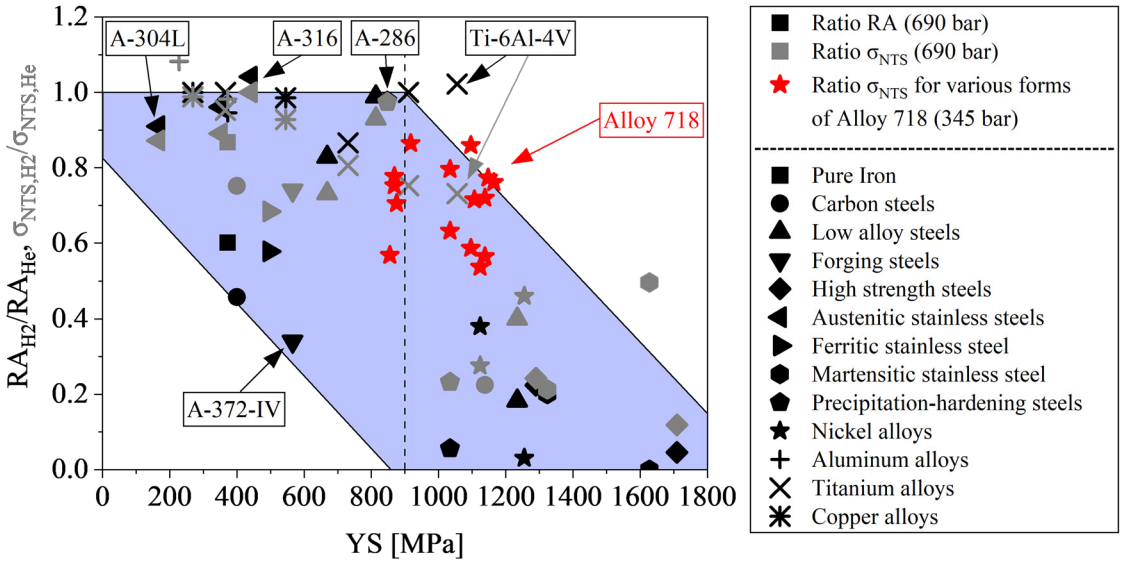


Figure 1.1: Hydrogen embrittlement index (RA_{H2}/RA_{He} or $\sigma_{NTS,H2}/\sigma_{NTS,He}$) as a function of the yield strength for various metallic materials (690 bar helium or hydrogen) and Alloy 718 (350 bar helium or hydrogen). For Alloy 718, 3 different heat treatment conditions are considered for rolled bars, forgings, thick plates, welds and heat-affected zones, respectively. Data of the various metallic materials was taken from [12] and data of Alloy 718 from [13].

For investigating the mechanical properties of materials in a hydrogen atmosphere, autoclave test stands are commonly used. These allow for static and dynamic experiments under high hydrogen pressure. These test stands require high safety precautions due to the risk of explosion and involve high investment costs. Hence, only a few facilities can conduct these experiments.

An alternative technique is the use of hollow specimens, filled with hydrogen gas. In this way, only a small amount of hydrogen is necessary, and the samples can be tested on existing testing machines with minimal safety precautions. Although hollow specimens have already been used in the 1950s [14] and 1960s [15] to investigate hydrogen embrittlement of metals, this method

has only gained significant interest in recent years due to the ease of its implementation and the high demand [16–26]. Additionally, this technique allows for cooling with liquid nitrogen or heating with induction heating. The standardization of hollow specimens for slow strain rate tensile tests and low cycle fatigue tests is still ongoing and many questions, such as the influence of sample geometry and inner surface on the measured material properties need further investigations. Only a few direct comparisons between hollow specimens and conventional specimens in autoclaves have been conducted so far. A comprehensive comparison for different materials was carried out by Michler et al. on ferritic steels [27] and austenitic stainless steels [28].

Additive manufacturing of components is increasingly used to produce prototypes and small series and enables the freedom of complex geometries that are not possible with conventional manufacturing methods. For example, heat exchangers with additive manufactured fine structures allow for high heat transfer, small dimensions and light weight [29–32]. Heat exchangers are used in the hydrogen sector, for instance, in cooling compressed hydrogen at hydrogen refueling stations [33] and for heating cryogenic hydrogen for fuel cells in hydrogen-electric propulsion systems [34]. However, additively manufactured (AM) materials may differ significantly from conventionally produced materials. During selective laser melting (SLM) process, the rapid local heating and cooling can induce high residual stresses [35] and the formation of cellular structures [36–38] in the material. The microstructure changes to elongated grains [39,40], resulting in anisotropic material properties [37]. In addition, various defects can occur in additive manufactured material, such as gas porosity [41,42], lack of fusion [41,43] and micro-cracks [44]. Little is known about the influence of hydrogen on this microstructure and defects. Therefore, both wrought material (Alloy 718 wrought) and material produced by selective laser melting (Alloy 718 SLM) will be investigated in this work.

For the safe design of components, the consideration of fatigue loads is necessary, as these can lead to premature failure of a component, even though the maximum statically permissible load is not reached. Cyclic loads can cause cracks to form and grow until they lead to the failure of the component [45]. This was recognized already in the 1800s, and Wöhler developed the stress-life response diagram for fatigue design [46]. Since then, there have been many important contributions to the understanding of crack formation, growth, and lifetime assessment, such as the relationship between cyclic plasticity and fatigue life [47,48]. The behavior of cracks can largely be described today using linear-elastic and elastic-plastic fracture mechanics [49], and fatigue lifetimes for components under various operating conditions can be calculated. However, under environmental influences such as a hydrogen atmosphere, there can be increased crack growth and thus shorter fatigue lifetimes. Various models have been developed to describe the influence on threshold values [50], which represent a minimum load for crack growth, or on the growth of long cracks [51,52]. For components without significant defects, however, most of the fatigue lifetime occurs in short crack growth up to a technical crack initiation of 1-2 mm [53,54], for which there are currently no adequate models that can describe the physical relationships between hydrogen diffusion and damage at a crack tip.

This leads to the following research questions to be addressed in this thesis:

- Can hollow specimens be used to investigate hydrogen embrittlement of Alloy 718 in tensile and fatigue tests?
- How do temperature, hydrogen pressure, and mechanical loading range and speed affect the influence of hydrogen on Alloy 718?
- How does the microstructure of additive manufactured Alloy 718 affect hydrogen embrittlement?
- How can short crack growth under hydrogen influence be modeled to predict the fatigue life of components under the numerous operating conditions consisting of temperature, hydrogen pressure, load amplitude and frequency?

To answer these questions, Chapter 2 provides an overview of the state of the art in the areas of Alloy 718, the basics of fracture mechanics needed for modeling fatigue crack growth, fundamentals of hydrogen transport and solubility and hydrogen embrittlement of alloy 718 with the most common hydrogen embrittlement theories. Chapter 3 presents sample preparation and the various experimental techniques for hydrogen measurements, microscopy, and mechanical tests. The microstructural investigations of the conventional wrought alloy and the additively manufactured SLM alloy are presented and discussed in Chapter 4, along with investigations of the influences of different manufacturing processes on the near-surface microstructure. Chapter 5 focusses on the interactions between Alloy 718 and hydrogen, including hydrogen diffusion, solubility, and activation energies of hydrogen traps. Results are discussed with literature and microstructure-independent diffusion, solubility, and permeation constants are proposed for Alloy 718. Chapter 6 presents the results of static and dynamic mechanical experiments. Both conventional specimens tested in high-pressure hydrogen autoclaves and hollow specimens with inner hydrogen pressure were used for the tests. Various influencing factors on hydrogen embrittlement, such as temperature, pressure, gas purity, strain rate, and frequency, were investigated and individually discussed. Chapter 7 introduces an analytical approach to model short crack growth with elastic-plastic fracture mechanics. The effects of hydrogen on enhanced crack growth are considered by the developed hydrogen damage parameter $Z_{D,H}$, which is based on the damage parameter Z_D accounting for fatigue damage in air according to Heitmann [1]. Hydrogen diffusion is taken into account based on Fick's law and hydrogen occupation of dislocations based on Oriani's equilibrium relationship between lattice and trap occupation. With this model the fatigue life under hydrogen is modeled and compared to experiments over a wide range of temperature, pressure, frequency and strain range. The model is critically discussed in terms of its advantages and disadvantages. A global discussion including all results is presented in Chapter 8. Chapter 9 summarizes the key findings and draws conclusions.

2 Fundamentals of alloy 718, fatigue crack growth and hydrogen effects

In this chapter, the state of the art in the relevant fields is presented. Chapter 2.1 provides an overview of the nickel-based Alloy 718 with regards to microstructure, strengthening phases, and manufacturing process and gives an introduction to low cycle fatigue with respect to Alloy 718. As an analytical model is targeted to predict the fatigue lifetime under hydrogen gas atmosphere, chapter 2.2. provides an overview of fracture mechanics in the linear-elastic and elastic-plastic regime, which is the basis for the characterization of crack growth and models for lifetime prediction. A physically based approach is used to describe the crack propagation as a function of the crack tip opening displacement ($CTOD$). Various models for taking environmental influences such as oxygen and hydrogen into account are presented. Chapter 2.3 describes the fundamentals of hydrogen in the metallic lattice, from absorption at the surface to diffusion to the crack tip and bonding to hydrogen traps and gives the most important equations for describing these processes. Chapter 2.4 provides an overview of the theories of hydrogen embrittlement and goes into more detail on the hydrogen enhanced decohesion (HEDE) and hydrogen enhanced localized plasticity (HELP) theories, which are suspected to occur with Alloy 718 [55–57]. Typical characteristics of hydrogen embrittlement are illustrated by fracture surface images.

2.1 Alloy 718

Alloy 718 (2.4668), also known under the trademark INCONEL® 718 of the Special Metals Corporation, is an age-hardenable nickel-based superalloy [58]. It primarily consists of nickel, along with considerable quantities of chromium, iron, and additional elements like molybdenum, niobium, and titanium. The compositions of the materials examined in this work are specified in Chapter 3.1. Due to its excellent tensile, fatigue, and creep resistance properties, it is often used in applications involving high loads and harsh conditions [59]. As a result, Alloy 718 “revolutionized many aspects of gas turbine engine design, and enabled these engines to be made at significantly lower cost, less weight and with simplified construction” [11].Its ability to perform well over a wide temperature range enables its use not only in gas turbines and aircraft engines at up to 700 °C [8,60] but also in cryogenic tanks for rockets at liquid hydrogen temperature of -253 °C [8]. The high resistance to corrosion and oxidation, combined with outstanding mechanical properties, makes it a favorable candidate for nuclear reactors [61,62], as well as for the oil and gas industry [9,63], and the chemical industry. Additionally, it offers very good weldability and processability [11]. Because of its high performance even under extreme conditions, Alloy 718 is in high demand in some of the most challenging industries for critical applications where reliability and performance are paramount [8,11].

2.1.1 Microstructure and strengthening

Various phases occur in Alloy 718 depending on chemical composition, heat treatment, and operating conditions [8]. The γ-phase is the face-centered cubic (FCC) austenitic matrix material, which consists mainly of nickel. Various other elements, including chromium, iron, niobium, molybdenum, titanium, and aluminum, can form substitutional or interstitial solid solutions. This solid solution formation can increase the strength [64]. However, the γ-phase of Alloy 718 is relatively weak. The highest increase in strength is achieved by precipitation hardening. Second phases are precipitated, which then serve as a barrier to the movement of dislocations. The resulting particles must then either be bowed or coherent particles can be cut. This can be represented schematically for a constant volume fraction of particles as shown in Figure 2.1. In other words, smaller particles are more likely to be cut and particles with a critical radius greater than r_{crit} are more likely to be bowed [65].

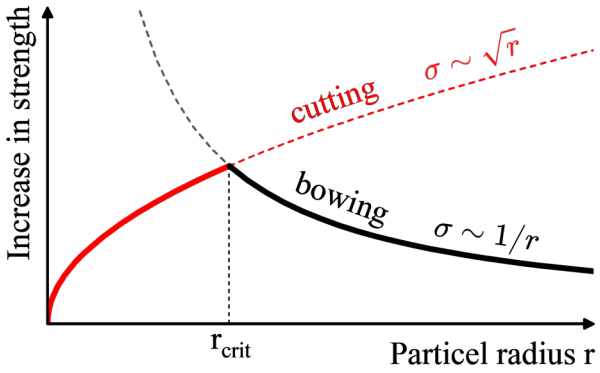


Figure 2.1: Schematic representation of the increase in strength due to precipitates. Depending on the particle size r, coherent particles are either cut or bowed. The maximum increase in strength results for the critical particle radius r_{crit}.

The main strengthening phases in nickel-based alloys are the gamma prime γ' phase, which is FCC ordered $Ni_3(Al,Ti)$ with a spherical shape, and the gamma double prime γ'' phase, which is body-centered tetragonal (BCT) ordered $Ni_3(Nb)$ with a disc-like shape [66]. However, in Alloy 718 the γ'' phase is considered the main strengthening phase by precipitation hardening [10,67–69]. As nickel has a low stacking fault energy, cross-slip with screw dislocations does not usually occur and dislocations remain in their slip planes [10]. This means that they must cut the γ' and γ'' phase. The situation is different at high temperatures, where dislocations start to climb and can bypass the particles [70]. Due to overaging, the γ'' phase can also be transformed into the delta phase (δ). The δ-phase is orthorhombic ordered Ni_3Nb and forms as large needles within grains and at grain boundaries [71,72]. Its effect on strength is minimal, but in limited quantities, it inhibits grain coarsening and increases the creep rupture resistance [73]. Furthermore, titanium nitrides (TiN) and various forms of carbides (MC, $M_{23}C_6$, M_6C, and M_7C_3) can be found in Alloy 718 [74,75]. The niobium rich hexagonal Laves phase (Fe_2Nb) can form in areas with a high niobium content [76]. As this phase can degrade Alloy 718's mechanical properties mainly through brittle fracture and by consuming most of the Nb needed for the primary strengthening phase γ'', care should be taken to ensure good homogenization of the niobium content [68].

2.1.2 Manufacturing process

Alloy 718 is used in industrial applications as a casting material as well as a wrought alloy [60,68]. Various processes such as forging, cold rolling or hot rolling are used to process the material into bars or plates. Hot rolling is carried out after homogenization and subsequent cooling in air, while cold rolling is carried out in the solution-annealed state. In this state, the strength is low and the material can be processed relatively easily. This is followed by precipitation hardening, which gives the material its high strength. A typical heat treatment is annealing at 954 °C for 1 hour with cooling in air and then a two-stage precipitation hardening at 718 °C for 8 hours, cooling at 55 °C/h to 621 °C and holding for an additional 8 hours [10,68]. Time temperature transformation diagrams (TTT diagrams) can be used to illustrate the development of the microstructure for different heat treatments. Figure 2.2 shows such a diagram for Alloy 718 with the above-mentioned heat treatment, which was also applied to the samples examined in this work.

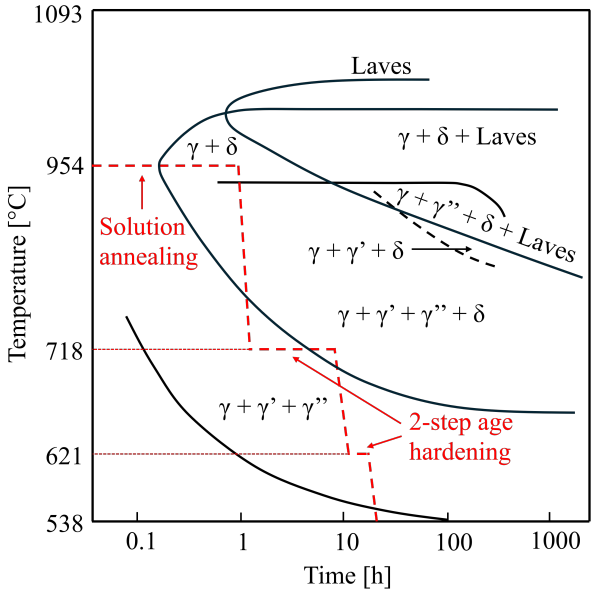


Figure 2.2: Time temperature transformation curve for Alloy 718 with commercial heat treatment of solution annealing (954 °C – 1 h) and two step age hardening (718 °C – 8h, 621 °C – 8 h) adopted from [10].

Alongside conventional manufacturing processes, additive manufacturing (AM) of components is gaining significant interest due to its considerable design flexibility [39,77,78]. AM facilitates the production of prototypes and small series with minimal investment, as well as the creation of near-net-shape components that require minimal post-processing. Laser powder bed fusion (LPBF), also known as selective laser melting (SLM), is the most widely used method for additive processing of metals [79]. Other additive manufacturing methods include direct energy deposition (DED) [80], where powder is supplied via a gas stream, and wire arc additive manufacturing (WAAM) [81], which uses wire as the material feed, like welding. These techniques are typically employed in the production of larger components. In this study, samples were examined that were manufactured using the SLM process, hence the other manufacturing processes are not discussed in detail here.

In the SLM process, metal powder is applied layer by layer and melted at selected points using a laser. Once a layer is finished, the print bed is lowered, new powder is provided, and a new layer is pushed onto the print bed using a "roller". In this way, computer aided design (CAD) models can be transferred directly and produced in a layering process. The process is shown in Figure 2.3 and details about this method can be found in Ref. [82–84].

The microstructure resulting from additive manufacturing of Alloy 718 has been investigated in several publications [37,40,44,78,85–92]. By local melting and rapid solidification, a unique microstructure is formed in additive manufacturing. Typically, the printing paths are still visible in a micrograph of the cross-section, and due to the heat flow in the building direction, a strong orientation in grain growth occurs in that direction [93]. The rapid solidification also leads to the formation of a dendritic cellular structure that increases the strength compared to Alloy 718 as cast, but is still lower than that of a precipitation-hardened Alloy 718 [36–38,94]. Additive manufacturing can also result in areas with Laves phase, which can severely impair the mechanical properties of the alloy [95,96]. When the additive-manufactured alloy is solution annealed (941 - 1010 °C), the cell structure disappears, the content of the Laves phase is strongly reduced and the formation of γ precipitates during ageing increases the strength. Mechanical values comparable to alloy 718 wrought can thus be achieved [37,40,88]. Therefore, the additive manufactured material examined in this study was always heat treated with solution annealing and two-stage precipitation hardening according to AMS5663 [97].

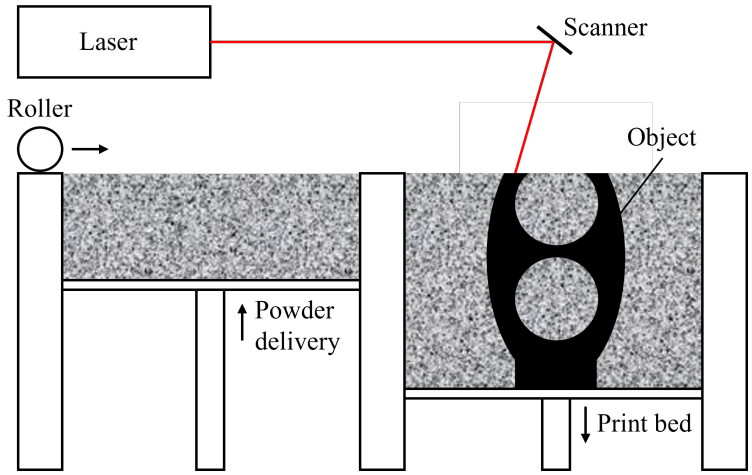


Figure 2.3: Schematic illustration of additive manufacturing using the laser powder bed fusion (LPBF) process. Metal powder is applied to the build platform using a roller and selectively melted by a focused laser beam. This process enables the component to be constructed layer by layer. Once completed, any loose powder is removed from the finished component.

2.1.3 Low cycle fatigue

During service components are usually subjected to dynamic loads which can cause fatigue damage. This can lead to component failure even though the critical static load is not reached. In this case, the load cycles until failure can be interpreted as the fatigue life of a component. Therefore, it is often necessary to consider dynamic load cases for a safe component design.

The initiation of cracks under fatigue loading is caused by local stress concentrations that lead to local plastic deformation [98]. These can occur due to surface roughness, notches, the formation of slip bands, inclusion particles, voids, precipitates, pores, and grain boundaries [99–101]. If a sufficient high load is applied to a crack it will start to grow. Depending on the length of a crack the growth can be divided into three stages [101]. In stage 1, microstructural short crack growth takes place, in which the crack is shorter than a grain and preferably grows through shear stresses in 45° orientation to normal stress. Stage 2 is dominated by physical short crack growth (length of a few grains), in which the crack is less influenced by the microstructure and the crack propagation is no longer determined by the shear stress, but by the normal stress. In this stage, cracks need high stress to grow and the plastic zone ahead of the crack is large compared to the crack length for ductile materials like Alloy 718. Crack propagation is then characterized by elastic-plastic fracture mechanics. In stage 3, cracks are long and require only low stress to grow. In this case the plastically deformed area ahead of the crack tip is small compared to the examined zone and linear-elastic fracture mechanics can be used to characterize the crack. Without significant initial defects and depending on the loading, around 90% of the fatigue life occurs in the region of microcrack growth [54]. This shows the importance of stage 2 crack growth for defect-free components and the calculation of crack growth using elastic-plastic fracture mechanics. If a component is expected to have significant defects at the start of service, which act as a starting crack $a_0 \sim 10\,mm$, the fatigue life is determined by stage 3 [101]. At this stage, the allowable loads are significantly lower, and crack propagation can be modeled using linear elastic fracture mechanics.

Alloy 718 is often used in highly stressed components under dynamic loads, such as turbine blades, nuclear reactors, and pressure vessels, due to its good mechanical properties. Under these high loads, severe plastic deformation can occur in addition to elastic deformation and only a limited number of fatigue cycles can be tolerated until a critical crack length is reached. The range of up to 10^5 cycles until failure is known as the low cycle fatigue (LCF) regime [102]. In LCF experiments failure is often defined as a technical crack length of 1-2 mm, which leads in strain controlled experiments to a drop of tensile stress by a few percent [103]. The number of cycles corresponding to this stress drop determines the fatigue life N_f. By plotting strain against fatigue life, a strain-life diagram is obtained, as illustrated for Alloy 718 in Figure 2.4. The fatigue behavior of alloy 718 has been extensively tested under various operating conditions to investigate influencing factors such as temperature [70,104–106], mean stress [107], building direction [86], fatigue creep [108] and chemical composition [109].

Temperature plays a significant role in fatigue experiments as it affects the mechanical properties of the material and consequently also its fatigue life. Especially for high-temperature applications such as gas turbines and aircraft engines, experimental results obtained at high temperatures are essential. Figure 2.4 shows the decrease in the fatigue life of alloy 718 during isothermal tests with increasing temperature and thermo-mechanical fatigue tests (TMF), where both, temperature and mechanical load is cyclically changed during the experiment.

At high temperatures, additional effects can occur that further reduce fatigue life. In alloy 718, additional damage due to oxygen has been observed at temperature above 500 °C. Carpenter et al. describe this effect as stress-assisted grain boundary oxidation [110], while Pfaendtner and

McMahon refer to it as atomic oxygen diffusion along grain boundaries and decohesion of the grain boundaries [111].

However, the influence of hydrogen on the fatigue life of alloy 718 has been relatively little studied to date. Therefore, extensive experiments under hydrogen atmosphere will be conducted in this work, and important influencing factors such as hydrogen pressure, temperature, frequency, and strain amplitude will be experimentally investigated. An overview of the current findings in literature on hydrogen embrittlement of alloy 718 is provided in Chapter 2.4.3.

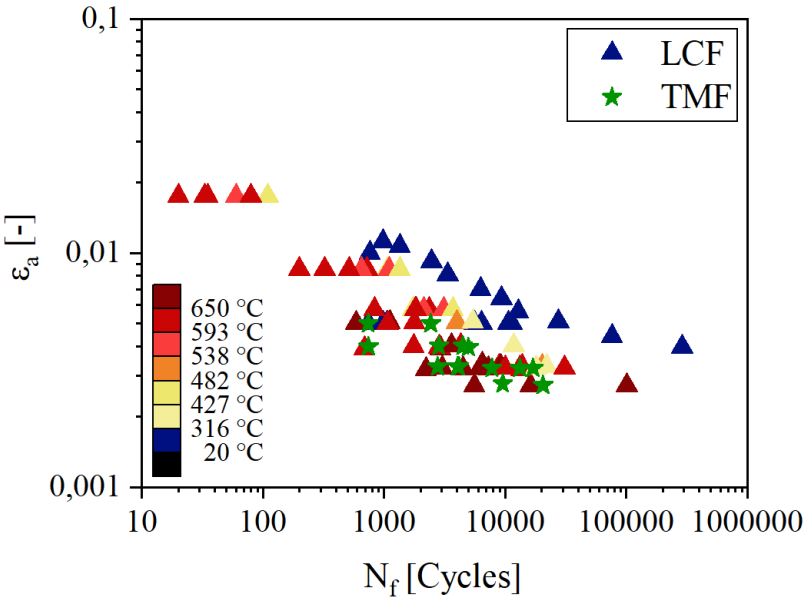


Figure 2.4: Low cycle fatigue (LCF) and thermo-mechanical fatigue (TMF) data of alloy 718 with data from Voese et al. [112] obtained for different temperatures.

2.2 Fundamentals of fracture mechanics

Fracture mechanics provides a framework for understanding the behavior of cracks under both static and dynamic loads. Utilizing fracture criteria, it allows for predictions regarding the failure of components. Cracks may develop in real materials during manufacturing due to factors such as inclusions, shrinkage cavities, or stress cracks, as well as during service from external influences.

Linear elastic fracture mechanics is effective for describing brittle fracture processes characterized by low plasticity at the crack tip, employing elasticity theory. The loading of the crack is quantified using the stress intensity factor K. Chapter 2.2.1 briefly outlines the derivation. This loading can manifest through three distinct modes of crack opening, classified as Mode I, II, and III [49], see Figure 2.5. In Mode I, stress acts normal to the plane of the crack, resulting in the opening of the crack flanks under tensile stress and their closure under compressive stress. Under Mode II and Mode III, the crack flanks slide on each other caused by shear stress. In Mode II the shear stress acts parallel to the plane of the crack and perpendicular to the crack front and in

Mode III parallel to the plane of the crack and parallel to the crack front. However, when a crack grows, it tends to align itself with the principal stresses, primarily exhibiting behavior consistent with Mode I. Consequently, for many practical applications, Mode I is often the most relevant, and thus will be the focus of this work.

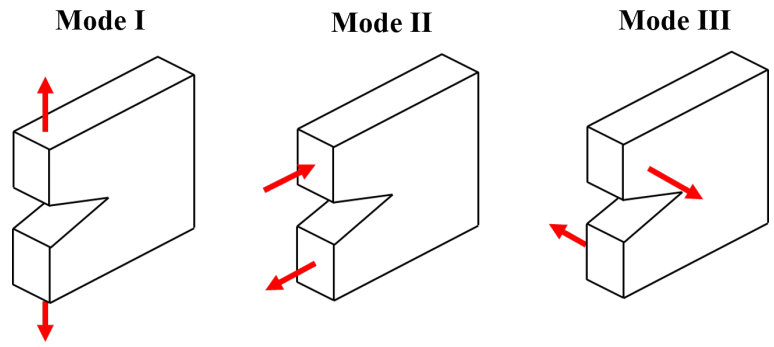


Figure 2.5: Crack loading modes: Mode I (opening), Mode II (sliding) and Mode III (tearing).

If the plastic deformations at a crack tip exceeds certain limits, linear elastic fracture mechanics becomes inadequate [1] and non-linear elastic fracture mechanics is employed to describe elastic-plastic or viscous material behavior, see Chapter 2.2.2. In this case, instead of the stress intensity factor K, the J-integral is calculated [113], which takes into account the flow behavior of the material and thus provides an adequate solution for crack loading in the elastic-plastic regime. Based on this, the crack tip opening displacement ($CTOD$) can be calculated, which represents a descriptive dimension for the load on a crack. Furthermore, experimental studies [114–116] suggest that there is a proportional relationship between $CTOD$ and the crack growth per cycle da/dN.

The following section outlines the fundamental principles of fracture mechanics that are required for the course of the work. For a detailed introduction to fracture mechanics with the derivation of formulas, reference is made to the textbook [49], for example.

2.2.1 Linear elastic material behavior

Linear elastic fracture mechanics assume that plastic deformation in front of the crack tip is small compared to the examined area, allowing the material behavior to be described in the one-dimensional case using Hooke's law

$$\varepsilon^{el} = \frac{\sigma}{E}\,, \tag{2.1}$$

where ε^{el} is the elastic strain, σ is the stress and E is the elastic modulus which quantifies the stiffness of a material.

In the case of a crack, the asymptotic stress field σ_{ij}

$$\begin{Bmatrix} \sigma_x \\ \sigma_y \\ \tau_{xy} \end{Bmatrix} = \frac{K_I}{\sqrt{2\pi r}} \tilde{f}_{\sigma_{ij}}(\varphi) \tag{2.2}$$

and the deformation u_i

$$\begin{Bmatrix} u_x \\ u_y \end{Bmatrix} = \frac{K_I}{2G} \sqrt{\frac{r}{2\pi}} \tilde{f}_{u_i}(\varphi) \tag{2.3}$$

can be described using polar coordinates centered at the crack tip with the radius r and the angle φ. The angular functions $\tilde{f}_{\sigma_{ij}}(\varphi)$ and $\tilde{f}_{u_i}(\varphi)$ are given for example by Gross and Seelig [49].

The loading of the crack tip field is described by the stress intensity factor K_I, which differs based on the crack and specimen geometries. These functions are usually calculated using finite element methods. Some examples for different crack shapes and specimen geometries are provided in Reference [49]. For a semi-circular surface crack in a semi-infinite medium, as illustrated in Figure 2.6, the stress intensity factor K_I can be calculated by

$$K_I(\lambda) = \sigma\sqrt{\pi a}\, f(\lambda)\,, \tag{2.4}$$

with the crack length a and the angular function

$$f(\lambda) = \frac{2}{\pi}\left(1.211 - 0.186\sqrt{\sin(\lambda)}\right)\,, \qquad (10° < \lambda < 170°) \tag{2.5}$$

where λ is the angle of the position of the crack front, see Figure 2.6. For the angle range from 10° to 170°, the values of the expression in parentheses in Equation (2.5) are between 1.025 and 1.133. A simple, angle-independent estimate of the stress intensity factor was proposed by Riedel [117], where the expression is substituted by a value of 1.12. This yields the simplified form

$$K_I = 1.12\frac{2}{\pi}\sigma\sqrt{\pi a}\,, \tag{2.6}$$

where the deviation from the exact solution of Equation (2.4) with (2.5) is only slight. This estimate is therefore used in the following.

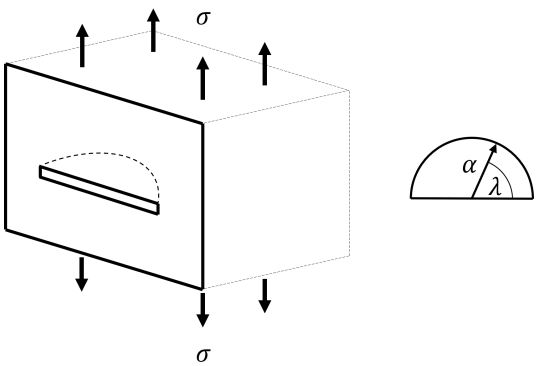


Figure 2.6: Illustration of a semi-circular crack in a semi-infinite medium, adopted from [49], where σ is the applied stress, a the crack length and λ the angle of the crack front.

2.2.2 Elastic-plastic material behavior

For ductile materials like alloy 718, the plastic zone in front of a crack becomes larger with increasing load until the material is completely plasticized. In this case, linear elastic fracture mechanics can no longer be applied, and elastic-plastic material behavior must be considered. Consequently, the K concept also becomes invalid. Alternative concepts for elastic-plastic material behavior are the J-integral concept, proposed by Rice and Rosengren [113], and the crack tip opening displacement ($CTOD$) concept [114–116].

The J-integral concept is based on the elastic-plastic material behavior of a hardening metallic material. This can be described by a simple formulation developed by W. Ramberg and R. Osgood [118]. With the three material parameters elastic modulus E, yield strength at 0.2% plastic strain σ_{YS} and the strain hardening exponent N', the Ramberg-Osgood relationship

$$\varepsilon = \varepsilon^{el} + \varepsilon^{pl} = \frac{\sigma}{E} + 0.002\left(\frac{\sigma}{\sigma_{YS}}\right)^{\frac{1}{N'}} \tag{2.7}$$

depicts the stress-strain curve that represents the flow behavior of a hardening material, where the strain ε can be divided into an elastic component ε^{el} and a plastic component ε^{pl}. In the case of significant plastic deformation ($\varepsilon^{el} \ll \varepsilon^{pl}$), the elastic strain can be neglected. In the multidimensional case, this results in the relationship

$$\varepsilon_{ij}^{pl} = \frac{3}{2} \cdot 0.002\left(\frac{\sigma_{eq}}{\sigma_{YS}}\right)^{\frac{1}{N'}-1} \frac{\sigma'_{ij}}{\sigma_{YS}}\,, \tag{2.8}$$

where σ'_{ij} is the deviatoric stress tensor and σ_{eq} the von Mises equivalent stress. According to Hutchinson [119] and Rice and Rosengreen [113], the singular stress fields σ_{ij} at a crack tip, also known as the HRR fields, can be described by

$$\sigma_{ij} = \sigma_Y\left(\frac{J}{I_{N'}0.002\sigma_Y r}\right)^{\frac{N'}{N'+1}} \tilde{\sigma}_{ij}(\varphi, N')\,. \tag{2.9}$$

Inserting this into Equation (2.8) gives the strain field

$$\varepsilon_{ij}^{pl} = 0.002\left(\frac{J}{I_{N'}0.002\sigma_Y r}\right)^{\frac{1}{N'+1}} \tilde{\varepsilon}_{ij}(\varphi, N') \tag{2.10}$$

and the displacement

$$u_i = 0.002r\left(\frac{J}{I_{N'}0.002\sigma_Y r}\right)^{\frac{1}{N'+1}} \tilde{u}_i(\varphi, N')\,. \tag{2.11}$$

Here, $\tilde{\sigma}_{ij}(\varphi, N')$, $\tilde{\varepsilon}_{ij}(\varphi, N')$ and $\tilde{u}_i(\varphi, N')$ are angular functions, which are normalized to one for there maximum value with the numerical constant $I_{N'}$. J is the J-integral, which functions as a loading parameter for a crack, similar to the K-concept in the linear elastic case. However, unlike

K, the J-integral also applies to elastic-plastic material behavior. In the two-dimensional case, it is defined as a contour integral

$$J = \oint_{\Gamma} \left(W' dy - \sigma_{ij} n_j \frac{\partial u_i}{\partial x} ds \right) , \tag{2.12}$$

with an arbitrary path Γ surrounding the crack tip [113]. Here W' is the strain energy density, n_j is the normal vector along the contour Γ with the path increment ds and u_i is the displacement vector. The strain energy density W' is defined as

$$W' = \int_0^{\varepsilon_{ij}} \sigma_{ij} d\varepsilon_{ij} \ . \tag{2.13}$$

According to [120], the J-integral can be approximated as the sum of an elastic and a plastic part

$$J = J^{el} + J^{pl} = \frac{K_I^2}{E'} + J^{pl} \ . \tag{2.14}$$

Riedel gives an approximate solution for the J-Integral of a semi-circular crack in a semi-infinite medium [117]. It is based on the solution from [121] for a circular crack in an infinite medium. With the correction factor used in Equation (2.6) for the stress intensity factor K_I of a semi-circular crack and the Poisson's ratio $\upsilon = 0.3$ of alloy 718 [58], we thus obtain the approximate solution

$$J = \left(1{,}45 \frac{\sigma^2}{E} + 2{,}4 \frac{\sigma \varepsilon^{pl}}{\sqrt{(1 + 3N')}} \right) a \tag{2.15}$$

of the J-integral for a semi-circular crack of length a.

In addition to the J-integral, the crack tip opening displacement $CTOD$ is used in fracture mechanics. It is seen as a measure of the plastic deformation at the crack tip, caused by the displacement of the crack flanks. Like the J-integral, the $CTOD$ can also be derived from the HRR crack tip fields and is therefore equivalent to the J-integral. The $CTOD$ can be defined as the displacement of a point X on the crack flank, see Figure 2.7. In the undeformed state, point X has the distance r_X from the crack tip. Under load, this point is displaced by u_x and u_y. If an angle of 45° is used to evaluate $CTOD$, the relationship between u_x and u_y is

$$u_y = r_X - u_x \ . \tag{2.16}$$

By inserting the HRR displacement fields defined in Equation (2.11) into u_x and u_y, the definition of $CTOD$ is

$$CTOD = 2 \left| u_y(r_X) \right|_{\theta=\pi} = \left[2 \frac{0{,}002^n}{I_n} \left(\tilde{u}_y(\pi) + \tilde{u}_x(\pi) \right)^n \tilde{u}_y(\pi) \right] \frac{J}{\sigma_y} = d_{N'} \frac{J}{\sigma_y} \ . \tag{2.17}$$

In Ref. [122], the expression in brackets was named $d_{N'}$ and values were calculated. Schweizer et al. described these table values with a 3rd order polynomial

$$d_{N'} = 0.78627 - 3.41692 N' + 6.11945 N'^2 - 4.2227 N'^3 \ , \tag{2.18}$$

which gives an approximate solution of $d_{N'}$ [123].

Based on the description of elastic-plastic material behavior using Equation (2.17), Chapter 2.2.3 describes the crack progression per cycle under dynamic loads. This model forms the basis for fatigue life prediction under air atmosphere and is further developed in Chapter 7 to account for the influence of hydrogen on crack propagation.

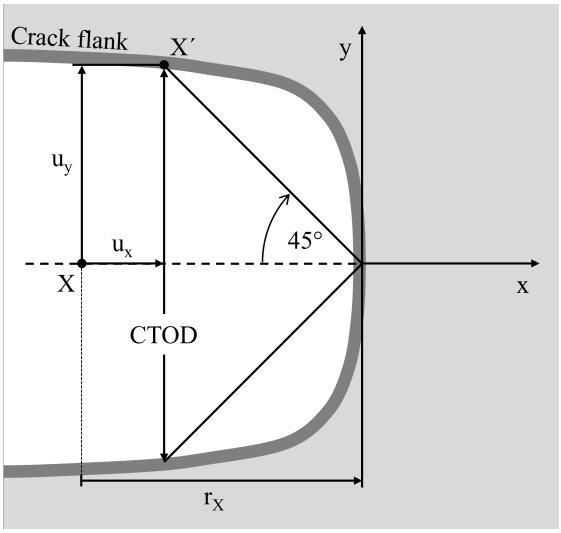


Figure 2.7: Definition of the crack tip opening displacement ($CTOD$), adopted from Ref. [124].

2.2.3 Fatigue crack growth

If the conditions of linear fracture mechanics are satisfied (low plasticity at the crack tip), fatigue crack growth can be described by the cyclic stress intensity factor ΔK. A typical progression of crack growth as a function of ΔK is shown in Figure 2.8. A crack begins to propagate only above a threshold value ΔK_{th} in stage I. In a certain range between ΔK_{th} and ΔK_{cr}, the crack growth curve can be approximated by a straight line when plotted on a double logarithmic scale, also known as Paris regime or stage II. At a critical load ΔK_{cr}, catastrophic failure occurs in stage III regime. The equation describing stage II crack growth is known as Paris' law [125]

$$\frac{da}{dN} = M(\Delta K)^m \,, \tag{2.19}$$

with the cyclic stress intensity factor ΔK, which is defined as

$$\Delta K = K_{max} - K_{min} \,, \tag{2.20}$$

and the material constants M and m. These depend on factors such as temperature, environment, load ratio, and frequency. This dependency makes it necessary to experimentally determine the material parameters for different operating conditions. Therefore, physical models that can describe these dependencies are often favored.

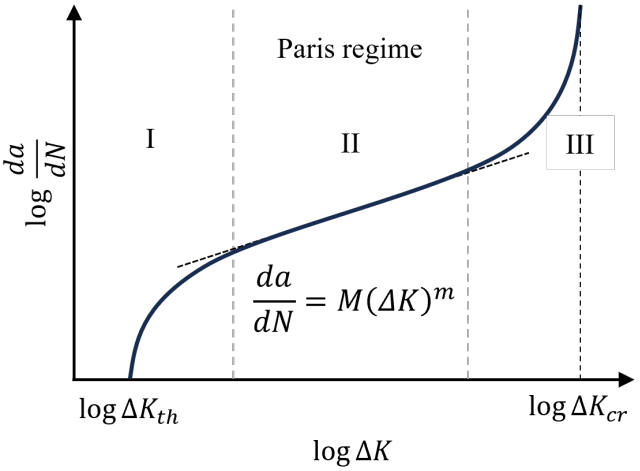


Figure 2.8: Example for the dependence between logarithmic crack growth per cycle $log(da/dN)$ and the logarithmic stress intensity factor $\log(\Delta K)$ with classification into three regimes. I. Threshold region, II. Stable crack growth region, where Pari's law accounts and III. Instable crack growth.

For elastic-plastic loading, where the linear elastic ΔK concept is no longer applicable, an elastic-plastic approach becomes necessary. In this context, the mechanism of alternating slip is considered. This mechanism states that when the crack opens under Mode I loading, plastic deformation and blunting of the crack tip takes place due to the movement of two slip systems. The resulting crack propagation cannot or only partially be reversed by crack closure. Experimental studies have consistently demonstrated this mechanism [114–116]. Therefore, this mechanism is used as the basis for a physically based crack growth model. Similar to Paris law, this model correlates crack growth per cycle $\frac{da}{dN}$ with the cyclic crack tip opening displacement $\Delta CTOD$

$$\frac{da}{dN} = \beta(\Delta CTOD)^B = \beta\left(d_{n'}\frac{\Delta J}{\sigma_{cy}}\right)^B , \tag{2.21}$$

which is proportional to the cyclic J-integral (ΔJ). B and β are material dependent proportionality factors, where B is typically between 1 and 2 and β between 0.1 and 0.5 μm^{1-B} [126,127]. These constants are determined for alloy 718 in Chapter 7.3 based on LCF tests in air.

The cyclic J-Integral was proposed by Dowling and Begley in 1976 to describe fatigue crack growth similar to the ΔK concept but in the elastic plastic regime [128]. Wüthrich showed that under certain conditions the path-independent J-integral for monotonic loads remains valid even under dynamic loads [129]. It is obtained by substituting the cyclic stress range $\Delta\sigma = \sigma_{max} - \sigma_{min}$, the cyclic strain range $\Delta\varepsilon = \varepsilon_{max} - \varepsilon_{min}$ and the cyclic hardening exponent n' into Equations (2.12) and (2.13). Using the approximation for a semi-circular crack in a semi-infinite medium under mode I loading, Equation (2.15), one obtains

$$\Delta J = \Delta J_{el} + \Delta J_{pl} = \left(1{,}45\frac{\Delta\sigma_{eff}^2}{E} + 2{,}4\frac{\Delta\sigma\Delta\varepsilon_{pl}}{\sqrt{(1+3n')}}\right)a = Z_D\, a\,, \tag{2.22}$$

where the expression in brackets is the damage parameter Z_D according to Heitmann [1]. Here, n' ist the cyclic hardening exponent according to Ramberg-Osgood and the effective stress range $\Delta\sigma_{eff}$ takes into account the fact that the crack flanks may contact prematurely during the crack's unloading phase. The effective stress range is then given by

$$\Delta\sigma_{eff} = \sigma_{max} - \sigma_{op} \,, \tag{2.23}$$

where σ_{op} is the crack opening stress. Considering the stress ratio

$$R_\sigma = \frac{\sigma_{min}}{\sigma_{\max}} \tag{2.24}$$

according to Schijve [130] and adapting it for a physically proper course for $R \leq -1$ according to Heitmann [1], the effective stress range is

$$\Delta\sigma_{eff} = 3.72\ (3 - R_\sigma)^{-1.74}\ \Delta\sigma \,. \tag{2.25}$$

2.2.4 Lifetime prediction

Based on the previously described crack growth model, the fatigue life can be estimated. For this, the number of cycles required for a crack to grow from an initial crack length a_0 to a final crack length a_f is calculated. By substituting Equation (2.22) and Equation (2.23) into Equation (2.21), one obtains

$$\frac{da}{dN} = \beta(\Delta CTOD)^B = \beta\left(d_{n'}\frac{Z_D}{\sigma_{cy}}a\right)^B \,. \tag{2.26}$$

The lifetime in cycles to failure is then calculated by separating the variables and integrating Equation (2.26) from a crack of length a_o at cycle N_0 to the final crack length a_f at cycle N_f according to Schweizer [131]

$$\int_{N_0}^{N_f} dN = \frac{1}{\beta Y^B}\int_{a_0}^{a_f}\frac{1}{a^B}da \,, \tag{2.27}$$

where a_o is typically defined as the initiation of a micro crack ($\sim 0.02\ mm$) and a_f as the initiation of a technical crack ($\sim 1\ mm$). For simplification of the integration, the crack length independent variables are summarized as

$$Y = d_{n'}\frac{Z_D}{\sigma_{cy}} \,. \tag{2.28}$$

The integration gives two different results, which are for $B = 1$

$$N_f - N_0 = \frac{\ln\left(\frac{a_f}{a_0}\right)}{\beta Y^B} \qquad (B = 1) \tag{2.29}$$

and for $B > 1$

$$N_f - N_0 = \frac{1}{\beta Y^B} \frac{\left(a_f^{1-B} - a_0^{1-B}\right)}{1-B} \,. \qquad (B > 1) \qquad (2.30)$$

Under LCF conditions the number of cycles to micro crack initiation N_0 is typically very small compared to the cycles to technical crack initiation N_f. Therefore, the cycles N_0 can be neglected when calculating the fatigue life.

The fatigue crack growth model as derived in Chapter 2.2.3 and the calculation of fatigue life as shown in Chapter 2.2.4 is used later on in Chapter 7 to model the fatigue life of LCF experiments in air from -100 °C up to 400 °C.

2.2.5 Models for environmental effects

Unidimensional analytical models were developed early on to describe the influence of hydrogen on mechanical properties or crack growth. Akhurst and Baker developed a model to predict the threshold stress intensity factor K_{th} dependence on hydrogen pressure p_{H_2} by combining a hydrogen decohesion model with the stress field ahead of a stationary crack [50]. The model assumes that subcritical cracking occurs when the tensile stress σ_{yy} exceeds the hydrogen-reduced cohesive stress

$$\sigma^* = \sigma_0^* - A\sqrt{p_{H_2}} \exp\left(\frac{\bar{V}_H\left(2.6\sigma_{yy} - 1.3\sigma_{YS}\right)}{3RT}\right) \qquad (2.31)$$

over a critical ligament length x_c. While the model successfully predicted the decrease in K_{th} with increasing hydrogen pressure p_{H_2}, it faced challenges such as uncertainty in defining the critical length x_c and measuring the material constant A and difficulty in predicting high stress concentrations near the crack tip [50].

When looking at models for crack growth under hydrogen influence, they can be classified according to Gangloff into superposition, competition, and others [132,133]. A few of these approaches are briefly described below to provide an overview of the already available models.

Superposition

The first category is superposition, where the total crack growth per cycle da/dN_{tot} consists of a mechanical fatigue component in an inert atmosphere da/dN_{fat} and an environment-related component da/dN_{env}

$$\left.\frac{da}{dN}\right|_{tot} = \left.\frac{da}{dN}\right|_{fat}(\chi) + \left.\frac{da}{dN}\right|_{env}(\psi)\,, \qquad (2.32)$$

where χ and ψ are the proportions of the total crack propagation ($\chi + \psi = 1$). This approach was used, for example, by Amaro et al. for a phenomenological model of fatigue crack growth

$$\left.\frac{da}{dN}\right|_{tot} = A\Delta K^b + \delta\left(p_H - p_{H_{th}}\right)\left.\frac{da}{dN}\right|_H , \tag{2.33}$$

Which is based on the Paris equation [134,135]. They incorporated a hydrogen pressure-dependent crack growth term, where $p_{H_{th}}$ represents the lower threshold pressure below which no hydrogen damage occurs. The crack growth under hydrogen influence is defined as

$$\left.\frac{da}{dN}\right|_H = \left(\left(\left.\frac{da}{dN}\right|_{P_H}\right)^{-1} + \left(\left.\frac{da}{dN}\right|_{\Delta K}\right)^{-1}\right), \tag{2.34}$$

where the first term is the transient component and the second term is the steady-state component of hydrogen assisted fatigue crack growth. Both terms are formulated as a function of the stress intensity, the hydrogen pressure, and the stress-dependent hydrogen concentration

$$\left.\frac{da}{dN}\right|_x = a_x\, \Delta K^{B_x}\left(p_x^{m_x} \exp\left(\frac{-Q + \bar{V}_H\sigma_h}{RT}\right)\right)^{d_x} , \tag{2.35}$$

with $x = 1$ for the transient term and $x = 2$ for the steady-state term. This model from Amaro et al. describes phenomenologically what was observed in fatigue crack growth tests on pipeline steels. However, since it is not completely based on physical principles, the transferability to other testing conditions, such as higher temperatures or other test frequencies, is not guaranteed.

Competition

The competition between fatigue and environmental crack growth is a special case of Equation (2.32) where ψ and χ are either 0 or 1. An example is the model of Austen for corrosion fatigue crack growth rates in aqueous environments [136]. In this model it is distinguished between the fatigue crack growth in reference atmosphere with crack tip blunting

$$\left.\frac{da}{dN}\right|_{tot} = \left.\frac{da}{dN}\right|_{fat} = c\left(\Delta K\sqrt{\frac{r_s}{r_b}}\right)^m , \tag{2.36}$$

where r_s and r_b are the sharp and blunted notch root radius, and fatigue crack growth with localized hydrogen embrittlement

$$\left.\frac{da}{dN}\right|_{tot} = \left.\frac{da}{dN}\right|_{env} = \left(\frac{x_p - s}{z - s}\right)(\delta_{max} - s) , \tag{2.37}$$

where x_p is the hydrogen penetration depth, z the plastic zone size, $s = M\Delta K^m$ the striation width described by Paris' Law with material constants M and m, and δ_{max} the maximum crack opening.

Other

A model to describe stage II crack growth under constant load was developed by Gerberich et al., which takes into account both hydrogen trapping and temperature effects [51]

$$\left(\frac{da}{dt}\right)_{II} = \frac{4D_{eff}}{X_{cr}}\left(1 - \exp\left(\frac{\left(E_{t,b} + \beta'\right)(T - T_{cr})}{RTT_{cr}}\right)\right)^2 , \tag{2.38}$$

where $\beta' = H_b + (\sigma_{ii}\,\bar{V}_H)/3$ with the binding energy at trap site H_b, the effective diffusion coefficient D_{eff}, the trap binding energy $E_{t,b}$, a critical distance parameter X_{cr} and the critical temperature T_{cr} above which no cracking occurs.

Existing models can already account for the influence of electrochemical or gaseous hydrogen on crack growth under many conditions, with some being more empirical in nature and others already depicting certain physical relationships. These models typically describe a time-dependent crack growth, as the model of Gerberich et al. [51], or the model for crack propagation under cyclic loading for long cracks using linear elastic fracture mechanics by Amaro et al. [134]. Currently, there are only a limited number of models that take into account crack initiation life for cracks up to 1-2 mm in length under environmental influences, although in the absence of defects, approximately 90% of the fatigue life occurs during the crack initiation phase [53,54].

A model to consider the environmental effect of oxygen on alloy 718 at elevated temperature in a short crack growth model was proposed by Schlesinger et al. [124,137]. In this model, the fatigue crack growth is modeled as presented in Equation (2.21) for short cracks with elastic-plastic fracture mechanics, based on $\Delta CTOD$. An additional environmental crack propagation is added $da/dN_{tot} = da/dN_{fat} + da/dN_{env}$, which is based on the oxygen diffusion with the penetration depth x_p. This can be described by $x_p = \sqrt{Dt} = \left(D_0 \exp\left(-\frac{H_D}{RT}\right) t\right)^{0.5}$. The proportion of oxygen in air is accounted for by the ratio of oxygen partial pressure p_{O2} to atmospheric pressure p_{atm}. The time of one load cycle is t_{cyc} and λ is an adjustable parameter that Schlesinger assumes to be 0.35 based on the value empirically determined by Gérard and Jaoul [138]. This results in the equation for crack propagation due to oxygen damage

$$\left.\frac{da}{dN}\right|_{env} = \left\{\left[\left(\frac{p_{O_2}}{p_{atm}}\right)^{\lambda} D_0^* \int_{t_{cyc}} \exp\left(-\frac{H_D}{RT}\right) dt\right]^{0.5} \Delta CTOD\right\}^{0.5} . \tag{2.39}$$

In addition to the one-dimensional models for hydrogen assisted crack growth, multidimensional modeling approaches have gained significant attention in recent years, particularly due to their ability to simulate the complex interactions between hydrogen transport and fracture mechanics. Cohesive zone models [139–147], node release models [148–150], crystal plasticity models [151–153] and phase field models [154–158] have been used to model hydrogen assisted failure and fatigue crack growth, with the various models having their advantages and disadvantages. However, these models are often associated with a high computational effort and are therefore only suitable to a limited extent for calculating crack growth with high number of cycles and many different operating conditions. The approach of this work is to find an analytical solution that can describe the crack growth of short cracks under hydrogen influence, thereby enabling a quick determination of the fatigue lifetime under various operating conditions based on physical relationships.

2.3 Fundamentals of hydrogen in metals

This chapter gives a short overview over the behavior of hydrogen as a non-ideal gas and thereafter, over the kinetics and the interactions of hydrogen and the metal lattice. This includes the adsorption, dissociation and absorption of the hydrogen molecule on the surface of the metal and the movement of atomic hydrogen in the metal lattice by diffusion processes driven by a concentration gradient [159].

2.3.1 Behavior of non-ideal gases

The behavior of an ideal gas can be described by the ideal gas law [160]

$$pV_m = RT\ , \tag{2.40}$$

where $V_m = \frac{V}{n}$ is the molar volume, R is the universal gas constant $8.3143\ J/(mol * K)$, T is the absolute temperature in Kelvin, and p is the pressure. While the ideal gas equation of state provides a good approximation for many real gases under certain conditions, factors such as intermolecular interactions and the finite volume of gas molecules can lead to significant deviations at low temperatures and high pressures. The compressibility factor

$$Z = \frac{V_m p}{RT} \tag{2.41}$$

describes the deviation of a real gas from ideal gas behavior [161]. For an ideal gas, the compressibility factor is $Z = 1$. However, for real gases applies $Z \neq 1$ and other effects like variable specific heat capacity, van der Waals forces or non-equilibrium thermodynamic effects may apply. For hydrogen gas Z increases with increasing pressure and with decreasing temperature as illustrated in Figure 2.9. There are several models to describe real gases, such as the Van der Waals, the Redlich–Kwong or the Berthelot model.

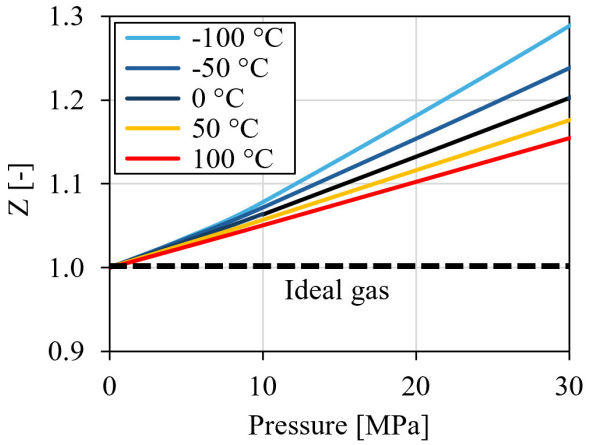


Figure 2.9: Illustration of the hydrogen compressibility factor as a function of pressure and temperature, with data from reference [162].

A simple one constant equation that can describe the behavior of hydrogen well over a very large range, by assuming that the pressure correction term a/V_m^2 of the Van der Waals equation is zero, is the Abel-Nobel equation of state [163,164]

$$V_m = \frac{RT}{p} + b_g \ , \tag{2.42}$$

where b_g is a constant for which San Marchi et al. provide a value of $b_g = 15.84\ cm^3/mol$ [165]. Due to the simplicity of the Abel-Noble model, it will be used in this work for hydrogen gas. San Marchi et al. showed that for hydrogen gas the compressibility factor

$$Z = 1 + \frac{pb_g}{RT} \tag{2.43}$$

derived from the Abel-Noble equation varies by less than 1 % from experimental data in the temperature range from 273 to 423 K and for pressure up to 200 MPa [165].

The deviations of a real gas from an ideal gas also result in a deviation of the chemical potential. The fugacity was introduced to take this into account. According to San Marchi et al. [165], this can be derived from the thermodynamic relationship

$$\ln\left(\frac{F}{p}\right) = \int_0^p \left(\frac{V_m}{RT} - \frac{1}{p}\right) dp \ . \tag{2.44}$$

By substituting V_m with the ideal gas Equation (2.40), we obtain $F = p$. Using instead of the ideal gas equation the Abel-Noble Equation (2.42), the fugacity is described by

$$F = p \exp\left(\frac{pb_g}{RT}\right) . \tag{2.45}$$

This is later used to describe the influence of hydrogen pressure in the fatigue lifetime model.

2.3.2 Hydrogen permeability, solubility and diffusivity

When a metal is exposed to a hydrogen-containing environment, hydrogen as the smallest of all atoms can diffuse into the metal lattice. This process is illustrated in Figure 2.10 and requires the following steps [166,167]:

(1) Hydrogen must be present in molecular or atomic form (if hydrogen is present in atomic form, e.g. from electrochemical processes, step 3 is omitted).
(2) Hydrogen molecules are physically adsorbed on the metal surface due to van der Waals interaction forces (physisorption).
(3) Physically Adsorbed molecular hydrogen chemically reacts with the metal surface and forms (by dissociative chemisorption) new bonds between atomic hydrogen and the metal.
(4) The atomic hydrogen is absorbed to sub-surface sites.
(5) Due to different chemical potentials, hydrogen diffuses and accumulates in regions of high hydrostatic tensile stresses such as crack tips, but also at defects such as inclusions, grain boundaries and dislocations. The latter are often referred to as hydrogen traps.

(6) Hydrogen interacts with the material and affects its mechanical properties. Two well-known theories about these interactions are presented in Chapter 2.2.

The slowest step in this sequence of processes is always decisive for the speed of hydrogen absorption into the material. The hydrogen adsorption step can be hindered by oxygen, which forms an oxide layer on the components surface [168–172]. However, this layer is usually not completely dense and mechanical stresses can lead to cracks with fresh, unoccupied surfaces where hydrogen adsorption is not hindered [171,173]. The effects of oxygen are investigated with hollow specimens and discussed in Chapter 6.1.

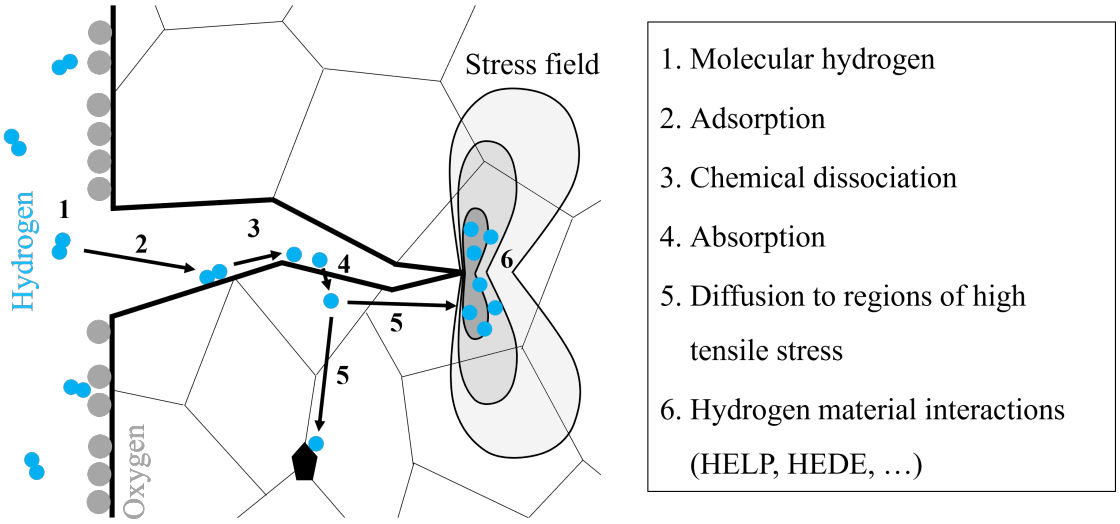


Figure 2.10: Hydrogen transport steps from gas phase to the dissolved state in the metal lattice and the diffusion to regions of high stress, such as crack tips and inclusions.

In recent years, many studies have been carried out on barrier layers with a low permeation rate in order to minimize hydrogen uptake into an underlying material. Some promising approaches were summarized by Rönnebro et al. in a review article [174]. However, the requirements for a barrier layer can be very diverse and challenging depending on the application conditions. External loads, but also hydrogen absorption in the barrier layer [167], can lead to high stress and failure of the barrier layer.

Depending on the surface conditions and the diffusion distance, either the surface reactions (1-4), the bulk diffusion (5) or the hydrogen material interactions (6) can be the limiting step in the hydrogen reaction chain. The surface reactions have been studied in several works [175,176]. The main components of the Alloy 718 (Ni, Fe, Cr) investigated in this work all show chemisorption with a high sticking probability [176]. Once the molecular hydrogen adheres to the surface, it must be chemically dissociated into atomic hydrogen. It was shown that hydrogen adsorbs and dissociates at clean Fe (110), (100) and (111) [177] and Ni (110), (100) and (111) [178,179] surfaces at room temperature and below. However, hydrogen permeation tests on Fe, Fe-Ni, and Ni materials show that at room temperature, oxide layers on the surface can reduce hydrogen permeation, which is why these tests are usually conducted with a thin palladium coating [180–182].

Although hydrogen permeation is reduced by oxygen layers, it is not completely prevented. Otsuka et al. even found that the oxide layer on Fe-Ni alloy is removed during longer tests through the reduction of the oxides and normal steady-state permeation can take place [183]. Ikeda et al. conducted permeation tests on pure nickel at room temperature and above without palladium and found good agreement with other literature data, indicating that, for nickel, experiments were not affected by an oxygen layer or other surface effects [184]. Therefore, it is reasonable to assume that at least on fresh surfaces, such as those created by cracks, hydrogen uptake is not hindered by surface effects. Nevertheless, it also shows that oxygen impurities in hydrogen gas can cover fresh surfaces again, thereby affecting hydrogen uptake.

The diffusion of hydrogen is based on H-atoms moving from areas of high concentration to areas of low concentration until equilibrium is reached. The driving force is the chemical potential. When the chemical potential is determined solely by the concentration gradient, as is the case in this work, diffusion can be described by Fick's laws of diffusion [185]. These are based on the formulation of heat conduction derived some years earlier by Fourier [186]. The first law describes the relationship between diffusive flux and the concentration gradient, and the second law describes the change in the concentration gradient over time due to diffusion.

Fick's first law is given by

$$J_D = -D\frac{\partial C}{\partial x}\,, \tag{2.46}$$

where J_D is the diffusion flux, D is the diffusivity, C is the concentration, and x is the position. If diffusion through an infinite plate of width w in steady state is considered and $C_{x=0} = C$ and $C_{x=w} = 0$, the diffusible flux is

$$J_{\mathrm{D},\infty} = D\frac{C}{w}\,. \tag{2.47}$$

The concentration C of a gas dissolved in the metal lattice can be described according to Sievert's law [187] with

$$C = S\sqrt{p}\,, \tag{2.48}$$

where S is the solubility. Replacing the pressure with the fugacity, introduced previously in Equation (2.45), and inserting Equation (2.48) in Equation (2.47), the Flux is

$$J_\infty = \frac{DS}{t}\sqrt{F}\,, \tag{2.49}$$

where D is the diffusivity, S is the solubility and the permeability is $P = DS$. The permeability, solubility and diffusivity can be described by the following Arrhenius-type relationships since these processes are thermally activated [166,188].

Permeability:

$$P = P_0 \exp\left(\frac{-H_P}{RT}\right) \tag{2.50}$$

Diffusivity:

$$D = D_0 \exp\left(\frac{-H_D}{RT}\right) \tag{2.51}$$

Solubility:

$$S = S_0 \exp\left(\frac{-H_S}{RT}\right) \tag{2.52}$$

Here, P_0, D_0, S_0 are constants, H_P, H_D, H_S are the permeation, diffusion and solution enthalpies, and T is the absolute temperature in Kelvin.

Xu et al. found that the Arrhenius type relationship for hydrogen permeability, diffusivity and solubility in Alloy 718 were rather independent of their heat treatment. Therefore, the average values for 4 different conditions (cold rolled, solution-treated, solution treated and aged 720 °C and 620 °C for 8h each and solution treated and aged 720 °C for 100 h) are given in Table 2.1 [189].

Table 2.1: Hydrogen permeation parameters for Alloy 718 [189].

	$\boldsymbol{P_0}$ $\left[\frac{mol}{m*s*MPa^{0.5}}\right]$	$\boldsymbol{H_P}$ $\left[\frac{kJ}{mol}\right]$	$\boldsymbol{D_0}$ $\left[\frac{m^2}{s}\right]$	$\boldsymbol{H_D}$ $\left[\frac{kJ}{mol}\right]$	$\boldsymbol{S_0}$ $\left[\frac{mol}{m^3*MPa^{0.5}}\right]$	$\boldsymbol{H_S}$ $\left[\frac{kJ}{mol}\right]$
Alloy 718	$2.22\ x\ 10^{-4}$	60.3	$4.06\ x\ 10^{-7}$	48.63	$5.47\ x\ 10^{2}$	11.67

The hydrogen concentration in the metal lattice can be influenced by hydrostatic stresses. In this context, tensile stress fields lead to an increased hydrogen concentration, while compressive stresses result in a lower hydrogen concentration. This can be expressed by [190,191]

$$C_{\sigma_h} = \mathrm{C} \exp\left(\frac{\bar{V}_H \sigma_h}{RT}\right), \tag{2.53}$$

where $\sigma_h = \sigma_{ii}/3$ is the hydrostatic stress and $\bar{V}_H$ is the partial molar volume of hydrogen. While the molar volume of hydrogen in BCC metals like iron is about 2 cm³ [192,193], it is about 1.7 cm³/mol for different FCC metals over a large range of hydrogen concentration [194]. Flanagan and Oates give a value of 1.65 cm³/mol for hydrogen in nickel [195].

As mentioned before, Fick's second law describes the change in the concentration gradient over time due to diffusion:

Fick's second law yields

$$\frac{\partial C}{\partial t} = D \frac{\partial^2 C}{\partial x^2}. \tag{2.54}$$

According to Crank [196], by performing a Laplace transformation of Equation (2.54), the solution

$$C(x,t) = C_1 + (C_0 - C_1)\left(\mathrm{erf}\left(\frac{x}{2\sqrt{Dt}}\right)\right) \tag{2.55}$$

is obtained for the one-dimensional diffusion problem in a semi-infinite plate, where x is the distance, t is the time, C_1 is the constant concentration at the surface of the medium, C_0 is the initial concentration in the medium and erf is the error function. From this equation it can be deduced that the penetration depth of a certain hydrogen concentration is proportional to the square root of time. A useful estimation for the one-dimensional diffusion problem of the penetration depth x_p (with $C_1 = 0$ and $C(x_p) = 0.157\ C_0$) as a function of the diffusion coefficient and time [196] is therefore

$$x_p = 2\sqrt{Dt}\,. \tag{2.56}$$

For the diffusion into a plane sheet of width $w = 2l$ from both sides, Crank [196] gives a solution of Fick's second law at time $t \geq 0$

$$C(x,t) = C_0 - \frac{4C_0}{\pi}\sum_{k=0}^{\infty}\frac{(-1)^n}{2n+1}\exp\left(-\frac{D(2n+1)^2\pi^2 t}{4l^2}\right)\cos\left(\frac{(2n+1)\pi x}{2l}\right), \tag{2.57}$$

with $-l < x < l$ and the initial concentration $C_1 = 0$, which will be used in Chapter 5.1 to estimate the time to saturate a sample with hydrogen.

2.3.3 Hydrogen traps

In addition to hydrogen dissolved in the metal lattice, it can also be bound to imperfections such as voids, inclusions, precipitates, grain boundaries, and dislocations. Depending on the binding energy, loosely trapped hydrogen is referred to as reversible traps, while strongly bound hydrogen is associated with irreversible traps. The energy levels are schematically shown in Figure 2.11. For the diffusion of a hydrogen atom from one lattice site to the next, the activation energy of lattice diffusion $E_{l,d}$ is required. When a hydrogen atom is bound to a trap, it has the trap binding energy $E_{t,b}$. To release the hydrogen atom from the trap, the trap activation energy $E_{t,a} = E_{t,b} + E_s$ must be applied, where E_s is the saddle point energy, which can be lower or higher than $E_{l,d}$ and can therefore serve to facilitate trapping and detrapping or act as a barrier that must be overcome

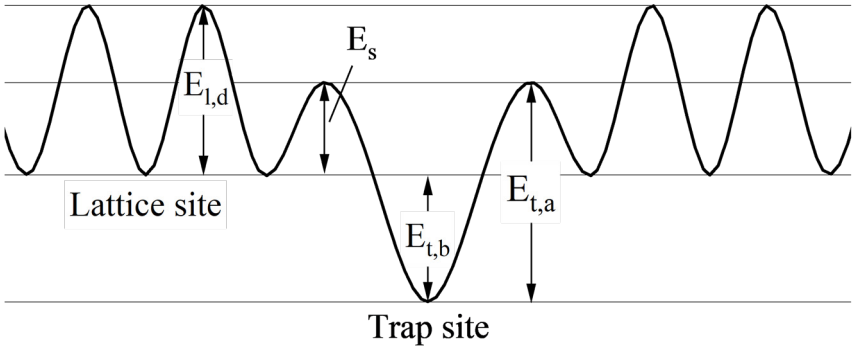


Figure 2.11: Schematic illustration of the energy levels in the metal lattice and at hydrogen traps: $E_{t,b}$ trap binding energy, $E_{t,a}$ trap activation energy, E_s saddle point energy and $E_{l,d}$ activation energy of hydrogen diffusion in the normal lattice.

The hydrogen evolution reaction between a lattice site and a trap site, which is energetically more favorable for a hydrogen atom, can be described by [197]

$$H_{trap} \rightleftharpoons Trap + H_{lattice} \,, \tag{2.58}$$

where H_{trap} is a hydrogen atom at a trap site, $Trap$ is an empty trap site and $H_{lattice}$ is a hydrogen atom at a lattice site. ΔE is the energy that is released when a hydrogen atom moves from a lattice to a trap site, which is here referred to as $E_{t,b}$ and which is inherently negative.

Based on Fermi-Dirac statistic [193], the equilibrium between hydrogen in the lattice and in traps can be described by the equilibrium constant K and the activities of hydrogen in the metal lattice a_l and in traps a_t with $K' = a_t/a_l$. If the activity is expressed in terms of fractional occupancies θ_x, with $a_x = \theta_x/(1 - \theta_x)$, the following equation is obtained [198],

$$K' = \frac{\theta_t}{(1-\theta_t)} \frac{(1-\theta_l)}{\theta_l} \,, \tag{2.59}$$

where

$$K' = \exp\left(-\frac{E_{t,b}}{RT}\right) . \tag{2.60}$$

The escape rate of hydrogen from a trap can be described based on Equation (2.58) [199] with

$$\frac{dx}{dt} = A_r(1-\zeta)^e \exp\left(-\frac{E}{RT}\right) , \tag{2.61}$$

where $\frac{dx}{dt}$ is the rate, ζ is the reacted fraction, A_r is a reaction constant and e is the empirical order of reaction.

Equation (2.61) can be used to determine the trap activation energy $E_{t,a}$ using thermal desorption spectroscopy (TDS) [197]. For this, the maximum escape rate is first determined, which is obtained by setting the derivative of Equation (2.61) to zero. According to Lee, Lee and Cho [197], this can be formulated by

$$\frac{d}{dt}\left(\frac{dx}{dt}\right) = \frac{dx}{dt}\left(\frac{E_{t,a}\phi}{RT^2} - A_r \exp\left(-\frac{E_{t,a}}{RT}\right)\right) = 0\,. \tag{2.62}$$

With the heating rate ϕ, the initial temperature T_0 and $T = T_0 + \phi t$, this can be reduced to

$$\frac{E_{t,a}\phi}{RT_p^2} = A \exp\left(-\frac{E_{t,a}}{RT_p}\right), \tag{2.63}$$

where T_p is the peak temperature at which the maximum hydrogen escape from the trap occurs. By taking the logarithm of Equation (2.63) and differentiation with respect to $1/T_p$ one obtains

$$\frac{\partial \ln\left(\phi T_p^2\right)}{\partial\left(\frac{1}{T_p}\right)} = -\frac{E_{t,a}}{R} \tag{2.64}$$

and $E_{t,a}$ can be easily determined from the slope of a $\ln\left(\phi T_p^2\right)$ vs. $\left(1/T_p\right)$ plot. Equation (2.64) is used in Chapter 5.4 for the evaluation of the activation energy by TDS experiments.

2.4 Hydrogen embrittlement

In 1875, W. Johnson reported his discovery that an iron or steel wire placed in acid subsequently breaks brittle and the tensile strain is strongly reduced. He found that after the exposure to acid, hydrogen escapes from the metal and after some time the original mechanical properties of the wire return [2]. Since then, many metallic materials have been studied in contact with hydrogen and theories on the mechanisms of hydrogen embrittlement (HE) have been proposed. Despite extensive research, the mechanisms of hydrogen embrittlement are still not fully understood. However, it is obvious that there is not just one mechanism, but that different mechanisms may take place depending on the material and environmental conditions. In some cases, several mechanisms are active simultaneously.

Hydrogen can either enter the material during the manufacturing process for example by welding or by electroplating [200,201], meaning it is already present in the material when it is put into service (internal hydrogen) or penetrate the metal during service due to corrosive processes with water, cathodic protection [202,203] or a gaseous hydrogen environment [201,204–206] (external hydrogen) .

The mechanisms of hydrogen embrittlement can be divided into reversible and irreversible HE. In reversible mechanisms mechanical properties, such as strength and ductility, can recover when hydrogen is removed by heat treatment and damage occurs only under mechanical load. In irreversible HE mechanisms, hydrogen uptake accompanies material changes, such as cracks, voids, or phase changes, that persist after hydrogen removal and can greatly reduce the material's service life [207,208].

The reversible HE mechanisms that occur only under a sufficient external load are hydrogen-enhanced strain-induced vacancies (HESIV), adsorption-induced dislocation emission (AIDE), hydrogen-enhanced decohesion (HEDE) and hydrogen-enhanced localized plasticity (HELP).

The literature provides good overviews of the hydrogen embrittlement mechanisms and its evidence [201,207]. However, it is mainly the HELP mechanism that is considered to be relevant for HE in Alloy 718 [56,209–211], but also HEDE may occur particularly at interfaces between the matrix and delta phase [56,212]. Therefore, the theories of the HELP and HEDE mechanism are presented in more detail in the following two subchapters. The current knowledge on hydrogen embrittlement of Alloy 718 is presented in Chapter 2.4.3.

Irreversible HE occurs for example when a material forms a chemical bond with hydrogen, resulting in a brittle hydride phase M_xH_y [166,213]. This transformation leads to a change in volume, which can cause significant stress and cracks in the material. This mechanism is known as hydrogen-induced phase transformation (HIPT) and materials for which this applies are V, Zr, Nb, Ta, and Ti [207]. Another irreversible mechanism, known as hydrogen pressure theory (HPT), can occur if the material has cavities in which atomic hydrogen can recombine to molecular hydrogen. This process can result in high gas pressures in the cavity, which can lead to crack growth and permanent damage [207]. High pressures in cavities, leading to permanent damage, can also occur when hydrogen combines with carbon to methane (CH_4) in carbon steels at high temperature, also known as the high temperature hydrogen attack (HTHA) [214].

In order to assess the degree of hydrogen degradation, the property of the material without hydrogen in a reference medium (air, nitrogen, helium) is usually set in relation to the property in a hydrogen atmosphere or with hydrogen pre-charging. For this purpose, the hydrogen embrittlement index (HEI)

$$HEI_{Property} = \frac{Property\ (H_2)}{Property\ (Ref)} \tag{2.65}$$

of a certain mechanical property is calculated [215]. Here a value of 1 corresponds to no difference between hydrogen and reference experiment. In tensile tests, the reduction of the cross-sectional area in the fracture region (RA) or the elongation to failure (ε_f) is usually used for assessment.

2.4.1 Hydrogen enhanced decohesion

The hydrogen enhanced decohesion (HEDE), sometimes also called hydrogen induced decohesion (HID), theory states that interatomic hydrogen leads to decreased cohesive bonding forces of the metal lattice, illustrated in Figure 2.12. The first decohesion theory was mentioned by L. Pfeil in 1926 [216]. According to Troiano's theory the electrons of the hydrogen atoms dissolved in the metal lattice can fill the d-bands of the metal atoms. The increased number of electrons in the d-band leads to an increase in the repulsive forces of the metal atoms and thus to a decrease in the cohesive forces between the metal atoms [217].

However, it is difficult to obtain experimental evidence for the exact mechanism of the HEDE theory [201]. What is generally agreed upon is that hydrostatic tensile stress at critical points, such as crack tips and interfaces between particles and the matrix, leads to hydrogen accumulation, resulting in high hydrogen concentrations. The hydrogen within the metal lattice is assumed to reduce the interatomic bonding forces, causing a sequential tensile separation of atoms at crack

tips when a critical load is reached. It is assumed that when the Crack Tip Opening Displacement ($CTOD$) reaches about half the interatomic spacing, separation occurs [201,207,218].

Dynamic simulations of grain-boundaries, performed for Ni and nickel-based alloys, support the effect of hydrogen on the destabilization of the metal-metal bonds [219]. First-principles and cohesive finite element simulations also show that cohesive energies of grain boundaries are reduced with increasing hydrogen content [220], which fits well with experimental observations of intergranular fracture under the influence of hydrogen [57,221].

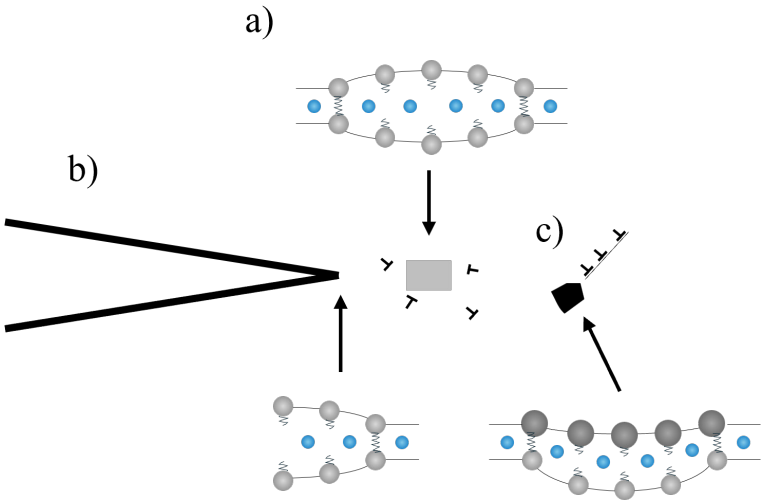


Figure 2.12: Illustration of the hydrogen enhanced decohesion (HEDE) theory showing separation of metal atoms by tensile stress. Bonding forces are weakened by (a) hydrogen atoms in the metals lattice in front of the crack tip at highest hydrostatic stresses, (b) absorbed hydrogen at crack tip and (c) hydrogen between inclusions and metal lattice, adopted from [201].

2.4.2 Hydrogen enhanced localized plasticity

The hydrogen enhanced localized plasticity (HELP) mechanism was first postulated by Beachem [222]. He states that the accumulated hydrogen due to hydrostatic stress in front of a crack tip leads to increased movement and formation of dislocations. Although this mechanism may seem contradictory to the wording embrittlement, it must be considered that due to the localization of stress and hydrogen at the crack tip, leading to a local reduction of flow stress, deformation and failure occur close to the crack tip. This reduces the macroscopic plastic deformation causing the failure to appear brittle [223].

Fractographic and in situ TEM studies by Birnbaum et al. and Lynch support the theory of increased plasticity at crack tips caused by hydrogen [223,224]. However, Lynch concludes from his results that adsorbed hydrogen at the surface of the crack tip enhances the nucleation of dislocations and induces localized slip processes and thus micro voids grow together faster, which then leads to increased crack growth [224]. This theory is also known as adsorption-induced dislocation emission (AIDE).

In contrast, Birnbaum supports the theory that the increase of plasticity is due to hydrogen, which is either already dissolved in the material or is absorbed via the crack tip, where the surface barriers are lowest due to plasticity. The segregation of hydrogen in the dilatation field of edge dislocations was for example investigated by Maxelon et al. [225]. The interactions of hydrogen and dislocations are discussed in detail by Birnbaum and Sofronis [226], where both macroscopic hardening and softening is explained. Hardening is attributed to localized slip that occurs in areas of higher hydrogen concentration, leading to increased resistance to further deformation. In contrast, softening is attributed to a reduction of dislocation barriers, allowing for easier dislocation motion. Which mechanism applies depends on conditions such as strain rate and material purity. The change of dislocation mobility is further explained by the shielding model. It states that hydrogen modifies the elastic interactions between dislocations and other stress centers, reducing the repulsive forces between dislocations and increasing the mobility [226]. The movement of a hydrogen atmosphere with a dislocation is also a strongly temperature dependent effect. At high temperature the hydrogen concentration in the atmosphere is small and at low temperature the mobility of the atmosphere is low [223]. This could explain why maximum hydrogen effects occur in the intermediate range of 200-340 K [227]. The effect of temperature will be further discussed for alloy 718 in Chapter 2.4.3.

Latest atomistic simulations support the influence of hydrogen on both, dislocation mobilization and nucleation [228]. A finite element crystal plasticity model was developed by Singh et al. to simulate the interaction between hydrogen and dislocations under the HELP mechanism. The model confirms the influence of hydrogen on the dislocation structures observed in experiments and can capture softening and hardening effects due to hydrogen [229].

2.4.3 Hydrogen embrittlement of Alloy 718

Hydrogen can enter Alloy 718 through a gaseous hydrogen atmosphere, cathodic charging, or corrosion processes. Practical applications involving hydrogen contact include rocket engines [230], sour gas applications [206], and oil and gas field applications [8,230]. When hydrogen is present as H_2 molecules, it must first dissociate at the surface to be absorbed as atomic hydrogen. From there it can diffuse via interstitial lattice sites. Lattice diffusion is relatively slow in Alloy 718 at room temperature, with a diffusion coefficient of $D \approx 10^{-15}\, m^2/s$ [231]. However, temperature, mechanical stresses, trapping, and pipe diffusion along dislocations can influence hydrogen transport through the material. Hydrogen accumulates in tensile stress fields such as those ahead of crack tips and at defects like grain boundaries, interfaces of γ' or γ'' precipitates, δ-phase, carbides, dislocations and slip bands [57,61,232,233]. Hydride phases such as TiH_x or ZrH_x do not form in Alloy 718 under technical conditions.

The mechanical properties of Alloy 718 are significantly affected by both internal and external hydrogen, with influencing factors including hydrogen concentration, pressure, gas purity, temperature, strain rate, and mechanical load amplitude, as well as the alloys' microstructure, which varies based on heat treatment and manufacturing processes. Consequently, the HEI of notched tensile strength (HEI_{NTS}) varies between 0.54 and 0.86 for different heat treatments and manufacturing processes of Alloy 718 in a 345 bar hydrogen atmosphere at room temperature [234].

Temperature plays a crucial role in hydrogen metal interactions, as its effects are reduced or eliminated at low and high temperatures [227,235]. For austenitic stainless steels the temperature of maximum hydrogen embrittlement $T_{HE,max}$ occurs at around -68 °C, while for iron- and nickel-based superalloys it is around room temperature [227]. This also applies to the $T_{HE,max}$ of smooth tensile tests and the threshold stress intensity factor $K_{I(TH)}$ /K_{IC} for Alloy 718, see Figure 2.13. The influencing factors on $T_{HE,max}$ are very complex. Depending on the temperature, different steps of the hydrogen reaction chain, as described in Chapter 2.3.2, can become limiting, as they are all temperature dependent. However, it can be said for very low temperatures that the comparably slow transport of hydrogen, especially in FCC materials like Alloy 718 with low diffusivity [231], is limiting for the interactions. At high temperatures, on the other hand, hydrogen can diffuse quickly within the material and is available in relatively high quantities. Borchers et al. conclude that the low interactions at high temperatures are due to the low trapping probability at dislocations, and activation energies for release can be easily overcome by thermal energy [236]. Birnbaum shares a similar perspective, emphasizing the critical role of the hydrogen atmosphere at dislocations. This atmosphere is most pronounced when the lattice concentration is high and the temperature is low, as illustrated by Equation (2.59) from Oriani, which describes the equilibrium between lattice occupancy and trap occupancy. Birnbaum attributes the limited interactions at low temperatures to the low mobility of the atmosphere, which cannot move along with the dislocation. And for high temperatures, he agrees with Borchers et al. that the low concentration at the dislocations is decisive for the low interaction [223]. These mechanisms play a crucial role in crack growth under hydrogen influence and are considered and further discussed in Chapter 7 of the mechanism-based lifetime model.

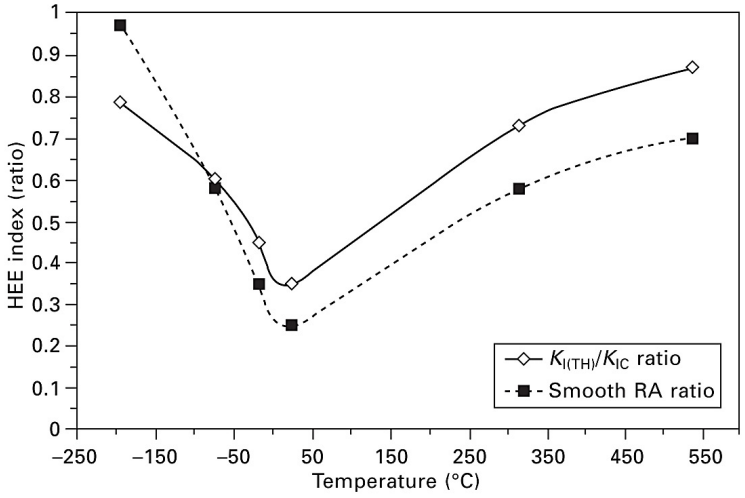


Figure 2.13: Dependence of the hydrogen environment embrittlement (HEE) index for threshold stress intensity factor ratio $K_{I(TH)}$ /K_{IC} and RA ratio on temperature for Alloy 718, tested in a 345 bar hydrogen atmosphere [166], reproduced from [237].

The influence of hydrogen pressure on the reduction of the threshold stress intensity was investigated by Moody et al. for nickel-based alloys 718 and 903 [238], see Figure 2.14. With increasing pressure, K_{th} initially decreases rapidly and then approaches a minimum. This trend is also observed for alloy 718 and other nickel-based superalloys in relation to notched tensile strength

[208]. Michler et al. examined the influence of pressure on HEI of various material classes and also found a dependence on pressure with a similar trend, which they described with an exponential function of the form $HEI \sim mf^n$ depending on the fugacity [239].

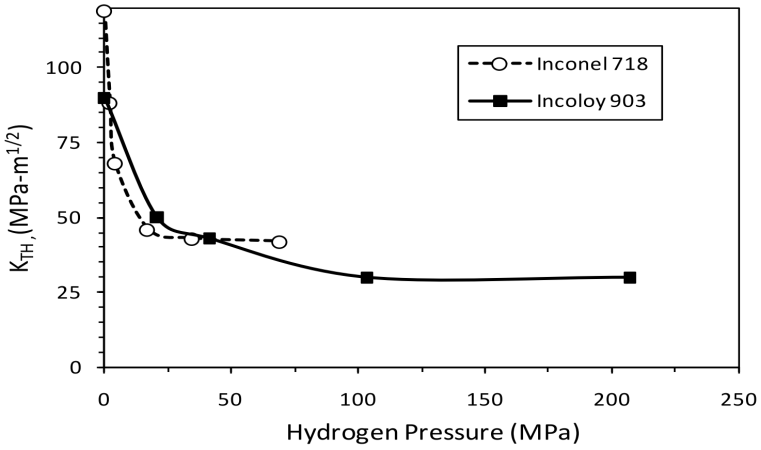


Figure 2.14: Reduction of threshold stress intensity K_{th} with increasing hydrogen pressure for alloy 718 and 903 [208], reproduced from [238].

The loading rate also has a significant effect on hydrogen damage. In pre-charged specimens, the time dependence arises from the redistribution of hydrogen by diffusion to regions with high tensile stresses [240], such as crack tips, whereas in in-situ experiments surface effects can play a role additionally, see Chapter 2.3.2. In in-situ tensile tests, little to no hydrogen embrittlement occurs at high strain rates ($\dot{\varepsilon} > 10^{-3}\ 1/s$), while a plateau forms for $\dot{\varepsilon} < 10^{-4}\ 1/s$, at which the maximum hydrogen embrittlement is reached [241]. This also applies to Alloy 718, see Figure 2.15, reproduced with data from [242]. This dependence on the loading rate not only occurs in quasi-static tensile tests, but also has a very large influence under dynamic loads [206].

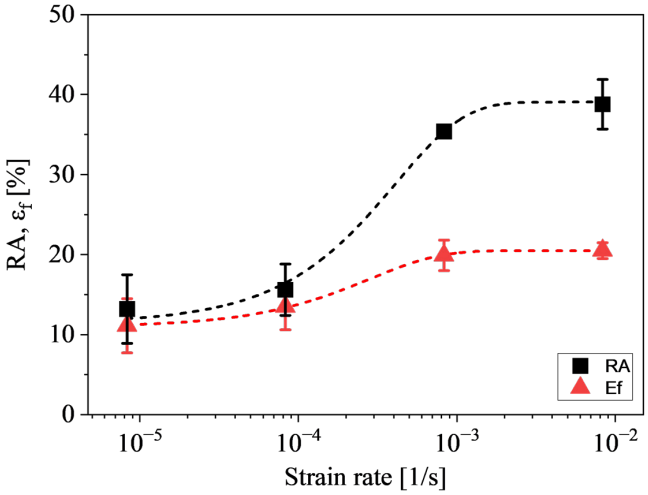


Figure 2.15: Dependence of the reduction of area (RA) and the elongation to failure (ε_f) on the strain rate for Alloy 718 in a 345 bar hydrogen atmosphere. Reproduced with data from [242].

The change in mechanical properties can be seen as a macroscopic change from ductile to brittle fracture behavior and is often associated with a change in fracture morphology, as can be seen in Figure 2.16 and Figure 2.17. Hydrogen-free Alloy 718 specimens typically exhibit quite high ductility, and the fracture surfaces are characterized by dimples and, in some cases, striations under cyclic load. If the sample is exposed to hydrogen, electrochemical or gaseous, the fracture surfaces show transgranular fracture with flat facets and steps or in some cases intergranular brittle fracture [243,244]. Flat facets that occur in transgranular fracture were identified in several studies as cleavage cracking along slip bands in {111} planes [55–57,244]. In some cases, open grain boundaries were also observed where precipitates of the δ phase were visible. The damage caused by hydrogen was predominantly attributed to the HELP mechanism, although damage caused by HEDE, particularly at δ phase-matrix interfaces are also not excluded [55–57]. For nickel-based alloy 903, Moody et al. found that a transition from slip band failure to intergranular failure occurs at high hydrogen pressure of about 1000 bar in crack growth threshold tests and calculates a hydrogen concentration of about 7000 atomic ppm (~ 125 weight ppm) in the stress field ahead of the crack tip for the specimen when transition to intergranular failure occurs [238].

Since Alloy 718 is a widely used material and is often considered for components in aerospace and nuclear industry, where they can be in direct contact to hydrogen, several factors related to hydrogen embrittlement have already been investigated, as outlined in this chapter. However, there are significant differences among the various studies regarding hydrogen charging, material condition, and experimental procedures, making direct comparisons often challenging. The influencing factors of temperature, hydrogen pressure, and strain rate have typically been assessed through tensile tests and, in some cases, fracture mechanics with long cracks. However, the impact on crack initiation in the low cycle fatigue regime has been scarcely examined. The experimental investigations presented in this work aim to provide a comprehensive foundation for understanding the factors influencing hydrogen damage in a gaseous environment. Studies of fracture surfaces offer insights into the damage mechanisms occurring at low and high temperatures, increasing hydrogen pressure, various loads, and diffusion times. Building on these findings the hydrogen damage parameter $Z_{D,H}$ will be developed to simulate fatigue life in hydrogen atmosphere under different operating conditions, based on physical relationships.

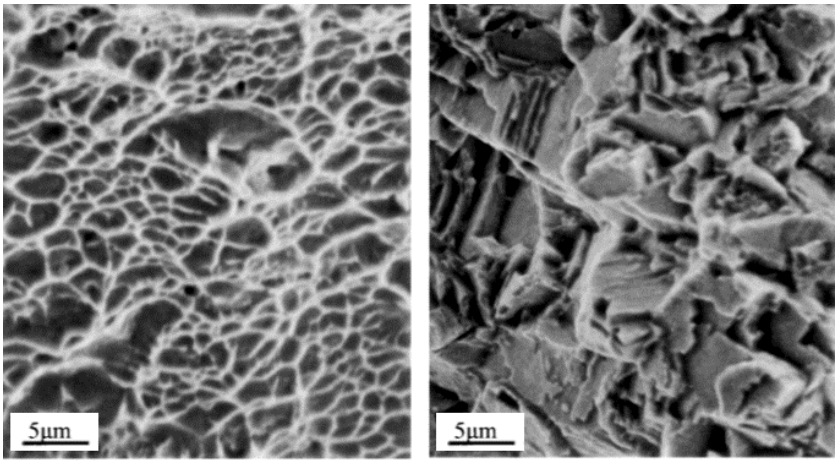


Figure 2.16: Fracture surfaces after slow strain rate tensile test of hydrogen free sample with dimples indicating ductile fracture (a) and electro-chemical pre-charged sample with cleavage morphologies indicating brittle fracture (b) [243] © copyright 2002, reprinted by permission of Informa UK Limited, trading as Taylor & Francis Group, https://www.tandfonline.com.

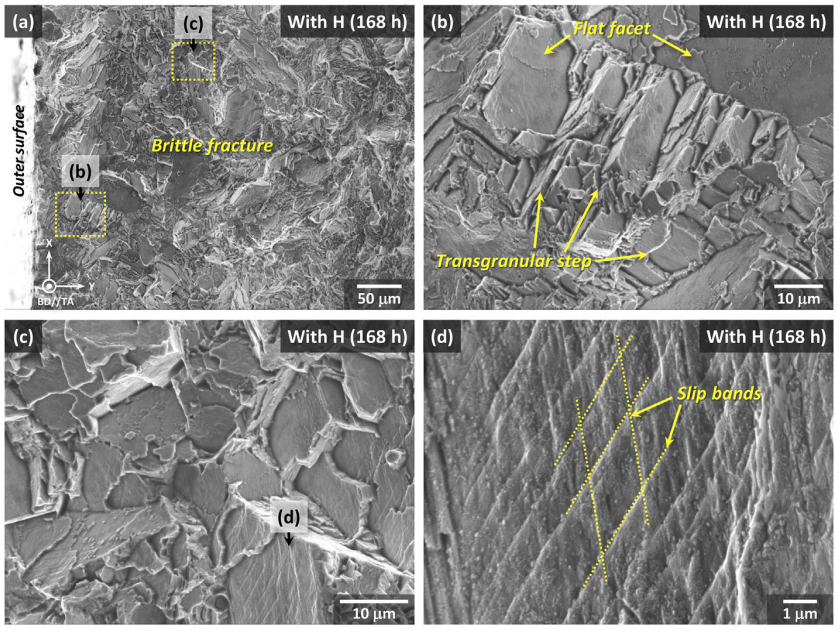


Figure 2.17: Slow strain rate tensile test of 168 h electrochemical pre-charged specimen to a diffusible hydrogen content of 32.8 wppm [244] (licensed under CC BY-NC-ND). Picture (a) shows the fracture surface of the specimen, dominated by transgranular brittle fracture (b) shows the magnification of a brittle area flat facets and transgranular steps, (c) shows a region with many flat facets and (d) a magnification of such a flat facet, where slip bands can be seen on that surface.

3 Methodology

In this chapter, the methodologies and testing procedures applied in this work are introduced. Chapter 3.1 presents the investigated materials and their heat treatment conditions. Chapter 3.2 presents a relatively small and simple setup for charging samples with hydrogen. The following chapters introduce methods for measuring hydrogen concentration (Chapter 3.3), activation energies (Chapter 3.4), and hydrogen diffusion (Chapter 3.5). Chapter 3.6 describes the microscopes used for fracture surface analysis and micrographs. In Chapter 3.7 and Chapter 3.8 the procedures for slow strain rate tensile tests and low cycle fatigue tests are explained. Chapter 3.9 describes the preparation of specimens. Experimental setups for mechanical experiments in hydrogen autoclaves and for cryogenic to elevated temperature are explained in Chapter 3.10.

3.1 Material

The conventional material Alloy 718 wrought was sourced from a supplier and the Alloy 718 SLM test pieces were manufactured by a project partner. In the SLM process, a powder with particle sizes between 10 and 63 µm was used, and the layer thickness was 50 µm. Samples were printed standing and lying with a length of 143 mm and a diameter of 14 mm [18]. The chemical composition of Alloy 718 wrought, from the material certificate, and SLM material after printing and heat treatment, measured by energy dispersive X-ray spectroscopy (EDX), are shown in Table 3.1. The chemical composition is in accordance with ASTM B637-12, except for a slightly higher molybdenum content for the SLM material. Both materials underwent a heat treatment according to AMS5663 [97] to achieve comparable strength between wrought and SLM material, whereby the cellular structure and possible Laves phase of the SLM alloy are dissolved, and γ'' precipitation increases the strength [37,40,88]. The heat treatment consists of solution annealing (941-1010 °C), air cooling, and a two-step precipitation heat treatment (718-760 °C for approximately 8 hours and 621-649 °C for approximately 8 hours). For the Alloy 718 SLM, the exact procedure was solution annealing at 980 °C for 1 hour, air cooling, and precipitation heat treated at 720 °C for 8 hours and 620 °C for 8 hours.

Table 3.1: Chemical composition of Alloy 718 wrought from material certificate and of Alloy 718 SLM measured by energy dispersive X-ray spectroscopy (EDX) (in weight %). Limit values according to ASTM B637-12.

Element	ASTM B637-12	718 wrought	718 SLM
Ni	50-55	52.91	53.04
Fe	Rest	18.45	17.67
Cr	17-21	18.39	18.54
Nb+Ta	4.75-5.5	5.19	
Nb		5.18	5.27
Mo	2.8-3.3	2.87	3.63
Ti	0.65-1.15	0.92	0.94
Al	0.2-0.8	0.55	0.64
Co	≤1	0.51	0.12
Mn	≤0.35	0.09	
Si	≤0.35	0.09	0.13
Cu	≤0.3	0.05	
C	≤0.08	0.04	
Ta		0.01	
P	≤0.015	0.008	
B	≤0.006	0.004	
S	≤0.0015	0.001	
Pb		0.0003	
Se		0.0003	
Bi		0.00003	

3.2 Hydrogen pre-charging

Hydrogen charging of samples can take place either before the mechanical test (ex-situ) or during the test (in-situ). In-situ hydrogen charging is explained in Chapter 3.10.1 for conventional specimens tested in a high pressure hydrogen autoclave and in Chapter 3.10.2 for hollow specimens with inner hydrogen pressure.

Gaseous hydrogen pre-charging was carried out to determine the hydrogen solubility in Alloy 718 wrought and SLM, as well as to perform experiments on hydrogen desorption. It was conducted at elevated temperatures to achieve saturation of the entire sample within a reasonable timeframe. Due to the slow hydrogen diffusivity in alloy 718 at room temperature ($D_{25\,°C} = 1.21\ x\ 10^{-15}\ m^2/s$) [189], this could otherwise take several years, see Chapter 5.1. Additionally, charging at elevated temperature can eliminate potential surface effects such as reduced hydrogen uptake due to oxide layers, see Chapter 2.3.2. Therefore, samples were charged at a temperature of 350 °C and a pressure of 100 bar. As precipitates form in Alloy 718 above 500 °C, see Figure 2.2, it is here assumed that the microstructure is not affected from pre-charging at 350 °C. This is confirmed by micrographs of the initial material and pre-charged material showing no difference in microstructure. Hydrogen charging tests were conducted on small cylindrical specimens (diameter 6.25 mm, length 7mm) of Alloy 718 wrought and on cubes with an edge length of 5 mm

of Alloy 718 SLM. A simple experimental setup was developed that can be filled from a hydrogen gas bottle, see Figure 3.1. The sample chamber is heated with a heating wire, which is controlled by a temperature sensor and a controller.

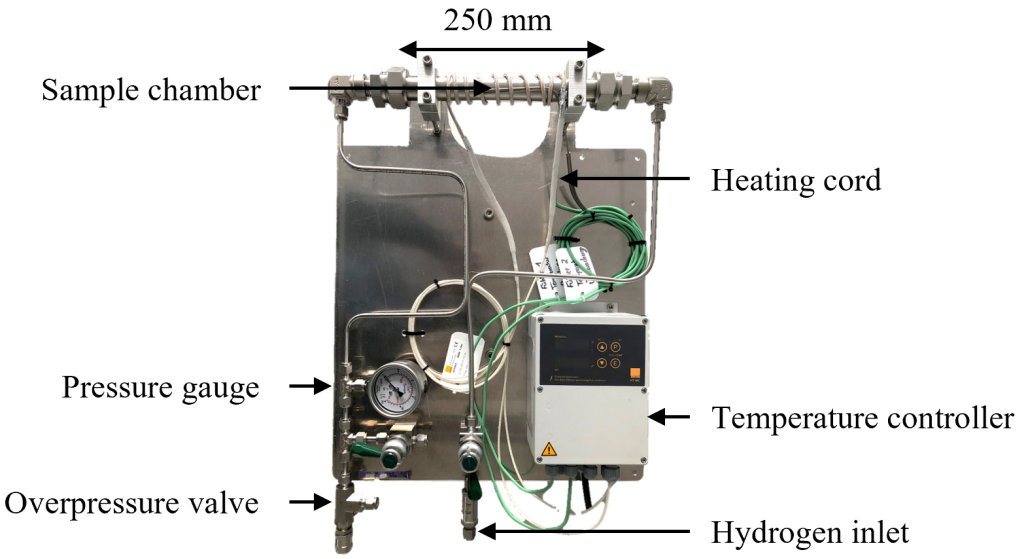


Figure 3.1: Hydrogen charging setup: Samples can be introduced to the sample chamber for hydrogen charging. The chamber can be flushed and pressurized with hydrogen gas up to 200 bar. The pressure can be measured by a manometer (as shown in Figure 3.1) or a pressure transducer to record the pressure. The sample chamber can be heated up to 400 °C with a heating cord and a temperature controller.

3.3 Carrier gas melt extraction

The hydrogen concentration in metallic samples was measured using the ELEMENTRAC OH p2 elemental analyzer from Eltra at Fraunhofer IWM. With this method, the sample is melted in a graphite crucible at temperatures reaching up to 3000 °C to release hydrogen and oxygen gas from the sample. The oxygen reacts with the graphite crucible to form carbon monoxide (CO), which is then carried away along with the released hydrogen by a carrier gas stream composed of purified nitrogen. The CO is subsequently converted to carbon dioxide (CO_2) in a catalyst oven and removed in an infrared cell with a CO_2 trap, leaving only hydrogen in the carrier gas. The concentration of hydrogen in the carrier gas is determined using a thermal conductivity detector, which compares the thermal conductivity of the measurement stream to that of a reference stream. Since hydrogen and nitrogen have different thermal conductivities, the amount of hydrogen in the measurement stream can be accurately calculated based on the difference. The measuring unit is calibrated using standards made of steel or titanium, which have a predefined hydrogen content. The final result is then the average hydrogen concentration of the measured sample [245].

3.4 Thermal desorption spectroscopy

The thermal desorption spectrometer (TDS) G4 Phoenix DH IR/TF from Bruker Elemental GmbH at Fraunhofer IWM was used in conjunction with a quadrupole mass spectrometer ESD 100 from InProcess Instruments (IPI) to measure hydrogen concentration and activation energies of hydrogen traps. Thin discs with a diameter of 12.7 mm and a thickness of 1 mm were machined from the bar material of Alloy 718 wrought and charged in a small autoclave, as described in Chapter 3.2, at 350 °C and 100 bar for 10 days. Samples were stored in liquid nitrogen after hydrogen charging to prevent it from hydrogen effusion until TDS measurements were conducted. In contrast to carrier gas melt extraction, the sample is not melted in the TDS, but heated up in an infrared oven at a settable heating rate to a maximum temperature of around 900 °C. The released hydrogen is transported through the carrier gas (N_2) to the thermal conductivity detector and additionally to a mass spectrometer. The system is calibrated using a unit that measures various volumes of calibration gas and directs it into the thermal conductivity cell. This allows for defined amounts of hydrogen to be measured for calibration.

To determine trap activation energies, the mass spectrometer signal is analyzed. By performing measurements at different heating rates, the activation energies $E_{a,T}$ for hydrogen desorption from various traps in the metal lattice (e.g., vacancies, dislocations, and inclusions) can be determined according to Lee, Lee, and Choo [197,246]. Specifically, a sample is heated at a constant heating rate while hydrogen escapes. Increasing the heating rate reduces the time available for chemical reactions to adjust, causing them to occur at higher temperatures. This results in a shift of the peak desorption temperature T_p to higher values. The activation energy can then be derived from this shift with the equation derived in Chapter 2.3.3

$$\frac{\partial \ln\left(\phi T_p^2\right)}{\partial \left(\frac{1}{T_p}\right)} = -\frac{E_{a,T}}{R}\ , \tag{3.1}$$

where T_p is the peak temperature and ϕ the heating rate. The trap activation energy $E_{a,T}$ can then easily be calculated from the slope of the $\ln\left(\phi T_p^2\right)$ vs. $\frac{1}{T_p}$ plot.

3.5 Gas permeation

A gas permeation test stand at Fraunhofer IWM was used to investigate hydrogen diffusion through Alloy 718 SLM with the aim of testing whether additive manufacturing can be used to produce a dense material and to what extent permeation is influenced by the microstructure. Since there are already many permeation measurements available in literature for Alloy 718 wrought [36,189,247,248], only the additively manufactured Alloy 718 SLM was examined in this study. Blanks with the dimensions 50x50x2 mm³ were additively manufactured. The samples were grinded from both sides down to 0.3 mm and cut out to obtain a circular metallic membrane with a diameter of 33.5 mm. The experimental setup for gas permeation tests is shown in Figure 3.2. The membrane like sample is installed between two test chambers. The low-pressure chamber is

evacuated with a turbomolecular pump and an ion getter pump down to a pressure of approximately $10^{-6}\ Pa$. The pressure side is subjected to hydrogen during the experiment (in this case with deuterium, to better distinguish the signal from hydrogen due to residual moisture). Gas that passes through the membrane into the low-pressure chamber is then measured with a quadrupole mass spectrometer of the type PrismaPlusTM QMG 220 from Pfeiffer Vacuum Technology AG. For measurements at elevated temperatures, a focused halogen radiation heater is used to heat the sample up to 260 °C, and the temperature is measured at the surface of the sample with a thermal imaging camera [249].

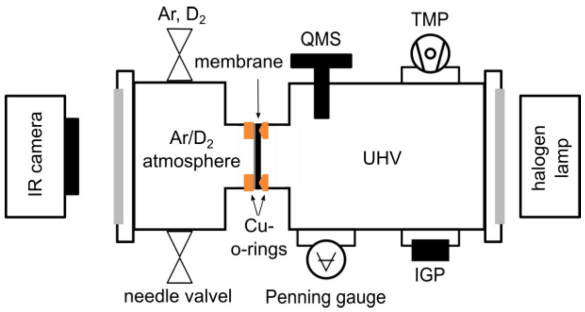


Figure 3.2: Illustration of the gas permeation test setup with quadrupole mass spectrometer (QMS), turbomolecular pump (TMP) and ion getter pump (IGP) [249] (licensed under CC BY).

3.6 Metallographic and fractographic examinations

Roughness measurements on conventional and halved hollow specimens in the hole were conducted on a Hommel T8000/TKU300 tactile profilometer with traversing length lt = 1.5 mm, cut-off wavelength λc = 0.25 mm and measuring speed vt = 0.15 mm/s according to ISO 4287/4288. The hollow samples were cut in half using wire cut EDM.

Microsections were prepared by grinding, polishing and for optical microscopy samples were etched. Beraha II or III etchant were used for etching with an etching duration of 10 to 20 seconds. The images were captured using an optical microscope, specifically the Nikon Eclipse ME 600. Additional images of the samples were taken with a Hitachi S-3400 scanning electron microscope (SEM) at Fraunhofer IWM, equipped with a tungsten cathode. In secondary electron (SE) mode, topographical images are obtained, while backscattered electron (BSE) mode provides information about the mass density of the elements. High-density elements appear brighter because they deflect more electrons than low-density elements. This allows for clear identification of precipitates in the microstructure that differ in density from the matrix material. Furthermore, the chemical composition of Alloy 718 SLM was determined using energy-dispersive X-ray spectroscopy. Details about the SEM method and the related analysis techniques can be obtained from reference [250].

Fractographic examinations of the fracture surfaces of tensile test and fatigue test samples were conducted in SE mode. Additionally, some blanks after processing the hole and some samples were sectioned to investigate sub-surface microstructure as well as secondary cracks on tested

samples. For these investigations, the Zeiss Sigma 300 scanning electron microscope at Fraunhofer IWM equipped with an electron backscattered diffraction (EBSD) system from EDAX was used. Data analysis was performed using OIM Analysis™ software version 8.6. The EBSD analysis allows for the determination of the crystallographic structure by using Kikuchi-line pattern [251]. The sample is tilted 70° to the electron beam to enhance the signal. This pattern provides information about grain structure and orientation. The kernel average misorientation (KAM) is determined from the average misorientation between a pixel and its surrounding pixels, allowing insights into the plastic deformation of the material [252–254]. This method was employed to investigate plastic deformation at crack tips and on surfaces affected by mechanical processing.

3.7 Slow strain rate tensile testing

Slow strain rate tensile (SSRT) testing was conducted to determine the quasi-static mechanical material properties in air and hydrogen atmosphere. The tests were carried out in accordance with ASTM G129-00 [255] for "Slow Strain Rate Testing to Evaluate the Susceptibility of Metallic Materials to Environmentally Assisted Cracking" and ASTM G142 – 98 [256] for the "Determination of Susceptibility of Metals to Embrittlement in Hydrogen Containing Environments at High Pressure, High Temperature, or Both". SSRT testing was performed on conventional specimens (CS) in a high-pressure hydrogen autoclave, on hydrogen pre-charged CS and on hollow specimens (HS) with inner hydrogen pressure. As it will be shown later in Chapter 6.2.5, the equivalent stress of 19.3 MPa caused by the inner pressure of 100 bar in hollow specimens is negligible compared to the yield stress of Alloy 718. The specimen geometries are shown in Figure 3.3. The extension rate for conventional specimens was 0.0009 mm/s and for hollow specimens it was 0.001 mm/s, resulting, with a parallel length of 30 mm and 33 mm, in a technical strain rate of $3x10^{-5}\ 1/s$ for both specimen geometries. This is in accordance with ASTM G129-00 [255] and below ASTM G142 – 98 [256]. The strain rate has a significant influence on hydrogen embrittlement, as will be investigated and discussed in Chapter 6.1. Another important factor for investigations under hydrogen atmosphere is hydrogen gas quality. In particular, oxygen can have a significant impact on hydrogen embrittlement. Even a few volumetric ppm of oxygen in the gas can alter the results. Therefore, a maximum oxygen content of 1 vppm is established for the test gas in [257]. The gas purity and its influence in the hollow specimen tests are also examined in Chapter 6.1. To compare SSRT tests in hydrogen atmosphere to tests in air, the relative elongation to failure

$$\mathrm{R}\varepsilon_\mathrm{f} = \frac{\varepsilon_{\mathrm{f,H_2}}}{\varepsilon_{\mathrm{f,air}}} x100\ [\%] \tag{3.2}$$

and relative reduction of area

$$\mathrm{RRA} = \frac{\mathrm{RA_{H_2}}}{RA_{air}} x100\ [\%] \tag{3.3}$$

can be calculated, where 100 % means no influence of hydrogen.

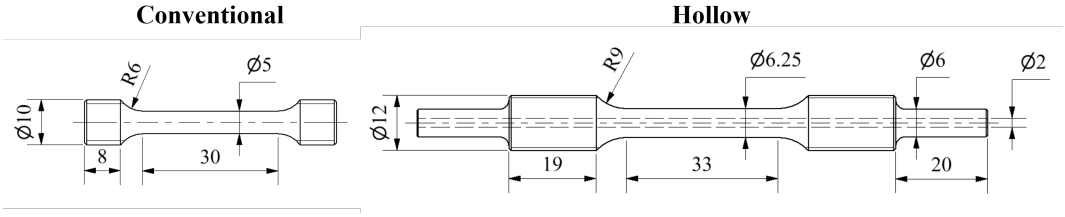


Figure 3.3: Geometries of conventional specimen (CS) and hollow specimen (HS).

3.8 Fatigue testing

Fatigue tests were carried out in the LCF regime under strain control according to E606/E606M-12 [258] and ISO 12106 [103]. As in tensile tests, LCF experiments were conducted on both, conventional and hollow specimens. However, for fatigue tests under tensile and compressive loads, specimens with a shorter gauge section are needed to avoid bending of the specimen under compressive load. The specimens' geometries are shown in Figure 3.4. The test atmospheres were either laboratory air or pressurized nitrogen or hydrogen up to 250 bar. For the hollow specimen this means that the test atmosphere is inside the hole and the outer side of the specimen is exposed to laboratory air at ambient pressure. In contrast, the conventional specimen is completely surrounded by the test atmosphere. The tests were carried out with a strain ratio of $R = -1$. The load form was sinusoidal wave, and the total strain ranges were selected so that the cycles to failure were in the range of 200 to 20,000 cycles. The same heating and cooling setups as shown in Chapter 3.10.3 for tensile tests were used for fatigue tests at low and high temperatures.

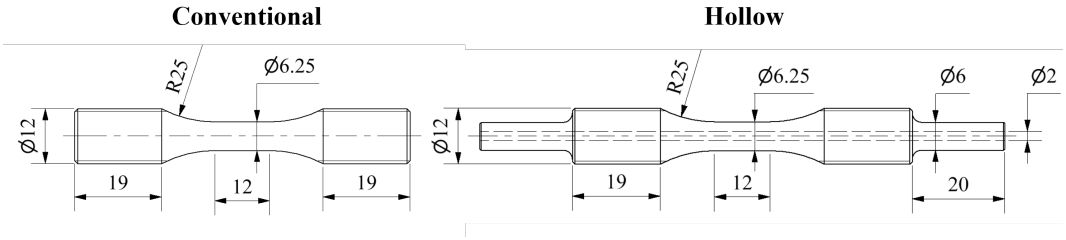


Figure 3.4: Geometries of conventional and hollow low cycle fatigue specimens.

According to ISO 12106 [103], there are different ways to determine the end of a fatigue test. The possible criteria are I) a decrease in the maximum tensile stress by a defined percentage, II) a decrease in the stress ratio by a defined percentage, or III) the fracture of the specimen. In this study, criteria I and/or II were used with a decrease of 5 % to evaluate the fatigue life, as illustrated in Figure 3.5. Assuming a semicircular surface crack of length a = 1 mm for the conventional specimen, this corresponds to a reduction of the cross-sectional area by 4.77% and thus approximately a decrease in load of 5%.

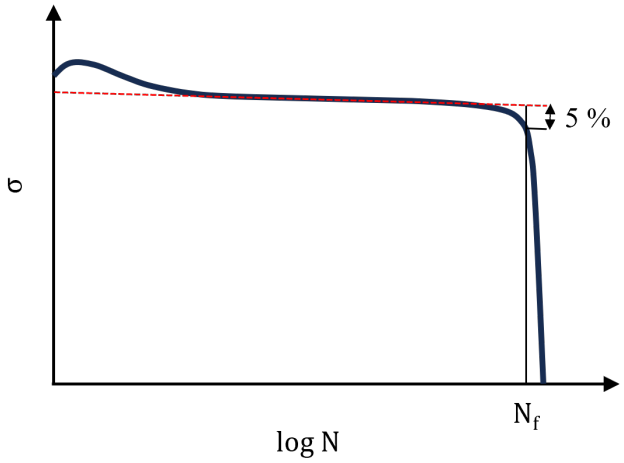


Figure 3.5: Illustration of 5 % stress drop failure criterion for hardening and then continuous softening material as is the case for the investigated alloy 718.

The results from the fatigue tests are usually presented in a $log(N_f)$-$log(\Delta\varepsilon_t)$-diagram [103], as used in Chapter 6.3. In the LCF regime, the results can usually be well fitted with a power law relationship of the form

$$\Delta\varepsilon_t = a * (N_f)^{\,b}\,. \tag{3.4}$$

In the log-log diagram, one obtains a straight line that describes the relationship between the total strain range $\Delta\varepsilon_t$ and the fatigue life N_f. Equation (3.4) is used in Chapter 6.3 to fit the experimental LCF data.

3.9 Specimen preparation

Conventional and hollow specimens were manufactured for SSRT tests and LCF tests according to the drawings in Figure 3.3 and Figure 3.4, respectively. The outer contour of the samples was manufactured on a lathe. In the last working steps, only a small amount of material was removed to reduce the entry of plastic deformation. In the final step, the surface was processed with lapping, where a small amount of material is removed to ensure minimal surface influence and low roughness. Lapping is classified as a metal cutting machining process. In this process, the surface of a workpiece is worked on using a lapping medium with loose grains in a liquid. This allows for very high form and dimensional tolerances, as well as fine surface qualities, to be achieved. The surface quality of samples can have a significant impact on the later test results, particularly in fatigue tests, as rough surfaces can serve as starting notches or residual stresses can alter the stress field.

During the manufacturing of hollow samples, a deep hole was first created in the blank. For this, a hole with a diameter of 2 mm and a length of approximately 120 mm was drilled through the blank. To create such a narrow and deep hole, the single-lip deep drilling method was used. In this method, the drill only has one cutting edge. The drill is guided by guiding rails that rest in the drilled hole. A cooling channel that runs through the drill supplies the cutting edge of the drill

with coolant and flushes the chips out of the drill hole with high coolant pressure [259,260]. This ensures high process reliability and drilling quality, however high forces may apply between the drill head and the bore wall resulting in plastic deformation within the sub-surface microstructure of the wall [261–263]. After drilling, the blank is centered on the hole in the lathe, and the outer contour is manufactured as described earlier. This ensures a high positional tolerance of the hole to the outer contour.

During this work, it became apparent that the surface-near microstructure was significantly influenced by the deep hole drilling process, see Chapter 4.2. Various manufacturing processes were investigated to achieve a surface in the hole that closely resembles the outer surface in terms of surface-near microstructure and roughness. To reduce mechanical influences, the processes of electrical discharge machining (EDM) and electrochemical machining (ECM) were used to create a hole. EDM is a precise process that removes material through controlled electrical discharge without mechanical impact. With short pulses, material removal mainly occurs through electrostatic pulses, whereas with longer pulses, melting of the material predominates [264]. Therefore, a thin heat-affected layer can be created [265–267], which must be removed. To insert a hole fast, start hole drilling EDM was used to insert a hole of about $D = 1.5\ mm$. This process takes only 3-4 minutes in contrast to sink EDM which can take several hours. However, the hole is of poor surface quality and straightness. Therefore, wire cut EDM is used to enlarge the hole to about $D = 1.95 - 1.97\ mm$ to obtain a straight hole. Several finishing cycles are performed by wire cut EDM to achieve a good surface quality.

The ECM process was also examined in this work, which uses anodic metal dissolution to remove material. An electrolyte is required between the electrode and the workpiece to enable the flow of electrons, and a flow of the electrolyte removes dissolved material. This process does not affect the surface through heat or process forces [267]. Although this technique has the advantage that no edge layer is formed that needs to be removed and low surface roughness can be expected, developing the technique to the point where samples can be produced is complex and could not be carried out in this work.

For the post-processing of the hole and the removal of an edge layer, the various processes of honing, reaming and abrasive flow machining (AFM) were investigated. In honing, material is removed with a geometrically undefined cutting edge. A rotating and oscillating motion is executed, which results in a cross-hatch pattern [268]. In reaming, a geometrically defined cutting edge is used to enlarge the hole to the desired diameter through rotating motion [269,270]. In abrasive flow machining a media with small particles is extruded through the workpiece to generate material removal, as illustrated in Figure 3.6. This process is used in aerospace, automotive, and biomedical industries for surface finish of complex parts [271].

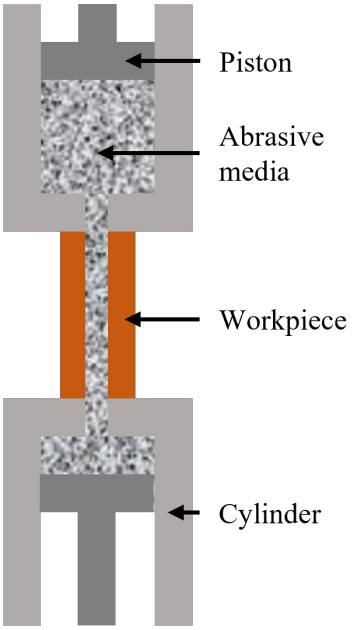


Figure 3.6: Illustration of the abrasive flow machining (AFM) process. An abrasive media is pumped through the workpiece from both sides.

3.10 Mechanical test setups

3.10.1 High pressure hydrogen autoclave

SSRT tests on conventional specimens in hydrogen gas atmosphere were conducted in a high-pressure autoclave testing system at Fraunhofer IWM. The testing setup is shown in Figure 3.7a and a drawing of the autoclave with a specimen, load cell and pull rod is presented in Figure 3.7b. It consists of a servo-hydraulic testing machine LFV 100kN from Walter + Bai, which has been equipped with a pressure vessel. This vessel can be filled with hydrogen or nitrogen at pressures up to 1000 bar and can be temperature-controlled from -40 °C to 90 °C. A linkage from the testing machine to the pressure chamber allows for mechanical loading of a sample while it is exposed to the testing medium. Both static and dynamic loads can be applied. Special cable feed-throughs into the pressure chamber enable the use and connection of measuring instruments such as load cells and extensometers within the chamber. Due to the large amount of hydrogen and the high pressure, the testing system and the laboratory are equipped with extensive safety measures.

Low cycle fatigue experiments were conducted at the Fraunhofer LBF in Darmstadt in an autoclave test system as shown in Figure 3.7c [272]. This system has a maximum pressure of 50 bar hydrogen or 10 bar nitrogen and is equipped with a servo hydraulic testing machine. The autoclave system was flushed several times until an oxygen content of < 5 vppm was reached.

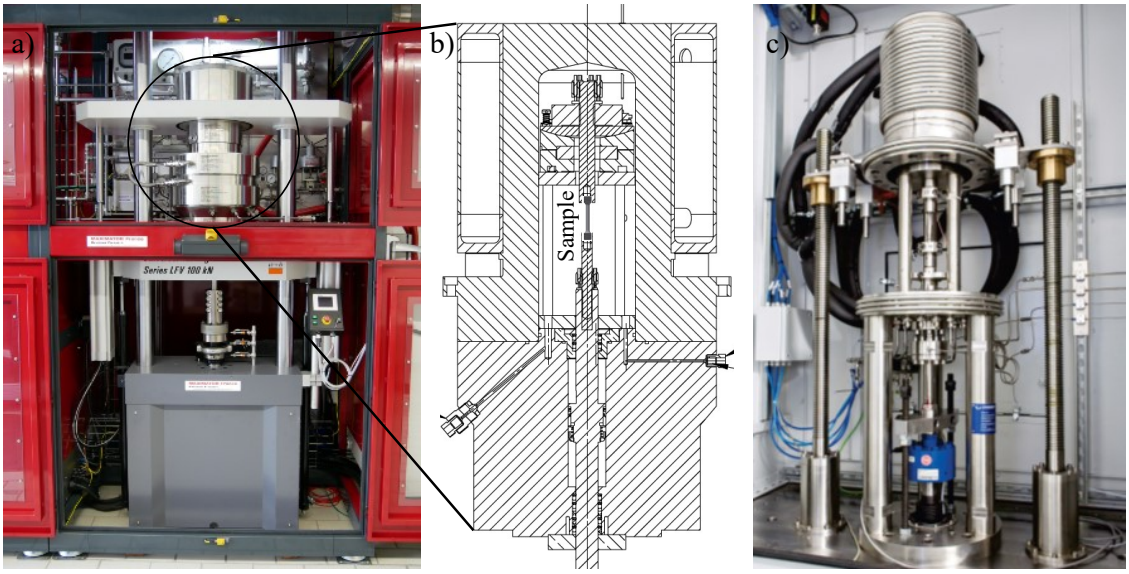


Figure 3.7: High pressure hydrogen autoclave test system at Fraunhofer IWM (a), drawing of autoclave with sample, load cell and pull rod (b) and autoclave system at Fraunhofer LBF [272] (c).

3.10.2 Hollow specimen test setup

Hollow specimen testing enables to investigate the effects of a liquid or gaseous medium on the material properties with a simple experimental setup, adaptable to existing test systems. Due to the system's small volume, highly flammable gases such as hydrogen or methane can be used without major safety precautions and experiments can be conducted in laboratory environment. With an internal system volume of approximately 0.0025 liters, an experiment at 200 bar of hydrogen pressure releases only about 0.5 liters of hydrogen to the laboratory. When the specimen ruptures, the hydrogen disperses rapidly, preventing the formation of an ignitable gas mixture in the laboratory. The gas supply connected with the hollow specimen is designed to be a portable system, allowing to flush and fill it with hydrogen outdoors before being transported indoors and installed on the testing machine. This eliminates the need for a hydrogen line in the laboratory, which is always a hazard due to possible leaks. To achieve high hydrogen gas quality, the system is flushed with 10 cycles between 10 bar and 100 bar. The theoretical remaining oxygen contamination can be calculated according to [257] with

$$C_{f,O_2} = C_{i,O_2}\left(\frac{p_{vent}}{p_{purge}}\right)^n , \tag{3.5}$$

where C_{f,O_2} is the final oxygen concentration after purging, C_{i,O_2} is the initial oxygen concentration (for ambient air $C_{i,O_2} = 20{,}94\ \%$), p_{vent} is the total minimum pressure to which the gas is released, p_{purge} is the total maximum pressure used for purging and $n \in \mathbb{N}$ is the number of purging cycles. If purging would be conducted with pure hydrogen and the specified purging procedure, a theoretical oxygen contamination of $4.87x10^{-7}$ vppm remains in the gas. However, hydrogen is typically supplied in quality grades of 5.0, with an oxygen content of ≤ 2 vppm, and

6.0, with an oxygen content of ≤ 0.5 vppm. Therefore, the theoretical value cannot be reached with the supplied gases as oxygen contamination is higher than the calculated value.

The test setup is schematically shown in Figure 3.8. The specimen is screwed into the two specimen fixtures and for LCF experiments also tightened with lock nuts. The ends of the specimen are then connected to the pipes with valves to close the system and the attached pressure gauge. This system is then filled with the test gas and installed in the testing machine. During the test, the pressure in the system is monitored via a digital pressure transducer on the testing machine. This ensures that any leaks in the system are detected, guaranteeing the desired test pressure is maintained throughout the test. Tests were conducted on a Walter + Bai LFMZ electromechanical testing system with a PCS8000 high resolution digital controller and a 100 kN load cell. The elongation during experiments was measured with a clip-on extensometer of type 3542-030M-050-LHT from Epsilon Technology Corp. with a gauge length of 25 mm for CS and 31.25 mm for HS (5 x diameter). For LCF tests a Sandner EXA 10-0,25o clip on gage is used. For high temperature experiments a MAYTEC PMA extensometer with ceramic sensing fingers was used. The pressure inside the specimen was recorded with a pressure transducer of type IMK331P with a measuring range of 0-400 bar and an accuracy of ± 0.5 %.

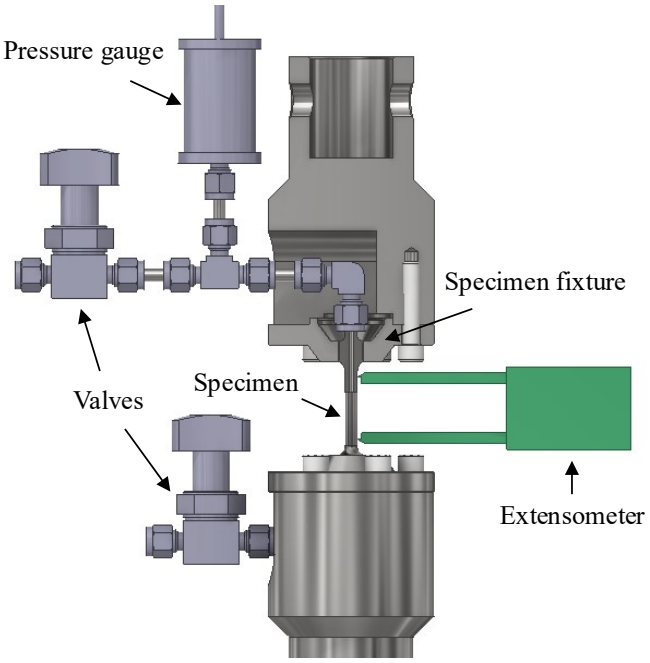


Figure 3.8: Visualization of the specimen clamping and hydrogen charging setup for slow strain rate tensile tests and low cycle fatigue tests on hollow specimens [273]. The specimen is connected with tubes to a pressure gauge and valves, which can be pressurized with hydrogen gas. The specimen is mounted to the fixtures of the pull rods. An extensometer is clipped on the specimen to measure the elongation.

3.10.3 Heating and cooling setups

Three different test rigs were built during this work to test hollow specimens between cryogenic (-196 °C) and elevated (600 °C) temperatures to investigate the influence of temperature on hydrogen embrittlement. For cryogenic experiments at -196 °C, a new testing setup was established as part of an accompanying master's thesis of Ishak Antty [274], featuring an insulated container around the test setup, which can be filled with liquid nitrogen during the experiment, see Figure 3.9. The chamber can be filled with liquid nitrogen from a tank. A fill level controller measures the nitrogen level via a sensor and automatically refills it if excessive nitrogen has evaporated. This setup allows for long-term tests over several days. Due to the high evaporation rate of nitrogen, the oxygen in the room can be displaced. Therefore, an oxygen sensor monitors the oxygen content in the room and issues a warning if it drops too low.

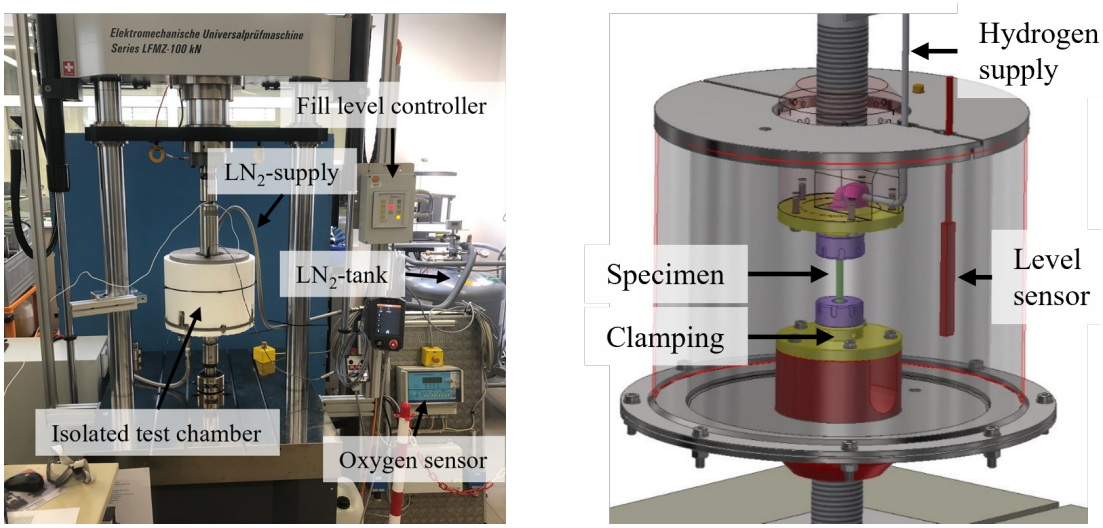


Figure 3.9: Liquid nitrogen test setup (-196 °C) on servo-electric central spindle testing machine W+B LFMZ 100 kN for tensile and LCF experiments in a liquid nitrogen bath (left). CAD drawing of the test chamber with liquid nitrogen level sensor, specimen clamping, and hydrogen supply [274].

A temperature chamber was designed and set up within this work to conduct experiments on hollow specimens in the temperature range from -100 °C to 200 °C, see Figure 3.10. The chamber was manufactured by Grip-Engineering Thümler GmbH. It can either cool by injecting kryogenic nitrogen or heat using a heating coil. The temperature chamber is connected to the testing machine, allowing the temperature to be recorded during the test. Additional thermocouples can be attached to the specimen for more accurate measurements. Due to the heat input from the specimen's clamping, the temperature measured on the specimen was significantly higher than that recorded by the temperature sensor in the chamber. Therefore, a thermocouple was directly attached to the specimen to adjust the temperature in the chamber based on the specimen's surface temperature within the gauge section.

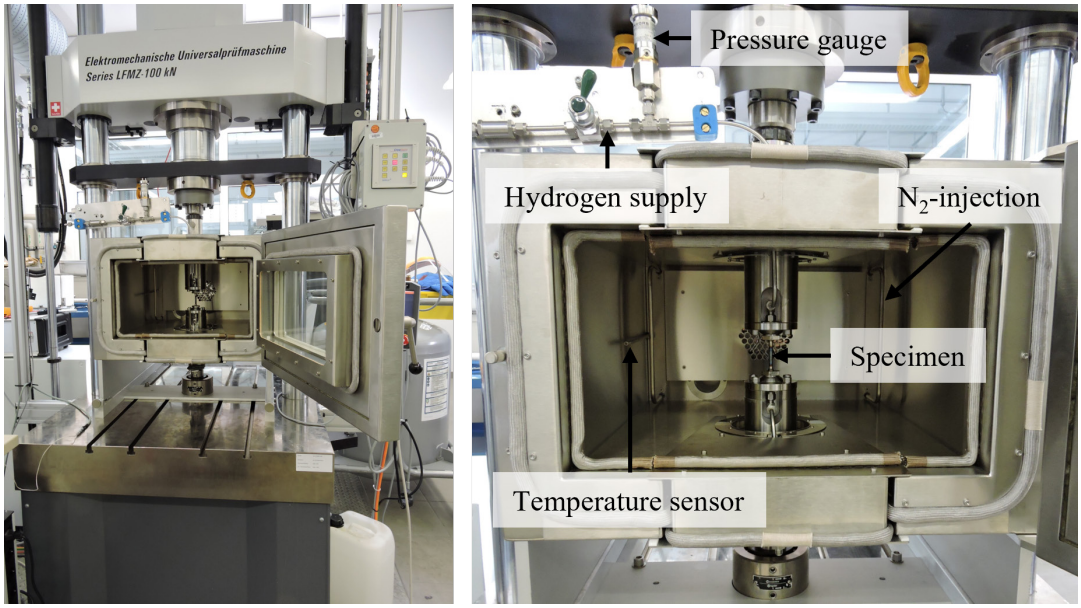


Figure 3.10: Test setup with temperature chamber (-100 °C to 200 °C) on servo-electric central spindle testing machine W+B LFMZ 100 kN for tensile and LCF experiments. Overview of testing machine (left) and detail view of the temperature chamber (right). The specimen with clamping is placed in the chamber and is temperature-controlled. The gas supply with pressure gauge and valves is outside of the chamber.

Another test stand was established during this thesis to conduct high-temperature experiments up to 1000 °C using an induction heating system, see Figure 3.11. This system induces an electromagnetic field within the induction coil, which heats electrically conductive materials. Unlike other heating methods, induction heating generates heat directly inside the specimen rather than transferring it via heat conduction, allowing for precise and rapid heating. The induction coil was bent in such a way that an opening remains through which the entire system of specimen and connected pipes can be easily installed in the induction coil. It was later adjusted to get an even temperature distribution over the gauge section. Three type K thermocouples were used to measure the temperature at different points of the gauge section of the specimen and to control the induction heating. To prevent the clamping from overheating and breaking, cooling water flows through the clamping system during experiments.

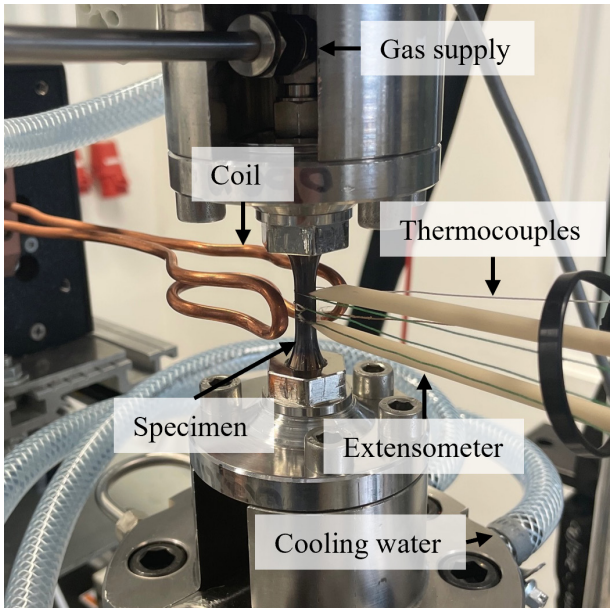


Figure 3.11: Test set up with induction heating (up to 1000 °C) on servo hydraulic multipurpose fatigue test system W+B LFV 250 kN. A water cooled induction coil is used to heat the specimen. Three thermocouples are used to regulate and control the temperature. An extensometer with ceramic sticks is used to withstand the high temperature. The clamping is cooled with water.

4 Microstructural investigations

In Chapter 4.1, the microstructure of Alloy 718 wrought and SLM conditions were investigated. Micrographs were examined by light and scanning electron microscopy to investigate grain size, shape, and precipitates. In Chapter 4.2, the effects of different manufacturing methods on surface roughness and sub-surface microstructure were investigated. Chapter 4.3 discusses the effects of additive manufacturing on microstructure, as well as the effects of the manufacturing processes of hollow specimens on surface roughness and sub-surface microstructure.

4.1 Microstructure of Alloy 718 wrought and SLM

The microstructure of both, Alloy 718 wrought and SLM, were analyzed, see Figure 4.1. The wrought material exhibits clearly defined grain boundaries with some twin boundaries. Primary precipitates were found and identified as titanium nitrides (TiN) and niobium carbides (NbC) by EDX, see Figure 4.1a. Several NbCs show cracks that must have occurred during the forming process in material production, see magnification in Figure 4.1a. Larger δ-phase precipitates (Ni_3Nb) were identified at grain boundaries using EDX. Finer precipitates can be seen in the grains, presumably at slip bands due to the strong orientation, see Figure 4.1b. γ'/γ" precipitates were not visible in the BSE image of the wrought material (Figure 4.1e). Since these are the precipitates responsible for the hardening of the material, it can be assumed that they are still present and only not visible due to their size. They can be smaller than 20 nm and are in this case only visible in TEM [68]. No significant differences were observed between the microstructures in the longitudinal and transverse directions (Figure 4.1a and c).

The SLM material exhibits elongated grains with a strong orientation in the building direction (BD), see Figure 4.1d. The grain boundaries are less distinct, with few twin boundaries observable. Some small pores, up to a few microns in size, are also present. Conversely, a slight checkered pattern is observed in the transverse direction, indicated by the white dashed lines in Figure 4.1f, resulting from the printing tracks. The BSE image (Figure 4.1b) reveals needle-like δ-phase as it was observed in the wrought material. Some smaller precipitates are visible, which could be either γ'- or γ"-phase. Based on the fact that γ" is the main strengthening phase in Alloy 718, see Chapter 2.1.1, and has about 5-6 times the thickness of γ'-phase [68], it is likely that the γ"-phase is observed here. However, due to its small size, this could not be determined with certainty.

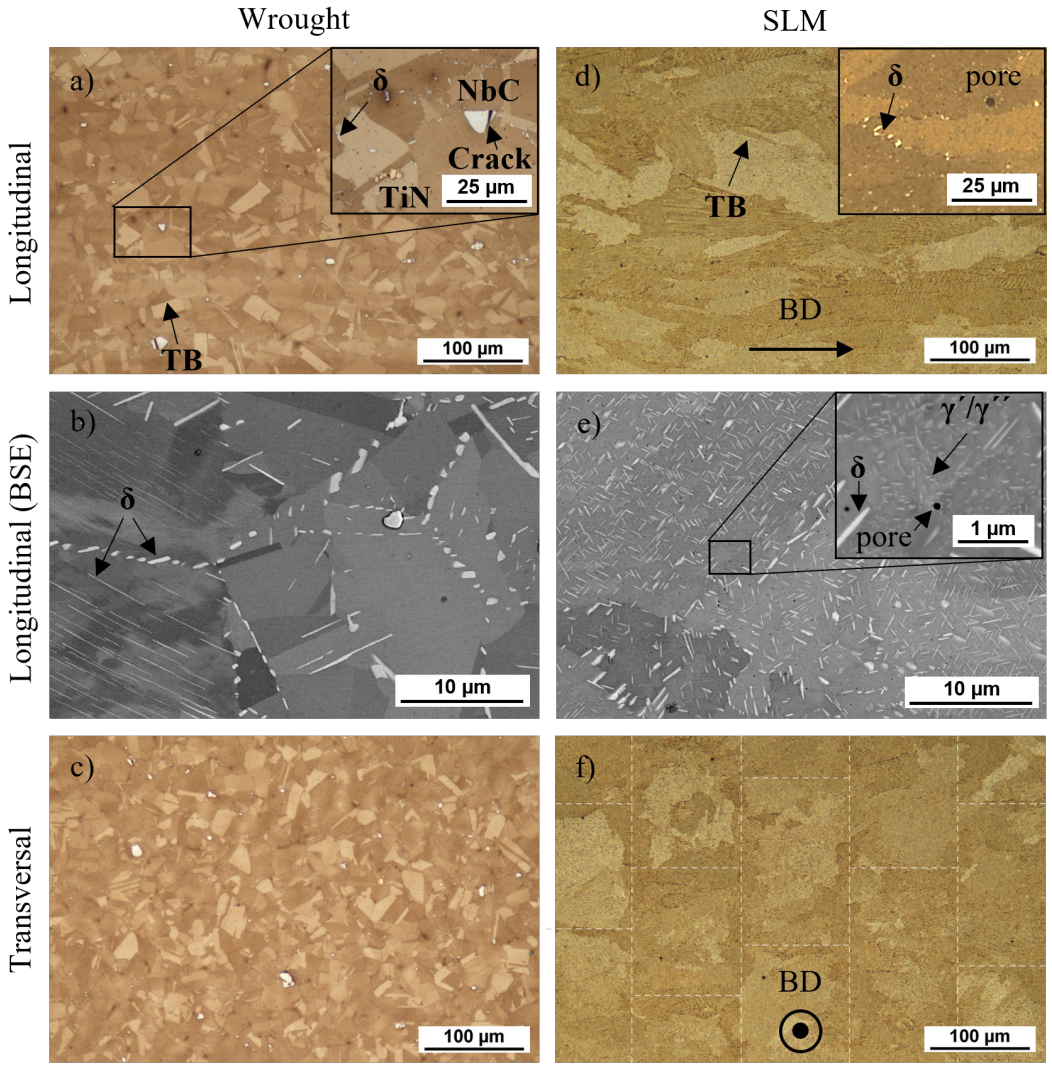


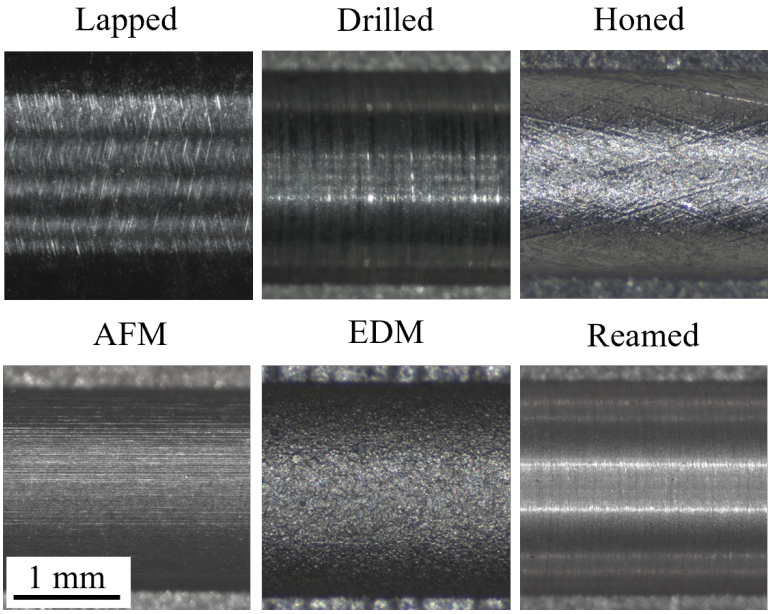
Figure 4.1: Micrographs taken by light microscope (a,c,d,f) and SEM (BSE detector) (b,e) of Alloy 718 wrought (a-c) and SLM (d-e) [273]. Wrought material with titanium nitrides (TiN), niobium carbides (NbC) and δ-phase precipitates. SLM material with pores, δ-phase precipitates, γ'- or γ''-phase precipitates and a checkered pattern in the transversal cross section (f), indicated by white dashed lines.

4.2 Roughness and microstructural changes after machining

As surface properties can have a major impact on the results of mechanical experiments [215], standards recommend procedures for specimen preparation. For SSRT tests, it is recommended not to remove more than a total of 50 µm in the last two machining passes and to obtain a maximum surface roughness of $RMS = 0.25\ \mu m$ [255]. For strain and force controlled fatigue tests, it is recommended to remove $125\ \mu m$ of the diameter in steps of $5\ \mu m$ and finally to remove $25\ \mu m$ by polishing in order to obtain a maximum roughness of $Ra = 0.2\ \mu m$ [258,275]. In addition to achieving a good surface roughness, the procedure reduces the introduction of cold work and

residual stresses. However, the recommended procedure was developed for sample preparation on a lathe. The post-processing of a hole of approximately 120 mm in length and only 2 mm in diameter is very challenging, as there are only a few methods available to machine the inner surface of such a deep hole. Therefore, various manufacturing processes for inserting the hole and to improve its quality were investigated. The details about the processes are given in chapter 3.9.

The light microscope images in Figure 4.2 and the roughness measurements, performed as described in Chapter 3.6, show that in the conventional manufacturing process using machining on the lathe followed by lapping, a fine cross-hatch pattern is created on the outer surface of the sample, and the roughness is very low with Ra = 0.025 µm. In contrast, deep hole drilling results in a bore surface with circumferential grooves. The introduction of the hole through EDM creates a comparatively rough surface (Ra = 2.23 µm), which must be post-processed in subsequent steps. Honing, reaming, and abrasive flow machining were investigated for this purpose. Honing produced a cross-hatch pattern similar to lapping, but with significantly higher roughness (Ra = 0.49 µm). Reaming, on the other hand, causes circumferential grooves similar to drilling with slightly lower roughness (Ra = 0.14 µm). AFM creates axial grooves with a roughness of Ra = 0.05 µm. ECM resulted in a roughness of Ra = 0.42 µm. Therefore, the lowest surface roughness in the hole and closest to the outer surface was reached by AFM.



Process	*Ra [µm]*	*Rz [µm]*
Lapped (outside)	*0.025*	*0.15*
Drilled	*0.23*	*1.32*
Honed	*0.49*	*3.21*
Reamed	*0.14*	*0.85*
AFM	*0.05*	*0.43*
EDM	*2.23*	*11.61*
ECM	*0.42*	*2.44*

Figure 4.2: Light microscope images of the outer surface (lapped) and the inner hole (drilled, honed, abrasive flow machined (AFM), electrical discharge machined (EDM) and reamed) with the corresponding roughness Ra and Rz.

The influence of the manufacturing processes on the microstructure was investigated using EBSD on cross-microsections of the samples, prepared as described in Chapter 3.6, see Figure 4.3. The images are arranged so that the surface appears at the right-hand side. The image of the lapped sample serves as the target surface. Here, the microstructure close to the surface (right-hand side of Figure 4.3, Lapped) was only slightly affected by the small mechanical forces during lapping, as can be seen by little change of color within the grains and some slip bands only close to the

machined surface. In contrast, the deep-hole drilling process caused significant changes of the microstructure to a depth of around 13 µm, as can be seen in Figure 4.3 (Drilled) by the greyish region where no grains can be distinguished anymore. In this region, the material is heavily deformed and recrystallized into micro grains to a depth of about 30 µm. A similar appearance can be seen in the honed (see Figure 4.3, Honed) and reamed samples (see Figure 4.3, Reamed), where the area without individual grain identification (grey region) goes about 7 µm and 5 µm deep into the material and the plastically deformed area is about 20 µm and 10 µm deep, respectively. The AFM processed surface (see Figure 4.3, AFM) only shows a little zone of influence, similar to the surface after lapping. In the electrical discharge machining (EDM) and electrochemical machining (ECM) processes, no change in the microstructure can be detected, as was to be expected, since these processes are not mechanically abrasive (see Figure 4.3, EDM and ECM). The ECM processed surface appears somewhat more smooth and precise, indicating lower surface roughness. The EBSD images indicate that mechanical processes such as drilling, honing, and reaming strongly influence the sub surface microstructure in the hole. EDM, in combination with AFM, shows only a slight influence similar to lapping on the outer surface, and is therefore the preferred process. ECM also shows promising results, but in this work it could not be developed into processing a complete sample.

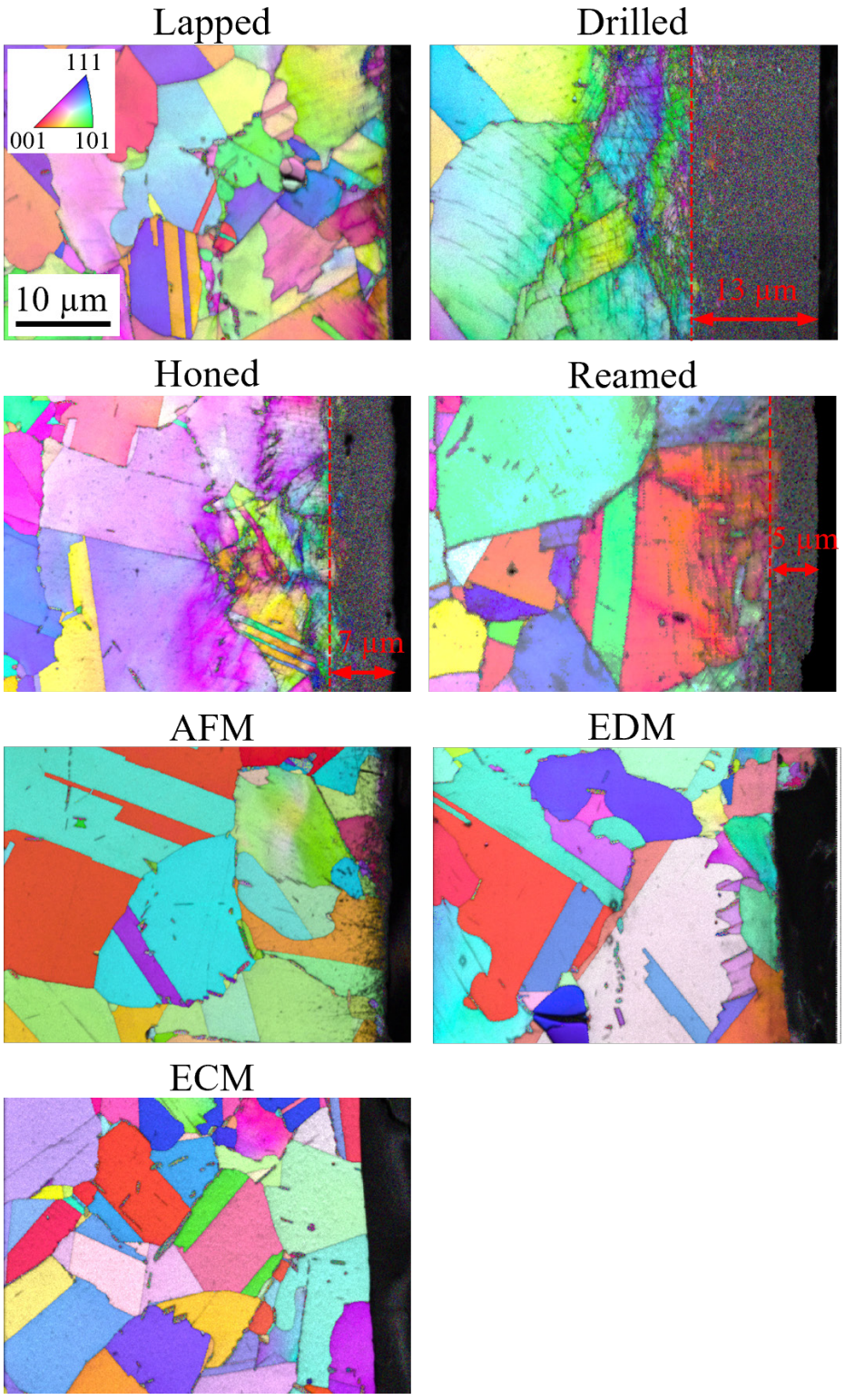


Figure 4.3: EBSD maps (image quality and inverse pole figure) of sections of the lapped outer surface and along the holes, prepared by drilling, honing, reaming, abrasive flow machining (AFM), electrical discharge machining (EDM) and electrochemical machining (ECM). The relevant surface is for all pictures at the right side.

4.3 Discussion

The microstructures of Alloy 718 wrought and SLM differ significantly, see Figure 4.1, even though both were heat treated according to AMS5663 with solution annealing (1h, 941-1010 °C), which is 250-400 °C below the melting point of Alloy 718 [58], and two-step aging (8h, 718-760 °C and 8h, 621-649 °C) [97]. The SLM material showed strongly orientated grains in building direction, as mentioned in Chapter 2.1.2. But the for the SLM process typical cellular structure [36–38,94] was not observed. This structure is destroyed by the heat treatment.

As surface properties of tensile and especially fatigue specimens can greatly influence the results of mechanical experiments, manufacturing routines and surface requirements are specified in various standards [255,258,275]. Whether these requirements can be achieved in the holes of hollow specimens was therefore of concern. Although the investigations of the hole in the hollow specimen, which was initially created by deep hole drilling, showed a relatively low surface roughness (see Figure 4.2, Drilled), the sub-surface microstructure was strongly influenced (see Figure 4.3, Drilled). This influence arises from the single-lip drill used in deep hole drilling. Due to the single cutting edge, the drill must be supported and guided against the borehole wall. This results in high friction forces and local temperatures [261–263] that affect the microstructure. This is supported by studies of Baak et al., who showed that deep hole drilling significantly alters the microstructure [262], and Nick et al., who showed that the hardness increases towards the surface, reaching up to $H_m = 725\ HV_{0.01}$ compared to $H_m = 350\ HV_{0.01}$ in the center of the specimen [261,263].

To improve the manufacturing of hollow specimens, further methods were investigated to create and post-process the holes. EDM and ECM were identified as potential processes to create a hole in the blank without mechanical influence. A small test hole made with ECM showed promising results. However, this process could not be fully developed in this work to manufacture hollow specimens with a length of approximately 120 mm. The EDM process showed that a straight hole of full length could be quickly and cost-effectively created without mechanical influence. However, the surface needs to be post-processed due to high roughness and a thin surface layer (see Figure 4.2, EDM). Honing, reaming, and AFM were investigated for this purpose. Both honing and reaming showed a mechanical influence on the microstructure of about 10 µm to 20 µm, see Figure 4.3, Honed and Reamed, which excludes these processes from post-processing, even though the affected zone is smaller than with drilling. The results align with studies by Leveille et al., who investigated the residual stresses introduced by reaming in martensitic stainless steel 15-5PH. Strong compressive residual stresses of about -800 MPa were measured [269], and the process could be numerically modeled [270]. Residual stresses are undesirable in a specimen for mechanical testing. The most promising processing method was AFM (see Figure 4.3, AFM), which mechanically removed the EDM-related surface while the roughness and the influence on the microstructure was little, similar to the influence during lapping of conventional specimens.

Most of the following experiments were conducted on as-drilled specimens as the investigations into the surfaces were developed in parallel and had not progressed that far at that time. While the surface roughness of a hole manufactured by deep hole drilling is low, the influence on the near-surface microstructure is considerable. The influence of the modified microstructure on the results is discussed in Chapter 6.

5 Investigation of the interactions between hydrogen and Alloy 718

Hydrogen embrittlement is strongly dependent on how much hydrogen is dissolved in the material, whether it is homogeneously distributed across the sample and if it is diffusible in the metal lattice or bound to hydrogen traps. Specimens for mechanical testing shall be pre-charged to saturation to achieve equilibrium, ensuring a homogeneous hydrogen distribution within the specimen. Samples were charged with hydrogen, and the concentration was measured after various charging durations using carrier gas melt extraction, see Chapter 5.1, to determine the required pre-charging time. Hydrogen charged samples were stored for several months in air at room temperature and in liquid nitrogen at -196 °C and then the hydrogen concentration was measured. This approach allows to quantify the hydrogen diffusion and desorption at both room temperature and low temperatures. Low hydrogen desorption allows to store samples prior to testing and to conducted tests over several days (Chapter 5.2). The microstructure of additive manufactured Alloy 718 SLM differs significantly from wrought material. For example grains are oriented and pores can form, see Chapter 4.1. The effects of the SLM microstructure on hydrogen diffusion were investigated in Chapter 5.3. In Chapter 5.4, the activation energies of hydrogen traps were determined using thermal desorption spectroscopy (TDS). The results are discussed in Chapter 5.5 and compared with the literature.

5.1 Hydrogen charging and solubility

Since FCC materials such as Alloy 718 have a low diffusion rate ($D_{25\,°C} = 1.21\ x\ 10^{-15}\ m^2/s$) [189] compared to BCC materials like X70 pipeline steel ($D_{25\,°C} = 7.6\ x\ 10^{-11}\ m^2/s$) [276], it can take a very long time for external hydrogen to penetrate to the center of a sample. In real life applications, hydrogen diffusion takes place over years and thus, hydrogen has time to penetrate the material. To obtain conservative test results, it is therefore advisable to pre-charge samples to saturation. Hydrogen pre-charging was conducted according to Chapter 3.2. Test results of pre-charged tensile and fatigue specimens are shown in Chapter 6.1.2 and Chapter 6.3.1.

The necessary diffusion time to reach equilibrium in the sample can be estimated by considering hydrogen charging of a plate from both sides. The time-dependent concentration profiles can be described using Equation (2.57) according to Crank [196]. With the temperature dependent diffusion coefficient, based on an Arrhenius type relationship (Chapter 2.3.2) with $D_0 = 4.06x10^{-7}\ m^2/s$ and $H_D = 48630\ kJ/mol$ [189], the hydrogen concentration profiles shown in Figure 5.1 for a plate of 5 mm thickness at 20 °C and 350 °C were simulated. At 20 °C, a month of charging results only in a few microns of penetration depth and saturation takes over 100 years. Since testing non-saturated specimens gives non-conservative results, charging must be performed at elevated temperature. At 350 °C, saturation of hydrogen in the sample can be achieved after just 4 days of charging, as shown in Figure 5.1.

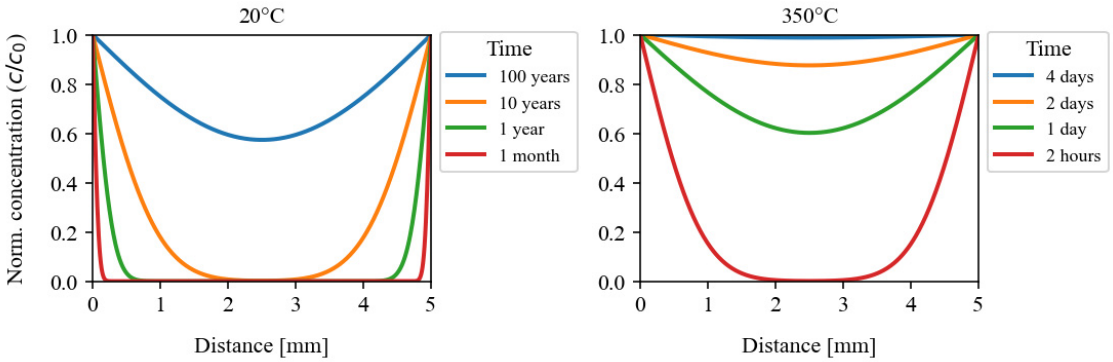


Figure 5.1: Hydrogen concentration in a plane sheet of thickness 5 mm after hydrogen diffusion from both sides for Alloy 718 at 20 °C and 350 °C.

Hydrogen charging experiments were conducted at 350°C and a hydrogen gas pressure of 100 bar, as explained in Chapter 3.2. The hydrogen content was measured using carrier gas melt extraction, see Chapter 3.3, on non-charged specimens and after several days of charging. Results are shown in Figure 5.2, with each data point representing the mean value of at least three measured specimens and their standard deviation. After three days of charging, the hydrogen content in Alloy 718 wrought was strongly increased, although the maximum content has not yet been reached. Thus, after three days, the samples were not saturated with hydrogen. After seven days of charging for Alloy 718 SLM and ten days of charging for Alloy 718 wrought, there was no significant increase in the hydrogen content with increasing charging time. It is therefore assumed here that saturation of samples with the before mentioned dimensions is achieved after ten days of charging at the latest. The average measured hydrogen concentrations after 20 days for the wrought material was 26.9 ± 2 wppm and after 50 days for the SLM material it was 32.8 ± 0.5 wppm.

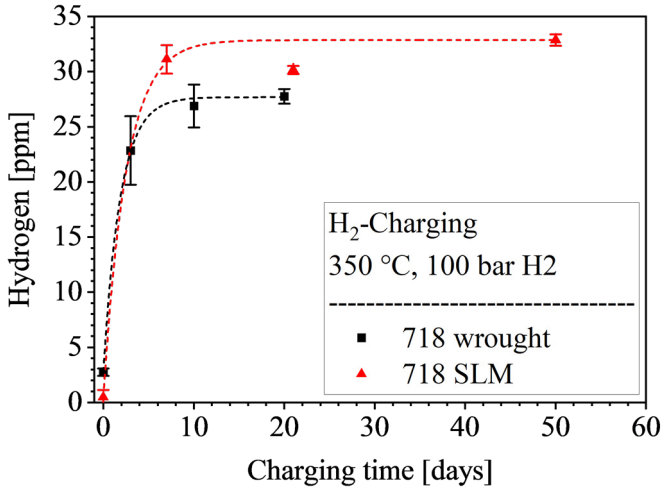


Figure 5.2: Hydrogen concentration measurements after different charging times for Alloy 718 wrought (cylindrical specimens with $d = 6.25$ mm and $l = 7mm$) and SLM (cubic specimens with $l = 5\,mm$). Hydrogen charging was conducted at 350 °C and 100 bar hydrogen gas pressure.

5.2 Hydrogen desorption experiments

Just as hydrogen can diffuse into the metal lattice under a hydrogen atmosphere, it can also effuse out in an air atmosphere. In FCC metals, this process occurs significantly slower than in BCC metals due to the smaller diffusion coefficient. This allows samples made of Alloy 718 to be pre-charged with hydrogen and to conduct mechanical experiments over a long duration with a nearly constant hydrogen content. Hydrogen desorption experiments were conducted to investigate how much hydrogen can escape over a certain test period. For this purpose, hydrogen desorption experiments were performed both at room temperature in air, as is the case in a mechanical test, and at low temperature in liquid nitrogen at -196 °C to determine the extent of hydrogen loss during experiments and sample storage.

Samples of Alloy 718 SLM were charged with hydrogen at 350°C and 100 bar hydrogen pressure for 10 days and then left at room temperature in air and at -196°C in liquid nitrogen. After 56, 84, 112, and 140 days, the hydrogen content was measured again using carrier gas melt extraction. The results are shown in Figure 5.3. There is no difference in the hydrogen content directly after charging (26.2 ± 0.6 wppm) and after 140 days of desorption when stored in liquid nitrogen at -196 °C (26.0 ± 0.8 wppm). At room temperature, the hydrogen content after 140 days dropped by about 8 % to a content of 24.1 ± 0.5 wppm. For both types of samples, the measured content after 56 days is noticeably lower than that after 84 days and are considered outliers. One reason for this could be the calibration of the machine, which needed to be redone for each measurement series. In total, hydrogen loss is negligible for 140 days when the sample is kept at -196 °C, and for about 60 days, when the sample is kept at 20°C. Since both SSRT and LCF tests had a duration below 24 hours, see Chapter 6.1.2 and 6.3.1, no effect from hydrogen desorption is to be expected.

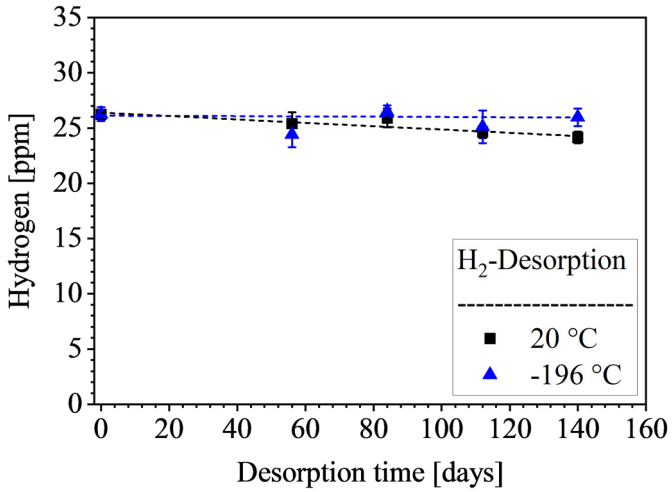


Figure 5.3: Hydrogen measurements of Alloy 718 SLM after different desorption times at room temperature in lab air (20 °C) and in liquid nitrogen (-196 °C).

5.3 Determination of hydrogen diffusion coefficient by gas permeation

To determine the hydrogen diffusion coefficient, hydrogen gas permeation measurements were carried out on thin metal disks ($d = 0.3mm$), as described in Chapter 3.5, at temperatures of 153 °C, 208 °C and 261 °C respectively. A representative measurement is shown in Figure 5.4. To prevent background noise from naturally occurring hydrogen, the measurement was conducted using the hydrogen isotope deuterium. Due to the different mol masses, $m(H2) = 2$ g/mol and $m(D2) = 4g/mol$, the signals can be clearly distinguished from each other in the mass spectrometer. Once the temperature was reached and the noise signal in the spectrometer had dropped to a minimum at the mass of deuterium, the charging chamber was filled with deuterium. The inflow of colder deuterium caused the sample temperature to drop slightly, see Figure 5.4. The D_2 signal then began to rise until it reached a maximum after about an hour of experimental duration.

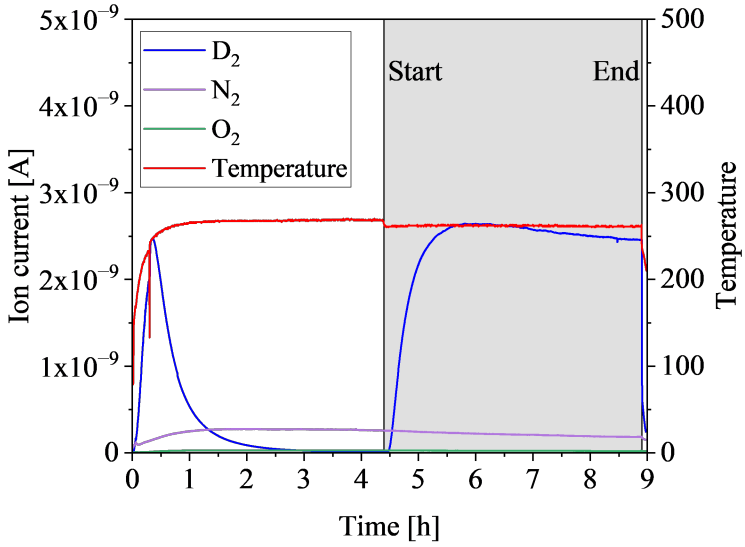


Figure 5.4: Example of a deuterium gas permeation measurement. Ion currents of D_2, N_2 and O_2 were measured by mass spectrometry. D_2 inlet started when the desired temperature was reached and the D_2 ion current had dropped to a minimum.

The effective diffusion coefficient was then determined from the D_2 signal using the time lag method. According to Daynes, the time lag $L = d^2/6D$ can be determined from the intersection of the integrated curve and the zero line $y = 0$ [277], see Figure 5.5, where d is the sample thickness. The diffusion coefficient D can be determined by rearranging the equation. The diffusion coefficient of deuterium D_D can be converted to that of hydrogen D_H by [165]

$$\frac{D_H}{D_D} = \sqrt{\frac{m_{D2}}{m_{H2}}} \,. \tag{5.1}$$

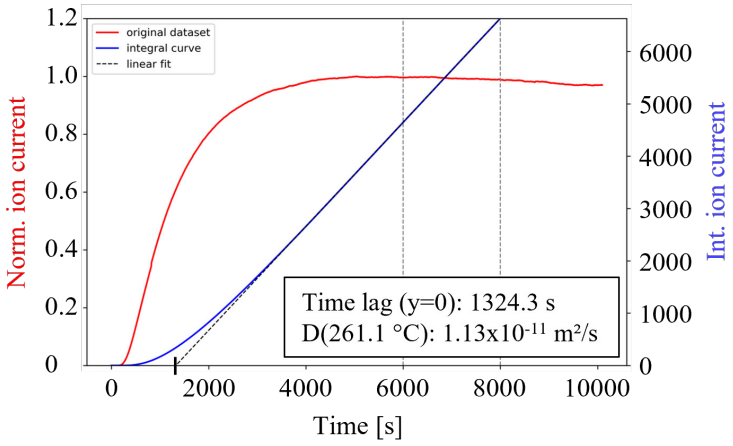


Figure 5.5: Determination of the diffusion coefficient of deuterium in alloy 718 by time lag method.

The experiment at the highest temperature was carried out 3 times in order to evaluate the repeatability. The results of the diffusion coefficients determined as a function of temperature are shown in Figure 5.6. Using an Arrhenius approach, the temperature-dependent diffusion coefficient, as obtained from the dotted line, can be described with $D_0 = 2.23x10^{-8}\, m^2/s$ and $H_D = 31946 J/mol$.

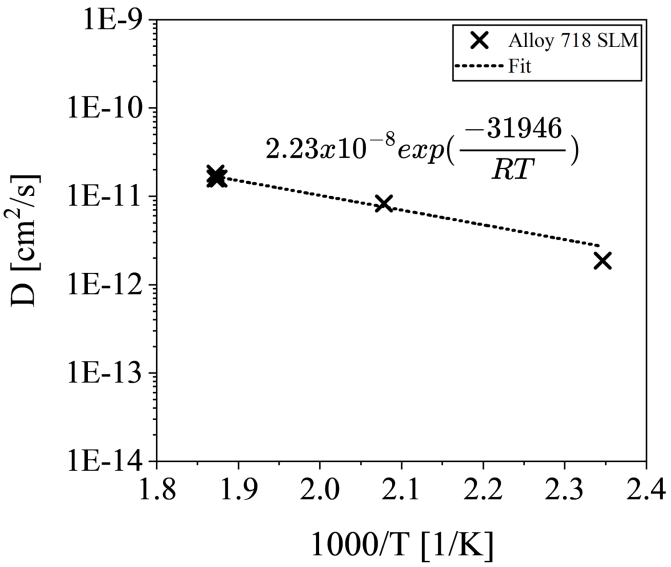


Figure 5.6: Gas permeation through membrane of Alloy 718 SLM. Fit with Arrhenius type relationship ($R^2 = 0.98$).

5.4 Determination of activation energies

Using thermal desorption spectroscopy, the activation energies for hydrogen desorption from traps were determined for alloy 718 wrought. The experimental setup and specimen preparation are described in Chapter 3.4. Samples were pre-charged at 100 bar hydrogen pressure, at 350 °C, and for a charging duration of 10 days. According to the pre-charging experiments in Chapter 5.1, it can be assumed that the material was saturated and that there was a uniform hydrogen distribution. The activation energies of lattice diffusion and hydrogen trapping can be determined by TDS experiments with different heating rates, as explained in Chapter 2.3.3.

Figure 5.7a shows the desorption curves recorded with the mass spectrometer for heating rates of 3, 6, and 10 K/min as a function of temperature. The highest peak occurs at the fastest heating rate. The slowest heating rate of 3 K/min clearly shows that multiple peaks arise, indicating different traps with varying activation energies. In Figure 5.7 b, the fit of a Gaussian function to the 3 K/min curve is presented. The desorption curve can be well represented by three Gaussian distributions. Although the coefficient of determination was always very high with R^2=0.99 for the Gaussian fit, differences in peak temperature can arise from varying the initial values, especially when the individual peaks are not clearly defined. Therefore, certain deviations are possible.

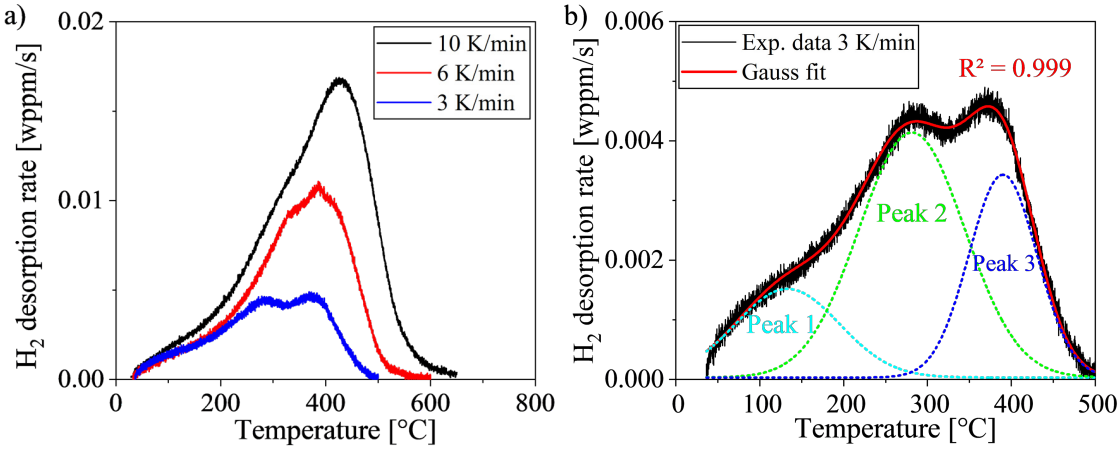


Figure 5.7: a) Hydrogen desorption curves of Alloy 718 wrought at heating rates of 3, 6 and 10 K/min. b) Example of the fit with Gaussian distribution to the curve obtained at a heating rate of 3 K/min.

By plotting the peak temperatures in the $\ln(\phi T_p^2)$ vs. $1/T_p$ diagram and applying a linear fit through the peaks for all heating rates, the activation energies can be determined, as described in Chapter 2.3.3. This is shown in Figure 5.8. The trap activation energies can be determined from the slope of the fitted curves and multiplication with the negative of the gas constant R. The energies are 10.28 kJ/mol, 24.62 kJ/mol and 66.67 kJ/mol, respectively.

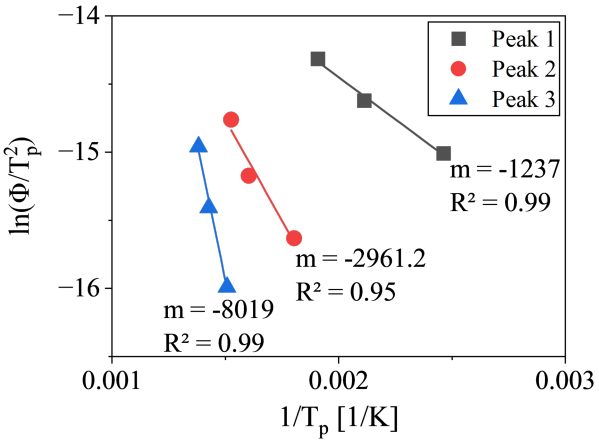


Figure 5.8: Plot of $\ln(\phi T_p^2)$ vs. $\frac{1}{T_p}$ for the three peaks of each TDS measurements of Alloy 718 wrought with the heating rates 3 K/min, 6 K/min and 10 K/min, respectively.

5.5 Discussion

5.5.1 Permeation, diffusion and solubility

After 10 days of hydrogen charging at 350 °C and 100 bar pressure, modeling (see Figure 5.1) and hydrogen measurements (see Figure 5.2) show hydrogen saturation for the samples in cylindrical shape ($D = 6.25\ mm$) as well as for the cubes ($l = 5\ mm$). This charging procedure was also used for tensile and fatigue specimens, which also have a diameter of 6.25 mm in the measuring region. It can therefore be assumed that the sample had a homogeneous hydrogen distribution in the measuring region. A hydrogen concentration of 26.9 ± 2 wppm was measured for the wrought alloy and 32.8 ± 0.5 wppm for the SLM alloy. The increased solubility in Alloy 718 SLM suggests that there are more hydrogen traps in this material. These can be, for example, grain boundaries, dislocations, precipitates, or pores.

The desorption tests (see Figure 5.3) have shown that samples can be stored in liquid nitrogen at -196 °C for a period of 5 months without significant loss of the dissolved hydrogen. Even at room temperature, only a slight loss of 8 % hydrogen was observed over the period of 5 months. Therefore, pre-charged specimens can be stored in liquid nitrogen before the experiment even for a few months and fatigue tests can be conducted at room temperature over several days without significant hydrogen loss.

The hydrogen permeation and diffusion in Alloy 718 are only slightly dependent on its heat treatment condition and microstructure, as can be seen in the diagrams in Figure 5.9. Literature data for numerous permeation measurements on Alloy 718 in different heat treatment states were compared here. The diffusivity of Alloy 718 SLM was determined from the gas permeation measurements in the temperature range from 153 °C to 261 °C. In this range the values of the additive manufactured samples also agree well with the conventional ones. Extrapolating to room temperature indicates that the diffusivity of the SLM material is higher than that of wrought material,

but validation was not possible because gas permeation at room temperature is too low. However, the material was heat treated, which destroys the cellular microstructure. Jin et al. demonstrated that the cellular sub-grain structure in additively manufactured 316L leads to significantly increased hydrogen diffusion [278]. This might also be the case for Alloy 718 SLM without heat treatment.

Using the formula $S = P/D$, the solubility can be calculated from the permeability and diffusivity. The solubility is shown in Figure 5.10. The calculated solubility shows a higher variance than the measured values of permeability and diffusivity. The hydrogen measurements from this work are added to Figure 5.10 by calculating the pressure-dependent solubility with $S = C/\sqrt{F}$ from the hydrogen concentration, where F is the fugacity, as defined in Equation (2.45), calculated from the charging pressure. Both, the measurements of this work, which were 26.9 ± 2 wppm for the wrought alloy and 32.8 ± 0.5 wppm for the SLM alloy when charged at 350 °C and 100 bar, and the measurements of Ogawa, which were 6 wppm, 28 wppm and 93 wppm when charged at 270 °C and pressures of 0.7 MPa, 11 MPa and 100 MPa [279], respectively, fall within the values calculated from permeability and diffusivity, see Figure 5.10.

Based on the literature review and experimental data, the following averaged coefficients for permeability, diffusivity, and solubility for Alloy 718 are proposed: $P_0 = 1.68x10^{-4}\ mol/(m^3 MPa^{0.5})$ and $H_P = 57974\ J/mol$, $D_0 = 9.01x10^{-7}\ m^2/s$ and $H_D = 49834\ J/mol$ for diffusivity, and $S_0 = 186\ mol/(m^3 MPa^{0.5})$ and $H_S = 8140\ J/mol$ [231].

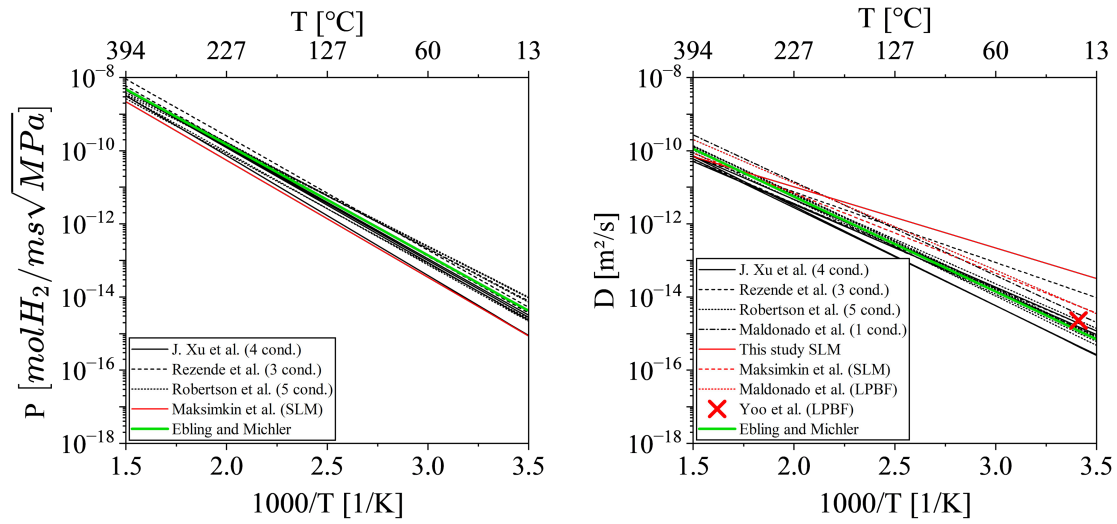


Figure 5.9: Hydrogen permeation (left) and diffusion (right) as a function of temperature from literature for alloy 718 in different conditions in black [36,189,247,248] and additive manufactured alloy 718 in red [36,244,280]. The average line found for different conditions of alloy 718 and published in [231] is plotted in green.

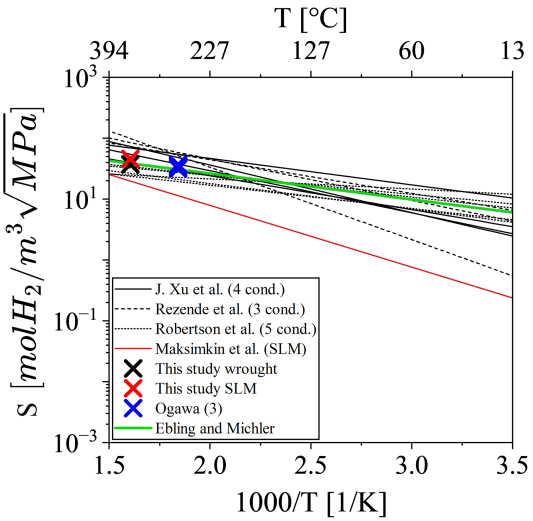


Figure 5.10: Hydrogen solubility as a function of temperature calculated from permeability and diffusivity data, shown in Figure 5.9, and measured points from this study for Alloy 718 wrought and SLM charged at 350 °C in 10 MPa and from Ogawa et al. charged at 270 °C in 0.7 MPa, 11 MPa and 100 MPa hydrogen atmosphere [279]. The average line found for different conditions of alloy 718 and published in [231] is plotted in green.

5.5.2 Activation and binding energies

While hydrogen permeation, diffusion and solubility have already been investigated quite well for Alloy 718 (see section 5.5.1), there is little literature about activation and binding energies of hydrogen traps, such as voids, inclusions, precipitates, grain boundaries and dislocations for Alloy 718. These have been investigated more for BCC materials to date. However, there are some studies on binding energies in nickel, the main component of Alloy 718, which is therefore discussed here as well.

Turnbull et al. investigated the transport of hydrogen for Alloy 718 in various heat treatment states using electrochemical permeation and attributed binding energies of $E_{\delta,b} = 30\ \mathrm{kJ/mol}$ to the δ-phase and $E_{\gamma'',b} = 23 - 27\ \mathrm{kJ/mol}$ to the γ''-phase [281]. Furthermore, trapping of particles and voids have been investigated. Lee and Lee estimated the binding energy of ThO_2-nickel interfaces to be $E_{ThO2,b} = 35\ \mathrm{kJ/mol}$ [282]. Robertson determined a binding energy of $E_{ThO2,b} = 29.7\ \mathrm{kJ/mol}$ for these interfaces [283]. And lastly, Lee and Lee found that voids act as strong trapping sites in nickel [284]. Symons et al. investigated the nickel-based alloy 600 and 690 with TDS and found activation energies for lattice diffusion to be $E_{l,d} = 48.6\ \mathrm{kJ/mol}$ and $E_{l,d} = 51.2\ \mathrm{kJ/mol}$ and for trapping at carbides $E_{c,a} = 28\ \mathrm{kJ/mol}$ and $E_{c,a} = 35\ \mathrm{kJ/mol}$, respectively [285].

Lassila and Birnbaum determined a binding energy for hydrogen at grain boundaries in polycrystalline nickel of $E_{gb,b} = 11.6\ \mathrm{kJ/mol}$. This finding is based on the bulk hydrogen concentration that is necessary for a transition from ductile rupture to transgranular rupture and it's dependence on temperature [286]. Yao and Meguid also reported a binding energy of $E_{gb,b} = 11.3 -$

12.3 kJ/mol at grain boundaries in nickel due to the change from transgranular to intergranular fracture, occurring at a critical hydrogen concentration of 6.5-9.8 at % [287]. Lee and Lee determined the activation energy for grain boundary diffusion to be $E_{gb,a} = 18\ \mathrm{kJ/mol}$ from a low temperature peak at 373 K for polycrystalline nickel [288]. They could also measure a slight increase in hydrogen solubility in polycrystalline nickel compared to nickel single crystal indicating the amount of trapped hydrogen at grain boundaries. Based on the change of trapped hydrogen for measurements at different temperature, a binding energy at grain boundaries was determined to be $E_{gb,b} = 20.5\ \mathrm{kJ/mol}$ [288].

While the binding energies of dislocations in BCC iron are in the range $E_{d,b} = 20.2 - 27.2\ kJ/mol$ and some measurements were even in the range $E_{d,b} = 48 - 59.9\ \mathrm{kJ/mol}$ [289], the binding energies of dislocations in FCC materials tend to be lower. Lee and Lee found that cold rolling of nickel led to higher hydrogen solubility, indicating that dislocations act as hydrogen traps. However, the activation energy is lower than that of bulk diffusion in nickel, meaning hydrogen is desorbed from both dislocations and bulk material simultaneously, so that the binding energy could not be determined from the activation energy. However, they predict from their results that the traps activation energy must be smaller than the activation energy of lattice diffusion ($E_{l,d} = 40.2\ kJ/mol$), as they cannot see a second peak, and the binding energy to dislocation must be in the range of $E_{d,b} = 7.5 - 13.4\ \mathrm{kJ/mol}$ based on literature review [288]. Boniszewski and Smith determined the activation energy for hydrogen diffusion in nickel to be between $E_{d,a} = 34.3 - 38.9\ \mathrm{kJ/mol}$ and the maximum binding energy of hydrogen at dislocations to be $E_{d,b} = 7.7\ \mathrm{kJ/mol}$. This was determined from the lower critical temperature, at which serrations occur in the tensile test of hydrogen-charged nickel [290]. Using the same method, Blakemore found a maximum binding energy at dislocations of $E_{d,b} = 13.5\ \mathrm{kJ/mol}$ [291]. Young et al. give a range of $E_{d,b} = 7.7 - 19.3\ \mathrm{kJ/mol}$ as binding energy of hydrogen at dislocations in nickel based on a literature review [292]. The average value of this range is $E_{d,b} = 13.5\ \mathrm{kJ/mol}$.

Comparing the measured activation energies of this work, which are $10.28\ kJ/mol$, $24.62\ kJ/mol$ and $66.67\ kJ/mol$, respectively, the lowest activation energy might be the activation energy for grain boundary diffusion $E_{gb,a}$. This could be clarified in future by measurements on very fine grained Alloy 718, where grain boundaries should have a significant impact on the material properties. Such a structure can be produced by high pressure torsion. The medium value might be associated with the activation energy for lattice diffusion $E_{l,d}$ in nickel which is closest to the range given by Boniszewski and Smith with 34.3 – 38.9 kJ/mol [290]. For the highest measured energy it is assumed that the saddle point energy E_s corresponds to the activation energy for lattice diffusion $E_{l,d}$, as done by Maldonado et al. [36]. This way one obtains the binding energy with $E_{t,b} = E_{t,a} - E_{l,d}$. Therefore, a binding energy from the highest activation energy can be calculated as $E_{c,b} = 66.67\ kJ/mol - 24.62\ kJ/mol = 42.05\ kJ/mol$, which might be associated with trapping at carbides. The different energy levels are sketched in Figure 5.11.

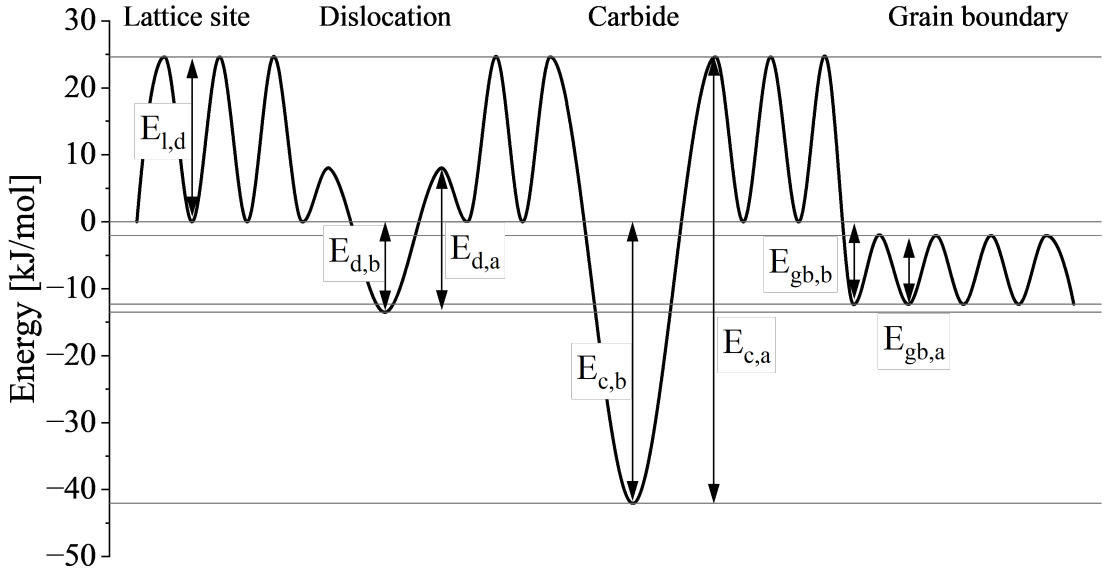


Figure 5.11: Energie diagram of lattice diffusion $E_{l,d}$ activation energy, dislocation activation $E_{d,a}$ and dislocation binding $E_{d,b}$ energies, carbide activation $E_{c,a}$ and carbide binding $E_{c,b}$ energies and grain boundary activation $E_{gb,a}$ and grain boundary binding $E_{gb,b}$ energies,

Determining the binding and activation energies gives a fundamental understanding of how hydrogen diffuses in the material, where it accumulates locally, and how it can influence damage mechanisms. For alloy 718, for example, grain boundaries can become embrittled by hydrogen enrichment in the presence of a high niobium content, and decohesion can occur at interfaces between the matrix and the γ′-, γ″- or δ-phases [57]. Knowledge of the binding energies of different traps allows to quantify how hydrogen is distributed between the metal lattice and the various trapping sites. As discussed in Chapter 2.4.3, hydrogen-induced damage in alloy 718 is predominantly attributed to the HELP mechanism. Therefore, in Chapter 7 the binding energy of hydrogen to dislocations $E_{d,b} = 13.5\,\mathrm{kJ/mol}$ is used in the hydrogen damage parameter $Z_{D,H}$ for fatigue life predictions.

6 Mechanical experiments

The effects of hydrogen on the mechanical properties of Alloy 718 were investigated under quasi-static and dynamic loads. Slow strain rate tensile (SSRT) tests were conducted on both conventional and hollow specimens (Chapter 6.1). Although the interest in hollow specimens testing has increased strongly in recent years, due to the simplicity compared to autoclave tests, the technique is rather little investigated, and the standardization is still ongoing. The slow strain rate tensile test on hollow specimens with internal pressure was standardized in 2024 in ISO/FDIS 7039 [293] and hydrogen-specific test parameters are currently in discussion in the technical committee ISO/TC 164/SC. The standardization of HS for fatigue testing has not started yet.

Since hydrogen embrittlement of pipeline steels has recently attracted great interest, many experiments have been carried out on these materials [6,294,295]. To qualify the hollow specimen technique and compare it with other tests, SSRT experiments were performed on an X60 pipeline steel. The influence of the strain rate on the test results and whether sufficient gas purity is achieved during filling of the hollow specimens was investigated in Chapter 6.1.1. The results are discussed and compared with literature in Chapter 6.2.1 and 6.2.2.

Further SSRT experiments were carried out on Alloy 718 wrought (Chapter 6.1.2), using both conventional and hollow specimens to further qualify the hollow specimen technique. The influence of hydrogen was investigated at pressures up to 250 bar. The differences in the geometry of the two specimens and their effects on the failure mode, multiaxial stress state, and measured mechanical properties are discussed in Chapter 6.2.

As components are usually subjected to both static and dynamic loads, the influence of hydrogen under dynamic loads is of great interest. Therefore, strain-controlled fatigue tests were conducted in the low cycle fatigue (LCF) regime (200 to 20,000 cycles), Chapter 6.3. First, the effect of internal hydrogen on alloy 718 wrought was tested with pre-charged conventional specimen (Chapter 6.3.1). Experiments under external gaseous hydrogen atmosphere were conducted on both conventional and hollow specimens (Chapter 6.3.2). The effects of test frequency, hydrogen pressure and temperature were examined in Chapters 6.3.3 to 6.3.5. The compatibility of additive manufactured alloy 718 SLM was investigated in Chapter 6.3.6. The experimental results of Chapter 6.3 are discussed in Chapter 6.4.

6.1 Slow strain rate tensile tests

6.1.1 Qualification of hollow specimen testing on X60 pipeline steel

Since standardization of the hollow specimen technique was still an ongoing process during this work, experiments were carried out to qualify the method. Due to the current interest in pipeline materials and the resulting good availability of literature data, the tests were performed on an X60

pipeline steel. First, the influence of strain rate on hydrogen embrittlement was investigated. Subsequently, experiments with different numbers of purging cycles were conducted to determine when a sufficiently high gas purity inside the specimen is achieved.

SSRT tests were conducted on hollow specimens at different crosshead speeds, resulting in technical strain rates ranging from $1x10^{-5}\ 1/s$ to $1.2x10^{-2}\ 1/s$, see Figure 6.1. The hydrogen pressure was 100 bar. The reference tests in air were conducted at a technical strain rate of $6x10^{-5}\ 1/s$. When tested with 100 bar hydrogen pressure in the HS, a plateau forms in the range of $1x10^{-5}\ 1/s$ bis $1x10^{-3}\ 1/s$. At higher strain rates, the reduction of area increases towards RA in air and therefore the hydrogen effect decreases.

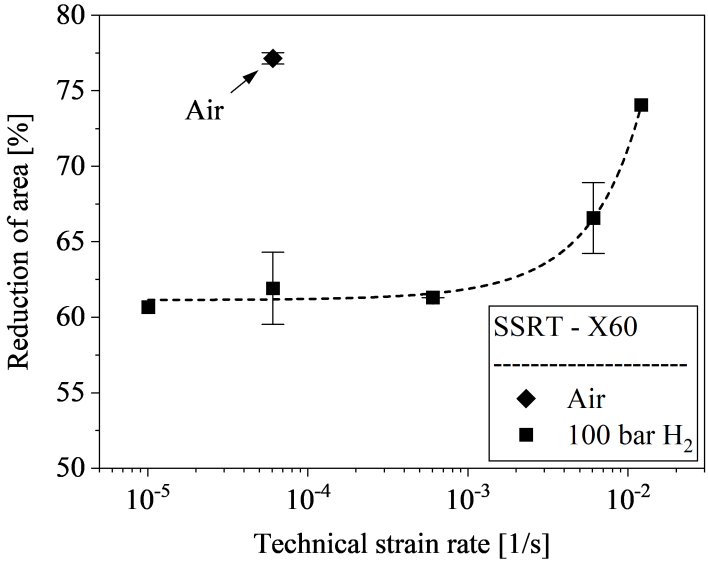


Figure 6.1: Reduction of area for slow strain rate tensile tests over the technical strain rates of X60 pipeline steel. Experiments were conducted on hollow specimens in air and with 100 bar inner hydrogen pressure. Amended published in Reference [296].

The fracture surfaces of the tested specimens, see Figure 6.2, suggest that at the low technical strain rates of $1x10^{-5}\ 1/s$ and $6x10^{-5}\ 1/s$, nearly the entire fracture was influenced by hydrogen, as the entire fracture surface shows a bright area in the image, indicating a change in fracture morphology caused by hydrogen. With increasing strain rate, this hydrogen-influenced area becomes smaller, and shear fracture without hydrogen influence increasingly occurs in the outer area of the specimen. In the specimen tested in air, no bright area, as seen in the specimens tested with hydrogen, is visible.

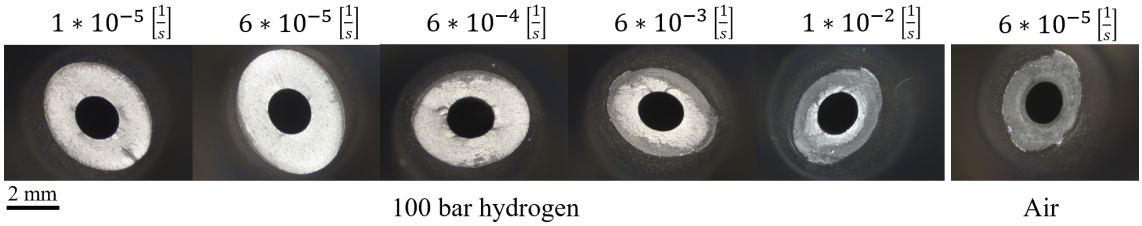


Figure 6.2: Light microscope images of the fracture surfaces of the hollow specimens tested in air and with 100 bar hydrogen at different crosshead speeds. The corresponding technical strain rates are indicated.

Hydrogen gas quality can have a significant impact on the results of SSRT tests. Oxygen contamination in particular can lead to reduced hydrogen embrittlement. The amount of gas in the hollow specimens is not sufficient to perform a gas analysis and measure the oxygen content in the hydrogen gas. Therefore, SSRT tests were conducted with varying numbers of purging cycles to analyze when the maximum hydrogen embrittlement is reached, see Figure 6.3. Purging was conducted by filling the specimen with 100 bar hydrogen. Then the pressure was released to 10 bar and filled again to 100 bar. This was repeated up to 10 times. According to Equation (3.5), a theoretical oxygen content in the air-hydrogen gas mixture can be calculated based on the number of purging cycles. When the specimen is filled with air in the beginning, after 5 purging cycles with hydrogen gas between 10 bar and 100 bar a theoretical residual oxygen content of 0.29 vppm is reached, which is below the contamination in hydrogen gas of quality 5.0 (≤2 vppm O_2) and quality 6.0 (≤ 0.5 vppm O_2). Since purging can never improve the gas quality beyond that of the purging gas, the oxygen contamination of the respective gas quality was assumed after 10 purging cycles.

The SSRT tests show that the highest average reduction in area RA = 77.15% is achieved in air. Three tests were conducted, and the standard deviation is marked in Figure 6.3. With an increasing number of purge cycles and thus higher gas purity, RA decreases. After 10 purge cycles, it is assumed that the purity of the respective purge gas has been reached. Two tests with 10 purging cycles were conducted for each case. Only a slight difference can be observed between H2 5.0 and H2 6.0. For further experiments, it was determined that the tests should always be conducted with hydrogen 6.0 and 10 purging cycles between 10 bar and 100 bar to achieve the best possible hydrogen purity.

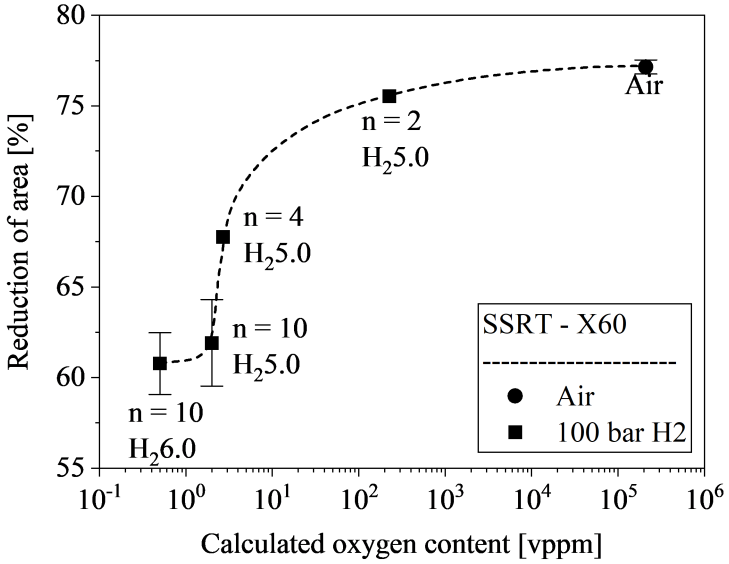


Figure 6.3: Reduction of area depending on oxygen content for different numbers of flushing cycles n and on gas quality. Amended published in Reference [296].

6.1.2 Comparison of conventional and hollow specimens of Alloy 718 in slow strain rate tensile tests

Slow strain rate tensile tests were carried out on conventional and hollow specimens of Alloy 718 wrought. Different hydrogen charging conditions were used. Experiments were carried out with in-situ hydrogen charging on CS in an autoclave and on HS with internal hydrogen pressures of 10, 50, 100, 150 and 200 bar. Reference tests were carried out in air and with internal pressure of 150 bar nitrogen. In addition, one CS was pre-charged with hydrogen at 350 °C and 100 bar hydrogen pressure for 10 days. The expected hydrogen concentration is around 27 wppm, as the pre-charging experiments in Chapter 5.1 have shown.

The results shown in Figure 6.4 indicate that the yield strength ($R_{p0.2,CS,Air} = 1173\,MPa$ and $R_{p0.2,HS,Air} = 1176\,MPa$) and maximum tensile strength ($R_{m,CS,Air} = 1411\,MPa$ and $R_{m,HS,Air} = 1414\,MPa$) are not affected by the geometry of the hollow specimen. However, the HS exhibit different necking behavior. While the reference test on the CS shows significant necking and the technical stress gradually decreases as a result, the HS experience a more sudden failure after reaching ultimate tensile strength. The results of the specimen filled with 150 bar nitrogen show no significant difference compared to the results of the reference specimen in air.

The specimens filled with hydrogen do not show any change in strength compared to the reference test, but an increase in hydrogen pressure leads to a reduction in elongation to failure ε_f. While 10 bar hydrogen pressure has little effect, ε_f decreases significantly at 50 bar and even more at 100 bar. The difference from 100 bar to 200 bar is comparatively small. The greatest embrittlement is shown by the hydrogen pre-charged CS.

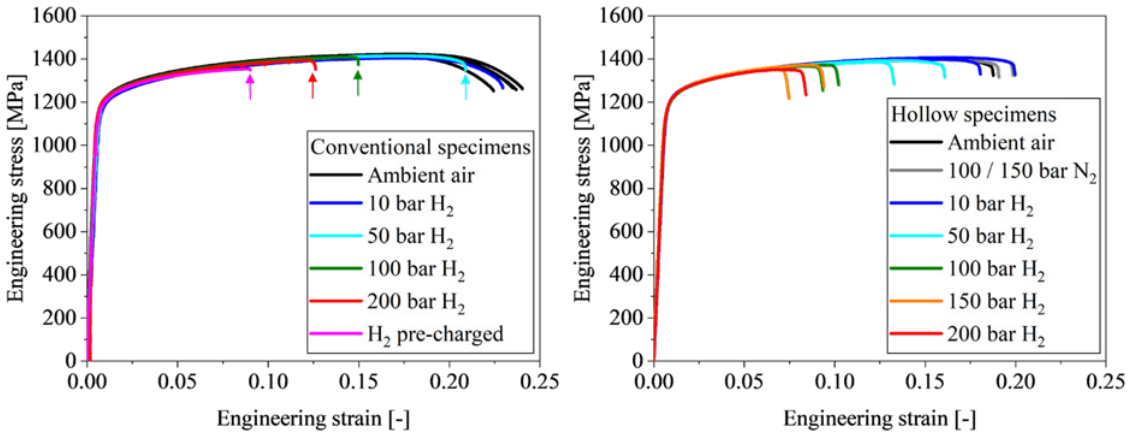


Figure 6.4: Slow strain rate tensile tests on Alloy 718 wrought with conventional and hollow specimen. Hydrogen charging in-situ with 10 to 200 bar and hydrogen pre-charging at 350°C and 100 bar hydrogen pressure for 10 days [273].

In addition to the wrought material, additively manufactured samples of Alloy 718 SLM were tested. As shown in Figure 6.5, the material in the as-built state exhibits significantly lower strength than the heat-treated state. After heat treatment, the SLM material achieves comparable strength with $R_{p0.2} = 1042\ MPa$ and $R_m = 1281\ MPa$ to the wrought material with $R_{p0.2} = 1168\ MPa$ and $R_m = 1414\ MPa$. Thus, as mentioned in Chapter 3.1, all results on SLM samples shown in the following, relate to specimens that underwent the same heat treatment as the wrought material.

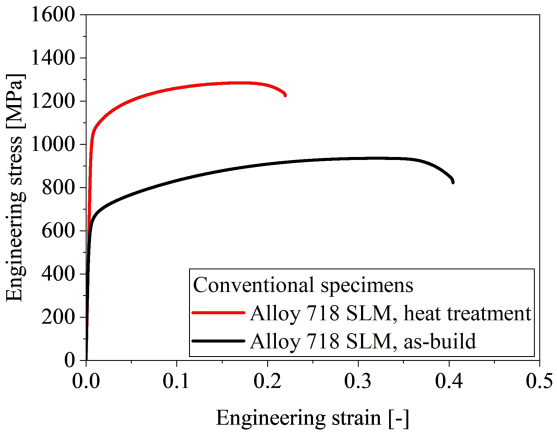


Figure 6.5: Slow strain rate tensile tests on Alloy 718 SLM in as-build and heat treated condition (solution annealing at 980 °C for 1 hour, air cooling, and precipitation heat treating at 720 °C for 8 hours and 620 °C for 8 hours).

In hydrogen atmosphere, the additively manufactured specimens of Alloy 718 SLM exhibit similar behavior to the specimens of the wrought material. Again, CS are compared with HS in air and at 10 bar and 100 bar hydrogen pressure, see Figure 6.6. The strength is not affected by hydrogen, but the elongation to failure decreases with increasing hydrogen pressure. Notably, the

HS show a significantly stronger hydrogen effect on the elongation to failure compared to the CS. Again, CS show a little more necking at the end of the test.

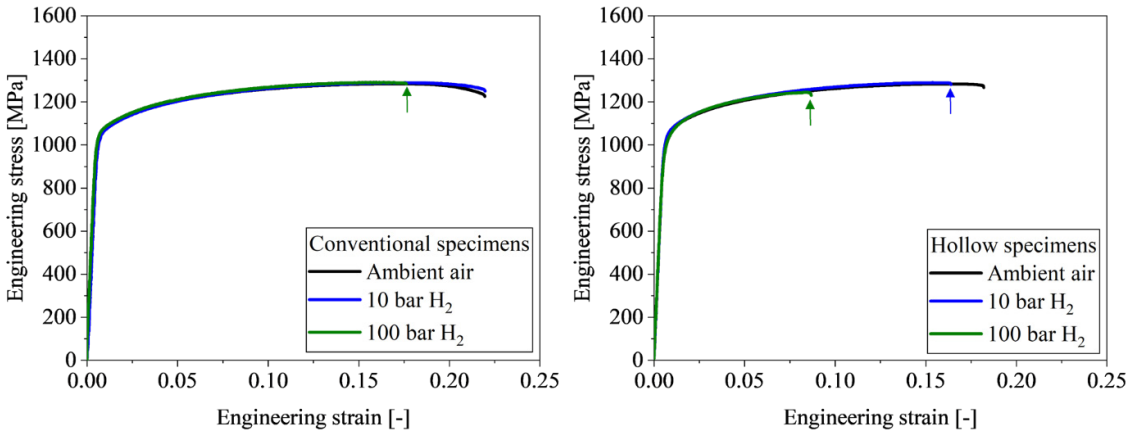


Figure 6.6: Slow strain rate tensile tests on Alloy 718 SLM with conventional and hollow specimen. Hydrogen charging in-situ with 10 and 100 bar [273].

To investigate the different damage behaviors of CS and HS in more detail, the fracture surfaces were examined using a scanning electron microscope, see Figure 6.7 to Figure 6.10. Figure 6.7 shows the fracture surfaces of the CS made of Alloy 718 wrought. The specimen tested in air exhibits a typical cup and cone fracture with dimples in the center of the specimen, which are surrounded by shear fracture, see Figure 6.7 a and b. The shear fracture can be recognized by its 45° angle to load direction and the dimples that are sheared off, giving them a teardrop shape. The specimen pre-charged with hydrogen shows a large area with some dimples and a high proportion of flat surfaces, which is also surrounded by a small ring of 45° shear fracture, see Figure 6.7 c and d. In contrast to the pre-charged specimen, the specimen tested in-situ in a 200 bar hydrogen atmosphere shows only dimples and no flat surfaces in the center of the specimen. However, there is an area that connects the outer side of the specimen with the inner region and shows flat facets and secondary cracks, as can be seen in Figure 6.7 f. This area is marked in red in Figure 6.7 e. Along the remaining circumference of the specimen, a large shear area is again visible.

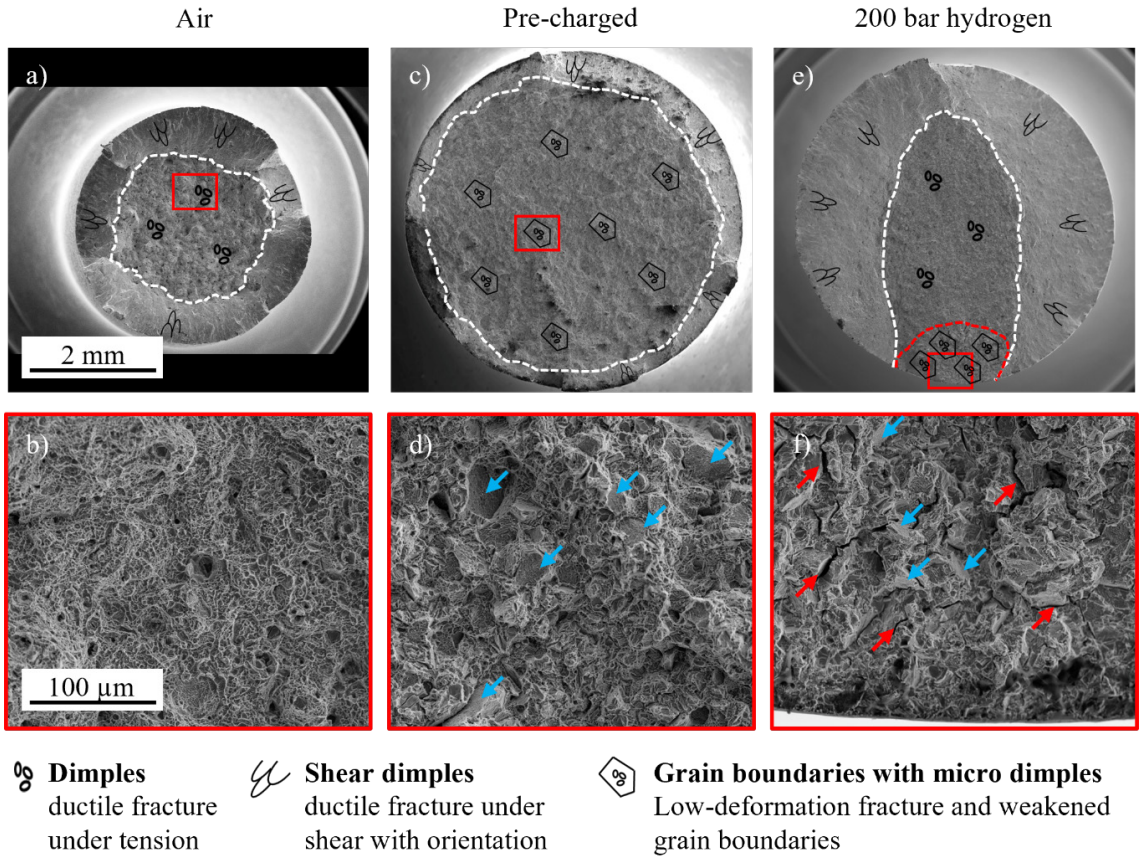


Figure 6.7: Fracture surfaces of conventional specimens of Alloy 718 wrought: Reference specimen tested in air (a, b), pre-charged specimen (c, d) specimen tested in 200 bar hydrogen atmosphere. Blue arrows indicate flat surfaces and red arrows indicate secondary cracks [273].

Figure 6.8 shows the fracture surfaces of the hollow specimens made of Alloy 718 wrought. The specimen tested in air and the one tested with 150 bar internal nitrogen pressure exhibit similar fracture surfaces. Figure 6.8 a and c show a region with dimples, marked with a dashed white line. The dimples can be seen in the magnifications Figure 6.8 b and d. However, unlike the conventional specimen, this region is not in the center of the specimen but is asymmetrically displaced from the specimen's central axis. The rest of the specimen shows 45° fracture with shear dimples. The specimen tested with 200 bar inner hydrogen pressure shows flat facets and secondary cracks in the red marked area of Figure 6.8 e, which can be seen in the magnification Figure 6.8 f. Around the inner hole which is exposed to hydrogen, a strip of approximately 20 µm width exhibits a slightly smoother fracture morphology. The red marked area is surrounded by a dimpled area (white dashed line), which then transitions into a shear fracture on the outside of the specimen.

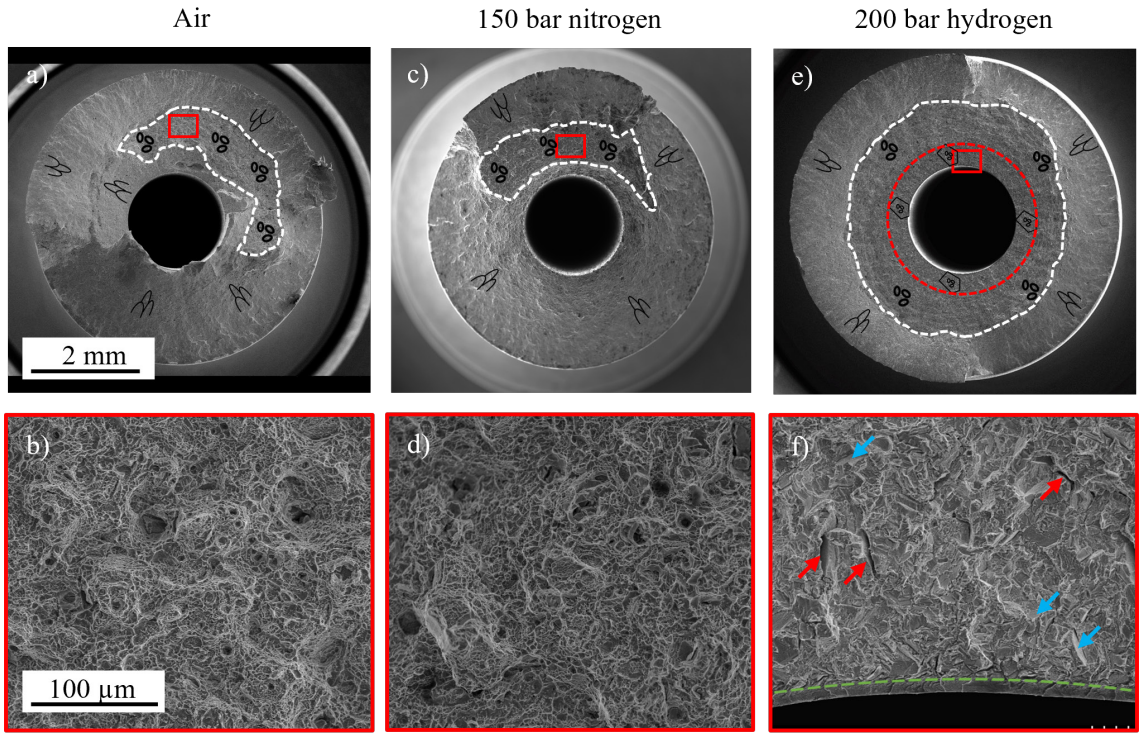


Figure 6.8: Fracture surfaces of hollow specimen of Alloy 718 wrought: Reference specimen tested in air (a, b), specimen tested with 150 bar inner nitrogen pressure (c, d) and specimen tested with 200 bar inner hydrogen pressure. Blue arrows indicate flat surfaces and red arrows indicate secondary cracks [273].

The conventional specimen of Alloy 718 SLM, tested in air, shows a large area with mainly dimples but also few flat areas and a pore. This area is again completely surrounded by shear fracture, see Figure 6.9 a and b. The CS tested in 100 bar hydrogen shows a region with flat facets and secondary cracks starting from the outside (marked in red), but also within the center of the specimen, as can be seen in Figure 6.9 c and d. The shear fracture around the circumference is interrupted at the region marked in red. The HS SLM tested with 100 bar inner hydrogen pressure exhibits a similar fracture surface to the HS wrought, shown before in Figure 6.8 e. Starting from the inner hole a small ring with a slightly smoother surface and some orientation can be seen (marked in red), then a larger ring with flat facets and secondary cracks was observed, see Figure 6.9 f. This is surrounded by a more dimpled region (marked in white) and the final shear fracture at the circumference.

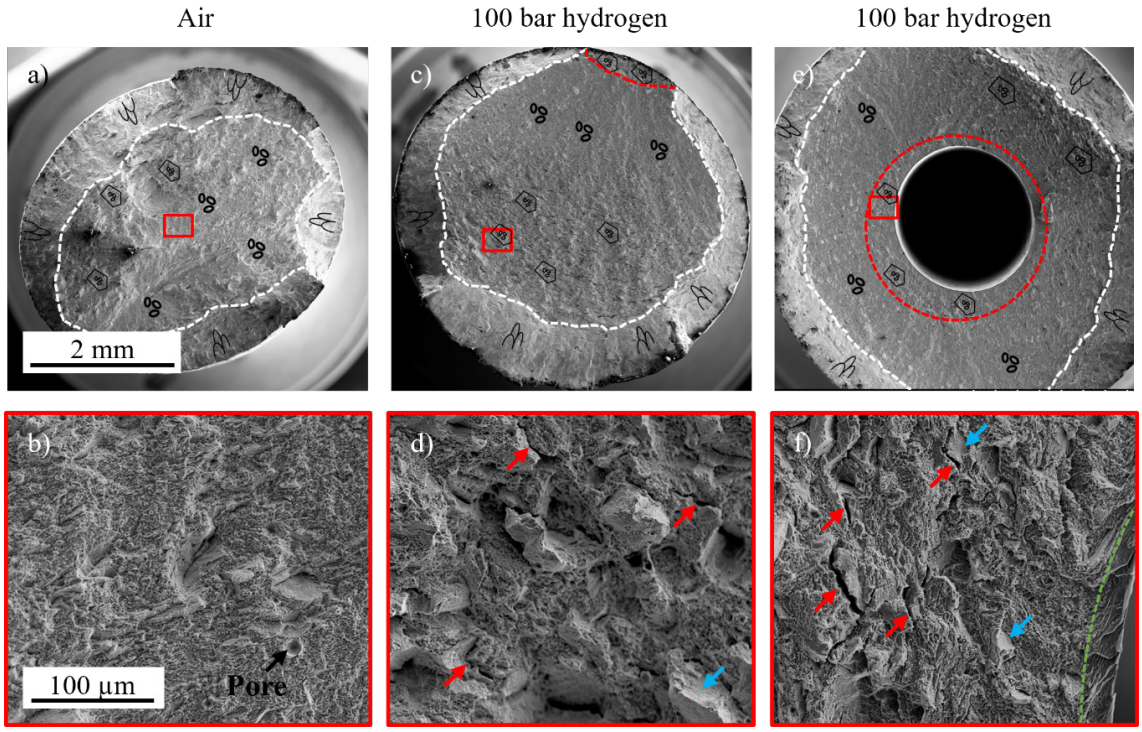


Figure 6.9: Fracture surfaces of Alloy 718 SLM: Conventional reference specimen tested in air (a, b), conventional specimen tested in 100 bar hydrogen atmosphere (c, d) and hollow specimen tested with 100 bar inner hydrogen pressure. Blue arrows indicate flat surfaces and red arrows indicate secondary cracks [273].

EBSD was used to analyze the crack growth of secondary cracks along the crystallographic structure in air and in hydrogen gas in the hole of hollow specimens, see Figure 6.10 a and e. In the specimen tested in air, it can be seen that the crack grows transcrystalline at an angle of 45° to the tensile load direction. Along the crack edges, the grains are strongly deformed, and the crack tip is blunted. Under hydrogen, on the other hand, the crack grows predominantly at 90° to the load direction. Both transcrystalline and intercrystalline crack growth occurs here. Figure 6.10 b and f are KAM maps of the two cracks. KAM is a measure of local lattice misorientation which is closely connected to the plastic deformation. Under the influence of hydrogen, plastic deformation (green areas) occurs more locally at the grain boundaries. In contrast, in the air test the entire grains are strongly deformed and in some cases can hardly be resolved in the EBSD (white areas). Figure 6.10 c and g show macrographs of the specimens tested in air and in hydrogen, also illustrating the before mentioned 45° shear fracture in air and 90° crack growth from the borehole with internal hydrogen pressure. The damage behavior is illustrated in the sketches in Figure 6.10 d and h.

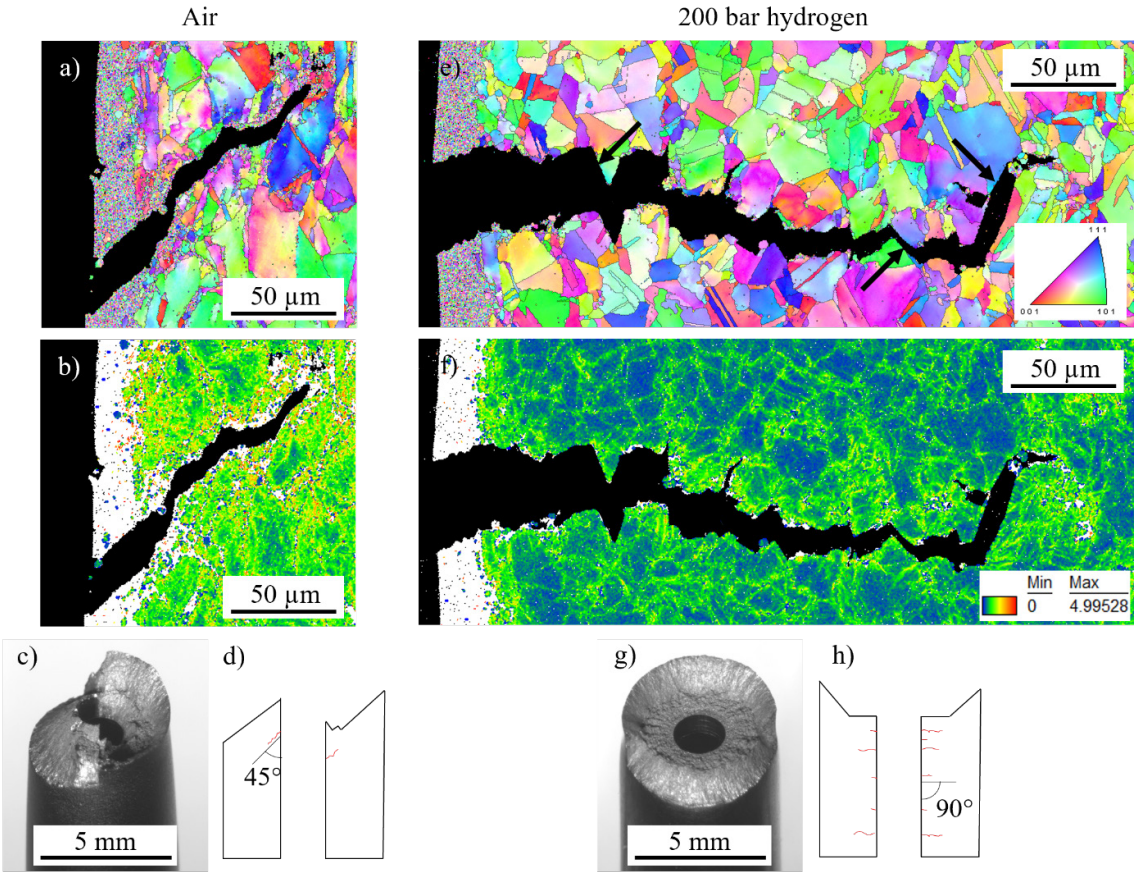


Figure 6.10: EBSD (a, e) and KAM maps (b, f) of cracks in hollow specimens appearing at the borehole, for specimens tested in air and with 200 bar internal hydrogen pressure, respectively. Macrographs of the failed specimen (c, g) and illustration of crack growth (d, h) [273].

6.2 Discussion of slow strain rate tensile tests

6.2.1 Effect of strain rate

The strain rate has a significant influence on the hydrogen embrittlement of metals, as hydrogen needs time to be absorbed by the material and to diffuse to regions of high stress such as crack tips and defects. Furthermore, these high stress regions can propagate themselves and hydrogen needs time to follow or to reach the propagating region. Therefore, it is important that the tests are conducted sufficiently slowly to obtain conservative results. It has been shown that for several FCC and BCC steels as well as Alloy 718, tested at room temperature, a plateau forms below strain rates in the range of $10^{-5}\ 1/s$ to $10^{-3}\ 1/s$, and lower strain rates do not necessarily lead to further increase of hydrogen embrittlement [241].

The results of SSRT tests on X60 pipeline steel in Chapter 6.1.1 showed that the typical dependence of strain rate on hydrogen embrittlement is also observed for hollow specimens. If the tests are conducted at strain rates below $10^{-3} 1/s$ a plateau of maximum embrittlement is reached, see

Figure 6.1. This is in good agreement with results of tensile tests in a hydrogen autoclave on conventional specimens of X100 pipeline steel, in which the RA showed a plateau up to $7\ x\ 10^{-3}\ 1/s$ and, at higher strain rates, the RA increased sharply [294]. This shows that the hollow specimens behave similarly to conventional specimens. This transition strain rate is higher than the proposed technical strain rate of ASTM G142 [256]. This specifies an extension rate of $0.002\ mm/s$, which corresponds to a technical strain rate of $8.33x10^{-5}\ 1/s$. This is significantly slower than the transition at $>10^{-3}1/s$ for the X100 pipeline steel and therefore conservative. Other materials reach a plateau at lower strain rates. Michler et. al. [241] report the plateau for 23Cr-5Ni duplex steel, tested at 2 bar hydrogen pressure, being reached at about $3x10^{-5}\ 1/s$ with data from reference [297] and for Alloy 718, tested at 340 bar hydrogen pressure, it is reached at about $1x10^{-4}\ 1/s$ with data from [242].

In summary, the experiments on hollow specimen show good agreement for the transition strain rate separating the plateau RA region from the increasing RA region compared to experiments on conventional specimens in the hydrogen autoclave. With respect to the literature data mentioned, the strain rate of $3x10^{-5}\ 1/s$ chosen in this work is sufficiently slow also for Alloy 718.

6.2.2 Effect of gas purity

Even small amounts of oxygen in hydrogen gas can lead to the coverage of the specimen surface with oxygen, thus hindering hydrogen absorption. Due to the higher electronegativity of Oxygen (3.44) compared to Hydrogen (2.2) on the Pauling scale [298], the dissociation reaction of O_2 is favored over H_2. This results in a greater attraction of the surface to the O_2 molecule. Consequently, the catalytic activity of iron for hydrogen dissociation is suppressed and hydrogen absorption is hindered as modeled with density functional theory by Staykov et al. [172]. This can result in a reduction or complete prevention of hydrogen embrittlement. This effect depends on the partial pressure of oxygen and not on the total amount of oxygen [299]. Somerday et al. were able to show that oxygen shifts the critical ΔK value, as defined in Equation (2.20), at which hydrogen-accelerated crack growth occurs, to higher ΔK values based on the oxygen content in the hydrogen, but also depending on frequency and R-ratio, see Equation (2.24) [171]. The standard for determination of hydrogen susceptibility of metals ASTM G142 [256] recommends high purity gas with a low oxygen content ($< 1ppm$). Therefore, achieving high gas purity is very important for conservative test results. The results of the tests on X60 pipeline steel from this work show that the gas quality is improved through several flushing cycles, and after 10 flushing cycles between 10 bar and 100 bar with gas of quality 6.0, the maximum embrittlement behavior is achieved. Therefore, this flushing procedure was chosen in this work.

6.2.3 Comparison of mechanical properties obtained from conventional and hollow specimens

The tests on conventional and hollow specimens show a slight difference in the measured mechanical properties, see Figure 6.11. Even in air, HS exhibit lower fracture elongation and reduction in area compared to CS. While the trend in reduced fracture elongation continues with increasing hydrogen pressure, the reduction in area curves intersect. This means that the HS are

equal to or even more sensitive in terms of elongation to failure than CS ($R\varepsilon_{f_{HS,200}} = 42$ % and $R\varepsilon_{f_{CS,200}} = 52.6$ %). However, regarding reduction of area, hydrogen has a significantly smaller effect on HS than on CS ($RRA_{TS,200} = 55$ % and $RRA_{CS,200} = 27.9$ %). Thus, it can be said that the HS are less sensitive to hydrogen embrittlement than CS. The differences between CS and HS regarding failure mechanisms and multiaxial stress are discussed in Chapter 6.2.4 and 6.2.5.

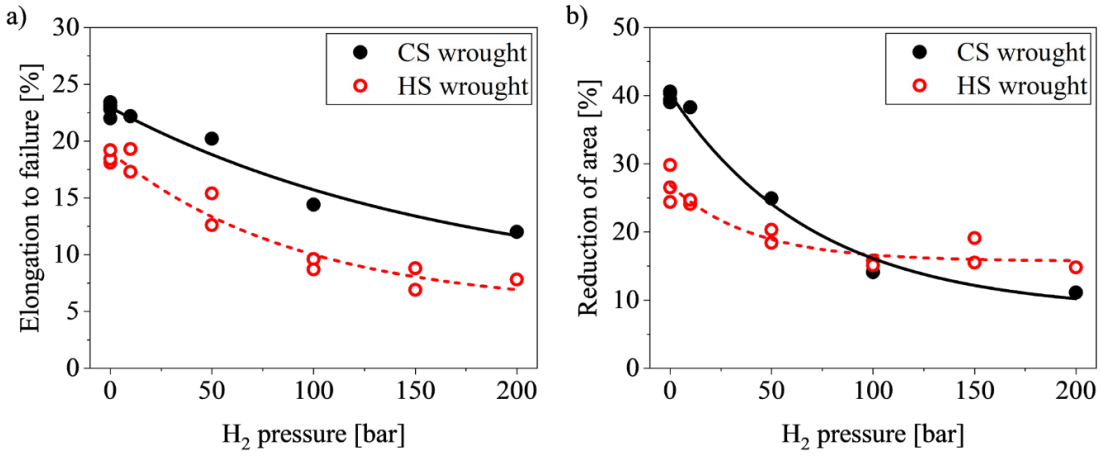


Figure 6.11: Elongation to failure (a) and reduction of area (b) over hydrogen pressure for conventional specimens (CS) and hollow specimens (HS) (Fit with exponential growth function with time constant parameter ($y = A_1 * exp(x/t_1) + y_0$) [273].

This difference in RA was also noted in a comparison of CS and HS by Michler et al. on austenitic steels [28] and ferritic steels [27]. When the results from this work are plotted in the diagram of the reduction of area dependency for HS and CS for austenitic steels (Figure 6.12), the points appear closer to the centerline with increasing pressure (see arrow), which indicates equal results for both specimens' geometries. However, the tests in air tend to lie below the line, while the tests conducted with hydrogen lie above, which also indicates the lower sensitivity of hollow specimes.

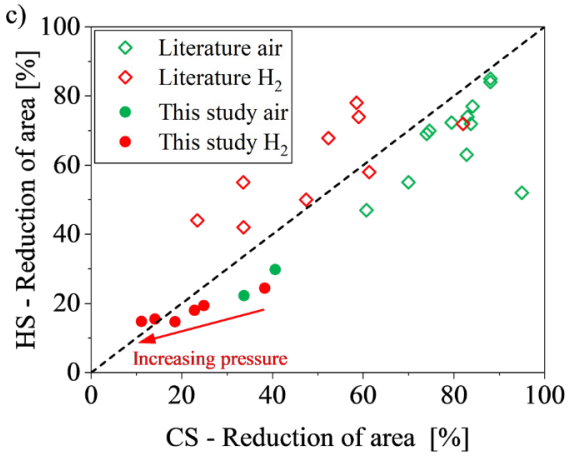


Figure 6.12: Comparison of the reduction of area of conventional specimens (CS) and hollow specimens (HS) from this work with data from Michler et al. for austenitic steels [28]. The arrow indicates increasing hydrogen pressure of the experiments.

6.2.4 Failure mechanisms

The differences in ductility (ε_f and RA) between CS and HS, as well as the fracture surface images from Chapter 6.1.2, indicate different damage mechanisms due to the specimen geometry and hydrogen availability. The different mechanisms are illustrated in Figure 6.13. In CS exposed to air, damage initiates from the center of the sample, where the highest hydrostatic stresses occur during the tensile test. This leads to the nucleation of microvoids, and the sample constricts significantly from the outside. Once critical damage due to microvoid coalescence is reached, the sample fails by shear fracture, resulting in the typical cup and cone fracture appearance, see Figure 6.7a. The same mechanisms can be observed in the HS in air, although they are distributed differently here. The microvoid nucleation does not occur in the central axis as with CS, but also within the material, which here is the wall. However, the area with dimples, indicating microvoids, is tendentially closer to the hole than to the outer wall, see Figure 6.8a. The distance between the dimpled area and the surface of the hole is significantly smaller for HS than in CS. Once critical damage is reached at one point, the shear fracture propagates around the entire sample. This may explain why the hollow specimen fractures faster and shows less necking.

Under hydrogen influence, both sample geometries exhibit reduced ductility. Hydrogen-assisted cracks initiate from the surfaces exposed to hydrogen and grow into the area damaged by void nucleation, see Figure 6.7e and Figure 6.8e. However, in CS, the surface exposed to hydrogen is the outer surface, while in HS, it is the inner surface (the hole). Therefore, it is assumed here that in CS, this leads to competition between crack growth due to hydrogen and necking from the outer surface. Under high hydrogen pressure, the damage caused by the hydrogen-assisted crack is so significant that there is hardly any necking. For HS, crack growth due to hydrogen occurs at the inner surface, while the necking mainly happens from the outer surface. Therefore, these mechanisms do not compete as strongly here, and hydrogen embrittlement appears less pronounced. This difference between CS and HS has also been discussed in [28], where it was found that in HS, necking mainly occurs from the outer surface and only slightly at the inner surface. Ogata and Ono studied the effect of the hole diameter on the mechanical properties by finite element analysis and found that yield strength and tensile strength are not affected by the hole but the elongation to failure decreases with increasing hole diameter and is even more pronounced under high inner pressure [300].

The damage mechanisms in the hydrogen pre-charged sample differ significantly from that of the in-situ tested sample. In the pre-charged specimen, hydrogen is already present in the specimen. Therefore, the damage caused by hydrogen does not occur from the sample surface as in the in-situ tests but also takes place within the specimen. The formation of voids competes with hydrogen-assisted crack growth. Once critical damage is reached, catastrophic failure of the sample also occurs, resulting in a cup and cone-like fracture, with the shear zone being significantly smaller than in the un-charged sample, see Figure 6.7c.

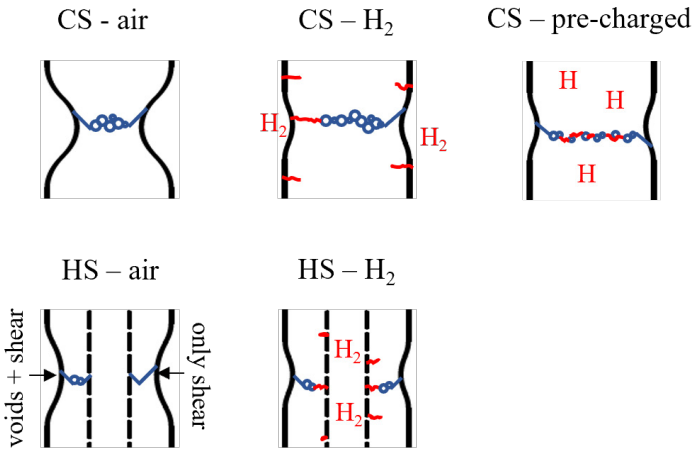


Figure 6.13: Illustration of the different failure mechanisms taking place in conventional specimens (CS) and hollow specimens (HS) when in contact with a hydrogen atmosphere or pre-charged with hydrogen. Voids are represented by blue circles, shear fractures are depicted by blue lines in a 45° direction, and hydrogen-assisted cracks are shown in red [273].

6.2.5 Multi axial stress in hollow specimens caused by internal pressure

For conventional specimens, the pressure of the test gas leads to hydrostatic compressive stresses in all 3 spatial directions $\sigma_h = 1/3(\sigma_{xx} + \sigma_{yy} + \sigma_{zz})$. In the case of hollow specimens, however, the pressure of the test gas is only present in the axial hole and not on the outer surface of the specimen. This internal pressure leads to multiaxial stresses in the HS, which can be calculated for a rotationally symmetrical body as follows [301].

$$\sigma_t = p_i \frac{r_i^2}{r_o^2 - r_i^2}\left(\frac{r_o^2}{r^2} + 1\right) \tag{6.1}$$

$$\sigma_r = -p_i \frac{r_i^2}{r_o^2 - r_i^2}\left(\frac{r_o^2}{r^2} - 1\right) \tag{6.2}$$

$$\sigma_a = p_i \frac{r_i^2}{r_o^2 - r_i^2} \tag{6.3}$$

σ_t, σ_r and σ_a are the tangential, radial, and axial stress components, p_I and p_o are the inner and outer pressure, r_i and r_o are the inner and outer radius of the body and r is the radius at a certain position.

The equivalent stress σ_v is determined by [302]

$$\sigma_v = \sqrt{\frac{(\sigma_t - \sigma_r)^2 + (\sigma_r - \sigma_a)^2 + (\sigma_a - \sigma_t)^2}{2}} \tag{6.4}$$

The stresses due to internal pressure of 100 bar were calculated using the formulas shown above and are illustrated in Figure 6.14. The highest stress occurs at the surface of the hole in the tangential direction. With a bore radius of $r_i = 1$ mm, 12.3 MPa of stress arises there. For larger inner radii, this increases further ($\sigma_t(r_i = 1.5\ \text{mm}) = 16\ \text{MPa}$, $\sigma_t(r_i = 2\ \text{mm}) = 23.9\ \text{MPa}$). The axial stresses caused by the cover forces are constant over the wall thickness and very low with 1.14 MPa. In the radial direction, compressive stress arises on the inner surface corresponding to the applied gas pressure. This decreases towards the outer radius. While the stresses scale linearly with the pressure, the bore diameter has an exponential effect on the axial and tangential stresses. The axial hole should therefore not be made too large. Equation (6.4) can be used to calculate the equivalent stress from the three stress components. For a pressure of 100 bar and a hole diameter of 2 mm, the maximum equivalent stress at the surface of the hole is 19.3 MPa. These stresses are low in relation to the strength of the Alloy 718 tested in this work. For materials with very low strength or significantly higher pressures, the diameter of the hole should be reduced further.

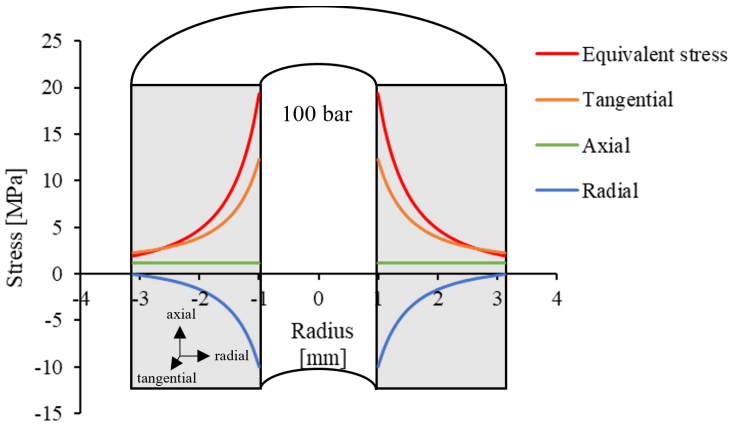


Figure 6.14: The multi axial stresses in the spatial directions tangential (σ_t), axial (σ_a) and radial (σ_r) in a hollow specimen for an internal pressure of 100 bar. Adopted from Reference [273].

6.2.6 Effect of additive manufacturing on hydrogen embrittlement of Alloy 718

Both the conventional Alloy 718 wrought and the additively manufactured Alloy 718 SLM exhibit hydrogen embrittlement. At 10 bar pressure, this is only minor, whereas at 100 bar, a significant reduction in ductility occurs. Both elongation to failure and reduction of area serve as indicators here. A significant difference between wrought and SLM cannot be determined based on the mechanical properties, see Figure 6.15. This is noteworthy because although the two materials were treated with the same heat treatment, there are significant differences in the microstructure, such as grain orientation, pores, and precipitates, as described in Chapter 4.1. But differences can also be observed on the fracture surfaces. For the SLM samples, flat surfaces tend to appear even in air, indicating a somewhat more brittle material behavior, and some pores can also be recognized. Under hydrogen influence, hydrogen-induced crack initiation is also observed from the

hydrogen-exposed surface. This crack then propagates into the area damaged by microvoids. Notably, there is a transition to an even more brittle area before failure occurs due to shear fracture, see Figure 6.9 c and d.

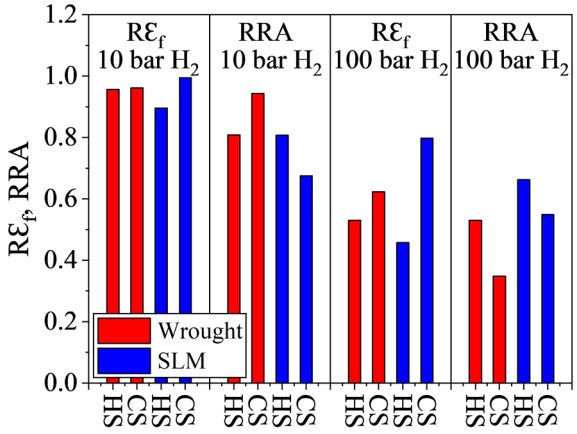


Figure 6.15: Hydrogen embrittlement indices relative elongation to failure $R\varepsilon_f = \varepsilon_{f,H_2}/\varepsilon_{f,Air}$ and relative reduction of area $RRA = RA_{H_2}/RA_{Air}$ of Alloy 718 wrought and SLM, tested at 10 bar and 100 bar hydrogen pressure with conventional specimens (CS) and hollow specimens (HS) [273].

The hydrogen embrittlement of Alloy 718 wrought and laser powder bed fusion was also investigated by Mohandas et al. using notched HS. They found strong hydrogen embrittlement at 150 bar hydrogen pressure. The hydrogen embrittlement index ($HEI = (RA_{N_2} - RA_{H_2})/RA_{N_2} \times 100$) was about 0.4 for the heat-treated wrought material. The LBPF material without heat treatment and less strength than the conventional material had an HEI of about 0.2. The LBPF with heat treatment according to AMS5663 [97], as used in this work, showed higher strength then the conventional material and the lowest HEI of about 0.1 [25]. However, the conventional material had a different heat treatment, strength and elongation to failure in air than the LPBF material, hindering a direct comparison of whether the AM material is more susceptible than conventional material. Yoo et al. investigated pre-charged Alloy 718 LPBF in SSRT tests and found similar hydrogen-induced features on the fracture surfaces as observed in this study, see Figure 6.7 to Figure 6.9. However, due to the strong electrochemical pre-charging, significantly more flat facets with slip bands were visible compared to the in-situ tests with gaseous charging in this thesis [244].

6.3 Low cycle fatigue experiments

In this chapter, the low cycle fatigue (LCF) behavior of the nickel-based Alloy 718 under the influence of hydrogen is investigated. LCF experiments are important for safe component design and the estimation of the fatigue lifetime of components in service. In Chapter 6.3.1 fatigue experiments were conducted on conventional specimens in air on material in the initial state and on hydrogen pre-charged material. In Chapter 6.3.2, experiments on hollow specimens are compared with conventional autoclave tests to determine the suitability of the hollow specimen technique

for fatigue testing. In the subsequent Chapters 6.3.3 to 6.3.5, the influencing factors of frequency, hydrogen pressure and temperature on fatigue lifetime under hydrogen atmosphere were investigated using hollow specimens. In Chapter 6.3.6 the influence of hydrogen on the Alloy 718 SLM was investigated. The damage behavior under the respective test conditions was examined using fractography to infer the mechanisms of hydrogen damage. In Chapter 7, a mechanism-based damage model was developed based on the test data and findings from fractographic investigations.

6.3.1 Pre-charged low cycle fatigue experiments

This chapter examines the influence of hydrogen on Alloy 718 wrought when the specimen is pre-charged with hydrogen. Conventional specimens were pre-charged for 10 days at 350°C and 100 bar hydrogen pressure in the developed hydrogen charging tube, see Chapter 3.2. The hydrogen concentration of the specimens was about 27 wppm, as described in Chapter 5.1. The results are compared with experiments without hydrogen pre-charging.

Figure 6.16 illustrates the cycles to failure for different strain ranges $\Delta\varepsilon_t$ of the reference CS (grey dots) and on the pre-charged CS (red dots). The fatigue life of the pre-charged samples is reduced by about 55% compared to the reference experiments at the same strain range. For both types of specimens, the number of cycles to failure N_f decreases strongly with increasing $\Delta\varepsilon_t$. The dependence of the load $\Delta\varepsilon_t$ and the fatigue life N_f can be fitted with a power law function for the reference tests and the pre-charged tests, see Equation (3.4). These fit curves are implemented in Fig. 6.16.

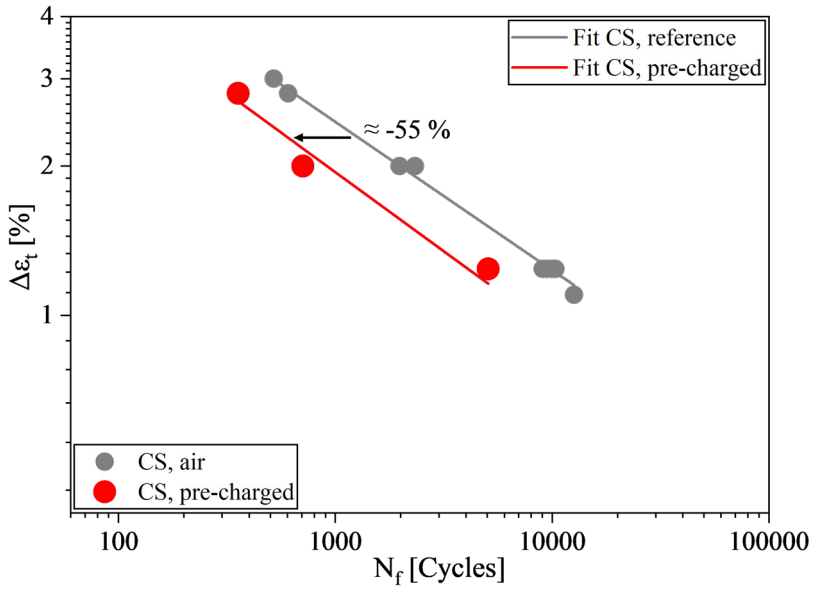


Figure 6.16: Low cycle fatigue experiments on conventional specimens (CS) of Alloy 718 wrought in the initial state for reference and in the hydrogen pre-charged state. ($R = -1$, $f = 0.1\ Hz$). Cycles to failure N_f are reduced by about 55 % for hydrogen pre-charged samples.

The fracture surfaces of the uncharged specimens, see Figure 6.17 a-c, show crack initiation from the surface, as expected under LCF loading [303,304]. For the specimen tested in air, several crack initiation points could be observed on the fracture surface, see Figure 6.17 a. In the area of crack initiation, striations are visible, which are usually formed by ductile deformation during crack propagation. The pre-charged specimen, see Figure 6.17 d-f, also shows that a crack initiated from the surface. No further crack initiation sites are visible here. Under hydrogen influence, no striations are visible. Instead, flat facets are seen here, indicating brittle crack growth due to the tearing of slip bands. Deformation-induced slip bands are visible on the facets.

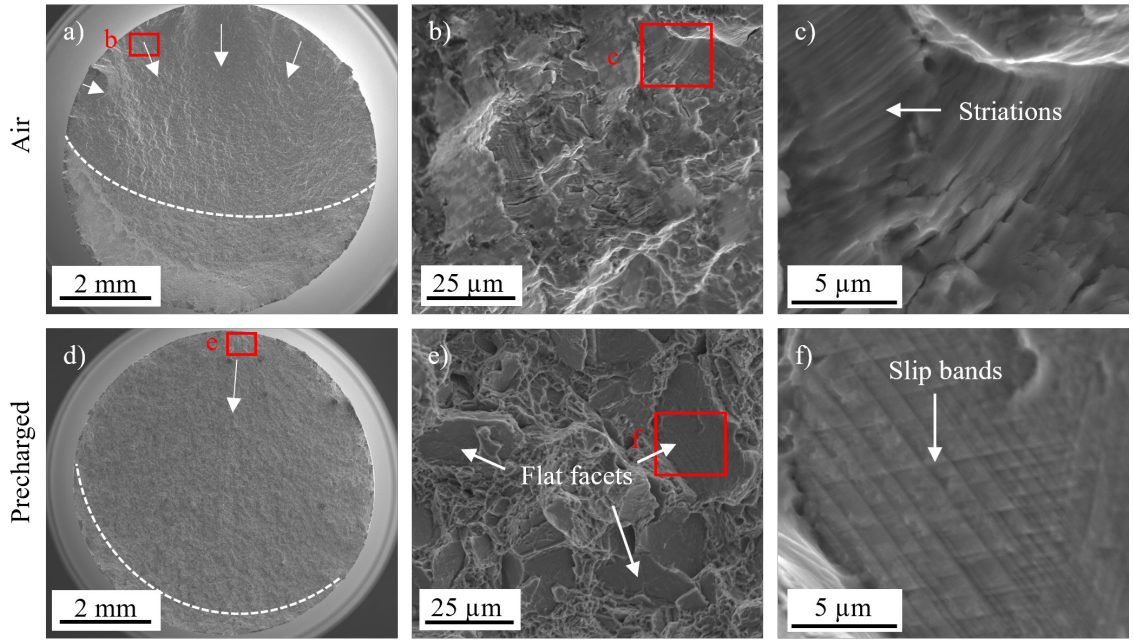


Figure 6.17: Fracture surface images, taken by SEM, of a conventional specimen tested in air (a-c) and pre-charged at 350 °C and 100 bar hydrogen pressure for 10 days (d-f). ($R = -1$, $\Delta\varepsilon_t = 1.24\ \%$ $f = 0.1\ Hz$, $T = 20\ °C$). The fracture surface of the air sample shows crack initiation from several points and ductile crack growth with striations. The pre-charged sample shows a single initiation point and flat facets with slip bands, indicating more brittle crack growth. Adapted from [305].

6.3.2 Comparison of conventional and hollow specimens in low cycle fatigue experiments

In order to use hollow specimens for investigating fatigue behavior under hydrogen influence, comparability between conventional specimens and hollow specimens must first be established. Comparative experiments were conducted on conventional and hollow specimens, tested in reference atmospheres, with inner hydrogen pressure and in a hydrogen autoclave at Fraunhofer LBF. Experiments were conducted on Alloy 718 wrought and SLM at different strain ranges, namely 1.1 %, 2.0 % and 3.0 %. Experimental results obtained in air from the previous chapter at strain ranges of 1.24 % and 2.8 % were added to have more data points. All experiments had a strain ratio of R = -1.

Figure 6.18 shows reference experiments in air and in nitrogen or with inner nitrogen pressure. Experiments on CS show no difference between experiments in air and with 10 bar nitrogen pressure in the autoclave. The same applies to the HS. Samples in air and samples with 50 bar inner nitrogen pressure show comparable cycles to failure N_f. However, it can be observed that the HS have a systematically lower lifetime than the CS. This reduction is approximately -33% for all tested strain ranges. At the highest strain range of $\Delta\varepsilon_t = 3\%$, the CS buckled under compressive load as the pull rods in the autoclave are long and alignment is difficult, causing it to fail after only 96 cycles. In contrast, Figure 6.19 shows the results of LCF experiments on Alloy 718 SLM on HS and CS and no significant difference between HS and CS tested in air is recognizable.

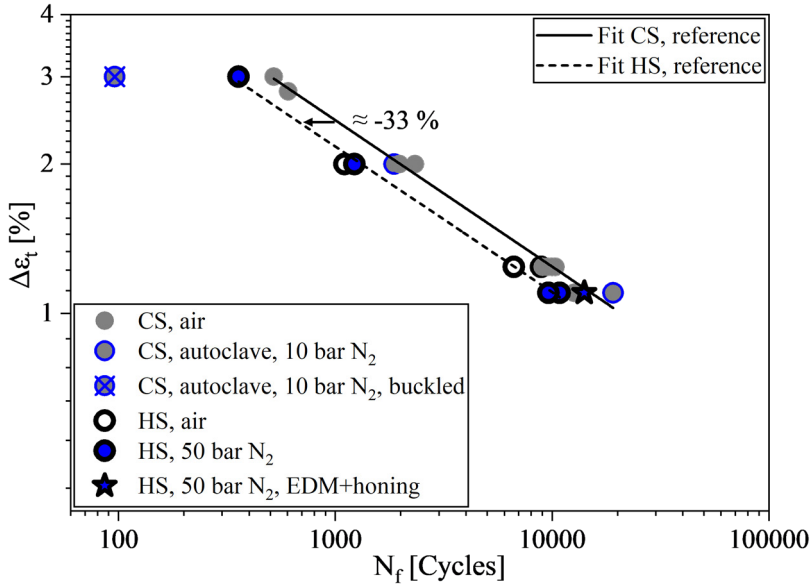


Figure 6.18: Low cycle fatigue experiments on conventional specimens (CS) and hollow specimens (HS) of Alloy 718 wrought in air, 10 bar nitrogen atmosphere and 50 bar nitrogen inner pressure. ($R = -1, f = 0.1\ Hz, T = 20°C$). While nitrogen pressure shows no influence on fatigue life, hollow specimens show about 33 % reduced cycles to failure N_f compared to conventional specimens. The sample tested in the autoclave at highest load must be excluded as it buckled.

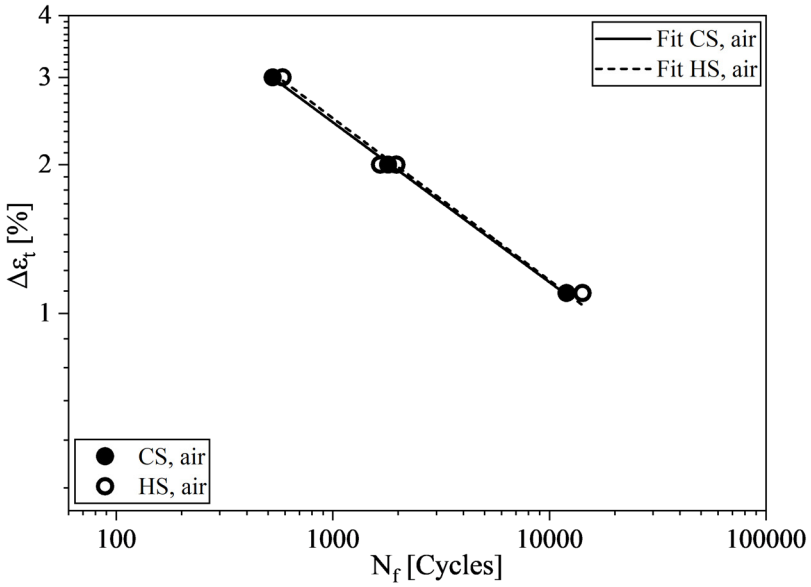


Figure 6.19: Low cycle fatigue experiments on conventional specimens (CS) and hollow specimens (HS) of Alloy 718 SLM in air. ($R = -1$, $f = 0.1\ Hz$, $T = 20°C$). Hollow and conventional specimens show about the same cycles to failure N_f.

In a 50 bar hydrogen gas atmosphere, both conventional specimens and hollow specimens (exposed to inner and outer pressure) showed a significant reduction in lifetime of about -60 % from reference tests, see Figure 6.20. The fit curves show a parallel shift of the lifetime lines for both specimen geometries. In the case of CS, the specimens buckled at the highest strain amplitude of $\Delta\varepsilon_t = 3\%$ as it was observed with the reference tests conducted in the autoclave at 10 bar nitrogen pressure.

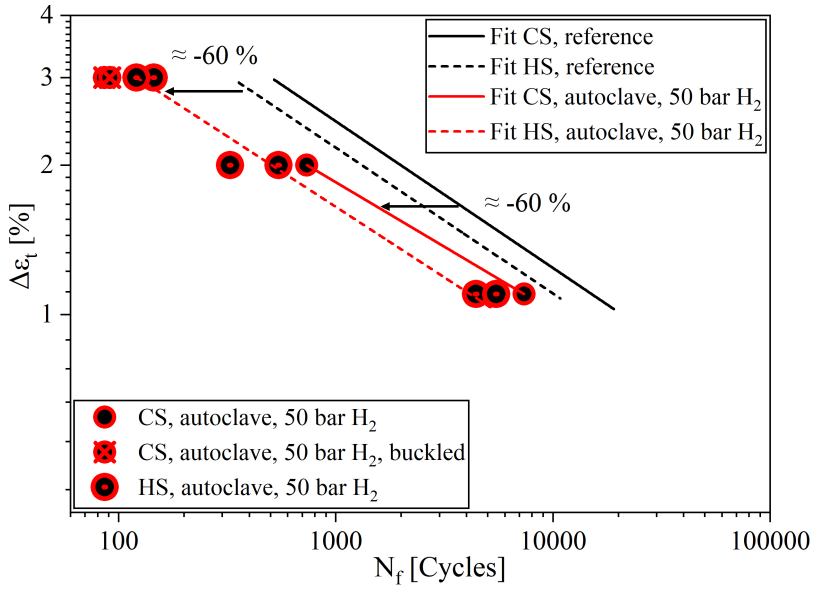


Figure 6.20: Low cycle fatigue experiments on conventional specimens (CS) and hollow specimens (HS) of Alloy 718 wrought in the autoclave at a hydrogen pressure of 50 bar. ($R = -1, f = 0.1\ Hz, T = 20°C$). Both, CS and HS show about 60 % reduced cycles to failure N_f und hydrogen atmosphere. Samples tested at highest load must be excluded as they buckled.

Hollow specimens with inner hydrogen pressure were tested at 50 bar and 100 bar hydrogen pressure and the results are compared to the fits of CS and HS tested in the autoclave at 50 bar, see Figure 6.21. The HS tested at 50 bar shows significant reduction in cycles to failure at 2 % strain range and fits well with the ones tested in the autoclave. However, the HS tests at 3 % strain range show a little less hydrogen damage and the ones tested at 1.1 % fall on the fit line of experiments tested in air. This is similar for the experiments conducted at 100 bar hydrogen pressure. Again, significant reduction in N_f be seen at 2 % and none at 1.1 %. However, a strong hydrogen effect is also visible at 3%.

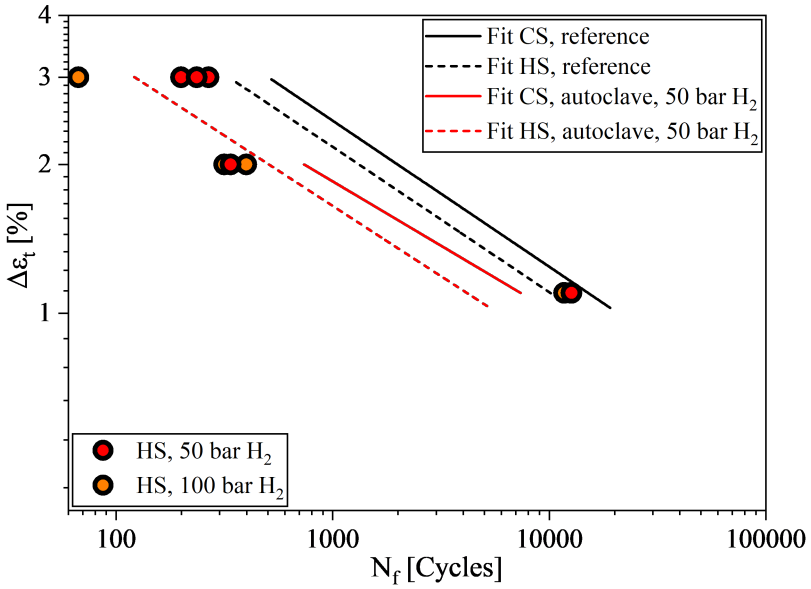


Figure 6.21: Low cycle fatigue experiments on hollow specimens (HS) of Alloy 718 wrought with 50 bar and 100 bar inner hydrogen pressure. ($R = -1$, $f = 0.1\ Hz$, $T = 20°C$). Reference lines of experiments tested in air and in the autoclave of HS and CS are plotted for comparison. 2 % strain range experiments fall on the reference line of hollow specimens tested in the autoclave. At 3 % the 50 bar experiments show more and the 100 bar experiments less cycles to failure N_f than the reference line. At 1.1 % the 50 bar and 100 bar fall on the reference line of experiments in air.

The examination of the fracture surfaces in Figure 6.22 shows that for the small strain range of 1.1 % the crack started from the outer surface, whereas for the larger strain ranges the crack always started from the inner surface, independent of whether the sample was tested in the autoclave with inner and outer pressure or if it was tested only with inner pressure. This means that at the higher strain ranges of 2 % and 3 %, the initiated cracks were always exposed to hydrogen. Thus, at the small strain range of 1.1 % the cracks initiated from the outside and only for the specimen tested in the autoclave with outer pressure, the cracks were exposed to hydrogen.

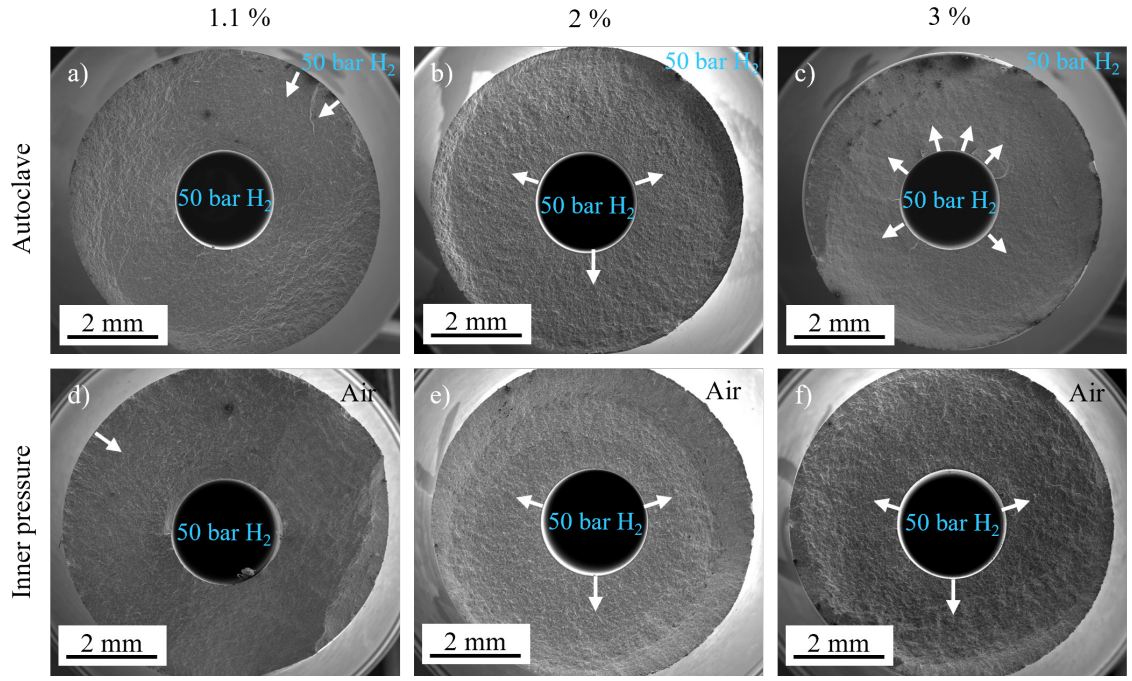


Figure 6.22: Fracture surface images, taken by SEM, of hollow specimens, tested in autoclave (a-c) and tested with inner hydrogen pressure (d-f) at 50 bar ($R = -1$, $f = 0.1\ Hz$, $T = 20\ °C$). White arrows indicate locations of crack initiation. For 1 % strain range, cracks initiated on the outer surface. For the experiments conducted with only inner pressure this means that the crack was not in contact with hydrogen. At 2 % and 3 % cracks initiated at the inner hole, which was in contact with hydrogen for both types of experiments.

Additional hollow specimens were produced in which the axial hole was manufactured by electrical discharge machining and then processed using abrasive flow machining (HS AFM) to eliminate any influence of the drilled microstructure, see Chapter 4.2, on the fatigue life. Figure 6.23 shows the results of the LCF tests in ambient air and with a hydrogen inner pressure of 50 bar. The fatigue life N_f of the reference tests in ambient air on HS AFM fall roughly between the CS and the drilled HS, with a slightly steeper fit line. With a hydrogen pressure of 50 bar, a clear reduction in N_f is observed for the HS AFM across all tested strain ranges. This reduction is about -60%, as seen in the experiments in the hydrogen autoclave, see Figure 6.20.

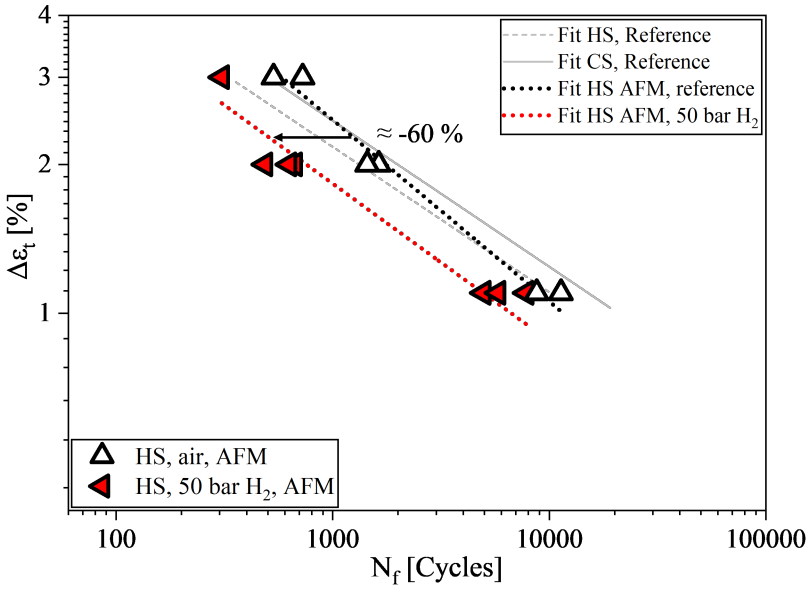


Figure 6.23: Low cycle fatigue experiments of hollow specimens (HS) of Alloy 718 wrought with the inner hole manufactured by electrical discharge machining and abrasive flow machining. Experiments were conducted in ambient air and with 50 bar inner hydrogen pressure ($R = -1$, $f = 0.1\ Hz$, $T = 20°C$). Fatigue life N_f in air falls between reference tests on CS and drilled HS. With 50 bar inner hydrogen pressure, N_f is reduced by about -60 % for all tested strain ranges, as it was observed by tests in the hydrogen autoclave.

6.3.3 Effect of frequency

The slow strain rate tensile tests show a strong dependence of hydrogen embrittlement on the strain rate, see Chapter 2.4.3 and 6.1.1. The aim of this chapter is to investigate the effects of test frequency in low cycle fatigue tests. Figure 6.24 shows the lifetime in cycles as a function of frequency. At 1 Hz and 100 bar internal hydrogen pressure the fatigue lifetime is slightly reduced when compared to tests in air at 0.1 Hz and at ambient pressure. The lifetime continues to decrease with decreasing frequency. A maximum of hydrogen degradation could be reached at 0.001 Hz, although there are not enough data points to determine this with certainty. It is remarkable that the average strain rate at 0.001 Hz is with $4x10^{-5}\ 1/s$ approximately in the range at which the plateau of maximum hydrogen embrittlement is typically reached in tensile tests. However, this frequency is too slow to carry out many experiments. Since a significant hydrogen damage can already be recognized at 0.1 Hz, the following tests are carried out at this frequency.

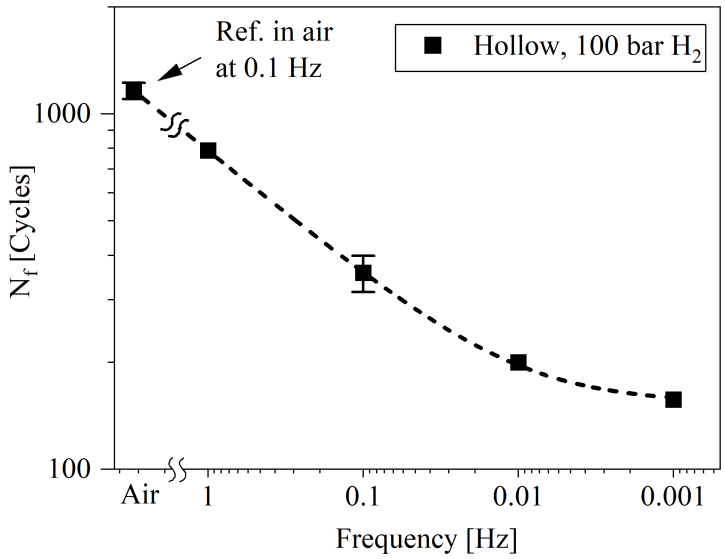


Figure 6.24: Low cycle fatigue life of hollow specimen tested with 100 bar hydrogen pressure at different test frequencies compared to experiment in air (tested at $f = 0.1\ Hz$). ($R = -1$, $\Delta\varepsilon_t = 2\ \%$, $T = 20°C$). With decreasing test frequency, the cycles to failure N_f of experiments with inner hydrogen pressure decrease.

The stress-strain hysteresis at half-life of the LCF tests (Figure 6.25) provide insights into the macroscopic material behavior. The hysteresis overlap at 0.1 Hz for the specimen tested in air and with hydrogen internal pressure. Even at lower frequencies, 0.01 Hz and 0.001 Hz, when hydrogen has more time to penetrate the material, no difference to the hysteresis in air can be observed. Only the hysteresis at 1 Hz shows a slight deviation from the other hystereses. The slope of the elastic straight line and the maximum stress decrease slightly. This effect is discussed in Chapter 6.4.4.

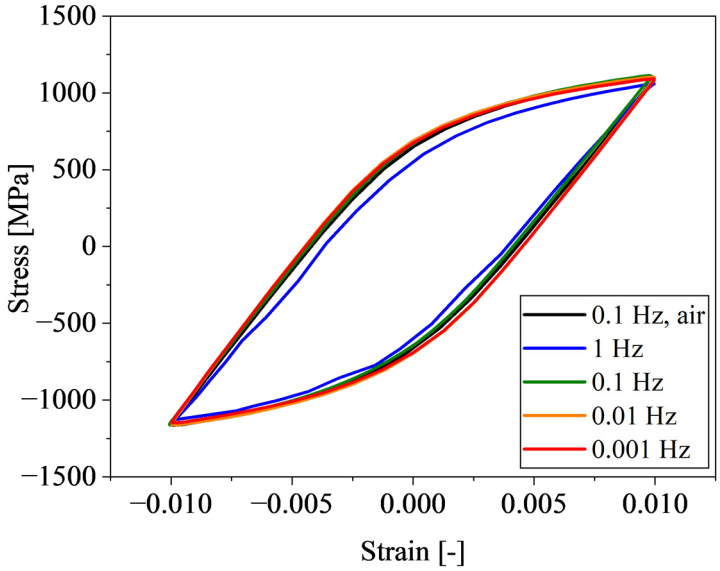


Figure 6.25: Stress strain hystereses of low cycle fatigue experiments at half cycles to failure with a strain range of $\Delta\varepsilon_t = 2\ \%$ in air and with 100 bar inner hydrogen pressure at test frequencies from 0.001 Hz to 1 Hz. ($R = -1$, $\Delta\varepsilon_t = 2\ \%$, $T = 20°C$). Hystereses measured in hydrogen fall on the hysteresis measured in air. Only the hysteresis for the experiment at 1 Hz slightly deviates (blue line).

In contrast to the macroscopic material behavior, the fracture surfaces of the specimens tested at 0.001 Hz and 1 Hz show significant differences, as seen in Figure 6.26. The specimen tested at low frequency shows over a large region flat facets from the borehole to the outer side. Only a small area with residual fracture surface is visible. In contrast, the sample tested at 1 Hz shows striations near the borehole, which indicate ductile crack growth. However, some hydrogen effect is still visible at 1 Hz as occasionally flat facets still occur and the fatigue life is little reduced compared to experiments in air.

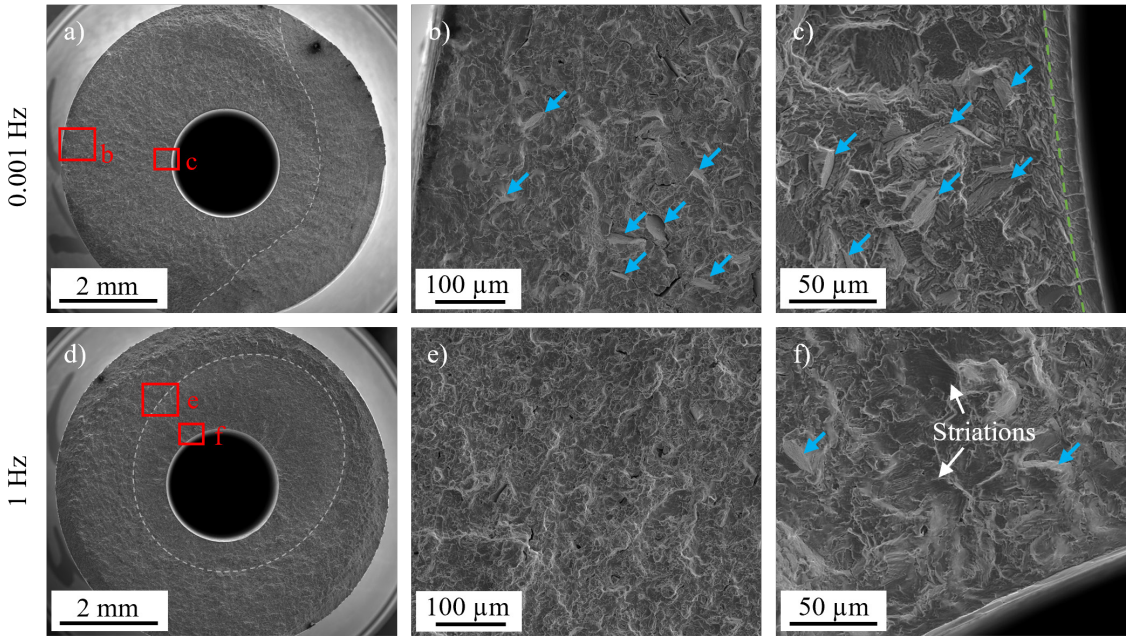


Figure 6.26: Fracture surface images, taken by SEM, of hollow specimens, tested at 0.001 Hz (a-c) and 1 Hz (d-f) with 100 bar hydrogen pressure ($R = -1$, $\Delta\varepsilon_t = 2\ \%$, $T = 20\ °C$). While the fracture surface of the 1 Hz experiment shows striations and only few flat facets around the borehole, as indicated by blue arrows, the specimen tested at 0.001 Hz exhibits many flat facets even at the circumference.

6.3.4 Effect of pressure

Hydrogen pressure is another influencing factor on hydrogen embrittlement of metals. While the diffusion rate of hydrogen is not affected by pressure, the hydrogen concentration increases with rising pressure, according to Sieverts' law. This also impacts hydrogen damage in the experiments. Figure 6.27 shows LCF tests on hollow specimens filled with nitrogen gas as reference. It should be noted that the influence of internal nitrogen pressure is negligibly small, as there is no trend towards shorter lifetimes with increasing nitrogen pressure. Thus, the internal pressure itself does not affect the lifetime, in the studied pressure range. However, under hydrogen pressure, a significant influence of the pressure is evident. At 10 bar, the fatigue life is only slightly affected. With increasing pressure, hydrogen damage increases and N_f is reduced. This decrease in fatigue life can be fitted with a power law relationship of the pressure $N_f = g * p^h$, where p is pressure and $g = 1587.5$ and $h = -0.344$ are material dependent constants.

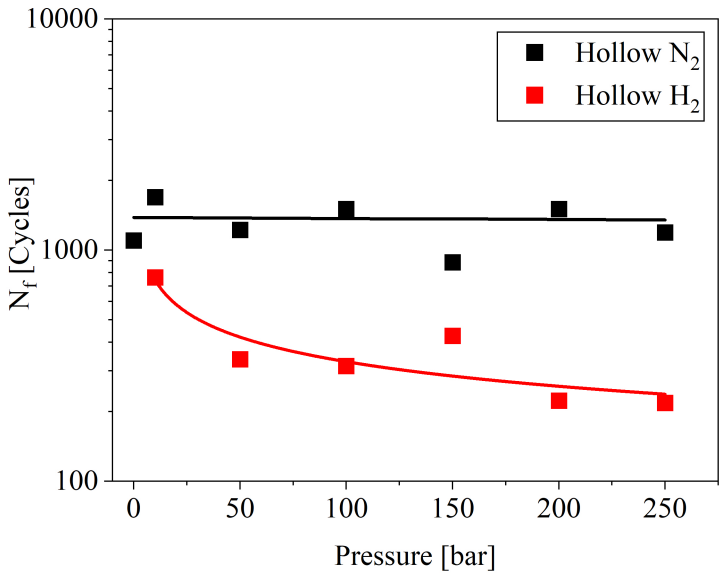


Figure 6.27: Low cycle fatigue life of hollow specimen tested with different pressures between 10 bar and 250 bar of nitrogen (0 bar = air) and the same pressures of hydrogen. ($f = 0.1\ Hz, R = -1, \Delta\varepsilon_t = 2\ \%$). Cycles to failure N_f are not significantly influenced by nitrogen pressure as the linear trendline shows. With increasing hydrogen pressure N_f decreases with a relationship of $N_f = g * p^h$.

6.3.5 Effect of temperature

Temperature is another important factor influencing hydrogen embrittlement. It affects both the material properties in air such as elastic modulus and strength, but also the diffusion and solubility of hydrogen in the metal lattice as these are Arrhenius type functions depending on temperature, see Chapter 2.3.2. This means that hydrogen effects on mechanical properties of alloy 718 are also strongly influenced by temperature, as shown in Chapter 2.4.3. Therefore, it is crucial to always consider the temperature effect in hydrogen embrittlement experiments.

Low cycle fatigue experiments were conducted over a wide temperature range (-100 °C to 600 °C) to investigate the influence of temperature on hydrogen embrittlement, as shown in Figure 6.28. Since hydrogen diffusion depends not only on temperature but also on time, particularly at lower temperatures with slow hydrogen diffusion, the test frequencies were varied between 0.001 Hz and 1 Hz. To narrow down the test field, all experiments were conducted at a strain range of $\Delta\varepsilon_t = 2\ \%$. Reference experiments were conducted in air at room temperature and above or nitrogen atmosphere below room temperature. Experiments with hydrogen were conducted at an internal pressure of 100 bar.

The Cycles to failure in air decrease with increasing temperature, as presented with the black trend line in Figure 6.28. Between room temperature and 200 °C, a slight plateau forms, and from 400 °C onwards, the cycles to failure decrease more rapidly. The experiments with hydrogen internal pressure (color symbols in Figure 6.28) show little deviation from the experiments in air at low temperatures. At 0.1 Hz in the temperature range from 20 °C to 200 °C, hydrogen damage

is highest. Here, the fatigue life is only about 20-30% compared to the fatigue life in air. At higher temperatures above 400 °C, hydrogen damage decreases strongly, and the experiments are similar to those in air. At room temperature and below, a strong dependence of embrittlement on the test frequency is evident. At 20 °C and 1 Hz, there is almost no hydrogen damage, while at 0.001 Hz, the most significant hydrogen damage is observed. This trend is also noticeable at -10 °C and -50 °C. From this it can be concluded that testing at temperatures below room temperature would have to be carried out at a very low frequency in order to obtain conservative results. As this can lead to test durations of several years per test, this range can hardly be covered experimentally. Mechanism-based lifetime models can help to estimate the fatigue life at these conditions.

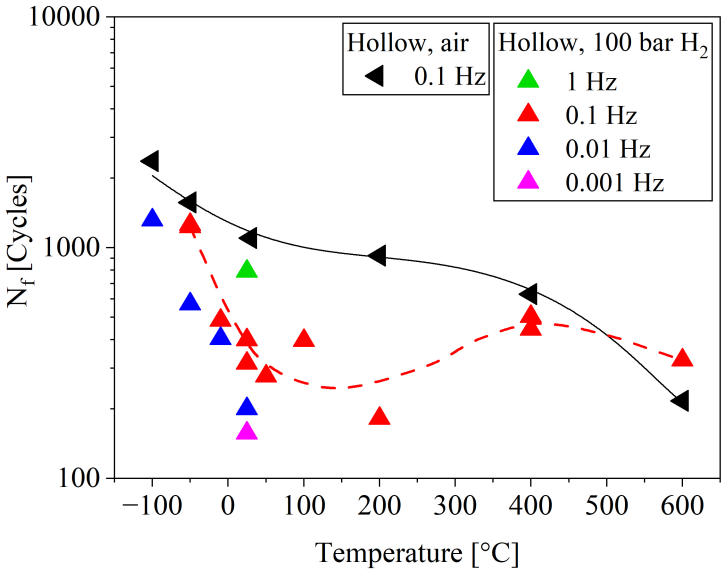


Figure 6.28: Low cycle fatigue life in cycles to failure N_f of hollow specimen tested in air (N_2 for temperatures below 20 °C) or with 100 bar hydrogen internal pressure at different temperatures between -100 °C and 600 °C and test frequencies between 0.001 Hz and 1 Hz. ($R = -1, \Delta\varepsilon_t = 2\ \%$). Lines are drawn for experiments in air and experiments with hydrogen at 0.1 Hz to guide the eye. The relationships of fatigue life and temperature, as well as other influencing factors are modeled in Chapter 6.4.8. The reduction in N_f is greatest in the range of 20-200 °C and at slow test frequencies. At low temperatures ($< -100\ °C$) and high temperatures ($> 400\ °C$), N_f under hydrogen influence approaches that in air again.

The fracture surfaces of the tested specimens were examined to identify changes in the damage behavior. In the specimens tested in air (see Figure 6.29), striations are visible in the temperature range of -100 °C to 400 °C, indicating ductile material behavior. In Figure 6.29 i (400°C) a cracked inclusion is visible. These were also observed in the micrograph before testing, see Figure 4.1, and it can be assumed that these cracks already occur during material production during metal forming. At 600 °C, the fracture appearance changes. In addition to striations, open grain boundaries are now also visible, as marked with orange arrows.

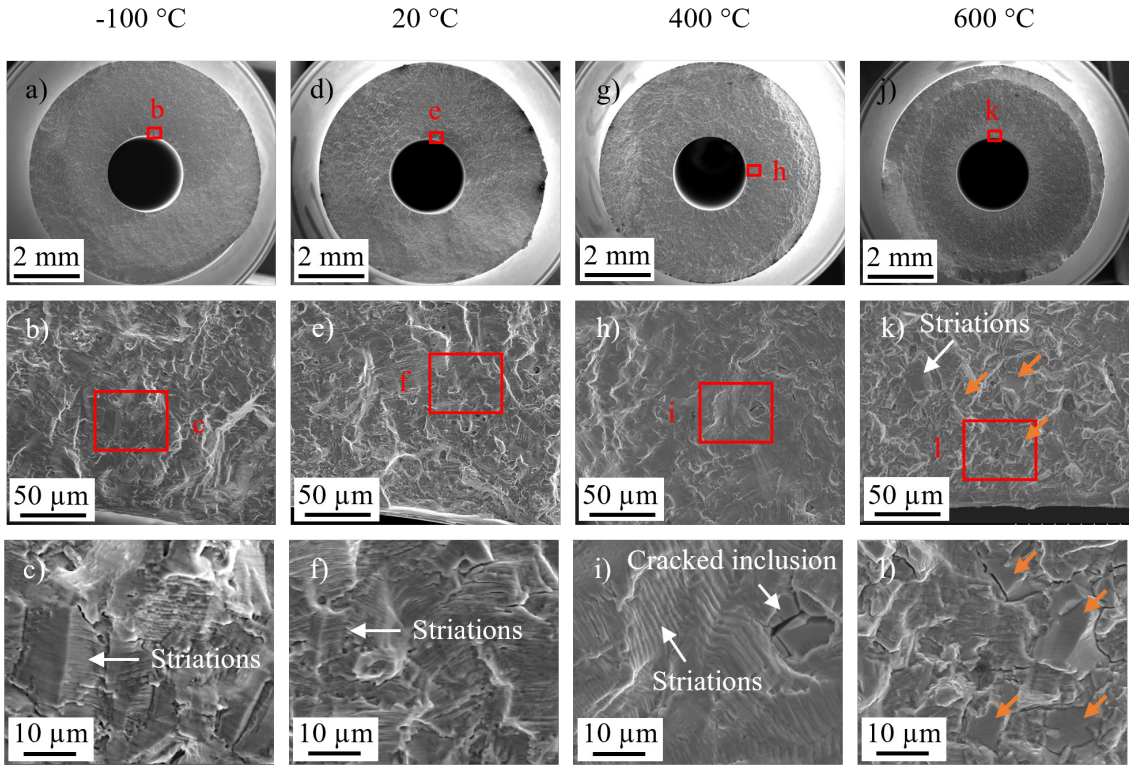


Figure 6.29: Fracture surface images, taken by SEM, of hollow specimens, tested at -100 °C, 20 °C, 400 °C and 600 °C in air. ($R = -1$, $\Delta\varepsilon_t = 2\ \%$, $f = 0.1\ Hz$). Orange arrows indicate open grain boundaries. A change is visible from fracture surfaces with striations up to 400 °C to a fracture surface containing open grain boundaries at 600 °C.

The fracture surfaces of the specimens tested under internal hydrogen pressure show significant differences depending on the temperature compared to the reference tests in air and nitrogen (see Figure 6.30). At -100 °C, striations are visible, similar to the reference tests, indicating ductile material behavior (Figure 6.30 a-c). At room temperature under hydrogen influence, flat areas are now evident. Additionally, an increased number of secondary cracks are observed (Figure 6.30 d-f). At 400 °C, flat surfaces and secondary cracks appear (Figure 6.30 g-i). Furthermore, step-like surfaces can be seen, with steps measuring approximately 1 µm in size. At 600 °C, cracks do not only initiate from the surface of the hole as usual but initiate also from the outer surface of the sample. The fracture surface around the hole shows no hydrogen influence in the form of brittle fractured grain boundaries or secondary cracks (Figure 6.30 k). In contrast, near the outer surface, where no hydrogen was present, open grain boundaries are visible, indicating intergranular crack growth (Figure 6.30 l).

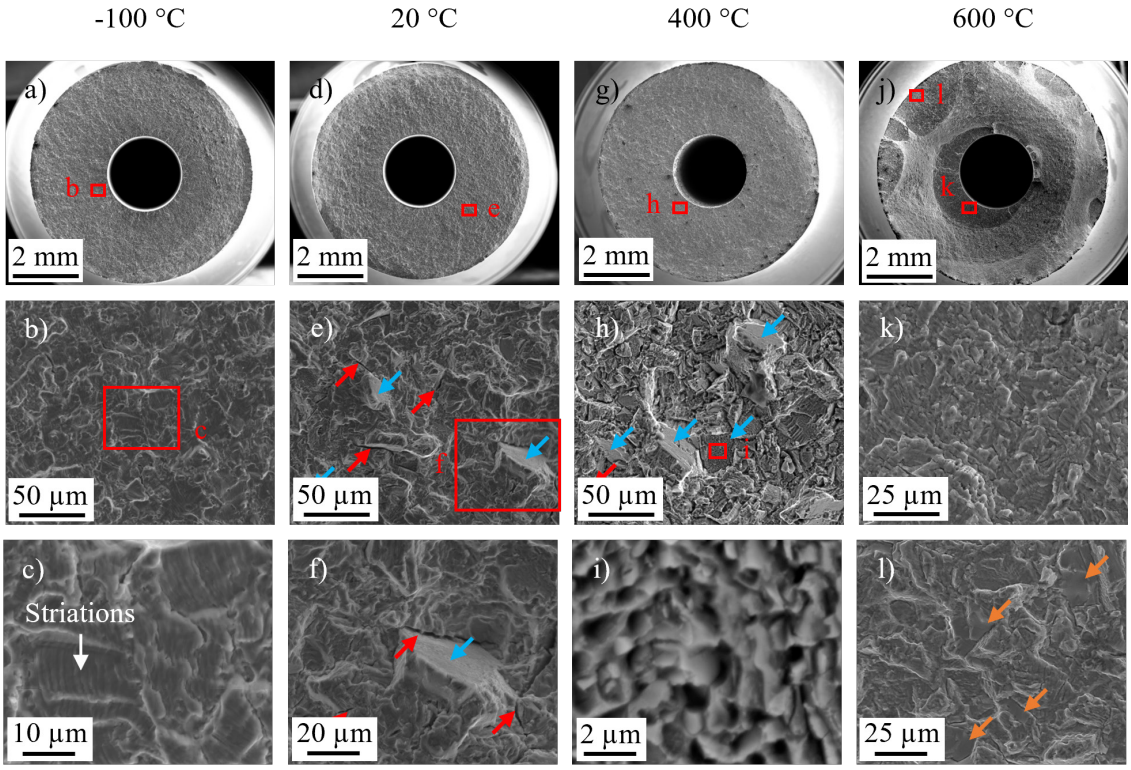


Figure 6.30: Fracture surface images, taken by SEM, of hollow specimens, tested at -100 °C, 20 °C, 400 °C and 600 °C with 100 bar inner hydrogen pressure. ($R = -1$, $\Delta\varepsilon_t = 2\,\%$, $f = 0.1\,Hz$, $p_{H_2} = 100\,bar$). Red arrows indicate secondary cracks, blue arrows indicate flat facets and orange arrows indicate open grain boundaries for the crack area exposed to air. At -100 °C the fracture surface is dominated by striations. At 20 °C and 400 °C flat facets are visible. At 400 °C open grain boundaries can be observed at the cracks that initiated from the outer surface, which was exposed to air during experiment.

6.3.6 Additive manufactured Alloy 718 SLM

LCF tests were conducted on HS of Alloy 718 SLM in build direction (0°) in air and 10 bar and 100 bar hydrogen, see Figure 6.31. The fatigue life of HS and CS of Alloy 718 SLM correlates very well with the fit of the CS from Alloy 718 wrought, see green and black lines. The influence of 10 bar hydrogen was minimal for all strain amplitudes. At 100 bar hydrogen pressure, significant hydrogen damage was observed at medium and high strain amplitudes. As with wrought Alloy 718, no hydrogen damage was detected at the small strain amplitude for samples with a drilled hole.

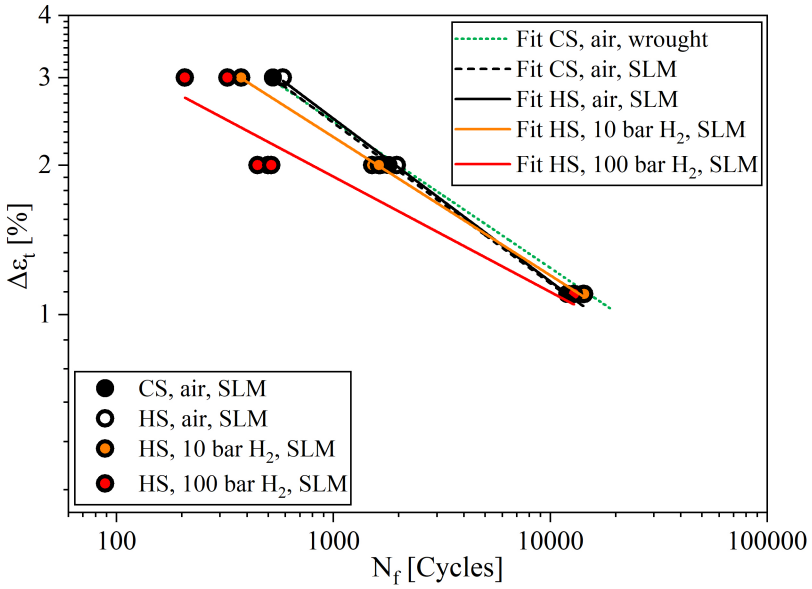


Figure 6.31: Low cycle fatigue experiments on conventional specimens (CS) and hollow specimens (HS) of Alloy 718 SLM in build direction (0°) in air, with 10 bar and 100 bar inner hydrogen pressure ($R = -1$, $f = 0.1\,Hz$, $T = 20°C$). Fatigue life is slightly reduced at 10 bar and significantly at 100 bar hydrogen pressure for 2 % and 3 % strain range. No hydrogen effect is observed at $\Delta\varepsilon_t = 1.1$ %. Adapted from [18].

Specimens were tested in 0° and 90° orientations relative to the build direction to investigate the influence of anisotropic material properties on fatigue life and hydrogen damage, see Figure 6.32. Since the microstructural investigations in Chapter 4.1 have shown a significant orientation of the grains in the build direction, an influence on the mechanical properties is to be expected. The 90° specimens show significantly lower lifetimes than the 0° specimens. This effect is visible across all strain ranges. The hydrogen influence at 10 bar pressure is rather low in both build directions, resulting in no significant influence on hydrogen damage from build direction.

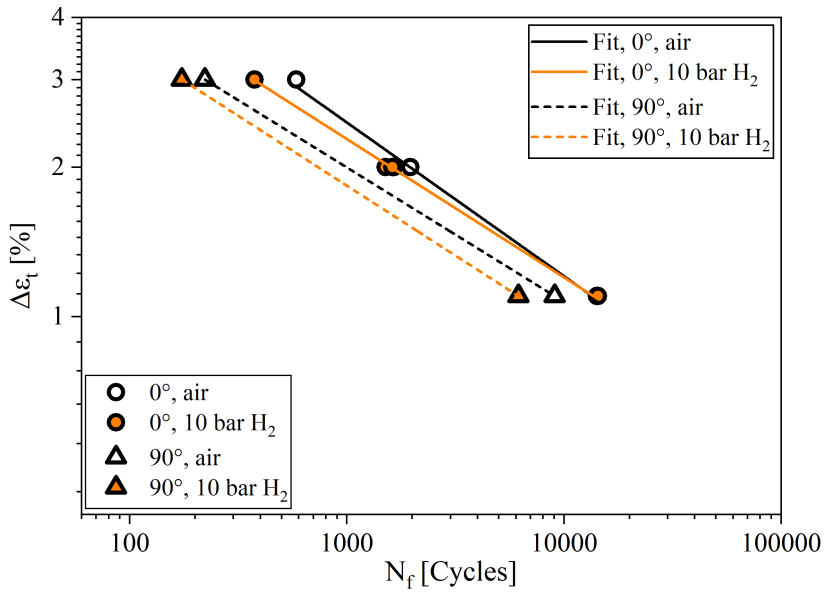


Figure 6.32: Low cycle fatigue experiments on hollow specimens of Alloy 718 SLM, printed in 0° and 90° to building direction, tested in air at ambient pressure with and without 10 bar inner hydrogen pressure ($R = -1$, $f = 0.1\ Hz$, $T = 20°C$). Fatigue life was significantly lower for the 90° printed specimens in both, air and hydrogen atmosphere. The effect of 10 bar hydrogen pressure was comparable between both orientations. Adapted from [18].

Alloy 718 SLM was also tested in a liquid nitrogen bath to investigate the influence of very low temperatures (-196 °C), see Figure 6.33. The results match at medium strain range, as the cycles to failure at room temperature and -196 °C are approximately the same. However, the slope of the lifetime curve differs significantly. At the large strain range of 3 %, the lifetime is significantly lower than at RT, while at the small strain range of 1.1%, the lifetime is higher than at RT. However, 10 bar hydrogen pressure showed no damaging influence at -196 °C, as the results (orange dashed line) meet the results obtained for the specimen measured in nitrogen at -196 °C (blue dashed line), in Figure 6.33.

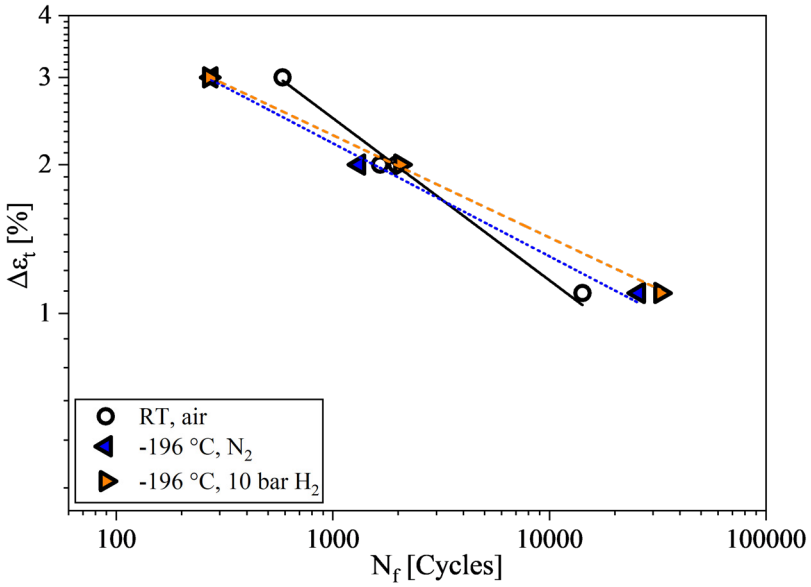


Figure 6.33: Low cycle fatigue experiments on hollow specimens (HS) of Alloy 718 SLM in air at 20 °C and in a liquid nitrogen bath at -196 °C with and without 10 bar inner hydrogen pressure ($R = -1$, $f = 0.1\ Hz$). At low temperature the slope of the fit line changed, leading to lower fatigue life at high load and higher fatigue life at low load. The effect of 10 bar hydrogen was negligible at -196 °C. Adapted from [18].

6.4 Discussion of low cycle fatigue experiments

6.4.1 In-situ vs. ex-situ

The Alloy 718 wrought specimens tested under a 50 bar hydrogen atmosphere (in-situ) and samples pre-charged at 350°C and 100 bar for 10 days (hydrogen concentration of 26.9 ± 2 wppm, ex-situ) both show hydrogen damage. The reduction of N_f was comparable with -60 % for in-situ tests on specimens at 50 bar hydrogen pressure and -55 % for the tests on the pre-charged specimens. Taking into account the temperature-dependent hydrogen solubility (Equation (2.52)) and Sievert's law (Equation (2.48)) with fugacity (Equation (2.45)), one obtains a theoretical hydrogen concentration of 30.6 wppm using the parameters determined in Chapter 5.5.1. This value is close to the measured concentration. When comparing this to the hydrogen concentration at a crack tip, calculated with stress dependent hydrogen concentration (Equation (2.53)) assuming the hydrostatic stress at a crack tip being about $\sigma_H = 3\sigma_{YS}$ [306], one obtains a local hydrogen concentration of 39.5 wppm for the tests at 50 bar and 20 °C. This local concentration is slightly higher than the mean concentration of the pre-charged specimens. The fracture surface reveals similar features for in-situ and ex-situ tested samples, which are flat surfaces and secondary cracks. However, it is expected that there may be significant differences between in-situ and ex-situ tests under different testing conditions. Since hydrogen is already present in the sample during ex-situ tests, surface effects do not impact hydrogen uptake, and hydrogen does not require much time to diffuse to critical locations, as it is available within the material. For example, Ogawa et al. found significant differences in the influence of the stress intensity factor range ΔK on crack growth

between ex-situ and in-situ tests: In in-situ tests Ogawa et al. observed a fatigue crack growth (FCG) acceleration ratio of about 10 over the entire tested range of $\Delta K = 20 - 80\ MPa\sqrt{m}$, while for ex-situ tests the FCG acceleration was found to increase from a ratio of 1 (no effect of hydrogen) at low ΔK to nearly 100 at high ΔK. Also, a significant influence of frequency was observed in both testing methods [206].

6.4.2 Comparability of conventional and hollow specimens

Tests were conducted on CS and HS in air and with nitrogen as a reference, in an autoclave under a complete hydrogen atmosphere, as well as with pressurized hydrogen from the inside and air from the outside, see Chapter 6.3.2. In air, HS made from Alloy 718 wrought showed approximately 33% lower lifetimes than CS, see Figure 6.18. In contrast, CS and HS made from Alloy 718 SLM lasted roughly the same duration, see Figure 6.19.

Finite element simulations of CS and HS of alloy 718 wrought under LCF load were conducted to compare the strain distributions in both specimens geometries according to the model of A. Reichenbacher [307] and to explain the difference in fatigue life. The material properties $E = 201.4\ GPa$, $\sigma_{cy} = 1893\ MPa$ and $n' = 0.104\ MPa$ for room temperature, evaluated from the experimental results in Chapter 7.3, and a strain range of $\Delta\varepsilon_t = 3\%$ and an inner pressure of 50 bar were used for the elastic plastic simulation. Figure 6.34 shows the plastic strain equivalent (PEEQ) across the parallel region of the CS (left side) and HS (right side) at the maximum tensile load of the first, fifth, and tenth cycle. For both specimen geometries, a comparable distribution of PEEQ across the specimen cross-section is observed, with local strain concentrations at the ends of the gauge section. With an increasing number of cycles, PEEQ increases but the distribution remains the same. On the outer surface, the maximum strain for both specimens is located in the middle of the gauge section. However, for the HS there is an additional surface at the hole from which cracks can initiate. At this surface there is a local increase in PEEQ at the edge of the gauge section by 4.56%. This increase is caused by the change in cross-section from the clamping area to the measuring area and is also visible in the CS. However, since the CS does not have a free surface there, crack initiation does not occur. Comparable results were obtained in other studies using finite element analysis [18,308,309]. For a X60 pipeline steel Michler et al. found a local strain peak at the same position which was increased by 3.5 % compared to the applied strain amplitude. They used a statistical approach to assess the impact on fatigue life with respect to the surface area where a crack can initiate. The result was that HS have a 5 % shorter fatigue life, but mainly because of the increase of surface area (+33%) by the hole. For a CS specimen with the same surface area the difference in fatigue life would be 1 %. Therefore, the small difference in strain distribution cannot explain the observed difference in fatigue life for wrought material.

It is more likely that there are differences in the surface microstructure, which have a significant impact on crack initiation. In Chapter 4.2, the surface roughness and the near-surface microstructure of Alloy 718 wrought were investigated, revealing significant differences between the polished outer surface and the drilled inner surface. The drilled inner surface exhibited higher roughness, see Figure 4.2, and the near-surface microstructure was influenced over a significantly larger

area, see Figure 4.3. In Chapter 6.3.2 it could be shown that HS manufactured by electrical discharge machining and abrasive flow machining, which have a significant less affected microstructure, see Chapter 4.2, had almost the same cycles to failure as CS.

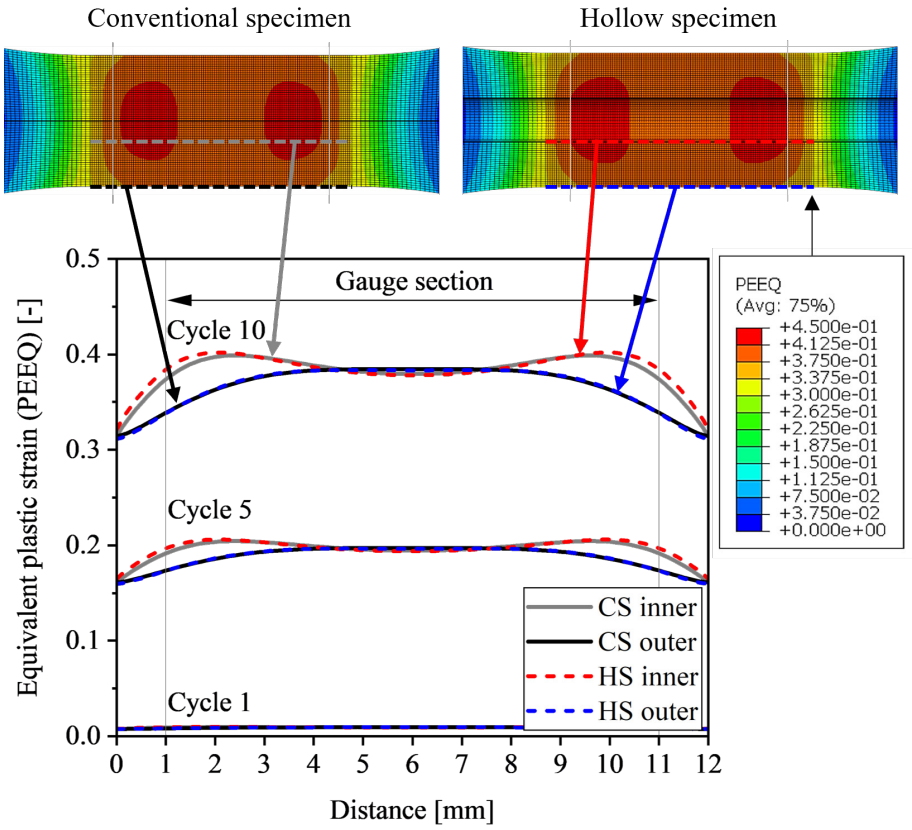


Figure 6.34: Finite element model of conventional and hollow specimens of alloy 718 wrought under cyclic load ($\Delta\varepsilon_t = 3\%$) with evaluation of the equivalent plastic strain (PEEQ) for cycle 1, 5 and 10. Maximum PEEQ is increased about 4 % on the inner surface of the HS.

Under hydrogen atmosphere in the autoclave test stand, both HS and CS made from Alloy 718 wrought showed a reduction in N_f of about 60%. This means that the hydrogen influence was equally strong for both specimen types at all three strain ranges tested. The situation is different for HS tested only under internal hydrogen pressure. With the medium strain range, the reduction in N_f was also about 60%, but at high strain range, hydrogen damage tended to be somewhat lower. At the small strain range of 1.1%, no hydrogen damage was detectable, and crack initiation occurred from the exterior surface that was not subjected to hydrogen exposure. It is assumed here that there is a strong influence from the altered microstructure at the inner surface, which was investigated in Chapter 4.2 and discussed in Chapter 4.3. The residual stresses introduced by mechanical processing methods (approximately -800 MPa in the case of reaming) cannot be relieved at the small strain amplitude of 1.1% because the plastic component in the experiment is too low. Due to the residual compressive stresses, the yield strength is not reached at the inner surface, and cracks tend to initiate at the outer surface. However, it was also shown in Chapter 6.3.2 that HS manufactured with AFM and EDM tested with internal hydrogen pressure yielded

the same reduction of N_f as CS tested in the autoclave for all tested strain ranges. This can be attributed to the manufacturing process as EDM does not introduce any mechanical forces and AFM affects the near-surface microstructure in a manner comparable to the lapping process used on conventional samples, see Chapter 4.2 and Figure 4.3.

6.4.3 Crack growth in hollow and conventional specimens

Under LCF loading, both HS and CS exhibit one or more semi-circular surface cracks, with cracks typically starting from the outer surface for CS and mostly starting from the inner surface for HS, compare Chapter 6.3.2. Two exemplary specimens with multiple semi-circular cracks are shown in Figure 6.35. Due to the curvature of the surface towards the crack (CS) or away from the crack (HS), there are differences in the area of the crack. This is sketched in Figure 6.35 c) and d). A typical technical crack of length $a = 1\,mm$ results for the CS in a crack area of $A_{crack} = 1.46\,mm^2$, which is 4.77 % of the total cross-sectional area. This fits well with the determination of the test end with a load drop of 5%, as described in chapter 3.8. In contrast, for the HS, sketched in Figure 6.35 d), the crack area is $A_{crack} = 1.91\,mm^2$, corresponding to 6.95 % of the total cross-sectional area. Therefore, theoretically, a 7 % load drop criterion should be used for HS. However, the load drop occurs in just a few cycles at the end of the test, and with test durations of approximately 200 to 20,000 cycles, a difference of individual cycles has little effect on the evaluation. A greater impact is likely due to the initiation of multiple cracks, as these significantly increase the crack area. However, the initiation of multiple cracks during the test cannot be controlled and can occur for both types of samples, HS and CS. Since crack growth is very fast at the end of the test, the slow crack growth at the beginning of the test has a significantly greater influence on the fatigue life. This should, however, be minimally affected by the specimen geometry.

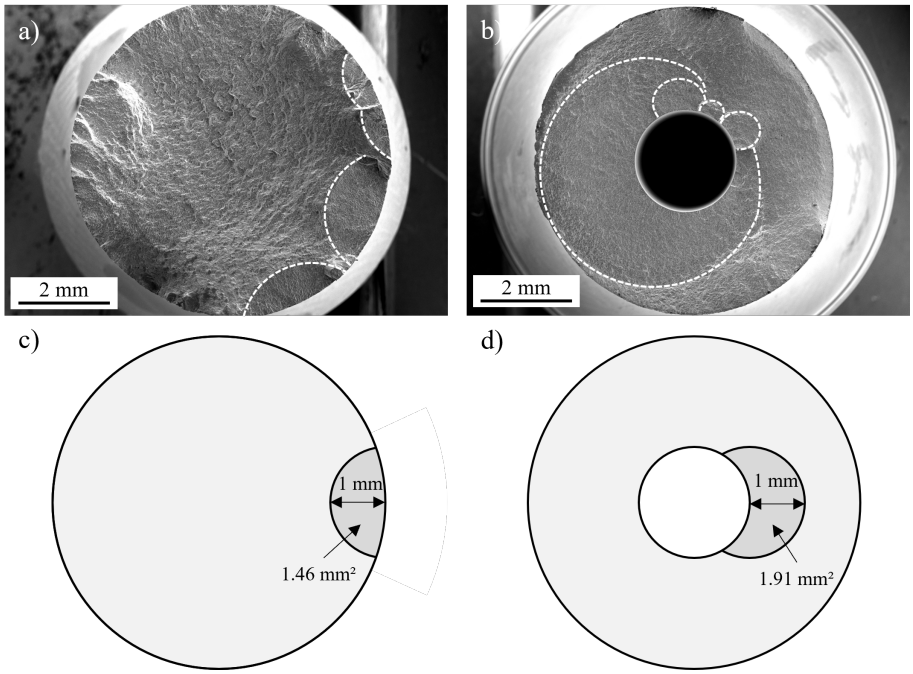


Figure 6.35: Fracture surface of a conventional specimen tested in 50 bar hydrogen atmosphere in the autoclave with crack initiation from the outer surface (a) and hollow specimen tested with 100 bar hydrogen inner pressure with crack initiation from the inner surface (b). Illustration of a single crack initiating from the outer surface of a conventional specimen (c) and from the inner hole surface of a hollow specimen (d). Due to the different curvature of the surface where the crack initiates, the fracture area of a crack of 1 mm length differs significantly for CS (1.46 mm²) and HS (1.91 mm²).

6.4.4 Effect of frequency

In Chapter 6.3.3, it was shown that the test frequency in LCF tests has a strong influence on hydrogen embrittlement, similar to the strain rate dependence in tensile tests. With decreasing the test frequency to 0.001 Hz, the N_f converge towards a minimum, meaning a maximum of hydrogen damage is reached, see Figure 6.24. This damage maximum can be explained by taking the H-diffusion length per cycle into account. Using Equation (2.56) for determining the penetration depth of hydrogen, one obtains with a cycle time $t = 1/f = 1000\ s$ and a diffusion coefficient at room temperature of $D_{718,20°C} = 1.18x10^{-15}\ m^2/s$ (from the Arrhenius type relationship defined in Chapter 5.5.1) the penetration depth per cycle being $x_p = 2\sqrt{Dt} = 2.18\ \mu m$. The average crack growth per cycle in a test with 1000 cycles and a critical crack length of 1 mm would be da/dN = 1 µm. Therefore, it can be assumed that the crack growth for a large part of the test is smaller than the penetration depth, and thus full hydrogen damage occurs. At 1 Hz, the penetration depth in 1 s is only $x_p = 0.0689\ \mu m$, which is significantly smaller than the crack growth. Therefore, the crack growth can only slightly be affected by hydrogen. Ogawa et al. also found a significant influence of frequency on FCG acceleration ratio $((da/dN_{H2})/(da/dN_{air}))$ for both, in-situ and ex-situ experiments. While fatigue crack growth was accelerated by a ratio of about 10 at 1 Hz this ratio increased to about 1000 at a frequency of 0.001 Hz [206]. Crack growth at 0.2 Hz and 0.02 Hz under in situ electrochemical hydrogen charging was investigated by Fu et al.

on additive manufactured Alloy 718 [38]. They also observed an increased crack growth under hydrogen. This was further accelerated by the slower test frequency. They also conclude that this is due the greater penetration depth of hydrogen at a lower test frequency [38]. This was also observed for other materials like X52 and X70 pipeline steel [205,310], SA-105 Grade II steel [311] and A6061-T6 Aluminum Alloy [312]. Bruchhausen et al. investigated alloy 718 in the HCF regime at a frequency of 20,000 Hz in 300 bar gaseous hydrogen [313]. Interestingly, they also found increased damage due to hydrogen at this high frequency. This could be related to the low crack advancement per cycle in the HCF regime, as the hydrogen only needs to penetrate a small distance. However, there is little data for the effect of frequency on LCF experiments. Michler et al. tested notched specimens of austenitic stainless steel in the LCF-regime and found that above 1 Hz hydrogen embrittlement was affected by frequency and below 1 Hz other frequency effects dominated [314].

The global stress strain behavior of Alloy 718 wrought was not affected by hydrogen at any frequency as can be seen in Figure 6.25. Only the hysteresis at the highest frequency of 1 Hz shows slightly deviation from the others. This can be attributed to the fact that the sample heats up during LCF experiments. The temperature of the specimen tested at 1 Hz was not measured, but in an experiment with $f = 0.1\,Hz$ and $\Delta\varepsilon_t = 3\%$. Here, the temperature increased by 6 °C at the beginning of the experiment. This temperature rise is caused by the plastic deformation of the sample, in which work is converted into heat. In a 1 Hz experiment, it can be assumed that this thermal energy cannot dissipate quickly enough, and the sample will heat up more. This rise in temperature slightly lowers the yield stress and elastic modulus, which causes the hysteresis to deviate slightly.

6.4.5 Effect of pressure

The hydrogen embrittlement of Alloy 718 is strongly influenced by hydrogen pressure, as the solubility of hydrogen increases with increasing pressure. As shown in Figure 6.27, damage increases rapidly at low pressures and then slowly towards a maximum at higher pressures, which has not yet been reached at 250 bar. The relationship between cycles to failure N_f and pressure p was found to follow a power law relationship of $N_f = g * p^h$, where g and h are constants. To account for the behavior of hydrogen as a non-ideal gas, the fugacity instead of pressure should be used here, as derived in chapter 2.3.1. This relationship was also observed by Michler et al. for the hydrogen embrittlement index of SSRT, fracture toughness, crack growth and fatigue tests and defined as $HEI \sim F^{|h|}$ with $|h| < 0.5$ [239]. In this study the exponent was found to be $h = -0.344$ for LCF life of alloy 718 wrought. This dependency was also observed for fatigue tests on notched specimens of X80 pipeline steel with $h = -0.4$ [315] and SCM435 [316] with $h = -0.432$. Although it is clearly evident that the results follow the power law relationship, it does not hold as in Sievert's law (Equation (2.48)) that $h = 0.5$, but rather $|h| < 0.5$. The value of $h = -0.344$ obtained in Chapter 6.3.4 suggests that time-dependent effects in the hydrogen reaction chain, see chapter 2.3.2, influence the effect of hydrogen on the mechanical properties. As the experiments on pressure dependency were conducted at a frequency of 0.1 Hz and it was shown in Chapter 6.3.3 and discussed in Chapter 6.4.4 that maximum hydrogen degradation is not reached at 0.1 Hz due to slow hydrogen diffusion it is clear that this time-dependent effect has an

impact. Furthermore, Michler et al. indicate hydrogen interactions with dislocations as a decisive time-dependent step [239].

6.4.6 Effect of temperature

Hydrogen damage in Alloy 718 wrought scales significantly with temperature during fatigue testing, as shown in Figure 6.28. At temperatures ≤ -100 °C, little damage occurs, and at high temperatures ≥ 400 °C, it also decreases significantly. Maximum damage occurs between room temperature and 200 °C. This matches well with literature, where Harris et al. studied Alloy 718 under LCF loading at -162 °C, 27 °C, and 678 °C, finding the greatest hydrogen damage at 27 °C, even though the temperature steps were too large to find the temperature of maximum embrittlement. At -162 °C, they observed an increased fatigue life, which they could not explain [317]. Michler et al. report a temperature range of -34 to 62 °C for maximum embrittlement of iron-based and nickel-based superalloys, evaluating reduction of area, fracture toughness, crack growth, and LCF from various test types. For austenitic stainless steels the temperature of maximum damage seems to be lower with -68 °C while BCC steels showed a wide range (-98 °C to 72 °C) for the the temperature of maximum embrittlement. Interestingly, the evaluation of Michler et al. of Alloy 718 from various test types (Tensile, LCF, K_H) showed a good agreement for the temperature of maximum hydrogen embrittlement around room temperature. In contrast, for 301 austenitic stainless steel, there was a difference of 150 °C between the temperature of maximum embrittlement determined from tensile tests and crack growth tests [227].

In addition to the cycles to failure, temperature also had a significant impact on fracture behavior in air and under hydrogen influence, as seen in the fracture surface images in Figure 6.29 and Figure 6.30. At -100 °C, the fracture surfaces in both air and hydrogen atmosphere showed striations (Figure 6.29 c and Figure 6.30 c), indicating ductile, transgranular crack growth. Accordingly, hydrogen had no effect on crack growth at this temperature. The situation changes for room temperature up to 400 °C. While striations appear in air (Figure 6.29 f and i), again indicating ductile material behavior, a noticeable change in the fracture surfaces under hydrogen is now evident. Striations are no longer visible, and instead, flat surfaces appear more frequently (Figure 6.30 e and h). As explained in Chapter 2.4.3, these surfaces are described as cleavage cracking along slip bands in {111} planes. The hydrogen embrittlement mechanisms involved are discussed in Chapter 6.4.8. At 600 °C, the fracture pattern changes significantly again. Cracks appear on all surfaces exposed to air, exhibiting quasi-cleavage fracture at grain boundaries (Figure 6.29 l). It is assumed that this effect occurs due to stress-assisted grain boundary oxidation [110] or atomic oxygen diffusion along grain boundaries and decohesion of the grain boundaries [111]. Interestingly, this effect is not observed in cracks occurring under pure hydrogen atmosphere in the borehole (Figure 6.30 k). At this high temperature, no flat facets appear in these regions. Thus, the fracture surfaces and the observed effects well reflect the influence on fatigue life.

6.4.7 Effect of additive manufacturing

Alloy 718 wrought and SLM were compared in strain-controlled LCF experiments in Chapter 6.3.6. Tests in air showed no significant differences in the fatigue life of wrought material and 0°-oriented to building direction specimen of SLM material, see Figure 6.31. However, the

90°-oriented specimens showed significantly reduced fatigue life, see Figure 6.32. This directional dependence arises from the inhomogeneous material microstructure in additive manufacturing with elongated grains in 0°-direction, see Chapter 4.1. Several works investigated the influence of orientation of printed specimens of Alloy 718. Gribbin et al. investigated specimens printed in 90° and 45° orientations. They found a strong dependence on orientation, particularly at low load amplitudes [86]. Konečná et al. examined three different orientations of as-printed samples and surfaces in the HCF regime and found a reduced fatigue life for the 0°-oriented samples [90]. This is in contrast to the results of this work, in which the 90°-orientation had a shorter fatigue life and appears as the weaker orientation. However, in the HCF regime, the surface roughness has an increasingly greater influence, and the specimens of Konečná et al. were tested as-printed with high roughness, which explains this change of the weaker orientation. Pei et al. found a shorter fatigue life of 0°-oriented Alloy 718 SLM specimens compared to forged Alloy 718 [318]. These different results show how all the influencing factors like orientation, print parameters, surface roughness, heat treatment and defects etc. influence the results.

There is currently little data on fatigue testing of additively manufactured Alloy 718 in hydrogen atmosphere. Puydebois et al. tested conventional AM samples in an autoclave at $p = 300\ bar$ with $R_\sigma = 0.1$ and $f = 0.5\ Hz$ under load control. A significant reduction in fatigue life was observed under hydrogen. However, a comparison with wrought alloy 718 was not conducted. It was found that the microstructure, after heat treatment, only differs from conventional material by a bimodal grain size distribution and little porosity [319]. Fu et al. investigated the influence of hydrogen on crack growth at $0.2\ Hz$ and $0.02\ Hz$ on notched samples of Alloy 718 SLM as printed with in-situ electrochemical charging [38]. They measured a significantly accelerated crack growth, which was further increased at the lower frequency. This aligns with the investigations in this study regarding the frequency influence, where a strong dependence was also measured in this frequency range, see Chapter 6.3.3. Furthermore, Fu et al. found that in the non-heat-treated alloy, cracks preferentially grow along the walls of the cell structure from the additive manufacturing process, where also hydrogen diffusion is increased [38].

6.4.8 Hydrogen embrittlement mechanisms

Hydrogen showed a significant reduction in fatigue life for Alloy 718. The crack growth per load cycle was strongly increased and a transition of the fracture surface from striations, indicating ductile crack growth, to a fracture surface with many flat facets was observed, see Figure 6.17, Figure 6.29 and Figure 6.30. To better understand the underlying mechanisms, micrographs and fracture surface images, see Figure 6.36, of a reference specimen, a hydrogen pre-charged specimen, and a hollow specimen tested with 50 bar internal hydrogen pressure were investigated. Figure 6.36 a shows the wrought material in its initial state with twin boundaries and no deformation. In contrast, the same material after a reference test in 50 bar nitrogen is shown in Figure 6.36 b. Due to the plastic deformation during the experiment, numerous dislocation slip bands (DSBs) are visible. These are mirrored at twin boundaries (TBs), and in some grains cross-slip (CS) is observed. The dislocations slip occurs on the activated {111} planes of the FCC metal lattice of Alloy 718 (Kreins et al., 2021). Figure 6.36 c shows a section along the main crack of the specimen tested with 50 bar hydrogen pressure. While the crack has mainly grown transgran-

ular, perpendicular to the loading direction, a section of crack growth in 45° to the loading direction is visible. Comparing the slip planes with the crack path reveals that the crack has grown precisely along the slip planes, visible as a flat facet (marked 'Facet' in Figure 6.36 c). This can also be observed on the hydrogen pre-charged sample (Figure 6.36 d). The main crack has grown directly along a slip plane and left a smooth facet. Branching from the main crack, slip planes can be observed in the grain. Along these slip planes, voids have formed which lead to damage along the slip planes. Figure 6.36 e and f show the fracture surface images of the 50 bar H_2 LCF test and the pre-charged LCF test. In both cases, flat facets due to failure at DSBs are visible with further DSBs on the facets. In Figure 6.36 e, also small facets with steps in between can be observed, where the crack has grown along different DSBs.

From this observations it can be concluded that hydrogen increases the dislocation movement on the active {111} slip planes, leading to the nucleation and enlargement of voids until failure occurs along the slip plane. This process is consistent with the HELP theory presented in Chapter 2.4.2, which states that hydrogen enhances local plasticity. It cannot be ruled out that final fracture along the pre-damaged slip plane occurs by hydrogen enhanced decohesion, as presented in Chapter 2.4.1. However, the driving mechanism is seen as the increased dislocation movement under hydrogen influence. Therefore, in the lifetime model in Chapter 7, hydrogen assisted fatigue crack growth is considered based on the HELP theory, assuming enhanced crack growth with increasing hydrogen occupation of dislocations.

Various studies also support the view that HELP is the primary hydrogen damage mechanism in Alloy 718. The hydrogen enhanced dislocation nucleation and movement along {111}-type slip planes was also observed by Hicks and Altstetter and associated with the HELP theory [55]. Yoo et al. were able to demonstrate through sections and EBSD recordings that the slip planes are indeed {111} planes and concluded that this is a HELP activated process, as slip bands are developed and strain is accumulated through hydrogen, ultimately leading to decohesion of the slip plane [244]. The formation of hydrogen-related voids along slip bands was also observed by Zhang et al. in Alloy 718 [211].

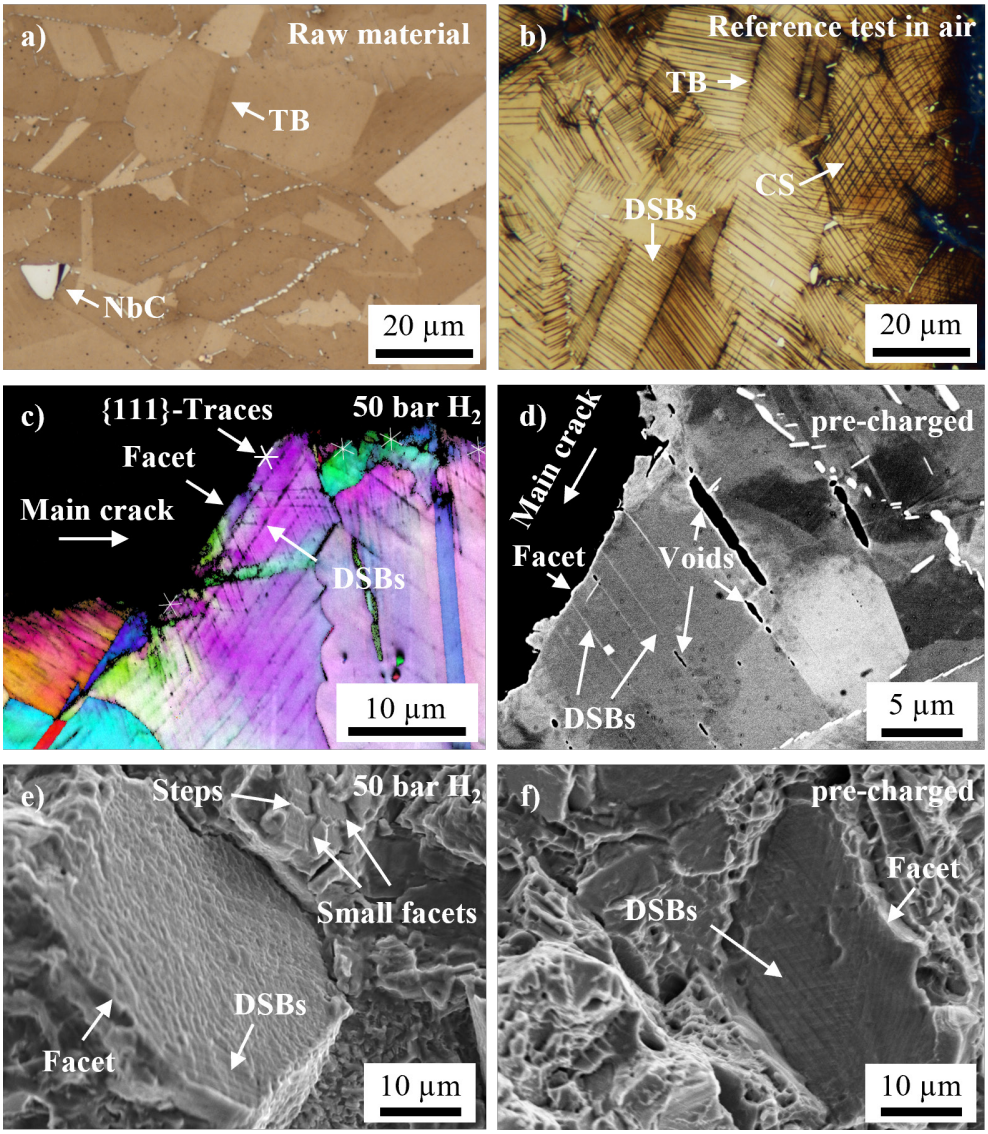


Figure 6.36: Microstructural characteristics in Alloy 718: a) Light micrograph of the etched Alloy 718 wrought in undeformed state with twin boundaries (TB) and Niobium carbide (NbC), b) etched micrograph of reference specimen after LCF test with dislocation slip bands (DSBs), TB and cross slip (CS), c) SEM-EBSD image of a specimen after 50 bar H_2 LCF test, taken at the main crack showing DSBs and fracture along DSBs (visible as flat facet), d) SEM micrograph of a hydrogen pre-charged specimen, taken at the main crack with voids nucleating at DSBs, fracture surface images taken with SEM of e) a 50 bar H_2 LCF and f) a pre-charged LCF specimen showing flat facets with DSBs.

In this Chapter 6, SSRT and LCF tests on hollow specimens were examined as a simple alternative testing method to investigate the influence of gaseous hydrogen on the mechanical properties compared to tests on conventional specimens in a hydrogen autoclave. The influence of hydrogen pre-charging in ex-situ tests as well as in-situ tests in pressurized gaseous hydrogen was considered, and the influencing parameters on hydrogen damage strain range, frequency, pressure, temperature and defects from additive manufacturing were examined. Fractographic investigations

provided insight into the damage behavior of Alloy 718 in air and hydrogen atmosphere. In Chapter 7, a crack growth model is applied to predict fatigue life based on the obtained results. The hydrogen damage parameter $Z_{D,H}$ is developed to describe the hydrogen damage and the physical relationships of the influencing factors studied here.

7 Mechanism-based lifetime model

In the previous chapters, it was demonstrated that hydrogen can have a significant impact on the mechanical properties and fatigue lifetime of alloy 718. There are many influencing factors, such as hydrogen availability, time, temperature, and mechanical load, that affect hydrogen embrittlement. Therefore, predicting the lifetime of components under hydrogen influence is challenging, and the testing effort to comprehensively evaluate all possible operating conditions of components is enormous. Additionally, there is a limited number of facilities that have these testing capabilities and costs can be several times higher than testing in air [320]. To minimize testing efforts as much as possible, mechanism-based lifetime models are suitable, as they have a wide range of applications due to their physical description of the mechanisms.

7.1 Hydrogen assisted fatigue crack growth model

A physically based approach is chosen for a crack growth model to describe the fatigue behavior of Alloy 718. It establishes a proportionality between the cyclic crack tip opening displacement $\Delta CTOD$ and the crack growth increment da/dN

$$\frac{da}{dN} = \beta(\Delta CTOD)^B \,, \tag{7.1}$$

where β and B are material-specific constants, which are determined in Chapter 7.3 for Alloy 718 wrought. The derivation of this equation is described in Chapter 2.2, where further literature on fracture mechanics is referenced. To consider the influence of hydrogen on crack growth, it is assumed that hydrogen affects the formation and movement of dislocations at the crack tip as proposed by Beachem in 1972, also known as the HELP theory, see Chapter 2.4.2. Furthermore, it is assumed that the influence on the dislocations depends on the hydrogen occupancy at dislocations. According to Oriani, this occupancy is in equilibrium with the occupancy of interstitial sites if hydrogen kinetics are fast [198]. The average hydrogen occupancy of dislocations in front of a crack tip will be derived in the following.

For a simple analytical estimate of the hydrogen concentration, the solution according to Crank of the partial differential equation that describes how the concentration changes over time due to diffusion, also known as Fick's second law, is used, see Equation (2.55). This is now used to determine the time and location dependent concentration ahead of a crack

$$C(x,t) = C_{L,max} + \left(C_{initial} - C_{L,max}\right)\left(\mathrm{erf}\left(\frac{x}{2\sqrt{Dt}}\right)\right) \,. \tag{7.2}$$

Here $C_{L,max}$ is the maximum lattice hydrogen concentration, $C_{initial}$ the initial hydrogen concentration and D is the diffusion rate. For the diffusion time t, it is assumed that hydrogen can only diffuse into the material when the crack is under tensile load, corresponding to the duration of

half a loading cycle $t = 0.5 * t_{cycl} = 1/(2f)$. It is also assumed that when the crack has propagated, the hydrogen concentration at the beginning of the next cycle again corresponds to $C_{initial}$. The maximum hydrogen concentration $C_{l,max}$ at certain temperature and hydrogen pressure in the metal lattice is obtained by substituting the solubility S (Equation (2.52)) and the fugacity for pressure (Equation (2.45)) into Sieverts' Law (Equation (2.48)). Additionally, considering the hydrostatic stress field ahead of a crack tip, Equation (2.53) provides the expression for the maximum hydrogen concentration

$$C_{l,max} = S\sqrt{F}\ \exp\left(\frac{V_H \sigma_h}{RT}\right) = S_0 \exp\left(\frac{-H_S}{RT}\right)\sqrt{p \exp\left(\frac{pb_g}{RT}\right)}\ \exp\left(\frac{\bar{V}_H \sigma_h}{RT}\right). \tag{7.3}$$

The hydrostatic stress in the process zone ahead of a crack is assumed to be in the order of three times the yield stress of the material ($\sigma_h = 3\sigma_{YS}$) which is in the range of the calculations of McMeeking for a blunting crack tip [306].

According to Oriani's theory, the hydrogen occupancy of traps and interstitial sites is in equilibrium when the kinetic of trap filling is fast, see Chapter 2.3.3. By substituting Equation (2.60) into Equation (2.59) and rearranging it for θ_d, the hydrogen occupancy at dislocations is obtained

$$\theta_d = \frac{\theta_l \exp\left(-\frac{E_{d,b}}{RT}\right)}{1 - \theta_l + \theta_l \exp\left(-\frac{E_{d,b}}{RT}\right)}, \tag{7.4}$$

where $\theta_d \in [0,1]$ and $E_{t,b}$ is the trap binding energy of dislocations, which is inherently negative. The connection between the volumetric concentration of hydrogen in the lattice and the lattice site occupancy θ_l is given by [198]

$$C_l = \theta_l \gamma N_l, \tag{7.5}$$

where γ is the number of normal interstitial lattice sites (NILS) per solvent atom and N_L is the number of solvent atoms per unit lattice volume. FCC metals like nickel have one octahedral interstitial site per metal atom and two tetrahedral interstitial sites per metal atom [321]. Since the octahedral interstitial sites in the FCC lattice offer more space than the tetrahedral interstitial site, hydrogen is predominantly located at octahedral interstitial sites, resulting in $\gamma = 1$ [322].

The hydrogen distribution $C(x,t)$ according to Equation (7.2) as well as the trap occupancy $\theta_d(x,t)$ according to Equation (7.4) are illustrated in Figure 7.1 for a temperature of 20 °C with $D = 1.19x10^{-15}\ m^2/s$, $t = 10\ s$ and $C_{L,max} = 0.00195\ atom\ H/atom\ Alloy718$.

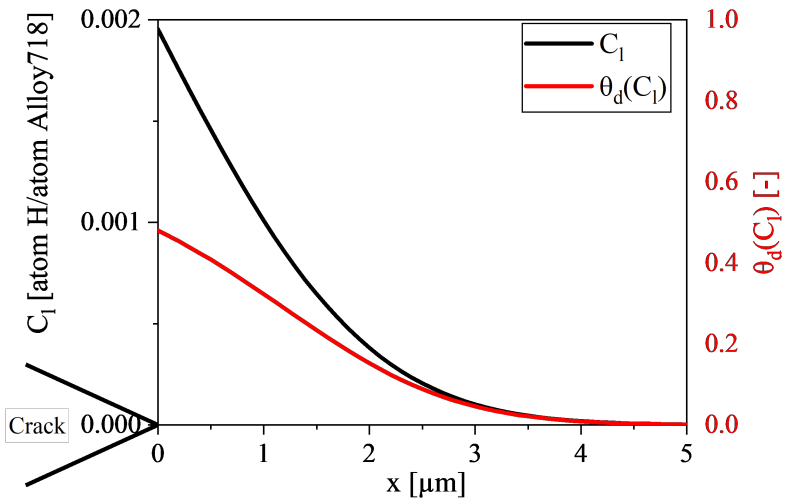


Figure 7.1: Illustration of the hydrogen concentration C_L and the dislocation occupation $\theta_D(C_L)$ ahead of a crack tip for any cycle at any time.

As hydrogen diffuses into the material during a loading cycle, a time-dependent hydrogen distribution occurs in front of the crack tip. It is assumed here that the average hydrogen occupation at dislocations $\bar{\theta}_d$ over the length of crack propagation Δa affects the crack growth. Therefore, as Δa depends on $\bar{\theta}_d$ and vice versa, this step must be solved iteratively. As a starting value, the crack growth increment of a specific cycle in air $\Delta a_{Air} = \beta(\Delta CTOD)^B$ is used to calculate $\bar{\theta}_d$

$$\bar{\theta}_d = \frac{1}{\Delta a}\int_0^{\Delta a} \theta_d(x,t)\, dx \ . \tag{7.6}$$

Although the global material properties are not affected by hydrogen, as shown by the identical hysteresis loops in air and hydrogen in Figure 6.25, the HELP mechanism suggests an enhanced localized plasticity at the crack tip in the presence of hydrogen. This effect is taken into account for crack growth by increasing the plastic portion of the cyclic J-integral, which is estimated by the damage parameter Z_D according to Heitmann for a semicircular surface crack, see Equation (2.22). The parameter Z_D consists of an elastic and plastic part. The plastic contribution of Z_D is increased as a function of the dislocation occupancy $\bar{\theta}_d$, resulting in the hydrogen-modified damage parameter

$$Z_{D,H} = \left(1{,}45\frac{\Delta\sigma_{eff}^2}{E} + (1+\alpha\bar{\theta}_d)\, 2{,}4\frac{\Delta\sigma\Delta\varepsilon_{pl}}{\sqrt{(1+3n')}}\right), \tag{7.7}$$

where α is a material dependent constant that is determined in Chapter 7.4 for the investigated Alloy 718 wrought. For $\bar{\theta}_d = 0$, which corresponds to no hydrogen at dislocations, the original damage parameter Z_D is obtained.

The dependency of plasticity is not fully covered by $Z_{D,H}$ as observed in Figure 7.12. Therefore, in the improved damage parameter $Z_{D,H}^*$ the occupancy is multiplied by ΔJ_{pl}, accounting for increasing hydrogen enhanced dislocation mobility with increasing crack tip plasticity.

$$Z_{D,H}^{*} = \left(1{,}45\frac{\Delta\sigma_{eff}^{2}}{E} + \left(1 + \alpha^{*}\bar{\theta}_{d}\Delta J_{pl}\right) 2{,}4\frac{\Delta\sigma\Delta\varepsilon_{pl}}{\sqrt{(1+3n')}}\right). \tag{7.8}$$

Substituting equation (7.7) or (7.8) into crack growth equation (7.1) yields

$$\frac{da}{dN} = \beta(\Delta CTOD)^{B} = \beta\left(d_{n'}\frac{\Delta J}{\sigma_{cy}}\right)^{B} = \beta\left(d_{n'}\frac{Z_{D,H}^{(*)}}{\sigma_{cy}}a\right)^{B}. \tag{7.9}$$

The process for calculating the fatigue life is illustrated in Figure 7.2. In the first cycle, $N_0 = 0$ and an initial crack length of $a_0 = 17.5\ \mu m$ are assumed based on investigations by Schlesinger [124]. In each cycle, the crack of length a grows by the crack growth increment Δa. Without hydrogen influence, this corresponds to Equation (7.1) with $\Delta a_{i=0} = \Delta a_{Air} = \beta(\Delta CTOD)^{B}$. Under hydrogen influence, the crack growth increment Δa_{H2} needs to be calculated iteratively, as hydrogen affects the crack growth and the crack length affects the effective hydrogen concentration. Based on Δa_i, the average dislocation occupancy $\bar{\theta}_d$ is calculated, and from that the new crack propagation Δa_{i+1} of iteration step i. This value is then again used for the next iteration to calculate $\bar{\theta}_d$. This process continues until the relative deviation from the last calculated crack growth increment $X_{Dev} < 0.001\ \%$ is reached. This is then the crack growth Δa_H for this cycle, and the new crack length is $a = a + \Delta a_H$. This process is repeated until the critical crack length $a_f = 1\ mm$ is reached. The number of cycles needed to reach a_f is the fatigue life until failure N_f. This process is carried out using a Python script. The computational effort is low. Thus, fatigue lives for 100 different conditions can be calculated in just a few minutes.

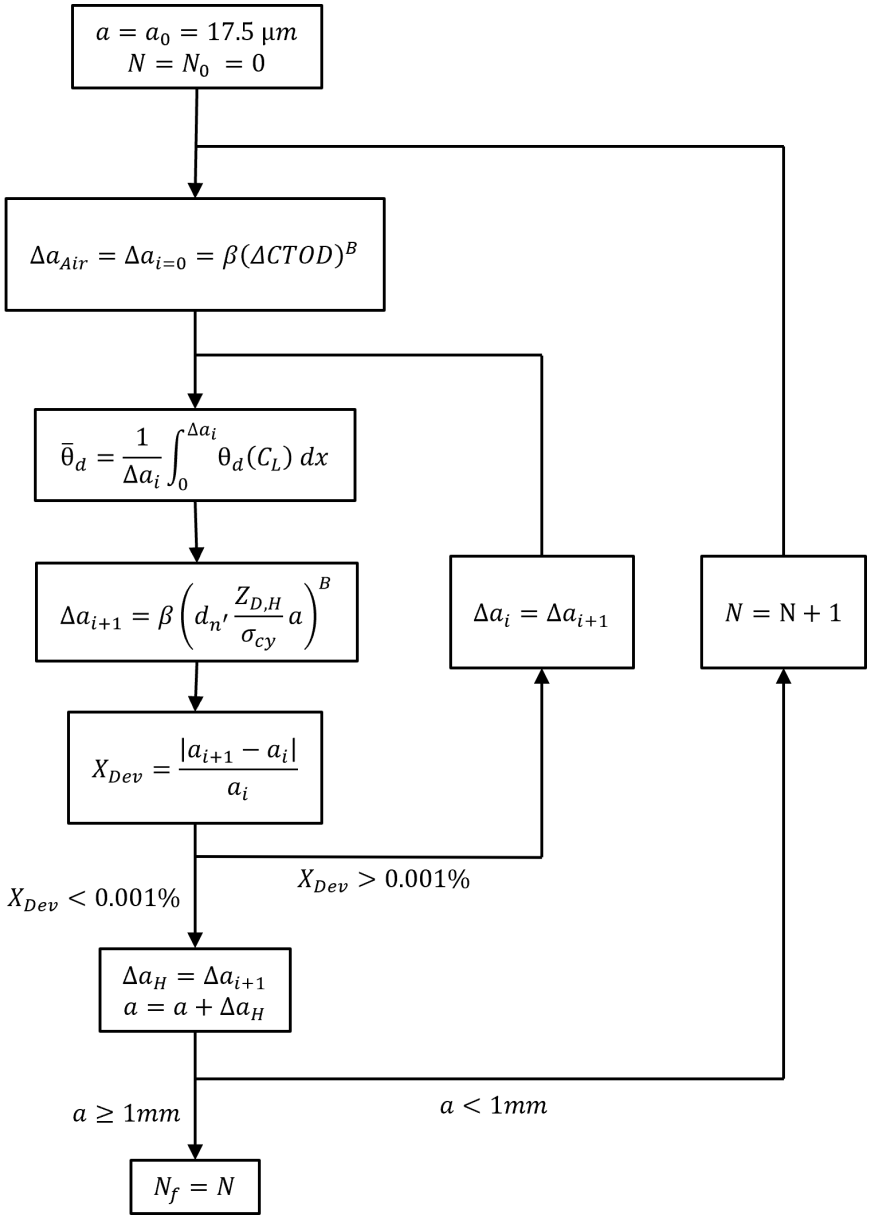


Figure 7.2: Iterative process to calculate the crack growth increment Δa_H affected by hydrogen and the cycles to failure N_f for a crack of length $a_0 = 17.5\ \mu m$ to reach the critical length $a_f = 1\ mm$.

7.2 Investigation of the model behavior

As described in Chapter 2.3.2 and 2.3.3, the dislocation occupancy θ_d and the diffusion coefficient D are strongly dependent on the temperature as calculated with Equation (2.51) and Equation (7.4). In Figure 7.3 it is illustrated how these parameters change over a temperature range for a hydrogen pressure of 100 bar. In Chapter 2.4.3 it was discussed how this affects hydrogen embrittlement. At low temperature of $< -100\ °C$, the trap sites at dislocations are almost completely occupied. But, the diffusion coefficient at this temperature is very small and hydrogen

diffusion from the surface to the critical areas is slow. At high temperatures, the diffusion rate is high, and hydrogen can quickly diffuse to the critical points. However, according to Oriani's equilibrium equation, at high temperature most of the hydrogen distributes in the metal lattice and does not segregate at dislocations.

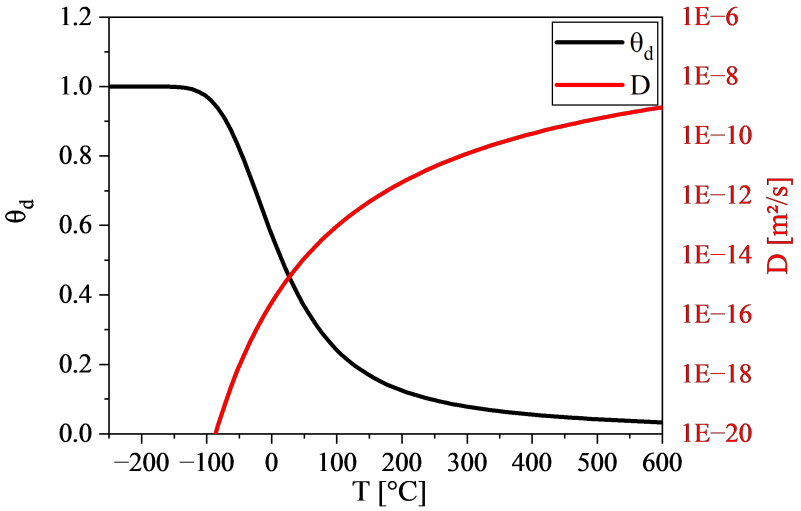


Figure 7.3: Dependence of dislocation occupancy and diffusion coefficient on temperature. (Calculated for $p = 100\ bar\ H_2$ and the material properties of Table 7.2).

Figure 7.4 shows the iterative calculated crack growth Δa, as illustrated in Figure 7.2, for calculating the crack growth increment for cycle 200 of a simulated experiment. Since $\bar{\theta}_d$ is calculated in the first iteration step based on the crack growth in air Δa_{Air}, hydrogen damage is overestimated in the first step. Since this value is then used for the next calculation, $\bar{\theta}_d$ is calculated too low, and the hydrogen damage is underestimated. Through this process, the crack growth settles on a realistic value of Δa_H that takes into account both the rapid growth through the area with high hydrogen concentration at the beginning and the crack growth at the end of the cycle through the material with low hydrogen concentration.

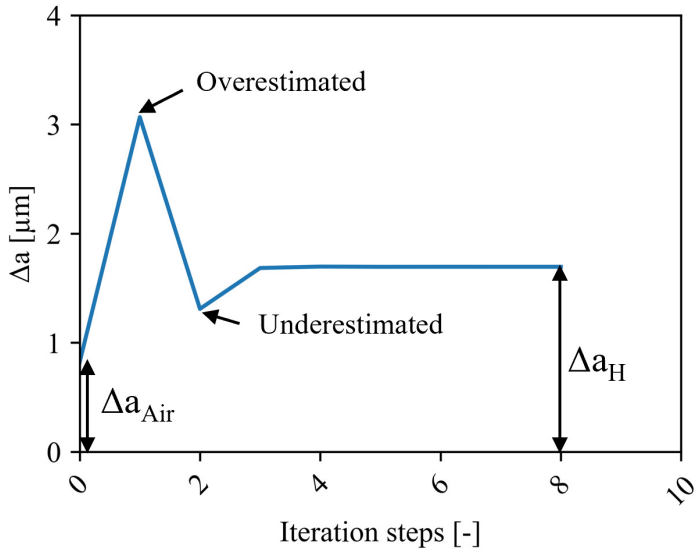


Figure 7.4: Determination of the crack propagation affected by hydrogen. Starting with the initial value Δa_{Air}, the crack propagation is determined taking the average trap occupancy in front of the crack tip into account in an iterative process until a relative deviation from the last iteration step smaller than 0.001 % is reached (final value Δa_H). Illustration for cycle 200 of a modeled crack at $T = 20\ °C$, $p = 100\ bar\ H_2$, $f = 0.1\ Hz$ and $\Delta\varepsilon_t = 2\ \%$.

Figure 7.5 shows the calculated average trap occupancy $\bar{\theta}_d$ for each cycle of simulated experiments at different temperatures. $\bar{\theta}_d$ is always highest in the first cycle of an experiment, when the crack propagation is small and diffusion paths short. As crack propagation increases with more cycles, the diffusion process is too slow to saturate the material in front of the crack and $\bar{\theta}_d$ decreases. This is more pronounced at low temperature as at high temperature, hydrogen can penetrate deeply into the material within the cycle time.

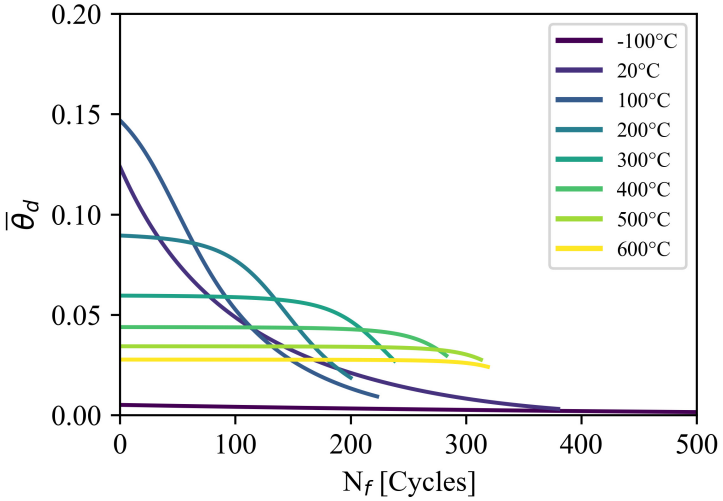


Figure 7.5: Illustration of the average trap occupancy $\bar{\theta}_d$ for each cycle of simulated experiments at different temperatures ($T = -100\ to\ 600\ °C$, $p = 100\ bar\ H_2$, $f = 0.1\ Hz$ and $\Delta\varepsilon_t = 2\ \%$).

7.3 Determination of the temperature-dependent material properties

The temperature-dependent material parameters elastic modulus E, cyclic hardening exponent n' and cyclic yield stress σ_{cy} were determined from low cycle fatigue experiments, presented in Chapter 6.3. The values of each experiment used for adaptation of the model are given in Table 7.1. The hysteresis of the cycle at half cycles to failure ($N_f/2$) was evaluated as shown in Figure 7.6.

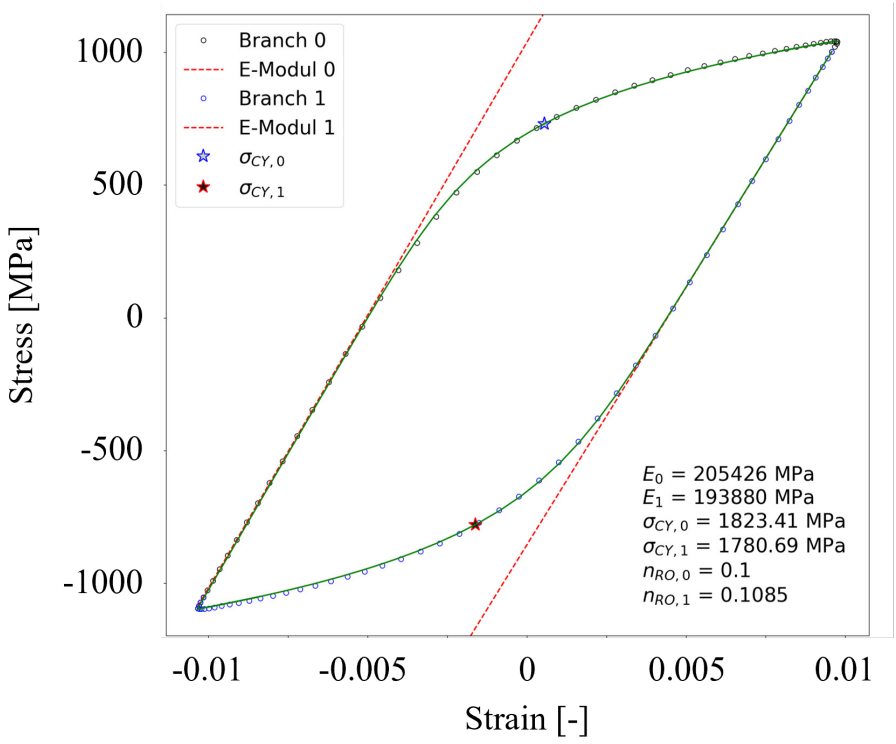


Figure 7.6: Example for the evaluation of the material parameters elastic modulus E, cyclic hardening exponent n' and cyclic yield stress σ_{cy} from the cycle at half cycles to failure ($N_f/2$).

Only the experiments with sufficiently open hystereses were taken into account. As no significant difference of the stress-strain behavior was found between tests in air and hydrogen internal pressure, see hystereses in Chapter 6.3.3, tests under all media were evaluated to obtain the best statistical analysis, see Figure 7.7. The values for E and n were fitted with a straight line and σ_{cy} with a third-degree polynomial. The standard error of the mean of E is $SEM_E = \pm 1.5\ GPa$, of σ_{cy} it is $SEM_{\sigma_{cy}} = \pm 12.2\ MPa$ and of n it is $SEM_n = \pm 0.0008$.

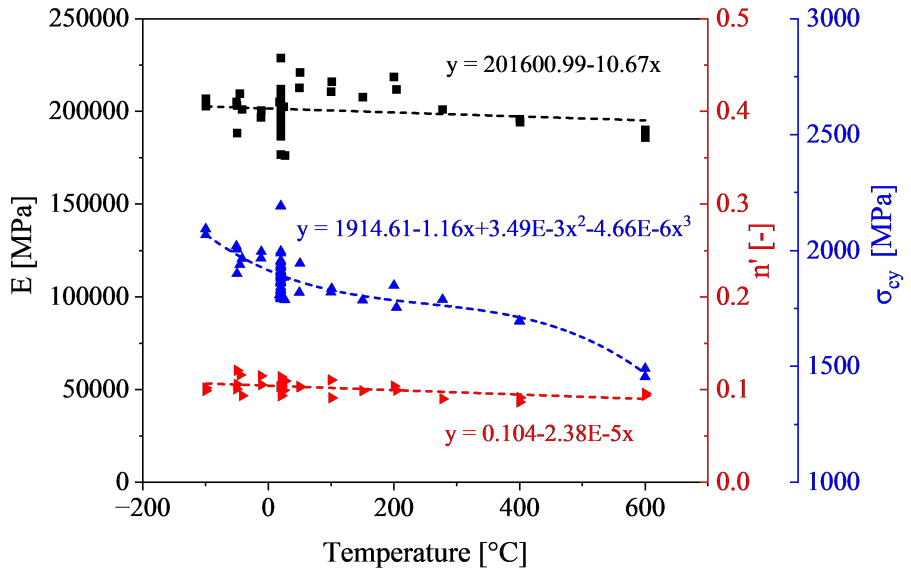


Figure 7.7: Determination of the temperature-dependent elastic modulus E, the cyclic hardening exponent n' and the cyclic yield stress σ_{cy} based on low cycle fatigue experiments. The material properties were evaluated at half cycles to failure, see Table 7.1.

Table 7.1: Material parameters evaluated at half cycles to failure ($N_f/2$) from low cycle fatigue tests (Experiments with almost closed hysteresis were not evaluated).

T [°C]	p [bar]	E [MPa]	σ_{cy} [MPa]	n'	N_f [Cycles]	$N_f/2$ [Cycles]
-99.9	81.4	206889	2093.4	0.099	1318	659
-99.6	0.0	202887	2067.1	0.102	2375	1187
-50.6	101.4	205123	2018.0	0.101	569	284
-50.0	105.8	203286	2004.9	0.105	1232	616
-50.0	111.0	188328	1900.6	0.121	414	207
-45.1	0.0	209671	1938.5	0.116	1585	784
-41.8	0.0	201131	1965.0	0.093	535	267
-11.6	103.1	196680	1966.6	0.115	403	201
-11.2	107.3	200595	1995.8	0.105	501	242
RT	52.1	205207	1807.7	0.103	1937	968
RT	50.5	205302	1879.0	0.093	351	175
RT	46.2	205996	1914.2	0.093	235	117
RT	56.0	199245	1895.7	0.094	267	133
RT	253.9	201245	1949.2	0.098	224	109
RT	98.2	176738	1796.3	0.098	794	394
RT	101.9	212011	1937.9	0.100	200	100
RT	52.4	201032	1832.3	0.100	1210	605
RT	100.4	202578	1926.9	0.101	316	157
RT	150.6	200068	1815.0	0.101	1508	754
RT	261.7	201313	1814.1	0.101	1194	597

RT	100.7	209312	1934.0	0.102	158	78
RT	197.1	205257	1956.5	0.103	224	111
RT	50.1	228853	2192.5	0.103	210	105
RT	49.7	188837	1862.5	0.104	200	99
RT	10.5	201696	1790.8	0.104	1696	848
RT	104.1	205999	1988.6	0.105	1259	629
RT	0.0	201689	1808.3	0.105	1122	550
RT	150.0	200399	1858.4	0.105	891	443
RT	151.2	200815	1818.6	0.105	916	458
RT	49.9	193981	1827.1	0.105	1224	612
RT	0.0	196292	1842.8	0.106	355	178
RT	0.0	186642	1819.0	0.106	520	260
RT	49.5	188318	1812.2	0.107	358	179
RT	101.4	209944	1995.9	0.107	67	33
RT	151.0	201169	1904.5	0.108	426	213
RT	196.3	204619	1801.1	0.108	1506	753
RT	9.8	200685	1868.1	0.108	761	380
RT	49.1	192234	1889.1	0.109	91	45
RT	50.3	191032	1888.3	0.109	86	43
RT	50.5	195248	1927.2	0.110	337	168
RT	103.0	190224	1912.6	0.113	398	199
RT	10.0	189954	2191.4	0.114	1778	6
RT	49.6	202633	1883.3	0.099	25	25
RT	51.1	176179	1787.2	0.109	419	209
49.7	100.0	212764	1819.3	0.104	970	485
50.2	0.0	221131	1944.6	0.103	562	138
99.9	100.0	210734	1820.6	0.110	708	318
100.8	0.0	216131	1835.8	0.091	631	197
150.3	100.0	207831	1785.6	0.099	447	201
200.0	0.0	218698	1849.2	0.104	501	91
204.2	0.0	211972	1754.4	0.099	923	461
277.7	100.0	201129	1788.8	0.090	158	25
399.9	0.0	195773	1696.7	0.086	631	314
400.5	100.0	194115	1693.7	0.091	503	251
600.0	0.0	185906	1455.3	0.096	224	108
600.3	100.0	190036	1490.0	0.094	325	162

7.4 Adaptation and validation of the model

The crack growth model was adapted based on the reference tests in air and with internal nitrogen pressure in the temperature range from -100 °C to 400 °C. It was shown in Chapter 6.3.4 that inner nitrogen pressure has no effect on the cycles to failure. Further, the experiment at 600 °C was not included here, as it can be assumed that oxygen affects fatigue life above 500 °C, see

Chapter 2.1.3. This effect is not considered by the basic model. The model by Schlesinger et al., as described in Chapter 2.2.5, is used in the following, to take oxygen effects into account [137].

Figure 7.8 shows the evaluation of $Y = d_{n'} Z_D / \sigma_{cy}$ for the reference tests. The procedure is described in Chapter 2.2.4. The experimental values in Figure 7.8 include data for temperatures ranging from -100 °C to 400 °C. With an power law fit of the form $N_{f,sim} = b\left(d_{n'} Z_D / \sigma_{cy}\right)^{-B}$, the cycles to failure are obtained as a function of $d_{n'} Z_D / \sigma_{cy}$, where slope and exponent are fitted as $b = 1.913$ and $B = 1.452$ with a correlation coefficient $R = -0.97$. As derived in Chapter 2.2.4, with Equation (2.30) $\beta = 137.52\ m^{1-B}$ is obtained, by implementing $b = 1.913$, an initial crack length $a_0 = 0.0000175\ m$ and a final crack length $a_f = 0.001\ m$. This results in a crack propagation per load cycle of $da/dN = 137.52(\Delta CTOD)^{1.452}\ m$ for the crack growth model in air, for temperatures of up to 400 °C.

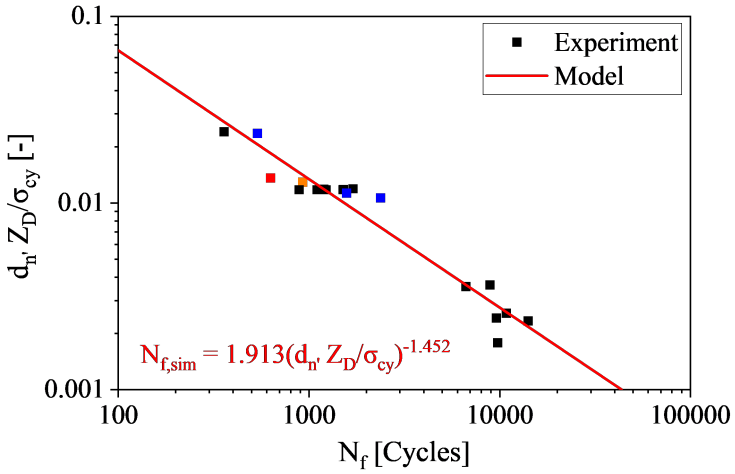


Figure 7.8: Fitting of $N_{f,sim} = b\left(d_{n'} Z_D / \sigma_{cy}\right)^{B}$ considering only reference tests in air and with nitrogen inner pressure up to 400 °C. (Blue < 20 °C, black = 20 °C, orange = 200 °C, red = 400 °C).

To adjust the model for the influence of hydrogen, the proportionality constant α of the Z_{HD} hydrogen damage parameter, see Equation (7.7), is determined based on the experimental data. α indicates how much hydrogen and global plastic strain enhances the localized plasticity at the crack tip by increasing the plastic part of Z_D and therefore increasing the plastic part of the cyclic J-Integral ΔJ_{pl}. When the dislocations are fully occupied by hydrogen ($\bar{\theta}_d = 1$), α corresponds to the maximum enhancement of plasticity at a certain strain range. All other parameters included in the model are material and load-specific values that were either determined in this work or taken from the literature. For air atmosphere, the model considers additional crack growth caused by oxygen diffusion at high temperature ($> 400\ °C$) based on the model of Schlesinger presented in Chapter 2.2.5. All model parameters and references are summarized in Table 7.2.

For comparison between experimental results and model predictions with the hydrogen damage parameter $Z_{D,H}$, see Equation (7.7), the model curves (lines) and the experimental data (circles and crosses) from Chapter 6.3.5 are shown in Figure 7.9, for the temperature range of -100 °C to

600 °C and frequencies ranging from 0.001 Hz to 1 Hz. The experiments conducted in air, represented in black, are very well captured by the model. By taking into account oxygen degradation, the temperature range of ≥ 400 °C is also represented, showing a significant decrease in fatigue life at elevated temperature. To determine the fatigue life under hydrogen influence, $Z_{D,H}$ was used as described in Chapter 7.1. The material-dependent parameter α was chosen as $\alpha = 3600$ for all model curves to get the best fit. This allows for a very accurate description of the hydrogen influence across the entire temperature range, considering the mechanisms of hydrogen diffusion and hydrogen occupation at dislocations. At low temperatures, no hydrogen degradation is observed due to the low diffusion rate, while at high temperatures, hydrogen degradation decreases because hydrogen is not at dislocations but in the metal lattice. The highest hydrogen degradation is also predicted by the model in the temperature range of 20-200 °C, depending on the testing frequency. At high temperatures, the fatigue life predictions for air and hydrogen intersect, as significant oxygen degradation occurs at this temperature while hydrogen degradation diminishes. Since the hollow specimens are also exposed to oxygen from the outside, it should be noted that within these tests, cracks initiate from the outside, as described in Chapter 6.3.5, and thus correspond to oxygen damage rather than hydrogen damage. Additionally, the model effectively accounts for the time-dependent effect of hydrogen diffusion. As can be seen from the appropriate match between experimental data and model curves, the fatigue life for different test frequencies can be predicted very accurately by the model. Overall, the experimental results almost all fall within the narrow scatter bands with a factor of 1.3.

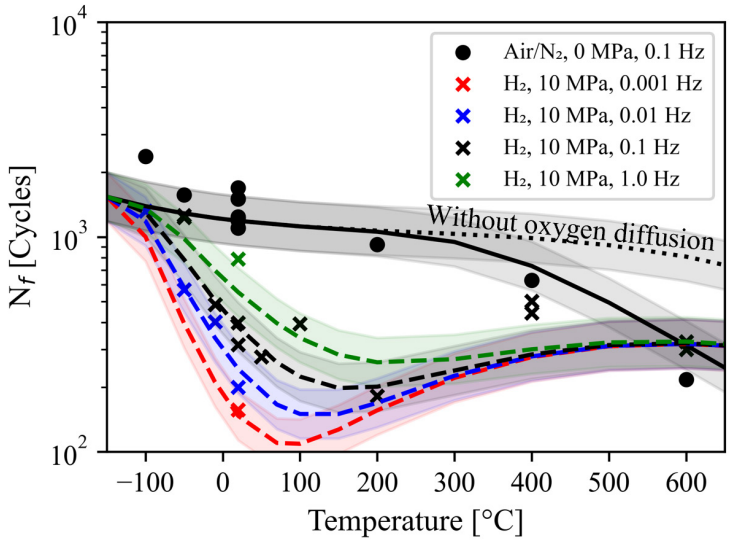


Figure 7.9: Comparison of experimental results (points for air and crosses for hydrogen) and prediction by the $Z_{D,H}$ model (solid line for air and dashed lines for hydrogen) for the temperature range from -100 °C to 600 °C and frequency range from 0.001 Hz to 1 Hz ($R = -1$, $\Delta\varepsilon_t = 2$ %). The model without oxygen diffusion at elevated temperature is represented with a dotted line. The model can very well represent the mechanisms that influence the hydrogen effect on fatigue life across the entire temperature and frequency range. Almost all experimental data points fall within the shaded scatter bands of factor 1.3.

The model can also represent the influence of hydrogen pressure on the number of cycles to failure, as shown in Figure 7.10. While nitrogen pressure has no effect, hydrogen pressure shows a strong influence. At small hydrogen pressures the cycles to failure decrease significantly, while at higher pressures slowly a maximum hydrogen damage approaches.

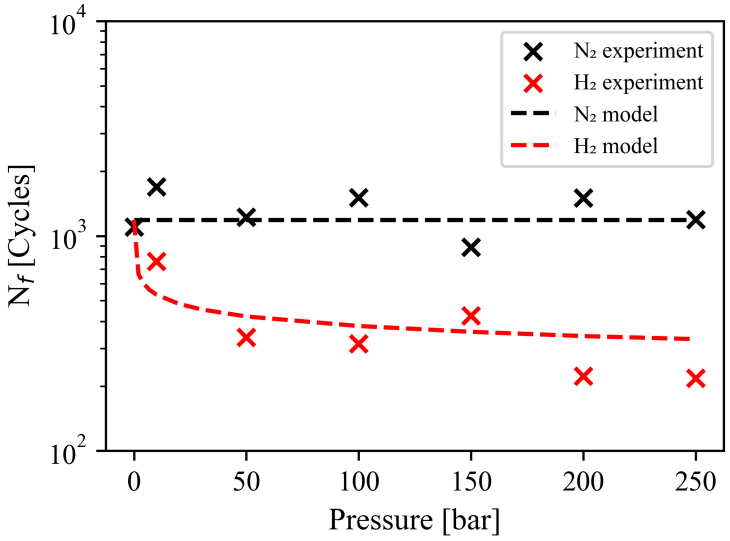


Figure 7.10: Comparison of experimental results and prediction by the $Z_{D,H}$ model (dashed lines) for different pressures of hydrogen and nitrogen. ($T = 20\,°C$, $f = 0.1\,Hz$, $R = -1$, $\Delta\varepsilon_t = 2\,\%$). With increasing hydrogen pressure, the cycles to failure N_f decrease as shown by experiments and model.

In Figure 7.11, the dependence of the frequency was modeled and compared with experimental results. In the range from 0.001 Hz to 1 Hz, the model agrees well with the experiments. For higher frequencies, the model approaches the mean value of the reference tests in air and with nitrogen internal pressure (dotted line). For lower frequencies, N_f continues to decrease until a plateau slowly starts to form at a frequency of $10^{-6}\,Hz$. From the experiments it looks like the plateau might form earlier. However, experiments with lower frequency than $f = 0.001\,Hz$ take too much time and the data availability is too low to define the start of a plateau, where hydrogen saturation in front of the crack tip is reached in the distance of crack growth per cycle.

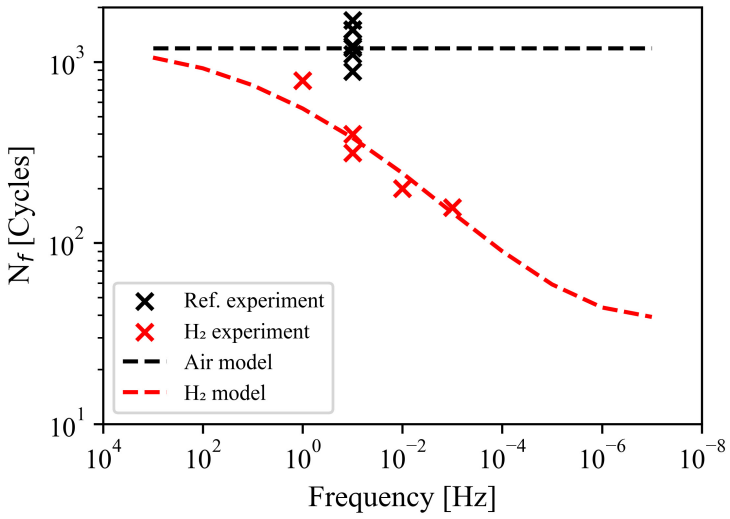


Figure 7.11: Comparison of experimental results and prediction by the $Z_{D,H}$ model for different frequencies at 100 bar hydrogen pressure ($T = 20\ °C$, $p = 100\ bar$, $R = -1$, $\Delta\varepsilon_t = 2\ \%$). At high frequencies $> 100\ Hz$, the model predicts little hydrogen degradation. In the tested range from 0.001 Hz to 1 Hz cycles to failure N_f from experiments and predicted by the model are in good agreement. At very low frequency of $f < 0.0000001\ Hz$ the model predicts that a maximum hydrogen degradation is approaching.

Figure 7.12 presents experimental results of HS and CS tested in air, 50 bar and 100 bar hydrogen atmosphere and predictions with the hydrogen damage parameter $Z_{D,H}$ for variations of total strain ranges $\Delta\varepsilon_t$ and frequencies f. As the influence of hydrogen pressure is small between 50 bar and 100 bar, see Chapter 6.3.4, for clarity only the model predictions for 100 bar are shown in Figure 7.12. The model curves for air and hydrogen atmospheres converge at a low strain range of $\Delta\varepsilon_t = 0.006$ and a number of cycles $N_f \approx 10^5\ Cycles$. With increasing $\Delta\varepsilon_t$, hydrogen damage increases significantly and a strong frequency influence on hydrogen damage is observed. The increasing frequency influence can be attributed to the higher crack growth per cycle and the slow penetration of hydrogen. Therefore, in order to saturate the region ahead of the crack tip in the length of the crack propagation with hydrogen, a low test frequency is required. However, the model with $Z_{D,H}$ does not perfectly describe the strain range dependency. At $\Delta\varepsilon_t = 0.011$ the fatigue life N_f is predicted lower and at $\Delta\varepsilon_t = 0.03$ it is predicted slightly higher than experimental results.

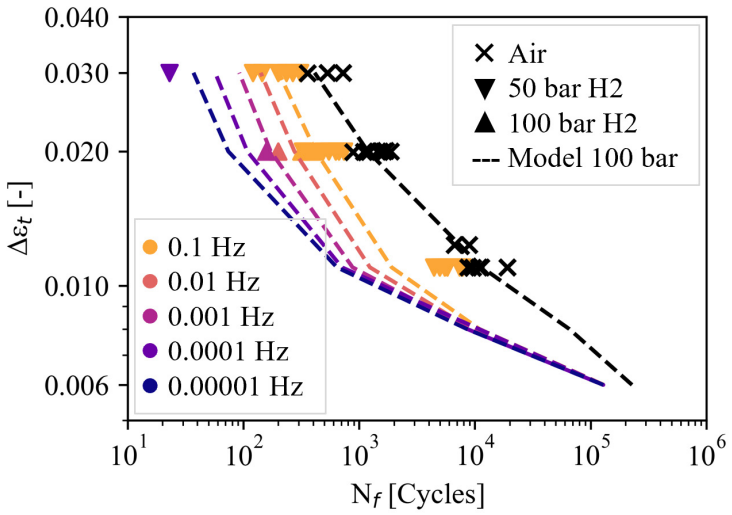


Figure 7.12: Presentation of experimental results of HS and CS tested in air, 50 bar and 100 bar hydrogen pressure (crosses and triangles) and prediction with the hydrogen damage parameter $Z_{D,H}$ and $\alpha = 35$ for air and 100 bar hydrogen pressure (dashed lines) for different strain ranges $\Delta\varepsilon_t$ and frequencies f ($T = 20\,°C$, $R = -1$). No hydrogen degradation of fatigue life N_f below $\Delta\varepsilon_t = 0.008$. Hydrogen degradation increases with increasing strain range $\Delta\varepsilon_t$ and decreasing frequency.

To cover this stronger dependency on plasticity, $Z_{D,H}$ is modified by multiplying the hydrogen occupancy at dislocations with ΔJ_{pl}, accounting for increasing hydrogen enhanced dislocation mobility with increasing crack tip plasticity, resulting in $Z^*_{D,H}$, see Equation (7.8). The prediction of this modified hydrogen damage parameter is shown in Figure 7.13. Now both, the dependency on strain range and frequency are nicely covered by the model compared to the experimental results. The previously examined dependencies of temperature (Figure 7.9), pressure (Figure 7.10), and (frequency) Figure 7.11 at $\Delta\varepsilon_t = 0.02$ are hardly affected by the adaptation of $Z^*_{D,H}$ and are still well described by the model. Due to the high test duration at low frequencies, only few experiments could be performed here, and only the prediction for f = 0.1 Hz could be statistically validated. More data at low test frequencies could help to validate the model even better in the future.

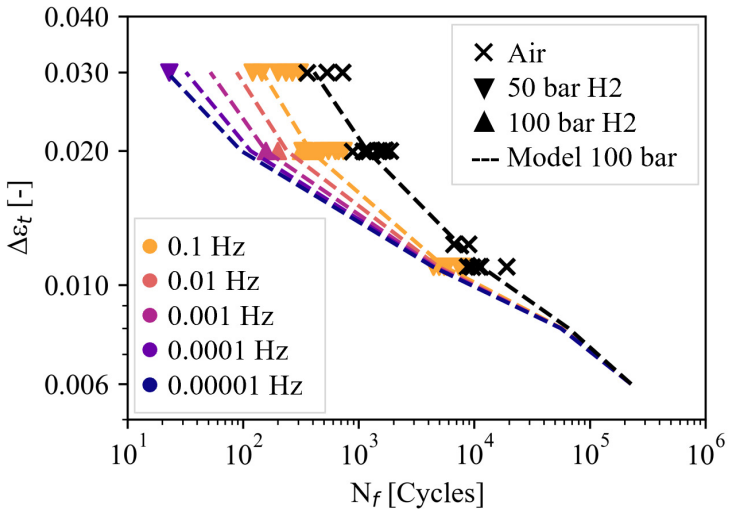


Figure 7.13: Presentation of experimental results of HS and CS tested in air, 50 bar and 100 bar hydrogen pressure (crosses and triangles) and prediction with the hydrogen damage parameter $Z^*_{D,H}$ and $\alpha^* = 12000\ m^2/J$ for air and 100 bar hydrogen pressure (dashed lines) for different strain ranges $\Delta\varepsilon_t$ and frequencies f ($T = 20\ °C$, $R = -1$). No hydrogen degradation of fatigue life N_f below $\Delta\varepsilon_t = 0.008$. Hydrogen degradation increases with increasing strain range $\Delta\varepsilon_t$ and decreasing frequency.

Even though the crack growth model with the hydrogen damage parameter $Z_{D,H}$ primarily bases on measurable material and loading parameters, as presented in Tab. 7.2, it predicts the measured lifetimes of experiments in air and in hydrogen atmosphere in a convincing manner over a wide range of service conditions. Only the proportionality factors β and B need to be adjusted on experiments in air, as is usually the case for any crack growth law, and the factor α needs to be adjusted to hydrogen experiments. The influence of hydrogen under different operating conditions is then represented in the model by physical relationships. Theoretically, α can be calibrated in a single room temperature experiment and still provide good predictions for other temperatures and hydrogen pressures. However, calibrating it to multiple experiments for validation is favorable.

Table 7.2: Parameters of the crack growth model.

Crack growth model parameters			*Reference*
β	m^{1-B}	137.52	*Fit to reference experiments in air in the temperature range -100 to 400 °C and strain range 1.1 to 3 %*
B	–	1.45	*Fit to reference experiments in air in the temperature range -100 to 400 °C and strain range 1.1 to 3 %*
a_0	m	0.0000175	[124]
a_f	m	0.001	*Load drop of ~5% (Chapter 6.4.3)*

Hydrogen specific parameters			*Reference*
R	$J/Kmol$	8.314	[323]
V_H	cm^3/mol	1.65	[195]
b	cm^3/mol	15.84	[165]
S_0	$mol\ H2 /(m^3\sqrt{Mpa})$	186	[231]
H_S	J/mol	8140	[231]
D_0	m^2/s	$9.01x10^{-07}$	[231]
H_D	J/mol	49834	[231]
$E_{t,b}$	J/mol	15000	[292]
α	$-$	35	*Fit to hydrogen experiments in the pressure range 10 to 250 bar, temperature range -100 to 600 °C, frequency range 0.001 Hz to 1 Hz and strain range 1.1 to 3 %*
α^*	m^2/J	12000	*Fit to hydrogen experiments in the pressure range 10 to 250 bar, temperature range -100 to 600 °C, frequency range 0.001 Hz to 1 Hz and strain range 1.1 to 3 %*
Molecular weights			*Reference*
H	g/mol	1.008	[324]
Ni	g/mol	58.693	[324]
Fe	g/mol	55.845	[324]
Cr	g/mol	51.996	[324]

7.5 Discussion of the crack growth model and the hydrogen damage parameter $Z_{D,H}$

A physically based crack growth law was used to calculate crack propagation in air atmosphere, which is based on the HRR stress fields [113,119] and the cyclic J-integral [129]. The cyclic J-integral was estimated according to Heitmann using the damage parameter Z_D for a semi-circular surface crack. From this, the crack tip opening displacement (CTOD) is calculated, which, according to the alternating slip approach, is in a proportional relationship with the crack propagation. The fatigue life is determined by the number of cycles required for crack growth from an initial length a_0 to a failure crack length a_f. This approach has proven to be particularly useful for LCF loads in order to describe crack growth under elastic-plastic material behavior. In the past, this approach has been expanded to describe, for example, viscous material behavior at high temperatures [325,326] and the environmental influence of oxidation [137].

In this work, the estimation of the cyclic J-integral according to Heitmann was adapted so that an increased local plasticity at the crack tip due to hydrogen is accounted for in line with the HELP theory. In Chapter 6.4.8, it was shown that this mechanism is primarily responsible for the damage caused by hydrogen in Alloy 718. In the developed hydrogen damage parameter $Z_{D,H}$, the plastic portion is increased based on the hydrogen occupancy of dislocations and the cyclic plastic strain range, accounting for time-dependent and temperature-dependent hydrogen effects such as diffusion and equilibrium states between lattice sites and hydrogen traps considered by the binding and activation energies. Based on these physical relationships, the hydrogen influence on crack growth under varying factors such as hydrogen pressure, temperature, loading frequency, and strain range can be estimated with the $Z_{D,H}$ parameter. It was shown in Figure 7.12 that the $Z_{D,H}$ parameter did not perfectly cover the effect of strain range for small strain ranges ($\Delta\varepsilon_t \approx 0.01$). This is attributed to a stronger dependence of hydrogen damage on the local plasticity at the crack tip. This is accounted for in the $Z^*_{D,H}$ parameter by multiplication with ΔJ_{pl}.

For the time- and temperature-dependent hydrogen concentration at the crack tip, Fick's law of diffusion is applied with a mathematical solution from Crank for diffusion in a semi-infinite medium [196]. This simplification allows for an analytical solution of the diffusion problem, eliminating the need for computationally intensive finite element models. The extent of the deviation caused by this simplification cannot be determined with certainty yet. The solution of the partial differential equation from Crank [196], that describes the change of concentration by diffusion, assumes an infinite surface from which hydrogen diffuses into the material in one dimension. However, at a crack tip, hydrogen not only diffuses forward but also into the crack flanks. This three-dimensional condition could affect the hydrogen concentration. A comparison between a 3-dimensional finite element model and the 1-dimensional solution can provide certainty here. Furthermore, hydrogen transport through dislocation movement, grain boundary diffusion, and changes in the diffusion coefficient due to microstructural changes at the crack tip are not considered yet and could be included in future work. Another simplification is the sequential consideration of diffusion and crack growth, as these two processes occur simultaneously in reality. However, an analytical solution that describes both time-dependent processes simultaneously is not possible and, sequential consideration is a typical approach to such a problem. The challenge of

location-dependent crack growth speed due to the varying hydrogen concentration ahead of the crack tip was solved by iterative calculation of the average dislocation occupancy over the crack growth increment, which increases the crack growth per cycle. At the beginning of each cycle the concentration ahead of the crack tip is set to $C_{initial}$, thereby neglecting the diffusion from the previous cycle. If the crack growth per cycle is greater than the penetration depth of hydrogen, this assumption is correct. However, in the case where the penetration depth is greater, the already penetrated hydrogen is not considered in the next cycle.

While the model is primarily based on measurable material and loading parameters and is adjusted only by proportionality factors, see Chapter 7.4, the binding energy of hydrogen to dislocations is the least well investigated parameter of the model. As discussed in Chapter 5.5.2, values measured in nickel range from $E_{b,d} = 7.7$ kJ/mol to 19.3 kJ/mol. The average value of 13.5 kJ/mol was used for the model validation in Chapter 7.4. The influence of the binding energy on the model was investigated through predictions with the lower and upper limits of $E_{b,d}$, see Figure 7.14. Since the binding energy describes the temperature-dependent equilibrium between lattice occupancy and dislocation occupancy, it was assumed that the temperature of maximum embrittlement is strongly influenced by changes in dislocation binding energy. However, using the minimum and maximum values for the binding energy of the mentioned range showed that, with adjustment of the proportionality factor α, the model was only slightly affected, and the temperature of maximum embrittlement shifted by only a few degrees Celsius. This shows that the model is robust, even if there are uncertainties in the exact determination of the binding energy, only the higher temperature range is stronger affected.

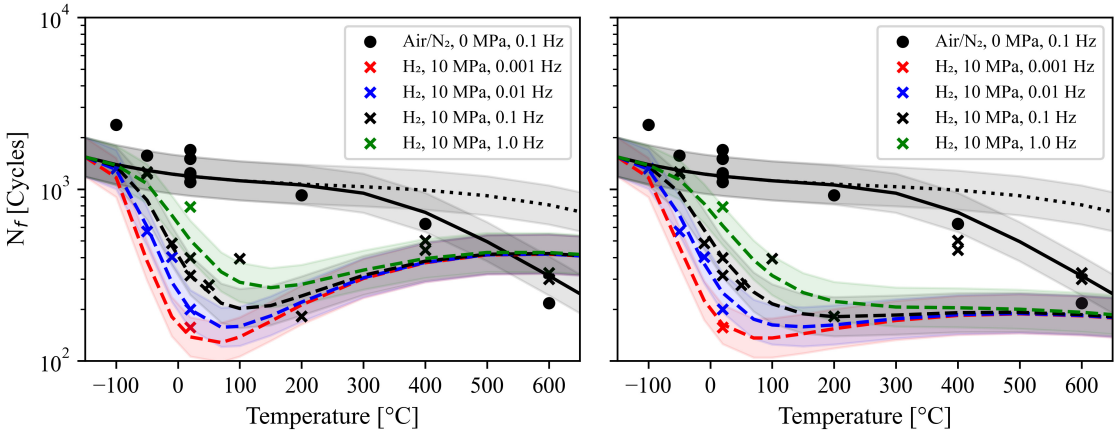


Figure 7.14: Comparison of fatigue life predictions with $Z^*_{D,H}$ for different parameters of binding energy at dislocations $E_{b,d}$ and parameter α^* (dashed lines) and experiments (circles and crosses). Predictions for the upper value of $E_{b,d} = 19.3\ kJ/mol$ and $\alpha^* = 3500\ m^2/J$ (left) and the lower value of $E_{b,d} = 7.7\ kJ/mol$ and $\alpha^* = 500$ (right) show similar curves.

8 Global Discussion

The nickel-based Alloy 718 is used in many fields from the oil and gas industry to nuclear reactors, gas turbines, and aircraft engines. In some of these applications the material is already in direct contact with hydrogen or will be used with hydrogen in the future as part of the energy transition. In this thesis, the influence of gaseous hydrogen on the mechanical properties of alloy 718 was investigated, new test methods were developed further, the effects of additive manufacturing were examined, and a model for predicting fatigue life under hydrogen influence was developed. The results are discussed in the following chapters.

Chapter 8.1 discusses investigations on hollow specimens regarding the manufacturing process, microstructural changes, geometric effects, damage behavior in static and dynamic tests, and the determined material properties, and compares them with conventional specimens. Chapter 8.2 covers the influence of temperature, hydrogen gas pressure, frequency, and load on the damage behavior. Chapter 8.3 addresses the differences between ex-situ tests with prior hydrogen charging and in-situ tests in a gaseous hydrogen atmosphere. The hydrogen diffusion, hydrogen saturation, and damage behavior are discussed, and the applicability of both test types for component design is considered. Chapter 8.4 addresses the influence of additive manufacturing and the specific microstructure and defects that arise on hydrogen-induced damage. Finally, the developed mechanism-based analytical model for lifetime prediction under hydrogen is discussed in Chapter 8.5, including simplifications, uncertainties and the applicability for the design and qualification of Alloy 718 components.

8.1 Hollow specimens and comparison to conventional specimens

Hollow specimens were extensively studied as a simple alternative testing method to conventional specimens testing in autoclaves to investigate hydrogen damage. HS can be tested on standard mechanical testing machines with little effort and cost as hydrogen is supplied by the inner hole. Because the system volume is small, at only about 0.0025 liters, no extensive safety precautions are required, and the specimen can be easily heated by induction and cooled by liquid nitrogen. HS for slow strain rate tensile tests were standardized in 2024 in the ISO/FDIS 7039 [293]. Results of this work regarding surface quality, comparability to conventional specimens, and experiment evaluation have been incorporated into the standardization process. The extension to include hydrogen-specific test parameters has started in the technical committee ISO/TC 164/SC. The standardization of this testing technique shows the current significant interest in it. However, testing of hollow specimens in fatigue experiments has not yet been standardized. The results of this work provide a foundation for that.

Drilling, reaming, honing, electrical discharge machining, electrochemical machining and abrasive flow machining of the inner hole of hollow specimen were investigated in Chapter 4.2 as the

surface roughness, microstructure and residual stress can have significant influence on experimental results. Drilling the hole with a single lip drill yields a roughness of $Ra = 0.23\ \mu m$, which is acceptable for SSRT testing and lies in the range of the specified roughness in ASTM G129 which is $RMS = 0.25\ \mu m$ (Ra ≈ RMS) [255]. The roughness recommended for fatigue tests ($Ra = 0.02\ \mu m$ [258,275]) and the roughness on the outer surface achieved by lapping ($Ra = 0.025\ \mu m$) are not achieved by drilling. Additionally, it was found that drilling causes significant changes to the near-surface microstructure. The material was deformed to a depth of approximately 30 µm during the drilling process, and at a depth of 13 µm, a microcrystalline structure was formed, see Figure 4.3. This substantial deformation indicates high residual stress and significant changes in the material, which can greatly influence crack initiation. Throughout this work, other manufacturing processes were examined. Electrical discharge machining followed by abrasive flow machining, as illustrated in Figure 8.1, was identified most promising. The EDM process with starting hole eroding and wire cutting creates a precise hole without mechanical impact on the material. The surface layer formed during the EDM process is removed by the AFM process with very small mechanical forces, similar to lapping used for CS. Through this manufacturing routine, the near-surface microstructure is preserved and a low roughness of Ra = 0.05 µm is achieved. This surface closely resembles the lapped outer surface, and thus, comparable crack initiation is expected.

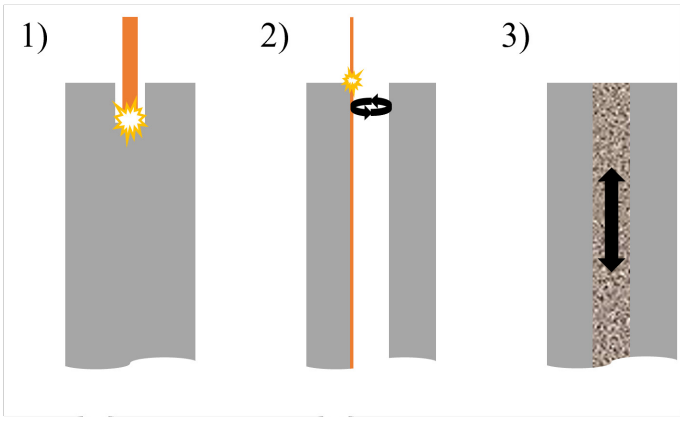


Figure 8.1: Developed manufacturing process for the hole of hollow specimens: 1) electrical discharge start hole eroding for a quick machining of a thin hole, 2) electrical discharge wire cutting for a straight and precise hole, 3) abrasive flow machining to remove the erosion layer in the hole and to reach a surface roughness of $Ra = 0.05\ \mu m$.

In addition to the microstructural influences from manufacturing, the specimen's geometry also affects the test results. While in SSRT tests the strength values in air for HS and CS are the same, the elongation to failure and reduction of area are somewhat lower, see Figure 6.4 in Chapter 6.1.2. This is attributed to the damage behavior observed at the end of the test. The CS exhibits the highest hydrostatic stresses in the center of the specimen, leading to void nucleation there, whereas for the hollow specimen, the highest stresses occur in the wall as can be seen in Figure 6.7 and Figure 6.8 by the areas with dimples where damage by void nucleation occurred. Due to the significantly smaller cross-section of the wall compared to the diameter of the HS, failure occurs more rapidly during necking, resulting in a larger residual shear fracture, see Chapter 6.2.4.

In contrast to the SSRT tests, the LCF tests do not involve damage through void nucleation but rather through crack initiation and growth. HS made from Alloy 718 wrought material showed a slightly lower fatigue life (-33%) compared to CS, while the fatigue life of both geometries in Alloy 718 SLM was the same, see Chapter 6.3.2. Possible reasons for the differing fatigue lives include surface effects such as variations in strain distribution due to different specimen geometries, roughness and microstructural changes, and the size of the available surface for crack formation. Finite element simulations revealed that the strain distributions for HS and CS are very similar, resulting in nearly identical strains on the outer surfaces. However, due to the hole in the HS, there is free surface in the center of the specimen that experiences approximately 4.56 % higher strain. Michler et al. reported similar findings with a local increase of about 3.5% for a X60 pipeline steel. Through the application of a statistical crack initiation model, they demonstrated that the fatigue life of HS is only about 5% lower than that of CS, primarily due to the larger surface area which is increased by the presence of the hole rather than the increased strain concentration [308]. Therefore, it is assumed that the surface quality in the tests is mainly responsible for the reduced fatigue life of HS compared to CS, and that improved fabrication of the specimens could reduce this difference to the calculated 5%, see Chapter 6.4.2.

Under hydrogen influence, both CS and HS exhibit the same strength values in SSRT tests, but elongation to failure and reduction of area are higher for HS, see Figure 6.4. This results in HS being slightly less sensitive to hydrogen embrittlement compared to CS, compare Figure 6.11. This can be attributed to hydrogen affecting HS only from the inside. A significant portion of necking and damage occurs on the outer side of the specimen, leading to hydrogen damage from the hole but unaffected necking from the outside. In contrast, for CS, hydrogen and necking directly compete because the entire surface is exposed to hydrogen, see Chapter 6.2.4. Interestingly, the multiaxial stresses caused by internal pressure in the hollow specimen have little effect as they are relatively small, see Chapter 6.2.5. At 100 bar, an equivalent stress of 19.3 MPa was calculated, which is small compared to the high yield stress ($R_{p0.2} = 1168\,MPa$) of alloy 718. Furthermore, experiments with nitrogen internal pressure showed no difference from tests in air. However, for materials with lower strength and for testing at higher pressures, the influence of multi-axial stress should be considered, and comparative tests with internal pressure using an inert gas should be conducted. Due to the differences in damage behavior, elongation to failure and reduction of area measured from HS deviate slightly from CS. But, for component design, the strength parameters, which are the same for both specimens, are primarily utilized. Therefore, HS are particularly suitable in SSRT tests as a quick and cost-effective screening method for hydrogen embrittlement and for material investigations under demanding conditions such as very low or high temperatures.

In LCF tests under hydrogen, crack initiation typically occurs at the surface exposed to hydrogen. This means for CS cracks initiate from the outside and for HS from the surface of the inner hole. Consequently, the crack initiation behavior of HS and CS is directly comparable as damage occurs only where hydrogen is present, and both HS and CS showed a reduction in fatigue life of approximately -60% compared to air tests, see Chapter 6.3.2. For HS subjected only to hydrogen from the inside, it was observed at low strain ranges, without significant plastic deformation, that crack initiation at the hole was suppressed due altered microstructure from the drilling process, leading to initiation from the outside without hydrogen influence, see Figure 6.22. As a result, no

hydrogen damage was detected at a strain range of 1.1%, see Figure 6.21. It is assumed that crack initiation is suppressed in the hole by high compressive residual stress caused by the drilling process and that the crack initiated therefore from the outside. Higher loads with significant plasticity reduce the residual stress which makes initiation from the hole possible and favorable under hydrogen.

The manufacturing process of HS with EDM and AFM could reduce the influence of microstructure and residual stress on fatigue life at small strain ranges as a clear hydrogen effect was observed at $\Delta\varepsilon_t = 1.1\%$, see Figure 6.23. This shows that the HS manufacturing process has a decisive influence on LCF life. Only considering surface roughness is not sufficient and microstructure and residual stresses must also be taken into account. It is therefore recommended to use the developed EDM and AFM procedure, illustrated in Figure 8.1, for LCF tests on HS, and if other procedures are used, surface roughness, microstructure, and residual stresses should be carefully examined.

In summary, HS with inner hydrogen pressure are a good alternative to CS tested in hydrogen autoclaves. However, it should be noted that in SSRT tests the different necking behavior, caused by the specimen geometry, slightly influences the determined mechanical parameters ε_f and RA. Therefore, HS testing SSRT experiments is primarily recommended here as a screening method to obtain a simple assessment of hydrogen sensitivity. In LCF tests, a good correlation of the hydrogen influence on fatigue life is achieved when surface effects can be excluded by a suitable manufacturing process of the axial hole.

8.2 Effect of hydrogen on the damage behavior of Alloy 718 wrought

In the slow strain rate tensile tests and low-cycle fatigue tests, a significant influence of gaseous hydrogen on the mechanical properties and fatigue life of Alloy 718 wrought was observed depending on test conditions, see Chapter 6. In the SSRT tests, the yield strength was not affected by hydrogen, and the stress–strain curves in air and hydrogen overlapped until sudden failure occurred, see Figure 6.4. Because the investigated Alloy 718 wrought exhibits little work hardening, the ultimate tensile strength is little influenced by the early failure. However, elongation to failure and reduction in area were strongly reduced with increasing hydrogen pressure, see Figure 6.4. The damage mode changed from a typical cup and cone fracture in air, usually appearing by void nucleation in the specimen center and a residual shear fracture at the circumference, to hydrogen-related damage initiated at the hydrogen exposed surface, see Figure 6.7 and Figure 6.8. From there, a crack propagates into the region damaged by void nucleation, followed by final fracture. In the hydrogen damaged region, secondary cracks and flat facets are observed instead of ductile dimples.

In the dynamic LCF tests, the mechanical parameters derived from the global stress–strain hysteresis were not affected by hydrogen. Nevertheless, hydrogen led to increased crack growth and earlier specimen failure. The fracture surface changed from ductile fatigue striations to flat facets and secondary cracks. It was shown in Chapter 6.4.8 that hydrogen enhances dislocation motion

along the {111} slip planes. This may lead to the nucleation and enlargement of voids, which are also found in the same planes (see Figure 6.36). Damage along the slip planes ultimately causes decohesion and the formation of flat facets. Although the HEDE mechanism cannot be ruled out as a contributor to slip-plane decohesion, it is suggested here that the primary damage arises from hydrogen enhanced dislocation motion in accordance with the HELP theory. This mechanism produces the hydrogen accelerated damage observed in both SSRT and LCF tests.

Tests under varying conditions (Chapter 6.1.2 and 6.3.2 to 6.3.5) showed that hydrogen damage strongly depends on operating conditions. In SSRT, increasing hydrogen pressure caused a greater reduction in ε_f and RA. While no significant effect was evident at 10 bar, a hydrogen pressure of 200 bar reduced ε_f by about 50% (see Figure 6.4). In LCF, increasing pressure also reduced the cycles to failure (see Figure 6.27). However, in both types of experiments, it was apparent that the damage asymptotically approaches a maximum and increases more slowly as the pressure increases. The increasing damage with pressure is attributable to the rising hydrogen concentration in the material. The square-root pressure dependence in Sievert's law explains why damage does not increase linearly with pressure. However, the damage trend does not fully follow the square-root dependence as the exponent h is typically lower, with $|h| < 0.5$. For the fatigue life of alloy 718 it was found to be $h = -0.344$.

A strong time dependence was also found in SSRT and LCF experiments. This was investigated with SSRT tests on X60 pipeline steel with different strain rates, see Figure 6.1, and in LCF tests on Alloy 718 wrought with different test frequencies, see Figure 6.24. As the strain rate decreased in SSRT tests, ε_f decreased and as test frequency decreased in LCF, the number of cycles to failure decreased. Fracture surfaces of LCF specimens at lower frequency showed significantly more flat facets and secondary cracks, indicating a stronger hydrogen effect. In both cases it can be concluded that hydrogen has more time to enter the material and diffuse to critical sites, with the slowest step in the hydrogen reaction chain being rate-controlling. Although oxide layers on nickel alloys can strongly hinder hydrogen uptake, hydrogen can dissociate and be absorbed at freshly created surfaces such as crack faces. Diffusion is very slow in FCC materials like Alloy 718. Thus, in mechanical tests with very pure hydrogen and plastic deformation, new oxide-free surfaces can form and hydrogen uptake becomes diffusion-controlled. Tests with insufficient purge cycles also showed that oxygen contamination in the test gas promotes new oxide formation, reducing hydrogen uptake and damage. In LCF on wrought Alloy 718, even at 0.001 Hz the maximum hydrogen damage was not yet reached. For fatigue tests with thousands of cycles, such low frequencies are impractical because a single test could take months. A model, as developed in this work in Chapter 7, can help translate the influence of hydrogen from practicable higher laboratory test frequencies to slower frequencies such as occur during operation.

Temperature also strongly affects hydrogen damage. In LCF tests, the highest hydrogen damage occurred between 20 °C and 200 °C, see Figure 6.28. At -50 °C it decreased significantly, and at -100 °C only a minor effect remained even at a slow frequency of 0.01 Hz. A strong dependence on the test frequency was evident, indicating that hydrogen damage can still occur, but the hydrogen diffusion is too slow at -100°C. Since both diffusion and solubility of hydrogen are thermally activated and follow an Arrhenius-type temperature dependence, both are low at low temperatures, see Chapter 2.3.2 and 5.3. The low diffusion rate is considered decisive here, as hydrogen

does not reach critical regions such as stress fields and defects. At higher temperatures (≥ 400 °C), hydrogen damage also decreases, even though diffusion and solubility continue to increase. This is because hydrogen in the lattice and at dislocations reach an energetic equilibrium if kinetics are fast enough, a phenomenon described by Oriani's relationship, see Equation (2.59). Based on the binding energy of traps at dislocations, the hydrogen occupancy can be calculated. Figure 7.3 illustrates that at low temperatures (< -100 °C), the hydrogen traps at dislocations are nearly fully occupied. However, at high temperatures (> 300 °C) the occupancy falls asymptotically toward zero. This explains why hydrogen damage, attributable to hydrogen-enhanced dislocation mobility, decreases at temperatures above 300 °C for Alloy 718.

Finally, the effect of strain range on hydrogen damage was investigated. In LCF tests on HS and CS in an autoclave, within the examined strain ranges of 1.1%, 2% and 3% under 50 bar hydrogen and a test frequency of 0.1 Hz, cycles to failure were reduced by about 60%. However, at lower test frequency of 0.0001 Hz and strain range of 3% the number of cycles to failure was reduced by 94 % from 358 cycles to 23 cycles. These experimental results, together with the simulations (see Figure 7.13), show that at sufficiently slow test frequencies there is also a strong dependence between the strain range and the hydrogen effect. As the strain range increases, the plasticity and the effect of hydrogen on dislocation movement increase, thereby accelerating crack growth.

The influencing factors on hydrogen damage are summarized and illustrated in Figure 8.2. Hydrogen damage is highest at moderate temperatures around room temperature and decreases at low temperatures due to the low diffusion rate, and at higher temperatures due to the lower hydrogen occupancy of dislocations. As pressure increases, the hydrogen concentration rises and hydrogen damage increases. At low frequencies, hydrogen has more time during a load cycle to diffuse to dislocations and to distribute within the material, which also leads to increased hydrogen damage. With increasing strain range plasticity and thus dislocation density rise. Consequently, there are more dislocations that can be influenced by hydrogen, and hydrogen damage increases.

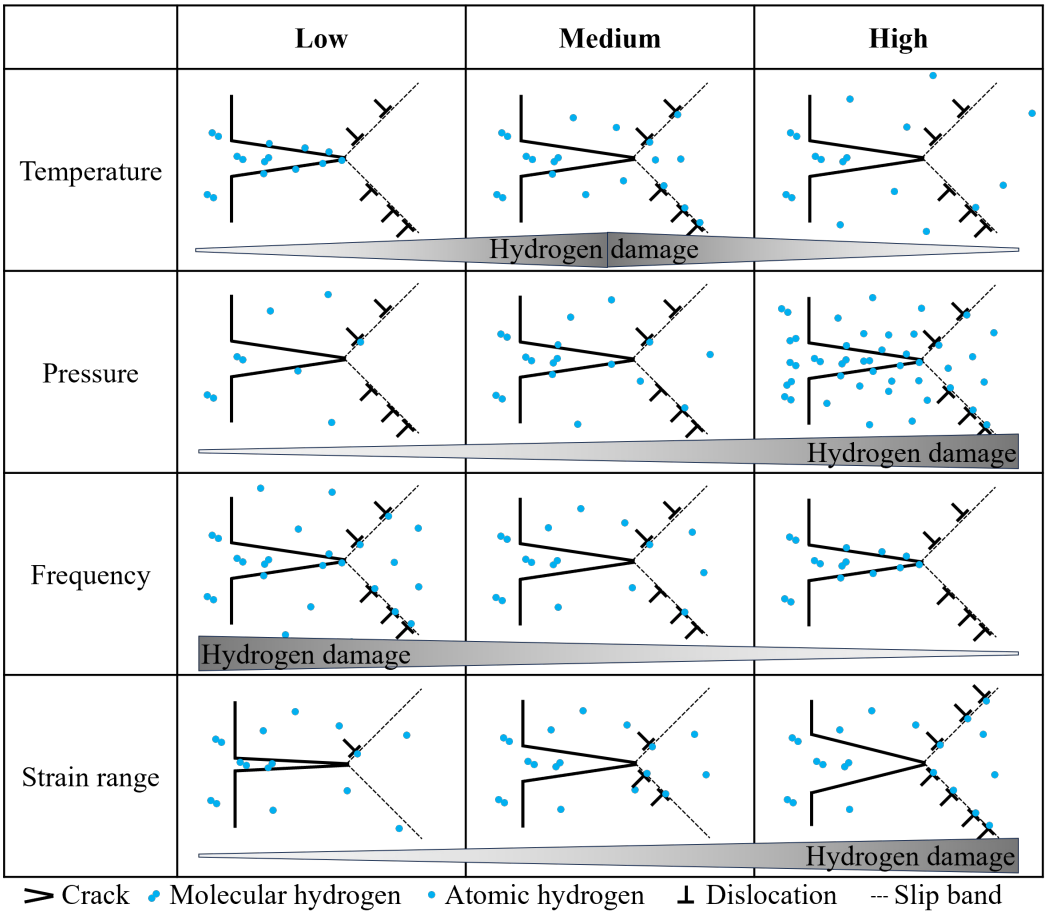


Figure 8.2: Illustration of the effects of temperature, pressure, frequency and strain range on hydrogen distribution around a crack tip, trapping at dislocations and formation of dislocations leading to hydrogen enhanced crack growth.

8.3 Ex-situ versus in-situ testing

Specimens of Alloy 718 wrought and SLM were pre-charged with gaseous hydrogen to saturation at 350 °C and 100 bar, see Chapter 5.1. While estimates based on Fickian diffusion suggested a charging time of about 4 days, see Figure 5.1, the experiments showed that saturation was reached after about 10 days of charging, see Figure 5.2. The measured hydrogen concentration was approximately 26.9 ppm for wrought Alloy 718 and 32.8 ppm for the additively manufactured material. The higher hydrogen solubility in Alloy 718 produced by SLM can be attributed to more defects and hydrogen traps in the material. When stored at room temperature or in liquid nitrogen, the hydrogen concentration decreased only slightly over a period of three months after pre-charging, making ex-situ testing feasible, see Chapter 5.2 and Figure 5.3.

The SSRT on a hydrogen pre-charged specimen showed severe hydrogen-induced damage, see Chapter 6.1.2. The elongation to failure was reduced more than in the in-situ tests at 200 bar hydrogen pressure. The fracture surfaces of the precharged specimen indicate a markedly differ-

ent damage mechanism than in in-situ tests. In the ex-situ test of the pre-charged specimen, damage initiates from the specimen interior where the highest hydrostatic stresses occur, and many flat facets are observed, see Figure 6.7, indicating strong hydrogen embrittlement. In the in-situ test, damage initiates at the outer surface where hydrogen is present at crack initiation, while the interior shows ductile damage by void nucleation as in the reference test, see Figure 6.7.

In LCF tests, specimens pre-charged with hydrogen exhibited damage comparable to specimens tested in a 50 bar hydrogen atmosphere, see Chapter 6.3.1 and 6.3.2. Unlike in tensile tests, damage here consistently initiates at the specimen surface through crack initiation and growth. In pre-charged specimens, hydrogen is already present in the material and, driven by the stress field, diffuses from the bulk to the crack tip. In contrast, in in-situ tests, hydrogen diffuses from the gas phase through the specimens' surface into the material. By pre-charging at elevated temperature and pressure, the entire specimen can be saturated with a hydrogen concentration similar to that in the stress field ahead of a crack tip. At 50 bar hydrogen pressure and room temperature, the hydrogen concentration at the crack tip is about 39.5 ppm, which is somewhat higher than the hydrogen content achieved by pre-charging at 350 °C and 100 bar (26.9 ppm), see Chapter 6.4.1.

Because of the different damage behavior in SSRT tests between in-situ and ex-situ tests, a direct comparison of the results of the two test types results is therefore not possible. In LCF tests, damage in both cases initiates at the surface, and estimating the hydrogen concentration ahead of the crack tip can help achieve comparable hydrogen damage between in-situ and ex-situ tests. To achieve conservative results that are less dependent on time, it may therefore be useful to pre-charge specimens for LCF tests. However, if the aim is to obtain the most application-relevant results and to account for time effects, in-situ tests in a hydrogen atmosphere are best suited.

8.4 Influence of additive manufacturing on hydrogen damage

Investigations of hydrogen solubility by hydrogen charging experiments at 100 bar and 350 °C followed by hydrogen concentration measurements by carrier gas melt extraction showed that the hydrogen concentration in the additively manufactured alloy is slightly higher, at about 32.8 ppm, than in wrought Alloy 718, at about 26.9 ppm, and thus the hydrogen solubility is also higher, see Chapter 5.1. Microstructural examinations in chapter 4.1 revealed that in Alloy 718 SLM the grains are elongated in the build direction, grain boundaries are more curved, small gas pores are present, and the γ' or γ" phases are significantly more pronounced than in the wrought material. These microstructural differences lead to more hydrogen traps and thereby explain the higher solubility. In the gas permeation tests, see Chapter 5.3, the diffusion coefficient of Alloy 718 SLM was determined in the temperature range from 153 °C to 261 °C. In this range it agrees very well with that of the wrought material. However, the trend line suggests that at room temperature hydrogen diffusion is higher than in the wrought material, see Chapter 5.5.1, which can also be attributed to microstructural differences, since diffusion along grain boundaries in particular can significantly increase the effective diffusion coefficient.

Through heat treatment according to AMS 5663 as with the wrought material, the strength of the additively manufactured alloy ($R_{p0.2} = 1042\ MPa$) was increased and thus matched to that of the wrought alloy ($R_{p0.2} = 1168\ MPa$). The cellular substructure typical of additive manufacturing is lost during this heat treatment, while other features such as anisotropic material properties, grain orientation, and defects like gas pores are not affected. In SSRT tests on HS with inner hydrogen pressure, Alloy 718 SLM showed a degradation of mechanical properties similar to that of the wrought material (reduced elongation to failure and reduction of area). Although fewer ductile dimples are visible on the fracture surface of the reference specimen, the same damage behavior as in the wrought material can be observed, with flat facets and secondary cracks originating from the hydrogen-exposed surface, see Chapter 6.3.2.

In the LCF tests, specimens were tested in two orientations (0° and 90° to the build direction), see Chapter 6.3.6. While the 90° oriented specimens showed a significantly shorter fatigue life than the 0° oriented specimens, the influence of 10 bar hydrogen was small for both orientations. Tests at 100 bar hydrogen on 0° oriented specimens showed hydrogen damage comparable to the tests on wrought Alloy 718 at 100 bar. Therefore, additively manufactured Alloy 718 is just as suitable for hydrogen applications as wrought material, after heat treatment according to AMS 5663. Although the AM-typical microstructure slightly increases the hydrogen solubility and probably also the diffusivity at room temperature, see Chapter 5.5.1, it has no significant influence on hydrogen damage when the material has been heat treated according to AMS 5663. However, the lower fatigue life in the 90° direction due to the oriented grains should be considered in component design.

8.5 Fatigue life prediction for hydrogen environments

Components used in hydrogen atmospheres often face a wide range of different operating conditions, consisting of combinations of hydrogen pressure, temperature, and varying load cycles. Experimentally covering every possible scenario is usually not feasible and involves high costs. Models can help to significantly reduce the experimental effort and allow a reliable estimate of the service life, even for extreme operating conditions. To realize the widest possible range of applications for the model, it is useful to base the model on observed mechanisms and physical relationships. This results in a robust model for safe component design under various operating conditions.

The established approach of modelling short crack growth based on the proportionality to the cyclic crack tip opening displacement ($\Delta CTOD$) according to alternating slip is used for fatigue life prediction in air. The fatigue life is determined by the number of cycles required for crack growth from the initiation of a microcrack (17.5 µm) to a technical crack (1000 µm). $\Delta CTOD$ is described using the relation $\Delta CTOD = d_{n'} Z_D / \sigma_{cy} a$, where Z_D is the damage parameter according to Heitmann [1]. This model is suitable for describing low-cycle fatigue life under elastic-plastic material behavior and has already been extended in several studies to account for viscous material behavior at high temperatures [325,326] or environmental effects such as oxidation [137].

In this work, Z_D was modified to include the influence of hydrogen on short crack growth under cyclic loading. Depending on the trap occupancy at dislocations with hydrogen, the crack growth per cycle is accelerated. This is taken into account by the newly developed hydrogen damage parameter $Z_{D,H}^{(*)}$, see Equation (7.7) and (7.8). This assumption follows the HELP theory, which states that hydrogen facilitates dislocation motion and thus increases local plasticity. In Chapter 6.4.8 it was shown that this mechanism is primarily responsible for hydrogen-induced damage in Alloy 718 as enhanced dislocation motion along {111} slip planes cause void nucleation and damage along these planes. The model accounts for time- and temperature-dependent hydrogen diffusion ahead of the crack tip and calculates the hydrogen occupancy of dislocations with the equilibrium condition between lattice sites and hydrogen traps under fast hydrogen kinetics, with a trap binding energy of $E_{t,b} = 13500\,J/mol$. The binding and activation energies of hydrogen traps in Alloy 718 were investigated in Chapter 5.4 and discussed in more detail in Chapter 5.5.2.

Several simplifications were made to obtain an analytical model. This avoids the need for a computationally intensive finite element model and allows the crack growth for each individual cycle across a large number of tests to be computed in seconds to minutes. I) For hydrogen diffusion at the crack tip, the analytical solution of Fickian diffusion from Crank for a semi-infinite, one-dimensional medium is used. II) Transport of hydrogen by dislocation motion, grain-boundary diffusion, and changes in the diffusion coefficient due to microstructural changes at the crack tip are not considered. III) Diffusion and crack growth are computed sequentially rather than simultaneously. IV) At the beginning of each cycle, the concentration ahead of the crack tip is set to $C_{initial}$. These simplifications are discussed in more detail in Chapter 7.5.

The model predictions were compared with experimental tests in air and with internal nitrogen or hydrogen pressure in the range $0 - 250\,bar$, over a temperature range of -100 $- 600\,°C$, frequency range of $0.001 - 1\,Hz$, and strain ranges of $1.1 - 3$ %, see Figure 8.3. All of the investigated conditions fall within the scatter band of factor 2 except of one point that is slightly outside. This shows that the model predicts very well the experimental results ($R^2 = 0.89$) and that the physical influences are correctly taken into account.

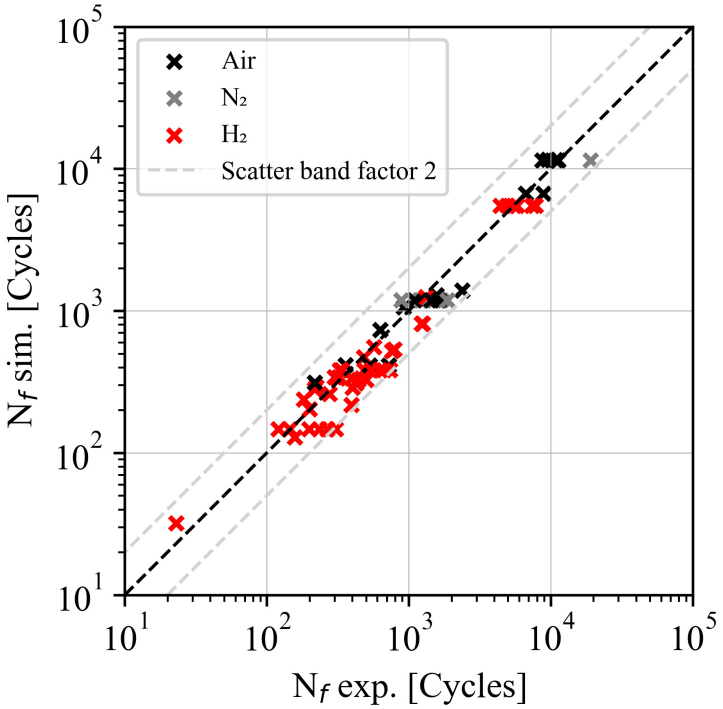


Figure 8.3: Simulated ($Z^*_{D,H}$ with $\alpha^* = 12000\ m^2/J$) versus experimental fatigue life N_f of CS and HS in air, nitrogen and hydrogen atmosphere for $p = 0 - 250\ bar$, T = -100 – 600 °C, $f = 0.001 - 1\ Hz$ and $\Delta\varepsilon_t = 1.1 - 3$ %. The model can predict the fatigue life for all conditions very well within a scatter band of factor 2 ($R^2 = 0.89$).

While large components such as pipelines and pressure vessels are usually designed according to codes and standards like ASME B31.12 [327] based on crack growth curves, the model presented is particularly suited for designing small, thin-walled components that are subjected to high mechanical loads. Potential applications include valves and heat exchangers in the cryogenic temperature range, hydrogen compressors and fittings in the high pressure range, and aircraft engines, gas turbines, and internal combustion engines in the high temperature range.

9 Summary and conclusions

The use of hydrogen as a climate-neutral energy carrier comes with challenges in materials science, as high-strength materials, such as the investigated Alloy 718, are susceptible to hydrogen damage. Due to the increasing demand for rapid and cost-effective material investigations for the qualification of components used in hydrogen atmospheres, new testing methods are required.

As a promising alternative to expensive tests on conventional specimens in hydrogen autoclaves, the hollow specimen technique has proven effective, where the specimen is subjected to hydrogen from an axial hole. Results of this work regarding surface quality, gas quality and comparability to conventional specimens have been incorporated into the standardization of HS in ISO/FDIS 7039 [293] and continues in the technical committee ISO/TC 164/SC for hydrogen-specific test parameters. The standardization of HS for fatigue testing has not yet started. However, the results of this work provide a good basis for this. It was shown that the surface condition of the hole has a major influence on fatigue life. Microstructural investigations of outer and inner surfaces revealed significant differences in roughness and surface-near microstructural changes between different manufacturing processes. Although the roughness of the drilled hollow specimens used in this work was low, a strong influence on the surface-near microstructure was observed. The roughness and microstructural changes of the axial hole could be significantly reduced by electrical discharge machining and abrasive flow polishing.

Mechanical testing of hollow specimens in SSRT tests revealed the characteristic strain rate dependence of hydrogen embrittlement and the inhibiting effects of oxygen contamination in the testing gas. Without adequate gas purging, it was observed that hydrogen embrittlement is significantly reduced due to oxygen contamination, and no conservative test results are obtained. An effective flushing procedure for HS was established with 10 flushing cycles between 10 bar and 100 bar for sufficiently high gas quality in the sample.

The comparative tests on conventional specimens and hollow specimens with a hydrogen pressure ranging from 0 bar to 200 bar showed significant hydrogen embrittlement with increasing pressure. While the strength values for CS and HS were similar, the HS exhibited slightly lower ductility in air but higher ductility in hydrogen, indicating HS were somewhat less sensitive to hydrogen. The difference of ductility in air can be attributed to the thinner wall thickness compared to the diameter of the CS, resulting in a different necking behavior. In hydrogen, the difference arises because, in HS, necking primarily occurs from the outside while hydrogen is only present in the hole, leading to less competition between these two mechanisms. In conclusion, HS testing is suitable for studying hydrogen embrittlement through SSRT tests and allows for the examination of various materials. However, direct comparisons with mechanical properties determined from CS are not possible.

The comparison of CS and HS in fatigue tests in air showed no difference for Alloy 718 SLM and a reduction of N_f for HS by about -33 % for Alloy 718 wrought when manufactured by drilling.

Both CS and HS exhibited a reduction in fatigue life of about 60 % under 50 bar hydrogen pressure compared to air. Drilled HS tested under a small strain range of 1.1% showed no hydrogen effect. It could be shown by microsections and EBSD images that the near-surface microstructure was strongly influenced by the drilling process. A new manufacturing procedure for the axial hole was developed, in which the hole is produced by electrical discharge machining and subsequently abrasive flow machining. This yields a surface comparable to the surface of CS. HS manufactured by this method showed comparable cycles to failure to CS when tested in air as well as under hydrogen, even at the small strain range.

Since the operating conditions of components such as liquid hydrogen tanks, hydrogen gas turbines, high-pressure hydrogen tanks, etc., vary significantly in temperature, pressure, mechanical loading range, and speed, these influencing factors on hydrogen damage were investigated using hollow specimens. Therefore, new test stands with liquid nitrogen cooling (down to -196 °C) and induction heating (up to 600 °C) were established.

The LCF experiments with varying test frequency between 0.001 Hz and 1 Hz showed a strong influence on hydrogen damage. While the damage at 1 Hz was small the fatigue life was strongly reduced at 0.001 Hz. Nevertheless, it can be assumed from the results that maximum degradation was still not reached. Increased hydrogen damage was also observed with increasing pressure. However, at a pressure of 250 bar the number of cycles to failure asymptotically reach a minimum. The temperature of maximum damage ranged from 20-200 °C, with no hydrogen damage observed at low temperatures of -100 °C and high temperatures of 600 °C. But, at 600 °C, increased damage caused by oxygen was observed.

Hydrogen pre-charging of samples resulted in significant damage due to hydrogen in both tensile and fatigue tests. Pre-charging to saturation with approximately 27 ppm of hydrogen at a pressure of 100 bar, temperature of 350 °C and duration of 10 days led to a higher reduction in elongation to failure than in-situ tests at 200 bar hydrogen pressure. In contrast, the reduction in fatigue life was comparable to tests at 50 bar, which can be explained by the longer duration of the fatigue test, allowing hydrogen to diffuse continuously to the crack tip, resulting in substantial damage even at 50 bar.

Additive manufacturing is increasingly used in the production of components. However, the resulting microstructure differs significantly from conventional manufacturing processes. Therefore, material produced by selective laser melting was examined. To achieve a comparable strength to wrought material, the samples were heat-treated after additive manufacturing according to [97]. Despite the same heat treatment, the microstructural analysis revealed notable differences: the wrought Alloy 718 exhibited a relatively uniform grain structure with coarse δ precipitates at grain boundaries and fine precipitates within the grains, while the SLM Alloy 718 showed significant grain orientation and some pores due to the additive manufacturing process, with δ precipitates only at the grain boundaries and very small γ'' precipitates inside the grains. However, defects and microstructures from additive manufacturing showed minimal influence on hydrogen damage. This could be attributed to the heat treatment involving solution annealing, which destroys the cellular microstructure typical of additive manufacturing. Other microstructural differences compared to the wrought alloy, such as gas pores and elongated grains with unclear grain

boundaries, were not eliminated by heat treatment. Consequently, anisotropic mechanical properties were measurable, with fatigue life in the 90° orientation to the build direction being lower than in the 0° orientation.

The numerous operating conditions consisting of temperature, hydrogen pressure, load amplitude and frequency make it nearly impossible to conduct experiments across the entire field. Therefore, a model for predicting service life that takes these influencing factors into account on the basis of physical relationships can significantly reduce the costs of component design, evaluation and testing. Based on the experimental data and fractographic examinations, a mechanism-based model was developed that can predict the fatigue life under hydrogen exposure. The model describes the micro crack growth based on elastic-plastic fracture mechanics from defects of approximately 20 µm to technical crack initiation of 1 mm. The influence of hydrogen on crack growth is represented in the hydrogen damage parameter $Z_{D,H}$ by physical principles of hydrogen diffusion and trapping. Hydrogen related material parameters like solubility, diffusivity and trap binding energies were determined by carrier gas melt extraction, thermal desorption spectroscopy and gas permeation. This results in a model that captures the time, pressure and temperature dependent hydrogen processes at the crack tip. Based on this, the hydrogen occupancy at dislocations is calculated, and an increased crack growth due to enhanced dislocation movement is assumed, in accordance with the hydrogen-enhanced localized plasticity theory (HELP). The model demonstrates that it effectively represents the influence of hydrogen over a wide range of temperature, pressure, frequency, and load. This results in a very good agreement between the model and the experiments. Therefore, the model allows to predict the fatigue life of components, even at operating conditions where experiments are difficult and expensive, and to safely operate them in a hydrogen environment.

References

[1] Heitmann HH, Vehoff H, Neumann P. LIFE PREDICTION FOR RANDOM LOAD FATIGUE BASED ON THE GROWTH BEHAVIOR OF MICROCRACKS. Fract. 84, Elsevier; 1984, p. 3599–606. https://doi.org/10.1016/B978-1-4832-8440-8.50388-4.

[2] Johnson WH. II. On some remarkable changes produced in iron and steel by the action of hydrogen and acids. Proc R Soc London 1875;23:168–79. https://doi.org/10.1098/rspl.1874.0024.

[3] Carpenter BJL, Moya N, Shaffer RA, Smith DM. BIBLIOGRAPHY OF INFORMATION ON MECHANICS OF STRUCTURAL FAILURE. 1973. https://doi.org/10.11316/butsuri1946.2.53.

[4] Li H, Niu R, Li W, Lu H, Cairney J, Chen YS. Hydrogen in pipeline steels: Recent advances in characterization and embrittlement mitigation. J Nat Gas Sci Eng 2022;105:104709. https://doi.org/10.1016/j.jngse.2022.104709.

[5] Venezuela J, Liu Q, Zhang M, Zhou Q, Atrens A. A review of hydrogen embrittlement of martensitic advanced high-strength steels. Corros Rev 2016;34:153–86. https://doi.org/10.1515/corrrev-2016-0006.

[6] Hoschke J, Chowdhury MFW, Venezuela J, Atrens A. A review of hydrogen embrittlement in gas transmission pipeline steels. Corros Rev 2023;41:277–317. https://doi.org/10.1515/corrrev-2022-0052.

[7] Stefan E, Talic B, Larring Y, Gruber A, Peters TA. Materials challenges in hydrogen-fuelled gas turbines. Int Mater Rev 2022;67:461–86. https://doi.org/10.1080/09506608.2021.1981706.

[8] Wagner H. J, Hall A. M. DMIC Report 217: Physical Metallurgy of Alloy 718. 1965.

[9] Kagay B. Hydrogen embrittlement testing of alloy 718 for oil and gas applications 2016:105.

[10] Keiser DD, Brown HL. A Review of the Physical Metallurgy of Alloy 718. Aero Jet Nucl Co 1976.

[11] Paulonis DF, Schirra JJ. Alloy 718 at Pratt & Whitney - Historical perspective and future challenges. Proc Int Symp Superalloys Var Deriv 2001;1:13–23. https://doi.org/10.7449/2001/superalloys_2001_13_23.

[12] Walter RJ, Chandler WT. Effects of high pressure hydrogen on metals at ambient temperature. 1969.

[13] Walter RJ, Hayes HG, Chandler WT. INFLUENCE OF GASEOUS HYDROGEN ON METALS. 1971.

[14] Dodge BF. High-Pressure Research in Chemical Engineering Department of Yale University. J Fluids Eng 1953;75:331–43. https://doi.org/10.1115/1.4015285.

[15] Klima SJ, Nachtigall AJ, Hoffman CA. PRELIMINARY INVESTIGATION OF EFFECT OF HYDROGEN ON STRESS-RUPTURE AND FATIGUE PROPERTIES OF AN IRON-, A NICKEL-, AND A COBALT-BASE ALLOY. vol. TECHNICAL. 1962.

[16] Ogata T. Hydrogen environment embrittlement evaluation in fatigue properties of stainless steel SUS304L at cryogenic temperatures. AIP Conf Proc 2010;1219:25–32. https://doi.org/10.1063/1.3402310.

[17] Nakamura J, Miyahara M, Omura T, Semba H, Wakita M, Otome Y. Degradation of fatigue properties in high pressure gaseous hydrogen environment evaluated by cyclic pressurization tests. Procedia Eng 2010;2:1235–41. https://doi.org/10.1016/j.proeng.2010.03.134.

[18] Ebling F, Oesterlin H, Wackermann K, Primus D, Rehme O. Hydrogen effects on low cycle fatigue of IN718 at RT and 77K using the tubular specimen technique. Proc Fourth Int Conf Met Hydrog 2022:10.

[19] Ueno A, Benjamin G. Effect of high-pressure H2 gas on tensile and fatigue properties of stainless steel SUS316L by means of the internal high-pressure H2 gas method. Procedia Struct Integr 2019;19:494–503. https://doi.org/10.1016/j.prostr.2019.12.053.

[20] Nietzke J, Konert F, Poka K, Merz B, Sobol O, Böllinghaus T. Comparison of Hydrogen Effects on Additively Manufactured and Conventional Austenitic Steels. CAMA Cent Appl Macroecon Anal 2024;7:285–92. https://doi.org/10.2139/ssrn.4932291.

[21] Boot T, Riemslag T, Reinton E, Liu P, Walters CL, Popovich V. Assessing the Susceptibility of Existing Pipelines to Hydrogen Embrittlement, Springer International Publishing; 2021, p. 722–9. https://doi.org/10.1007/978-3-030-65261-6_65.

[22] Konert F, Campari A, Nietzke J, Sobol O, Paltrinieri N, Alvaro A. Evaluation of the tensile properties of X65 pipeline steel in compressed gaseous hydrogen using hollow specimens. Int Conf Struct Integr 2023;7034:204–11. https://doi.org/10.1016/j.prostr.2024.01.074.

[23] Wan HJ, Wu XQ, Ming HL, Wang JQ, Han EH. Effects of Hydrogen Charging Time and Pressure on the Hydrogen Embrittlement Susceptibility of X52 Pipeline Steel Material. Acta Metall Sin (English Lett 2023. https://doi.org/10.1007/s40195-023-01625-5.

[24] Du J, Ming H, Wang J, Han EH. Hydrogen embrittlement of 20# seamless steel in medium and low pressure gaseous hydrogen. Mater Lett 2023;334:133734. https://doi.org/10.1016/j.matlet.2022.133734.

[25] Mohandas NK, Giorgini A, Vanazzi M, Riemslag T, Scott SP, Popovich V. Hydrogen Embrittlement of Inconel 718 Manufactured by Laser Powder Bed Fusion Using Sustainable Feedstock: Effect of Heat Treatment and Microstructural Anisotropy. Metals (Basel) 2023;13. https://doi.org/10.3390/met13020418.

[26] Michler T, Wackermann K, Ebling F, Oesterlin H. Comparison of Tensile Test Results in High Pressure Gaseous Hydrogen Using Conventional and Tubular Specimens. Vol. 4 Mater. Fabr., vol. 4, American Society of Mechanical Engineers; 2021, p. 1–6. https://doi.org/10.1115/PVP2021-61138.

[27] Michler T, Ebling F, Fischer C, Oeser S, Wackermann K. Tensile testing in high pressure gaseous hydrogen using conventional and tubular specimens: Ferritic steels. Int J Hydrogen Energy 2024;70:262–75. https://doi.org/10.1016/j.ijhydene.2024.05.238.

[28] Michler T, Freitas T, Oesterlin H, Fischer C, Wackermann K, Ebling F. Tensile testing in high pressure gaseous hydrogen using conventional and tubular specimens: Austenitic stainless steels. Int J Hydrogen Energy 2023;48:25609–18. https://doi.org/10.1016/j.ijhydene.2023.03.248.

[29] Sabau AS, Bejan A, Brownell D, Gluesenkamp K, Murphy B, List F, et al. Design, additive manufacturing, and performance of heat exchanger with a novel flow-path architecture. Appl Therm Eng 2020;180:115775. https://doi.org/10.1016/j.applthermaleng.2020.115775.

[30] Kaur I, Singh P. State-of-the-art in heat exchanger additive manufacturing. Int J Heat Mass Transf 2021;178:121600. https://doi.org/10.1016/j.ijheatmasstransfer.2021.121600.

[31] Thompson SM, Aspin ZS, Shamsaei N, Elwany A, Bian L. Additive manufacturing of heat exchangers: A case study on a multi-layered Ti-6Al-4V oscillating heat pipe. Addit Manuf 2015;8:163–74. https://doi.org/10.1016/j.addma.2015.09.003.

[32] Zaied M, Msolli S, Fourment H, Aubry E, Bolot R, Lebaal N, et al. The contribution of 515-nm green laser L-PBF to the thermal performance of lattice-based heat exchangers for hydrogen storage applications. Int J Adv Manuf Technol 2024;133:1501–18. https://doi.org/10.1007/s00170-024-13863-7.

[33] Sadiq M, Saeed M, Mayyas AT, Mezher T, El Fadel M. Pre-cooling systems for hydrogen fueling stations: Techno-economic analysis for scaled enactment. Energy Convers Manag X 2023;18:100369. https://doi.org/10.1016/j.ecmx.2023.100369.

[34] Vietze M, Evrim C. Development of additively manufactured cryogenic heat exchangers for hydrogen-electric aircraft propulsion. IOP Conf Ser Mater Sci Eng 2024;1301:012007. https://doi.org/10.1088/1757-899x/1301/1/012007.

[35] Shiomi M, Osakada K, Nakamura K, Yamashita T, Abe F. Residual stress within metallic model made by selective laser melting process. CIRP Ann - Manuf Technol 2004;53:195–8. https://doi.org/10.1016/S0007-8506(07)60677-5.

[36] Santos Maldonado C, Zafra A, Pañeda EM, Sandmann P, Morana R, Pham M-S. Inuence of dislocation cells in the hydrogen diffusivity, trapping and embrittlement of wrought and additively manufactured Inconel 718. Commun Mater 2024. https://doi.org/10.1038/s43246-024-00654-6.

[37] Chlebus E, Gruber K, Kuźnicka B, Kurzac J, Kurzynowski T. Effect of heat treatment on the microstructure and mechanical properties of Inconel 718 processed by selective laser melting. Mater Sci Eng A 2015;639:647–55. https://doi.org/10.1016/j.msea.2015.05.035.

[38] Fu Z, Wu P, Zhang Y, Gan K, Yan D, Li Z. Effects of hydrogen and load frequency on the fatigue crack propagation behavior of selective laser melted Inconel 718 alloy. Int J Fatigue 2022;160:106848. https://doi.org/10.1016/j.ijfatigue.2022.106848.

[39] Aydinöz ME, Brenne F, Schaper M, Schaak C, Tillmann W, Nellesen J, et al. On the microstructural and mechanical properties of post-treated additively manufactured Inconel 718 superalloy under quasi-static and cyclic loading. Mater Sci Eng A 2016;669:246–58. https://doi.org/10.1016/j.msea.2016.05.089.

[40] Popovich AA, Sufiiarov VS, Polozov IA, Borisov E V. Microstructure and mechanical properties of Inconel 718 produced by SLM and subsequent heat treatment. Key Eng Mater 2015;651–653:665–70. https://doi.org/10.4028/www.scientific.net/KEM.651-653.665.

[41] Gorelik M. Additive manufacturing in the context of structural integrity. Int J Fatigue 2017;94:168–77. https://doi.org/10.1016/j.ijfatigue.2016.07.005.

[42] Bauereiß A, Scharowsky T, Körner C. Defect generation and propagation mechanism during additive manufacturing by selective beam melting. J Mater Process Technol 2014;214:2522–8. https://doi.org/10.1016/j.jmatprotec.2014.05.002.

[43] Seifi M, Salem A, Beuth J, Harrysson O, Lewandowski JJ. Overview of Materials Qualification Needs for Metal Additive Manufacturing. Jom 2016;68:747–64. https://doi.org/10.1007/s11837-015-1810-0.

[44] Jia Q, Gu D. Selective laser melting additive manufacturing of Inconel 718 superalloy parts: Densification, microstructure and properties. J Alloys Compd 2014;585:713–21. https://doi.org/10.1016/j.jallcom.2013.09.171.

[45] Lampman SR. Fatigue and Fracture. vol. 19. 1996.

[46] Wöhler A. Versuche über die Festigkeit der Eisenbahnwagenachsen. Zeitschrift Für Bauwes 1860;10:160–1.

[47] Manson SS. Behavior Of Materials Under Conditions Of Thermal Stress. 1954.

[48] Coffin LF. A Study of the Effects of Cyclic Thermal Stresses on a Ductile Metal. J Fluids Eng 1954;76:931–49. https://doi.org/10.1115/1.4015020.

[49] Gross D, Seelig T. Bruchmechanik. Berlin, Heidelberg: Springer Berlin Heidelberg; 2011. https://doi.org/10.1007/978-3-642-10196-0.

[50] Akhurst KN, Baker TJ. Threshold Stress Intensity for Hydrogen-Induced Crack Growth. Metall Trans A, Phys Metall Mater Sci 1981;12 A:1059–70. https://doi.org/10.1007/BF02643487.

[51] Gerberich WW, L1vne T, Chen XF, Kaczorowski M. Crack growth from internal hydrogen-temperature and microstructural effects in 4340 steel. Metall Trans A 1988;19:1319–34. https://doi.org/10.1007/BF02662593.

[52] Lee SL, Unger DJ. A decohesion model of hydrogen assisted cracking. Eng Fract Mech 1988;31:647–60. https://doi.org/10.1016/0013-7944(88)90107-5.

[53] Polák J. Cyclic Deformation, Crack Initiation, and Low-Cycle Fatigue. 2016. https://doi.org/10.1016/b978-0-12-803581-8.00890-0.

[54] Schijve J. I. Fatigue crack growth and fracture mechanics. Eng Fract Mech 1979;11:169–81.

[55] Hicks PD, Altstetter CJ. Internal hydrogen effects on tensile properties of iron- and nickel-base superalloys. Metall Trans A 1990;21:365–72. https://doi.org/10.1007/BF02782416.

[56] Fournier L, Delafosse D, Magnin T. Cathodic hydrogen embrittlement in alloy 718. Mater Sci Eng A 1999;269:111–9. https://doi.org/10.1016/S0921-5093(99)00167-7.

[57] Galliano F, Andrieu E, Blanc C, Cloue JM, Connetable D, Odemer G. Effect of trapping and temperature on the hydrogen embrittlement susceptibility of alloy 718. Mater Sci Eng A 2014;611:370–82. https://doi.org/10.1016/j.msea.2014.06.015.

[58] METALS S. INCONEL® alloy 718. Https://WwwSpecialmetalsCom/Documents/Technical-Bulletins/Inconel/Inconel-Alloy-718Pdf 2021.

[59] Forni D, Mazzucato F, Valente A, Cadoni E. High strain-rate behaviour of as-cast and as-build Inconel 718 alloys at elevated temperatures. Mech Mater 2021;159:103859. https://doi.org/10.1016/j.mechmat.2021.103859.

[60] Pollock TM, Tin S. Nickel-based superalloys for advanced turbine engines: Chemistry, microstructure, and properties. J Propuls Power 2006;22:361–74. https://doi.org/10.2514/1.18239.

[61] Galliano F, Andrieu E, Cloué JM, Odemer G, Blanc C. Effect of temperature on hydrogen embrittlement susceptibility of alloy 718 in Light Water Reactor environment. Int J Hydrogen Energy 2017;42:21371–8. https://doi.org/10.1016/j.ijhydene.2017.06.211.

[62] Hu H, Zhao T, Du D, Guo X, Huang H, Lu C, et al. New insights into radiation damage in additively manufactured alloy 718. Addit Manuf 2025;108:104827. https://doi.org/10.1016/j.addma.2025.104827.

[63] Kolts J. Alloy 718 for the Oil and Gas Industry 2012:329–44. https://doi.org/10.7449/1989/superalloys_1989_329_344.

[64] Hosford WF. Mechanical Behavior of Materials. Cambridge University Press; 2. Edition; 2009.

[65] Maier HJ, Niendorf T, Bürgel R. Handbuch Hochtemperatur-Werkstofftechnik. Wiesbaden: Springer Fachmedien Wiesbaden; 2015. https://doi.org/10.1007/978-3-658-10591-4.

[66] Saarimäki J. Cracks in superalloys. 2018. https://doi.org/https://doi.org/10.3384/diss.diva-144397.

[67] Cozar R, Pineau A. Morphology of y’ and y" precipitates and thermal stability of inconel 718 type alloys. Metall Trans 1973;4:47–59. https://doi.org/10.1007/BF02649604.

[68] Radavich JF. The Physical Metallurgy of Cast and Wrought Alloy 718. Superalloys 718 Metall. Appl., TMS; 2004, p. 229–40. https://doi.org/10.7449/1989/Superalloys_1989_229_240.

[69] Oblak JM, Paulonis DF, Duvall DS. Coherency strengthening in Ni base alloys hardened by DO22 γ’’ precipitates. Metall Trans 1974;5:143–53. https://doi.org/10.1007/BF02642938.

[70] He Z, Zhang Y, Qiu W, Shi HJ, Gu J. Temperature effect on the low cycle fatigue behavior of a directionally solidified nickel-base superalloy. Mater Sci Eng A 2016;676:246–52. https://doi.org/10.1016/j.msea.2016.08.064.

[71] Sohrabi MJ, Mirzadeh H. Unexpected formation of delta (δ) phase in as-cast niobium-bearing superalloy at solution annealing temperatures. Mater Lett 2020;261:127008. https://doi.org/10.1016/j.matlet.2019.127008.

[72] Ning Y, Huang S, Fu MW, Dong J. Microstructural characterization, formation mechanism and fracture behavior of the needle δ phase in Fe-Ni-Cr type superalloys with high Nb content. Mater Charact 2015;109:36–42. https://doi.org/10.1016/j.matchar.2015.09.011.

[73] Desvallees Y, Bouzidi M, Bois F, Beaude N. Delta Phase in INCONEL 718: Mechanical Properties and Forging Process Requirements. Superalloys 718, 625, 706 Var. Deriv., TMS; 1994, p. 281–91. https://doi.org/10.7449/1994/Superalloys_1994_281_291.

[74] Ferreri NC, Vogel SC, Knezevic M. Determining volume fractions of γ, γ′, γ″, δ, and MC-carbide phases in Inconel 718 as a function of its processing history using an advanced neutron diffraction procedure. Mater Sci Eng A 2020;781:139228. https://doi.org/10.1016/j.msea.2020.139228.

[75] Lim KH, Ryou KH, Choi JH, Choi G, Choi WS, Lee JH, et al. Effect of titanium nitride inclusions on the mechanical properties of direct laser deposited Inconel 718. Extrem Mech Lett 2023;61:102009. https://doi.org/10.1016/j.eml.2023.102009.

[76] Sohrabi MJ, Mirzadeh H, Rafiei M. Solidification behavior and Laves phase dissolution during homogenization heat treatment of Inconel 718 superalloy. Vacuum 2018;154:235–43. https://doi.org/10.1016/j.vacuum.2018.05.019.

[77] Kirka MM, Medina F, Dehoff R, Okello A. Mechanical behavior of post-processed Inconel 718 manufactured through the electron beam melting process. Mater Sci Eng A 2017;680:338–46. https://doi.org/10.1016/j.msea.2016.10.069.

[78] Konečná R, Kunz L, Nicoletto G, Bača A. Long fatigue crack growth in Inconel 718 produced by selective laser melting. Int J Fatigue 2016;92:499–506. https://doi.org/10.1016/j.ijfatigue.2016.03.012.

[79] Abd-Elaziem W, Elkatatny S, Abd-Elaziem AE, Khedr M, Abd El-Baky MA, Hassan MA, et al. On the current research progress of metallic materials fabricated by laser powder bed fusion process: a review. J Mater Res Technol 2022;20:681–707. https://doi.org/10.1016/j.jmrt.2022.07.085.

[80] Ahn DG. Directed Energy Deposition (DED) Process: State of the Art. vol. 8. Korean Society for Precision Engineering; 2021. https://doi.org/10.1007/s40684-020-00302-7.

[81] Seow CE, Coules HE, Wu G, Khan RHU, Xu X, Williams S. Wire + Arc Additively Manufactured Inconel 718: Effect of post-deposition heat treatments on microstructure and tensile properties. Mater Des 2019;183:108157. https://doi.org/10.1016/j.matdes.2019.108157.

[82] Gibson I, Rosen D. Additive Manufacturing Technologies: 3D Printing, Rapid Prototyping, and Direct Digital Manufacturing. 2nd ed. 20. New York, NY : Springer, 2015; 2015. https://doi.org/10.1007/978-1-4939-2113-3.

[83] Vaezi M, Seitz H, Yang S. A review on 3D micro-additive manufacturing technologies 2013:1721–54. https://doi.org/10.1007/s00170-012-4605-2.

[84] Frazier WE. Metal Additive Manufacturing : A Review 2014;23:1917–28. https://doi.org/10.1007/s11665-014-0958-z.

[85] Zhang YN, Cao X, Wanjara P, Medraj M. Oxide films in laser additive manufactured Inconel 718. Acta Mater 2013;61:6562–76. https://doi.org/10.1016/j.actamat.2013.07.039.

[86] Gribbin S, Bicknell J, Jorgensen L, Tsukrov I, Knezevic M. Low cycle fatigue behavior of direct metal laser sintered Inconel alloy 718. Int J Fatigue 2016;93:156–67. https://doi.org/10.1016/j.ijfatigue.2016.08.019.

[87] Qi H, Azer M, Ritter A. Studies of standard heat treatment effects on microstructure and mechanical properties of laser net shape manufactured INCONEL 718. Metall Mater Trans A Phys Metall Mater Sci 2009;40:2410–22. https://doi.org/10.1007/s11661-009-9949-3.

[88] Schneider J, Farris L, Nolze G, Reinsch S, Cios G, Tokarski T, et al. Microstructure Evolution in Inconel 718 Produced by Powder Bed Fusion Additive Manufacturing. J Manuf Mater Process 2022;6. https://doi.org/10.3390/jmmp6010020.

[89] Blackwell PL. The mechanical and microstructural characteristics of laser-deposited IN718. J Mater Process Technol 2005;170:240–6. https://doi.org/10.1016/j.jmatprotec.2005.05.005.

[90] Konečná R, Nicoletto G, Kunz L, Bača A. Microstructure and directional fatigue behavior of Inconel 718 produced by selective laser melting. Procedia Struct Integr 2016;2:2381–8. https://doi.org/10.1016/j.prostr.2016.06.298.

[91] McLouth TD, Witkin DB, Lohser JR, Sitzman SD, Adams PM, Lingley ZR, et al. Temperature and strain-rate dependence of the elevated temperature ductility of Inconel 718 prepared by selective laser melting. Mater Sci Eng A 2021;824:141814. https://doi.org/10.1016/j.msea.2021.141814.

[92] Harrison NJ, Todd I, Mumtaz K. Reduction of micro-cracking in nickel superalloys processed by Selective Laser Melting: A fundamental alloy design approach. Acta Mater 2015;94:59–68. https://doi.org/10.1016/j.actamat.2015.04.035.

[93] Chen Y, Xu M, Zhang T, Xie J, Wei K, Wang S, et al. Grain refinement and mechanical properties improvement of Inconel 625 alloy fabricated by ultrasonic-assisted wire and arc additive manufacturing. J Alloys Compd 2022;910:164957. https://doi.org/10.1016/j.jallcom.2022.164957.

[94] Xu J, Hao Z, Fu Z, He X, Wang H, Xu G. Hydrogen embrittlement behavior of selective laser-melted Inconel 718 alloy. J Mater Res Technol 2023;23:359–69. https://doi.org/10.1016/j.jmrt.2022.12.196.

[95] Sui S, Tan H, Chen J, Zhong C, Li Z, Fan W, et al. The influence of Laves phases on the room temperature tensile properties of Inconel 718 fabricated by powder feeding laser additive manufacturing. Acta Mater 2019;164:413–27. https://doi.org/10.1016/j.actamat.2018.10.032.

[96] Qu FS, Liu XG, Xing F, Zhang KF. High temperature tensile properties of laser butt-welded plate of Inconel 718 superalloy with ultra-fine grains. Trans Nonferrous Met Soc China (English Ed 2012;22:2379–88. https://doi.org/10.1016/S1003-6326(11)61474-X.

[97] AMS5663. Alloy BARS, Forg RINGS, Corros HEAT Resist Nickel Base - 19Cr - 31Mo - 51(Cb + Ta) - 090Ti - 050Al Solut Precip Heat Treat Consum Electrode or Vac Induction Melted 2016.

[98] Krupp U. Mikrostrukturelle Aspekte der Rissinitiierung und -ausbreitung in metallischen Werkstoffen. 2004.

[99] Lankford J. The growth of small fatigue cracks in 7075-T6 aluminum. Fatigue Eng Mater Struct 1982;5:233–48.

[100] Newman JC, Phillips EP, Swain MH. Fatigue-Life Prediction Methodology Using Small-Crack Theory. NASA Tech Memo 110307 1997.

[101] Miller KJ. The Two Thresholds of Fatigue Behaviour. Fatigue Fract Eng Mater Struct 1993;16:931–9. https://doi.org/10.1111/j.1460-2695.1993.tb00129.x.

[102] Parida BK. Fatigue Testing. Encycl. Mater. Sci. Technol., Elsevier; 2001, p. 2994–9. https://doi.org/10.1016/B0-08-043152-6/00533-7.

[103] ISO 12106. Met Mater — Fatigue Test — Axial-Strain-Controlled Method 2017.

[104] Fournier D, Pineau A. Low cycle fatigue behavior of inconel 718 at 298 K and 823 K. Metall Trans A 1977;8:1095–105. https://doi.org/10.1007/BF02667395.

[105] Xie JZ. Low Cycle Fatigue and Fatigue Crack Growth Behaviors of Alloy IN718 2012:491–500. https://doi.org/10.7449/1991/superalloys_1991_491_500.

[106] Sanders TH, Frishmuth RE, Embley GT. Temperature Dependent Deformation Mechanisms of Alloy 718 in Low Cycle Fatigue. Metall Trans A, Phys Metall Mater Sci 1981;12 A:1003–10. https://doi.org/10.1007/BF02643481.

[107] Vantadori S, Carpinteri A, Ronchei C, Scorza D, Zanichelli A. Mean stress effects on Low-Cycle Fatigue behaviour of Inconel 718 alloy. MATEC Web Conf 2019;300:15004. https://doi.org/10.1051/matecconf/201930015004.

[108] Bartošák M, Horváth J, Gálíková M, Slaný M, Šulák I. High-temperature low-cycle fatigue and fatigue–creep behaviour of Inconel 718 superalloy: Damage and deformation mechanisms. Int J Fatigue 2024;186:108369. https://doi.org/10.1016/j.ijfatigue.2024.108369.

[109] Xiao L, Chen DL, Chaturvedi MC. Low-cycle fatigue behavior of INCONEL 718 superalloy with different concentrations of boron at room temperature. Metall Mater Trans A Phys Metall Mater Sci 2005;36:2671–84. https://doi.org/10.1007/s11661-005-0264-3.

[110] Carpenter W, Kang BS-J, Chang KM. SAGBO Mechanism on High Temperature Cracking Behavior of Ni-base Superalloys 2012:679–88. https://doi.org/10.7449/1997/superalloys_1997_679_688.

[111] Pfaendtner JA, McMahon JJ. Oxygen-induced intergranular cracking of a Ni-base alloy at elevated temperatures - An example of dynamic embrittlement. Acta Mater 2001;49:3369–77. https://doi.org/10.1016/S1359-6454(01)00005-2.

[112] Vöse F, Becker M, Fischersworring-Bunk A, Hackenberg HP. An approach to life prediction for a nickel-base superalloy under isothermal and thermo-mechanical loading conditions. Int J Fatigue 2013;53:49–57. https://doi.org/10.1016/j.ijfatigue.2011.10.018.

[113] Rice JR, Rosengren GF. Plane strain deformation near a crack tip in a power-law hardening material. J Mech Phys Solids 1968;16:1–12. https://doi.org/10.1016/0022-5096(68)90013-6.

[114] Neumann P. New experiments concerning the slip processes at propagating fatigue cracks—I. Scr Metall 1974;8:xxi. https://doi.org/10.1016/0036-9748(74)90163-X.

[115] Laird C, Smith GC. Crack propagation in high stress fatigue. Philos Mag 1962;7:847–57. https://doi.org/10.1080/14786436208212674.

[116] Pelloux RMN. Crack extension by alternating shear. Eng Fract Mech 1970;1. https://doi.org/10.1016/0013-7944(70)90008-1.

[117] Riedel H. Fracture at High Temperatures. Berlin, Heidelberg: Springer Berlin Heidelberg; 1987. https://doi.org/10.1007/978-3-642-82961-1.

[118] Ramberg W, Osgood WR. Description of stress-strain curves by three parameters. Natl Advis Comm Aeronaut 1943:Technical Note No. 902.

[119] Hutchinson JW. Singular behaviour at the end of a tensile crack in a hardening material. J Mech Phys Solids 1968;16:13–31. https://doi.org/10.1016/0022-5096(68)90014-8.

[120] Kumar V, German MD, Shih CF. An Engineering Approach for Elastic-Plastic Fracture Analysis. Electr Power Res Inst EPRI NP 1981.

[121] He MY, Hutchinson JW. The penny-shaped crack and the plane strain crack in an infinite body of power-law material. J Appl Mech Trans ASME 1981;48:830–40. https://doi.org/10.1115/1.3157742.

[122] Shih CF. Relationship between the J-integral and the COD for stationary and extending cracks. J Mech Phys Solids 1981;29:305–26.

[123] Schweizer C, Seifert T, Nieweg B, Von Hartrott P, Riedel H. Mechanisms and modelling of fatigue crack growth under combined low and high cycle fatigue loading. Int J Fatigue 2011;33:194–202. https://doi.org/10.1016/j.ijfatigue.2010.08.008.

[124] Schlesinger M. Experimentelle Untersuchung des zeitabhängigen Rissfortschritts unter thermomechanischer Ermüdung in Nickellegierungen und mechanismenbasierte Modelle zur Lebensdauerbewertung. 2014.

[125] Paris P, Erdogan F. A Critical Analysis of Crack Propagation Laws. J Basic Eng 1963;85:528–33. https://doi.org/10.1115/1.3656900.

[126] Ritchie R. Mechanisms of fatigue-crack propagation in ductile and brittle solids. Int J Fract 1999;100:55–83. https://doi.org/https://doi.org/10.1023/A:1018655917051.

[127] Kiyak Y, Fedelich B, May T, Pfennig A. Simulation of crack growth under low cycle fatigue at high temperature in a single crystal superalloy. Eng Fract Mech 2008;75:2418–43. https://doi.org/10.1016/j.engfracmech.2007.08.002.

[128] Dowling NE, Begley JA. Fatigue Crack Growth During Gross Plasticity and the J-Integral. ASTM Spec Tech Publ 1976;STP 590:82–103. https://doi.org/10.1520/STP33940S.

[129] Wüthrich C. The extension of the J-integral concept to fatigue cracks. Int J Fract 1982;20:35–7. https://doi.org/10.1007/BF01141264.

[130] Schijve J. Some formulas for the crack opening stress level. Eng Fract Mech 1981;14:461–5. https://doi.org/10.1016/0013-7944(81)90034-5.

[131] Schweizer C. Physikalisch basierte Modelle für Ermüdungsrisswachstum und Anrisslebensdauer unter thermischen und mechanischen Belastungen 2013.

[132] Gangloff RP. Corrosion Fatigue Crack Propagation in Metals. NASA Contract Rep 4301 1990.

[133] Gangloff, Richard P.; Kim S-S. Environment Enhanced Fatigue Crack Propagation in Metals: Input to Fracture Mechanics Life Prediction Models 1993.

[134] Amaro RL, Drexler ES, Slifka AJ. Fatigue crack growth modeling of pipeline steels in high pressure gaseous hydrogen. Int J Fatigue 2014;62:249–57. https://doi.org/10.1016/j.ijfatigue.2013.10.013.

[135] Amaro RL, Rustagi N, Findley KO, Drexler ES, Slifka AJ. Modeling the fatigue crack growth of X100 pipeline steel in gaseous hydrogen. Int J Fatigue 2014;59:262–71. https://doi.org/10.1016/j.ijfatigue.2013.08.010.

[136] Austen IM. QUANTITATIVE ASSESSMENT OF CORROSION FATIGUE CRACK GROWTH UNDER VARIABLE AMPLITUDE LOADING. 1988.

[137] Schlesinger M, Seifert T, Preussner J. Experimental investigation of the time and temperature dependent growth of fatigue cracks in Inconel 718 and mechanism based lifetime prediction. Int J Fatigue 2017;99:242–9. https://doi.org/10.1016/j.ijfatigue.2016.12.015.

[138] Gérard O, Jaoul O. Oxygen diffusion in San Carlos olivine. J Geophys Res Solid Earth 1989;94:4119–28. https://doi.org/10.1029/JB094iB04p04119.

[139] Varias AG, Massih AR. Hydride-induced embrittlement and fracture in metals - Effect of stress and temperature distribution. J Mech Phys Solids 2002;50:1469–510. https://doi.org/10.1016/S0022-5096(01)00117-X.

[140] Serebrinsky S, Carter EA, Ortiz M. A quantum-mechanically informed continuum model of hydrogen embrittlement. J Mech Phys Solids 2004;52:2403–30. https://doi.org/10.1016/j.jmps.2004.02.010.

[141] Ahn DC, Sofronis P, Dodds R. Modeling of hydrogen-assisted ductile crack propagation in metals and alloys. Int J Fract 2007;145:135–57. https://doi.org/10.1007/s10704-007-9112-3.

[142] Ahn DC, Sofronis P, Dodds RH. On hydrogen-induced plastic flow localization during void growth and coalescence. Int J Hydrogen Energy 2007;32:3734–42. https://doi.org/10.1016/j.ijhydene.2006.08.047.

[143] Olden V, Thaulow C, Johnsen R, Østby E. Cohesive zone modeling of hydrogen-induced stress cracking in 25% Cr duplex stainless steel. Scr Mater 2007;57:615–8. https://doi.org/10.1016/j.scriptamat.2007.06.006.

[144] Olden V, Thaulow C, Johnsen R. Modelling of hydrogen diffusion and hydrogen induced cracking in supermartensitic and duplex stainless steels. Mater Des 2008;29:1934–48. https://doi.org/10.1016/j.matdes.2008.04.026.

[145] Olden V, Alvaro A, Akselsen OM. Hydrogen diffusion and hydrogen influenced critical stress intensity in an API X70 pipeline steel welded joint-Experiments and FE simulations. Int J Hydrogen Energy 2012;37:11474–86. https://doi.org/10.1016/j.ijhydene.2012.05.005.

[146] Olden V, Thaulow C, Johnsen R, Østby E, Berstad T. Influence of hydrogen from cathodic protection on the fracture susceptibility of 25%Cr duplex stainless steel - Constant load SENT testing and FE-modelling using hydrogen influenced cohesive zone elements. Eng Fract Mech 2009;76:827–44. https://doi.org/10.1016/j.engfracmech.2008.11.011.

[147] Olden V, Thaulow C, Johnsen R, Østby E, Berstad T. Application of hydrogen influenced cohesive laws in the prediction of hydrogen induced stress cracking in 25%Cr duplex stainless steel. Eng Fract Mech 2008;75:2333–51. https://doi.org/10.1016/j.engfracmech.2007.09.003.

[148] Dadfarnia M, Somerday BP, Schembri PE, Sofronis P, Foulk JW, Nibur KA, et al. On modeling hydrogen-induced crack propagation under sustained load. Jom 2014;66:1390–8. https://doi.org/10.1007/s11837-014-1050-8.

[149] Dadfarnia M, Somerday BP, Foulk JW, Balch DK, Sofronis P, Nibur KA, et al. Modeling Hydrogen-Induced Fracture and Crack Propagation in High Strength Steels. Int Hydrog Conf (IHC 2016) Mater Perform Hydrog Environ 2017:572–80. https://doi.org/10.1115/1.861387_ch65.

[150] Hosseini ZS, Dadfarnia M, Kubota M, Nagao A, Somerday BP, Sofronis P, et al. Mechanistic model for hydrogen accelerated fatigue crack growth in a low carbon steel. Int J Hydrogen Energy 2024. https://doi.org/10.1016/j.ijhydene.2024.05.351.

[151] Stark A, Sonnweber-Ribic P, Elsässer C. Theoretical study of individual and combined effects of HELP- and HEDE-based damage models on the fatigue behavior of ferritic steel by hydrogen. Int J Hydrogen Energy 2025;109:27–39. https://doi.org/10.1016/j.ijhydene.2025.01.459.

[152] Kumar R, Mahajan DK. Modelling of hydrogen-assisted damage at the deforming single crystal crack-tip. Mech Mater 2023;178:104557. https://doi.org/10.1016/j.mechmat.2023.104557.

[153] Yuan S, Zhu Y, Huang M, Liang S, Li Z. Dislocation-density based crystal plasticity model with hydrogen-enhanced localized plasticity in polycrystalline face-centered cubic metals. Mech Mater 2020;148:103472. https://doi.org/10.1016/j.mechmat.2020.103472.

[154] Lucarini S, Dunne FPE, Martínez-Pañeda E. An FFT-based crystal plasticity phase-field model for micromechanical fatigue cracking based on the stored energy density. Int J Fatigue 2023;172:107670. https://doi.org/10.1016/j.ijfatigue.2023.107670.

[155] Martínez-Pañeda E, Golahmar A, Niordson CF. A phase field formulation for hydrogen assisted cracking. Comput Methods Appl Mech Eng 2018;342:742–61. https://doi.org/10.1016/j.cma.2018.07.021.

[156] Díaz A, Alegre JM, Cuesta I, Martínez-Pañeda E. A COMSOL framework for predicting hydrogen embrittlement-Part II: phase field fracture. Eng Fract Mech 2025;319:111008. https://doi.org/10.1016/j.engfracmech.2025.111008.

[157] Cui C, Bortot P, Ortolani M, Martínez-Pañeda E. Computational predictions of hydrogen-assisted fatigue crack growth. Int J Hydrogen Energy 2024;72:315–25. https://doi.org/10.1016/j.ijhydene.2024.05.264.

[158] Mandal TK, Parker J, Gagliano M, Martínez-Pañeda E. Computational predictions of weld structural integrity in hydrogen transport pipelines. Int J Hydrogen Energy 2024. https://doi.org/10.1016/j.ijhydene.2024.01.258.

[159] Fukai Y, Sugimoto H. Diffusion of hydrogen in metals. Adv Phys 1985;34:263–326. https://doi.org/10.1080/00018738500101751.

[160] Clapeyron PE. Puissance motrice de la chaleur. J Chem Educ 1934:351–4.

[161] Zucker RD, Biblarz O. FUNDAMENTALS OF GAS DYNAMICS. vol. 17. 2019.

[162] NIST Reference Fluid Thermodynamic and Transport Properties Database (REFPROP): Version 8.0 n.d.

[163] Chenoweth DR. Gas-transfer analysis. Section H - real gas results via the van der Waals equation of state and virial expansion extension of its limiting Abel-Noble form. Sandia Rep SAND83-8229 1983:87.

[164] Enkenhus KR. On the Pressure Decay Rate in the Longshot Reservoir. Von Karman Inst Fluid Dyn Tech Note 40, Rhode- Saint-Genese, Belgium 1967.

[165] San Marchi C, Somerday BP, Robinson SL. Permeability, solubility and diffusivity of hydrogen isotopes in stainless steels at high gas pressures. Int J Hydrogen Energy 2007;32:100–16. https://doi.org/10.1016/j.ijhydene.2006.05.008.

[166] Gangloff RP, Somerday BP. Gaseous hydrogen embrittlement of materials in energy technologies Volume 1: The problem, its characterisation and effects on particular alloy classes. vol. 1. Woodhead Publishing Limited; 2012.

[167] Pundt A, Wagner S. Hydrogen Interactions with Defects in Materials. Chemie-Ingenieur-Technik 2024:1–11. https://doi.org/10.1002/cite.202300235.

[168] Komoda R, Kubota M, Staykov A, Ginet P, Barbier F, Furtado J. Inhibitory effect of oxygen on hydrogen-induced fracture of A333 pipe steel. Fatigue Fract Eng Mater Struct 2019;42:1387–401. https://doi.org/10.1111/ffe.12994.

[169] Jewet RP, Walter RJ, Chandler WT, Frohmberg RP. HYDROGEN ENVIRONMENT EMBRITTLEMENT OF METALS. NASA Contract Rep CR-2163 1973.

[170] Kussmaul K, Deimel P, Fischer H, Sattler E. Fracture mechanical behaviour of the steel 15 MnNi 6 3 in argon and in high pressure hydrogen gas with admixtures of oxygen. Int J Hydrogen Energy 1998;23:577–82. https://doi.org/10.1016/s0360-3199(97)00104-3.

[171] Somerday BP, Sofronis P, Nibur KA, San Marchi C, Kirchheim R. Elucidating the variables affecting accelerated fatigue crack growth of steels in hydrogen gas with low oxygen concentrations. Acta Mater 2013;61:6153–70. https://doi.org/10.1016/j.actamat.2013.07.001.

[172] Staykov A, Yamabe J, Somerday BP. Effect of hydrogen gas impurities on the hydrogen dissociation on iron surface. Int J Quantum Chem 2014;114:626–35. https://doi.org/10.1002/qua.24633.

[173] Komoda R, Yamada K, Kubota M, Ginet P, Barbier F, Furtado J, et al. The inhibitory effect of carbon monoxide contained in hydrogen gas environment on hydrogen-accelerated fatigue crack growth and its loading frequency dependency. Int J Hydrogen Energy 2019;44:29007–16. https://doi.org/10.1016/j.ijhydene.2019.09.146.

[174] Rönnebro ECE, Oelrich RL, Gates RO. Recent Advances and Prospects in Design of Hydrogen Permeation Barrier Materials for Energy Applications—A Review. Molecules 2022;27. https://doi.org/10.3390/molecules27196528.

[175] Bonzel HP. Kinetic Processes on Well-Characterized Metal Surfaces. 1977;1:691–702.

[176] Christmann K. INTERACTION OF HYDROGEN WITH SOLID SURFACES. vol. 9. 1988.

[177] Bozso F, Ertl G, Grunze M, Weiss M. Chemisorption of hydrogen on iron surfaces. Appl Surf Sci 1977;1:103–19. https://doi.org/10.1016/0378-5963(77)90009-5.

[178] Christmann K, Schober O, Ertl G, Neumann M. Adsorption of hydrogen on nickel single crystal surfaces. J Chem Phys 1974;4540:4528–40. https://doi.org/10.1063/1.1680935.

[179] Christmann K. Adsorption of Hydrogen on a Nickel (100) Surface. Zeitschrift Fur Naturforsch - Sect A J Phys Sci 1979;34:22–9. https://doi.org/10.1515/zna-1979-0105.

[180] Koren E, M. H. Hagen C, Wang D, Lu X, Johnsen R, Yamabe J. Experimental comparison of gaseous and electrochemical hydrogen charging in X65 pipeline steel using the permeation technique. Corros Sci 2023;215. https://doi.org/10.1016/j.corsci.2023.111025.

[181] Kumnick AJ, Johnson HH. Steady State Hydrogen Transport Through Zone Refined Irons 1975;6:1087–91.

[182] Miller RF, Hudson JB, Ansell GS. Permeation of hydrogen through alpha iron. Metall Trans A 1975;6:117–21. https://doi.org/10.1007/BF02673678.

[183] Otsuka T, Shinohara M, Horinouchi H, Tanabe T. Hydrogen permeation in iron and nickel alloys around room temperature. J Nucl Mater 2013;442:S726–9. https://doi.org/10.1016/j.jnucmat.2013.04.021.

[184] Ikeda T, Otsuka T, Tanabe T. Hydrogen permeation in metals near room temperature by a tritium tracer technique. J Nucl Mater 2011;417:568–71. https://doi.org/10.1016/j.jnucmat.2010.12.116.

[185] Fick A. Ueber Diffusion. Ann Phys 1855;170:59–86. https://doi.org/10.1002/andp.18551700105.

[186] Fourier JBJ. Théorie analytique de la chaleur. 1822.

[187] Sieverts A. Palladium und Wasserstoff. II. Zeitschrift Für Phys Chemie 1914;88U:451–78. https://doi.org/10.1515/zpch-1914-8832.

[188] Nagumo M. Fundamentals of hydrogen embrittlement. 2016. https://doi.org/10.1007/978-981-10-0161-1.

[189] Xu J, Sun XK, Liu QQ, Chen WX. Hydrogen permeation behavior in IN718 and GH761 superalloys. Metall Mater Trans A 1994;25:539–44. https://doi.org/10.1007/BF02651595.

[190] Wriedt H., Oriani R. Effect of tensile and compressive elastic stress on equilibrium hydrogen solubility in a solid. Acta Metall 1970;18:753–60. https://doi.org/10.1016/0001-6160(70)90039-8.

[191] Van Leeuwen HP. The kinetics of hydrogen embrittlement: A quantitative diffusion model. Eng Fract Mech 1974;6:141–61. https://doi.org/10.1016/0013-7944(74)90053-8.

[192] Bogkris JOM, Beck W, Genshaw MA, Subramanyan PK, Williams FS. The effect of stress on the chemical potential of hydrogen in iron and steel. Acta Metall 1971;19:1209–18. https://doi.org/10.1016/0001-6160(71)90054-X.

[193] Hirth JP. Effects of hydrogen on the properties of iron and steel. Metall Trans A 1980;11:861–90. https://doi.org/10.1007/BF02654700.

[194] Baranowski B, Majchrzak S, Flanagan TB. The volume increase of fcc metals and alloys due to interstitial hydrogen over a wide range of hydrogen contents. J Phys F Met Phys 1971;1:258–61. https://doi.org/10.1088/0305-4608/1/3/307.

[195] Flanagan TB, Oates WA. Thermodynamics of metal/hydrogen systems. Berichte Der Bunsengesellschaft Für Phys Chemie 1972;76:706–14. https://doi.org/10.1002/bbpc.19720760804.

[196] Crank J. The Mathematics of Diffusion. J Am Chem Soc 1975;79:1267–8. https://doi.org/10.1021/ja01562a072.

[197] Lee JY, Lee JL, Choo WY. Thermal Analysis of Trapped Hydrogen in Aisi 4340 Steel. 1982;13:423–7.

[198] Oriani RA. The diffusion and trapping of hydrogen in steel. Acta Metall 1970;18:147–57. https://doi.org/10.1016/0001-6160(70)90078-7.

[199] Kissinger HE. Reaction Kinetics in Differential Thermal Analysis. Anal Chem 1957;29:1702–6. https://doi.org/10.1021/ac60131a045.

[200] Woodtli J, Kieselbach R. Damage due to hydrogen embrittlement and stress corrosion cracking. Eng Fail Anal 2000;7:427–50. https://doi.org/10.1016/S1350-6307(99)00033-3.

[201] Lynch S. Hydrogen embrittlement phenomena and mechanisms. Corros Rev 2012;30:105–23. https://doi.org/10.1515/corrrev-2012-0502.

[202] Schöneich H-G. Considerations on the Risk of Hydrogen Embrittlement of Pipeline Steel due to Cathodic Overprotection 2015;5:1–15.

[203] Kim CM, Kim WS, Kho YT. The effects of hydrogen embrittlement by cathodic protection on the CTOD of buried natural gas pipeline. Met Mater Int 2002;8:197–202. https://doi.org/10.1007/bf03027018.

[204] Ronevich JA, Somerday BP, San Marchi CW. Effects of microstructure banding on hydrogen assisted fatigue crack growth in X65 pipeline steels. Int J Fatigue 2016;82:497–504. https://doi.org/10.1016/j.ijfatigue.2015.09.004.

[205] Slifka AJ, Drexler ES, Amaro RL, Hayden LE, Stalheim DG, Lauria DS, et al. Fatigue measurement of pipeline steels for the application of transporting gaseous hydrogen. J Press Vessel Technol Trans ASME 2018;140:1–12. https://doi.org/10.1115/1.4038594.

[206] Ogawa Y, Takakuwa O, Okazaki S, Funakoshi Y, Matsuoka S, Matsunaga H. Hydrogen-assisted fatigue crack-propagation in a Ni-based superalloy 718, revealed via crack-path crystallography and deformation microstructures. Corros Sci 2020;174:108814. https://doi.org/10.1016/j.corsci.2020.108814.

[207] Li X, Ma X, Zhang J, Akiyama E, Wang Y, Song X. Review of Hydrogen Embrittlement in Metals : Hydrogen Diffusion , Hydrogen Characterization , Hydrogen Embrittlement Mechanism and Prevention. Acta Metall Sin (English Lett 2020;33:759–73. https://doi.org/10.1007/s40195-020-01039-7.

[208] Lee JA. Hydrogen Embrittlement. 2016. https://doi.org/10.1016/B978-044452787-5.00200-6.

[209] Tarzimoghadam Z, Ponge D, Klöwer J, Raabe D. Hydrogen-assisted failure in Ni-based superalloy 718 studied under in situ hydrogen charging: The role of localized deformation in crack propagation. Acta Mater 2017;128:365–74. https://doi.org/10.1016/j.actamat.2017.02.059.

[210] Hicks PD, Altstetter CJ. Comparison of Internal Hydrogen Embrittlement of Superalloys 718 and 625 1991:635–51. https://doi.org/10.7449/1991/superalloys_1991_635_651.

[211] Zhang Z, Obasis G, Morana R, Preuss M. Hydrogen assisted crack initiation and propagation in a nickel-based superalloy. Acta Mater 2016;113:272–83. https://doi.org/10.1016/j.actamat.2016.05.003.

[212] Tarzimoghadam Z, Rohwerder M, Merzlikin S V., Bashir A, Yedra L, Eswara S, et al. Multi-scale and spatially resolved hydrogen mapping in a Ni-Nb model alloy reveals the role of the δ phase in hydrogen embrittlement of alloy 718. Acta Mater 2016;109:69–81. https://doi.org/10.1016/j.actamat.2016.02.053.

[213] Dutton R, Nuttall K, Puls MP, Simpson LA. Mechanisms of Hydrogen Induced Delayed Cracking in Hydride Forming Materials. Met Trans A 1977;8 A:1553–62. https://doi.org/10.1007/BF02644858.

[214] Poorhaydari K. A Comprehensive Examination of High-Temperature Hydrogen Attack—A Review of over a Century of Investigations. J Mater Eng Perform 2021;30:7875–908. https://doi.org/10.1007/s11665-021-06045-z.

[215] Lee JA. Hydrogen embrittlement of nickel, cobalt and iron-based superalloys. Gaseous Hydrog. embrittlement Mater. energy Technol. Vol. 1 Probl. its characterisation Eff. Part. Alloy classes, 2012, p. 624–67. https://doi.org/10.1533/9780857093899.3.624.

[216] Pfeil LB. The effect of occluded hydrogen on the tensile strength of iron. Proc R Soc London Ser A, Contain Pap a Math Phys Character 1926;112:182–95. https://doi.org/10.1098/rspa.1926.0103.

[217] Troiano AR. The Role of Hydrogen and Other Interstitials in the Mechanical Behavior of Metals. Trans Am Soc Met 1960;52:54–80. https://doi.org/10.1007/s13632-016-0319-4.

[218] Guzmán AA, Jeon J, Hartmaier A, Janisch R. Hydrogen embrittlement at cleavage planes and grain boundaries in bcc iron—revisiting the first-principles cohesive zone model. Materials (Basel) 2020;13:1–16. https://doi.org/10.3390/ma13245785.

[219] Smith RW, Was GS. Application of molecular dynamics to the study of hydrogen embrittlement in Ni-Cr-Fe alloys. Phys Rev B 1989;40:10322–36. https://doi.org/10.1103/PhysRevB.40.10322.

[220] Wei X, Dong C, Chen Z, Xiao K, Li X. The effect of hydrogen on the evolution of intergranular cracking: A cross-scale study using first-principles and cohesive finite element methods. RSC Adv 2016;6:27282–92. https://doi.org/10.1039/c5ra26061b.

[221] Yoshino K, McMahon CJ. The cooperative relation between temper embrittlement and hydrogen embrittlement in a high strength steel. Metall Trans 1974;5:363–70. https://doi.org/10.1007/BF02644103.

[222] Beachem CD. A new model for hydrogen-assisted cracking (hydrogen "embrittlement"). Metall Trans 1972;3:441–55. https://doi.org/10.1007/BF02642048.

[223] Birnbaum HK. MECHANISMS OF HYDROGEN RELATED FRACTURE OF METALS. vol. University. 1989.

[224] Lynch SP. Environmentally assisted cracking: Overview of evidence for an adsorption-induced localised-slip process. Acta Metall 1988;36:2639–61. https://doi.org/10.1016/0001-6160(88)90113-7.

[225] Maxelon M, Pundt A, Pyckhout-Hintzen W, Kirchheim R. Small angle neutron scattering of hydrogen segregation at dislocations in palladium. Scr Mater 2001;44:817–22. https://doi.org/10.1016/S1359-6462(00)00654-0.

[226] Birnbaum HK, Sofronis P. Hydrogen-enhanced localized plasticity—a mechanism for hydrogen-related fracture. Mater Sci Eng A 1994;176:191–202. https://doi.org/10.1016/0921-5093(94)90975-X.

[227] Michler T, Schweizer F, Wackermann K. Review on the Influence of Temperature upon Hydrogen Effects in Structural Alloys. Metals (Basel) 2021;11:423. https://doi.org/10.3390/met11030423.

[228] Hasan MS, Kapci MF, Bal B, Koyama M, Bayat H, Xu W. An atomistic study on the HELP mechanism of hydrogen embrittlement in pure metal Fe. Int J Hydrogen Energy 2024;57:60–8. https://doi.org/10.1016/j.ijhydene.2023.12.274.

[229] Singh V, Kumar R, Charles Y, Mahajan DK. Coupled diffusion-mechanics framework for simulating hydrogen assisted deformation and failure behavior of metals. Int J Plast 2022;157:103392. https://doi.org/10.1016/j.ijplas.2022.103392.

[230] Chandler WT. Hydrogen Embrittlement and Its Control in Hydrogen-Fueled Engine Systems. NASA Conf Publ 1978;27980:195–249.

[231] Ebling F, Michler T. Permeability, solubility and diffusivity of hydrogen in alloy 718. Materwiss Werksttech 2025;56:575–80. https://doi.org/10.1002/mawe.202400192.

[232] Jebaraj JJM, Morrison DJ, Suni II. Hydrogen diffusion coefficients through Inconel 718 in different metallurgical conditions. Corros Sci 2014;80:517–22. https://doi.org/10.1016/j.corsci.2013.11.002.

[233] Khalid H, Shunmugasamy VC, DeMott RW, Hattar K, Mansoor B. Effect of grain size and precipitates on hydrogen embrittlement susceptibility of nickel alloy 718. Int J Hydrogen Energy 2024;55:474–90. https://doi.org/10.1016/j.ijhydene.2023.11.233.

[234] Walter RJ, Chandler WT. Influence Of Gaseous Hydrogen On Metals. Nasa-Cr-124410 1973:1–169.

[235] Xing X, Cheng R, Cui G, Liu J, Gou J, Yang C, et al. Quantification of the temperature threshold of hydrogen embrittlement in X90 pipeline steel. Mater Sci Eng A 2021;800:140118. https://doi.org/10.1016/j.msea.2020.140118.

[236] Borchers C, Michler T, Pundt A. Effect of hydrogen on the mechanical properties of stainless steels. Adv Eng Mater 2008;10:11–23. https://doi.org/10.1002/adem.200700252.

[237] Frick N V., Janser GR, Brown JA. Enhanced Flaw Growth in SSME Alloys in High Pressure Gaseous Hydrogen. Sp Shuttle Mater 1971;3:597–608.

[238] Moody NR, Perra MW, Robinson SL. HYDROGEN PRESSURE AND CRACK TIP STRESS EFFECTS ON SLOW CRACK GROWTH THRESHOLDS IN AN IRON-BASED SUPERALLOY. Scr Metall 1988;22:1261–6.

[239] Michler T, Wackermann K, Schweizer F. Review and Assessment of the Effect of Hydrogen Gas Pressure on the Embrittlement of Steels in Gaseous Hydrogen Environment. Metals (Basel) 2021;11:637. https://doi.org/10.3390/met11040637.

[240] Depover T, Elmahdy A, Vercruysse F, Verleysen P, Verbeken K. Effect of strain rate on the hydrogen embrittlement of a DP steel. EPJ Web Conf 2018;183:1–6. https://doi.org/10.1051/epjconf/201818303015.

[241] Michler T, Lindner M, Eberle U, Meusinger J. Assessing hydrogen embrittlement in automotive hydrogen tanks. Gaseous Hydrog Embrittlement Mater Energy Technol Probl Its Characterisation Eff Part Alloy Classes 2012:94–125. https://doi.org/10.1533/9780857093899.1.94.

[242] Vesely EJ, Jacobs RK, Watwood MC, McPherson WB. Influence of strain rate on tensile properties in high-pressure hydrogen. Hydrog Eff Mater 1996:363–74. https://doi.org/10.1002/9781118803363.ch34.

[243] Liu L, Tanaka K, Hirose A, Kobayashi KF. Effects of precipitation phases on the hydrogen embrittlement sensitivity of inconel 718. Sci Technol Adv Mater 2002;3:335–44. https://doi.org/10.1016/S1468-6996(02)00039-6.

[244] Yoo J, Kim S, Cheol M, Park H. Investigation of hydrogen embrittlement properties of Ni-based alloy 718 fabricated via laser powder bed fusion. Int J Hydrogen Energy 2022;47:18892–910. https://doi.org/10.1016/j.ijhydene.2022.04.045.

[245] ELTRA. Bedienungsanleitung OH-900 2002.

[246] Lee HG, Lee J-Y. Hydrogen trapping by TiC particles in iron. Acta Metall 1984;32:131–6. https://doi.org/10.1016/0001-6160(84)90210-4.

[247] Rezende MC, Araujo LS, Gabriel SB, Dos Santos DS, De Almeida LH. Hydrogen embrittlement in nickel-based superalloy 718: Relationship between γ' + γ'' precipitation and the fracture mode. Int J Hydrogen Energy 2015;40:17075–83. https://doi.org/10.1016/j.ijhydene.2015.07.053.

[248] Robertson WM. Hydrogen Permeation and Diffusion in Inconel 718 and Incoloy 903. Metall Trans A 1977;8A:1709–12.

[249] Gröner L, Mengis L, Galetz M, Kirste L, Daum P, Wirth M, et al. Investigations of the Deuterium Permeability of As-Deposited and Oxidized Ti2AlN Coatings. Materials (Basel) 2020;13:2085. https://doi.org/10.3390/ma13092085.

[250] Egerton RF. Physical Principles of Electron Microscopy. 2016. https://doi.org/10.1007/978-3-319-39877-8.

[251] Levine E, Bell WL, Thomas G. Further applications of Kikuchi diffraction patterns; Kikuchi maps. J Appl Phys 1966;37:2141–8. https://doi.org/10.1063/1.1708749.

[252] Shen RR, Ström V, Efsing P. Spatial correlation between local misorientations and nanoindentation hardness in nickel-base alloy 690. Mater Sci Eng A 2016;674:171–7. https://doi.org/10.1016/j.msea.2016.07.123.

[253] Kamaya M. Assessment of local deformation using EBSD: Quantification of accuracy of measurement and definition of local gradient. Ultramicroscopy 2011;111:1189–99. https://doi.org/10.1016/j.ultramic.2011.02.004.

[254] Sáez-Maderuelo A, Castro L, De Diego G. Plastic strain characterization in austenitic stainless steels and nickel alloys by electron backscatter diffraction. J Nucl Mater 2011;416:75–9. https://doi.org/10.1016/j.jnucmat.2010.11.092.

[255] ASTM G129-00. Pract Slow Strain Rate Test to Eval Susceptibility Met Mater to Environ Assist Cracking, ASTM Int 2013. https://doi.org/10.1520/G0129-00R13.

[256] ASTM G142 – 98. Stand Test Method Determ Susceptibility Met to Embrittlement Hydrog Contain Environ High Press High Temp or Both 2011. https://doi.org/10.1520/G0142-98R11.

[257] ANSI/CSA CHMC 1. ANSI/CSA CHMC 1 - 2014: Test Method for Evaluating Material Compatibility in Compressed Hydrogen Applications - Metals. CSA Gr 2014:2014.

[258] E606/E606M − 12. Test Method Strain-Controlled Fatigue Testing, ASTM Stand E606 2004;92:1–16. https://doi.org/10.1520/E0606-04E01.

[259] Fandiño D, Guski V, Wegert R, Schmauder S, Möhring HC. Numerical Investigations on Single Lip Deep Hole Drilling. Procedia CIRP 2021;102:132–7. https://doi.org/10.1016/j.procir.2021.09.023.

[260] Biermann D, Kirschner M. Experimental investigations on single-lip deep hole drilling of superalloy Inconel 718 with small diameters. J Manuf Process 2015;20:332–9. https://doi.org/10.1016/j.jmapro.2015.06.001.

[261] Nickel J, Baak N, Walther F, Biermann D. Investigation of the thermomechanical loads on the bore surface during single-lip deep hole drilling of steel components. Procedia CIRP 2022;108:805–10. https://doi.org/10.1016/j.procir.2022.03.125.

[262] Baak N, Nickel J, Biermann D, Walther F. Microstructure analysis of single-lip deep hole drilled bores by electron backscatter diffraction and magnetic Barkhausen noise. Procedia CIRP 2022;108:740–5. https://doi.org/10.1016/j.procir.2022.03.114.

[263] Nickel J, Baak N, Biermann D, Walther F. Influence of the deep hole drilling process and sulphur content on the fatigue strength of AISI 4140 steel components. Procedia CIRP 2018;71:209–14. https://doi.org/10.1016/j.procir.2018.05.069.

[264] Singh A, Ghosh A. A thermo-electric model of material removal during electric discharge machining. Int J Mach Tools Manuf 1999;39:669–82. https://doi.org/10.1016/S0890-6955(98)00047-9.

[265] Antar M, Hayward P, Dunleavey J, Butler-Smith P. Surface Integrity Evaluation of Modified EDM Surface Structure. Procedia CIRP 2018;68:308–12. https://doi.org/10.1016/j.procir.2017.12.069.

[266] Mercer J. EDM Effect on Surface Integrity. Spec Chem Eng Mater 2008.

[267] Steuer P, Rebschläger A, Weber O, Bähre D. The heat-affected zone in EDM and its influence on a following PECM process. Procedia CIRP 2014;13:276–81. https://doi.org/10.1016/j.procir.2014.04.047.

[268] Shokrollahi N, Shabgard M, Jahani K. Effects of honing process parameters on residual stress fields of grey cast iron engine cylinder liners: Experimental and numerical study. Proc Inst Mech Eng Part C J Mech Eng Sci 2023;237:3871–82. https://doi.org/10.1177/09544062231152133.

[269] Leveille T, Granier C, Valiorgue F, Pascal H, Rech J, Van-Robaeys A, et al. Characterization of residual stresses induced by a multistep hole making sequence. Procedia CIRP 2021;102:477–81. https://doi.org/10.1016/j.procir.2021.09.081.

[270] Leveille T, Valiorgue F, Dumas M, Masciantonio U, Brosse A, Karaouni H, et al. 3D numerical modelling of residual stresses induced by reaming. J Manuf Process 2024;113:47–60. https://doi.org/10.1016/j.jmapro.2024.01.050.

[271] Dixit N, Sharma V, Kumar P. Research trends in abrasive flow machining: A systematic review. J Manuf Process 2021;64:1434–61. https://doi.org/10.1016/j.jmapro.2021.03.009.

[272] Schoenborn S, Melz T, Baumgartner J, Bleicher C. Influence of compressed hydrogen on the fatigue behavior of a ferritic stainless steel. Procedia Struct Integr 2021;33:757–64. https://doi.org/10.1016/j.prostr.2021.10.083.

[273] Ebling F, Bratsch P, Wagner S, Pundt A, Preußner J, Oesterlin H, et al. Assessing hydrogen embrittlement of alloy 718: Hollow and conventional tensile tests. Eng Fract Mech 2025;319:111028. https://doi.org/10.1016/j.engfracmech.2025.111028.

[274] Antty I. Werkstoffqualifizierung von additiv gefertigten Werkstoffen für Anwendungen mit gasförmigem Wasserstoff. 2021.

[275] ASTM E466 − 07. Stand Pract Conduct Force Control Constant Amplitude Axial Fatigue Tests Met Mater 2007;03:4–8. https://doi.org/10.1520/E0466-07.

[276] Thomas A, Szpunar JA. Effect of cold-rolling on hydrogen diffusion and trapping in X70 pipeline steel. J Eng Mater Technol Trans ASME 2021;143:1–13. https://doi.org/10.1115/1.4049320.

[277] Daynes HA. The process of diffusion through a rubber membrane. Proc R Soc London Ser A, Contain Pap a Math Phys Character 1920;97:286–307. https://doi.org/10.1098/rspa.1920.0034.

[278] Lin J, Chen F, Liu F, Xu D, Gao J, Tang X. Hydrogen permeation behavior and hydrogen-induced defects in 316L stainless steels manufactured by additive manufacturing. Mater Chem Phys 2020;250:123038. https://doi.org/10.1016/j.matchemphys.2020.123038.

[279] Ogawa Y, Takakuwa O, Okazaki S, Okita K, Funakoshi Y, Matsunaga H, et al. Pronounced transition of crack initiation and propagation modes in the hydrogen-related failure of a Ni-based superalloy 718 under internal and external hydrogen conditions. Corros Sci 2019;161:108186. https://doi.org/10.1016/j.corsci.2019.108186.

[280] Maksimkin IP, Yukhimchuk AA, Malkov IL, Boitsov IE, Musyaev RK, Buchirin A V., et al. Effect of Hydrogen on the Structure and Mechanical Properties of 316L Steel and Inconel 718 Alloy Processed by Selective Laser Melting. Materials (Basel) 2022;15. https://doi.org/10.3390/ma15144806.

[281] Turnbull A, Ballinger RG, Hwang IS, Morra MM, Gates RM. Hydrogen Transport in Nickel-Base Alloys 1992;23.

[282] Lee S man, Lee JY. Hydrogen trapping in thoria-dispersed nickel. Metall Trans A 1989;20:2483–8. https://doi.org/10.1007/BF02666683.

[283] Robertson WM. Measurement and evaluation of hydrogen trapping in thoria dispersed nickel. Metall Trans A 1979;10:489–501. https://doi.org/10.1007/BF02697077.

[284] Lee SM, Lee JY. Hydrogen trapping by voids in nickel. Scr Metall 1987;21:1655–8. https://doi.org/10.1016/0036-9748(87)90152-9.

[285] Symons DM, Young GA, Scully JR. The effect of strain on the trapping of hydrogen at grain-boundary carbides in Ni-Cr-Fe alloys. Metall Mater Trans A Phys Metall Mater Sci 2001;32:369–77. https://doi.org/10.1007/s11661-001-0268-6.

[286] Lassila DH, Birnbaum HK. The effect of diffusive segregation on the fracture of hydrogen charged nickel. Acta Metall 1988;36:2821–5. https://doi.org/10.1016/0001-6160(88)90128-9.

[287] Yao J, Meguid SA. Hydrogen diffusion and intergranular cracking in nickel. Int J Hydrogen Energy 1997;22:1021–6. https://doi.org/10.1016/S0360-3199(97)00001-3.

[288] Lee SM, Lee JY. The Trapping and Transport Phenomena of Hydrogen in Nickel. Metall Trans A, Phys Metall Mater Sci 1986;17 A:181–7. https://doi.org/10.1007/BF02643893.

[289] Hagi H, Hayashi Y. Effect of Dislocation Trapping on Hydrogen and Deuterium Diffusion in Iron. Trans Japan Inst Met 1987;28:368–74. https://doi.org/10.2320/matertrans1960.28.368.

[290] Boniszewski T, Smith GC. The influence of hydrogen on the plastic deformation ductility, and fracture of nickel in tension. Acta Metall 1963;11:165–78. https://doi.org/10.1016/0001-6160(63)90209-8.

[291] Blakemore JS. The Portevin-Le Chatelier Effect in hydrogenated nickel. Metall Trans 1970;1:145–9. https://doi.org/10.1007/BF02819254.

[292] Young GA, Richey E, Morton DS. Hydrogen embrittlement in nuclear power systems. Gaseous Hydrog. Embrittlement Mater. Energy Technol., Elsevier; 2012, p. 149–76. https://doi.org/10.1533/9780857093899.1.149.

[293] ISO/FDIS 7039. Met Mater — Tensile Test — Method Eval Susceptibility Mater to Eff High-Pressure Gas within Hollow Test Pieces 2024.

[294] Nanninga NE, Levy YS, Drexler ES, Condon RT, Stevenson AE, Slifka AJ. Comparison of hydrogen embrittlement in three pipeline steels in high pressure gaseous hydrogen environments. Corros Sci 2012;59:1–9. https://doi.org/10.1016/j.corsci.2012.01.028.

[295] Hagen AB, Alvaro A. Hydrogen Influence on Mechanical Properties in Pipeline Steel - state of the art. SINTEF Industry - Materials Integrity and Welding. 2020.

[296] Michler T, Ebling F, Oesterlin H, Fischer C, Wackermann K. Comparison of tensile properties of X60 pipeline steel tested in high pressure gaseous hydrogen using tubular and conventional specimen. Int J Hydrogen Energy 2022;47:34676–88. https://doi.org/10.1016/j.ijhydene.2022.07.211.

[297] El-Yazgi AA, Hardie D. The embrittlement of a duplex stainless steel by hydrogen in a variety of environments. Corros Sci 1996;38:735–44. https://doi.org/10.1016/0010-938X(95)00162-D.

[298] Haynes WM. CRC Handbook of Chemistry and Physics. 97th ed. CRC Press; 2016.

[299] Michler T, Boitsov IE, Malkov IL, Yukhimchuk AA, Naumann J. Assessing the effect of low oxygen concentrations in gaseous hydrogen embrittlement of DIN 1.4301 and 1.1200 steels at high gas pressures. Corros Sci 2012;65:169–77. https://doi.org/10.1016/j.corsci.2012.08.015.

[300] Ogata T, Ono Y. Influence of roughness of inner surface of simple mechanical testing method to evaluate influence of high pressure hydrogen gas. Am Soc Mech Eng Press Vessel Pip Div PVP 2019;6B-2019:1–6. https://doi.org/10.1115/PVP2019-93492.

[301] Altenbach H. Holzmann/Meyer/Schumpich Technische Mechanik Festigkeitslehre. Wiesbaden: Springer Fachmedien Wiesbaden; 2022. https://doi.org/10.1007/978-3-658-41029-2.

[302] Dieter GE, Bacon DJ. Mechanical Metallurgy. 1988. https://doi.org/10.1002/crat.2170230211.

[303] Sangid MD. The physics of fatigue crack initiation. Int J Fatigue 2013;57:58–72. https://doi.org/10.1016/j.ijfatigue.2012.10.009.

[304] Kim JJ, Nam SW, Ryu JH. The sensitivity of surface crack initiation to surface roughness in low-cycle fatigue at high temperature. Mater Sci Eng A 1990;130:7–10. https://doi.org/10.1016/0921-5093(90)90069-F.

[305] Ebling F, Wackermann K. Gaseous Hydrogen Charging and Fatigue Testing on IN718. Vol. 4B Mater. Fabr., vol. 4- B, American Society of Mechanical Engineers; 2022, p. 1–5. https://doi.org/10.1115/PVP2022-84184.

[306] McMeeking RM. Finite deformation analysis of crack-tip opening in elastic-plastic materials and implications for fracture. J Mech Phys Solids 1977;25:357–81. https://doi.org/10.1016/0022-5096(77)90003-5.

[307] Reichenbacher A. Numerische Untersuchung von Hohlproben unter Wasserstoffeinfluss. 2022.

[308] Michler T, Schönborn S, Oesterlin H. Crack initiation due to low cycle fatigue in X60 pipeline steel tested in high pressure gaseous hydrogen using hollow and conventional specimens. Int J Fatigue 2025.

[309] Gill P, Madew C, James P, Currie C, Morley A. An Investigation Into the Lifetimes of Solid and Hollow Fatigue. Proc ASME 2017 Press Vessel Pip Conf 2017:1–10.

[310] Alvaro A, Wan D, Olden V, Barnoush A. Hydrogen enhanced fatigue crack growth rates in a ferritic Fe-3 wt%Si alloy and a X70 pipeline steel. Eng Fract Mech 2019;219:106641. https://doi.org/10.1016/j.engfracmech.2019.106641.

[311] Walter RJ, Chandler WT. Cyclic-Load Crack Growth in Asme Sa-105 Grade Ii Steel in High-Pressure Hydrogen At Ambient Temperature. 1976:273–86.

[312] Oda Y, Noguchi H, Higashida K. Loading Frequency Effect on Fatigue Crack Growth Rate in Low Pressure Hydrogen Gas in the Case of A6061-T6 Aluminum Alloy. J Solid Mech Mater Eng 2011;5:599–609. https://doi.org/10.1299/jmmp.5.599.

[313] Bruchhausen M, Fischer B, Ruiz A, González S, Hähner P, Soller S. Impact of hydrogen on the high cycle fatigue behaviour of Inconel 718 in asymmetric push-pull mode at room temperature. Int J Fatigue 2015;70:137–45. https://doi.org/10.1016/j.ijfatigue.2014.09.005.

[314] Michler T, Naumann J, Wiebesiek J, Sattler E. Influence of frequency and wave form on S-N fatigue of commercial austenitic stainless steels with different nickel contents in inert gas and in high pressure gaseous hydrogen. Int J Fatigue 2017;96:67–77. https://doi.org/10.1016/j.ijfatigue.2016.11.026.

[315] An T, Peng H, Bai P, Zheng S, Wen X, Zhang L. Influence of hydrogen pressure on fatigue properties of X80 pipeline steel. Int J Hydrogen Energy 2017;42:15669–78. https://doi.org/10.1016/j.ijhydene.2017.05.047.

[316] Miyamoto T, Matsuo T, Kobayashi N, Mukaie Y, Matsuoka S. Characteristics of fatigue life and fatigue crack growth of SCM435 steel in high-pressure hydrogen gas. Nihon Kikai Gakkai Ronbunshu, A Hen/Transactions Japan Soc Mech Eng Part A 2012;78:531–46. https://doi.org/10.1299/kikaia.78.531.

[317] Harris JA, Wanderham MC Van. PROPERTIES OF MATERIALS IN HIGH PRESSURE HYDROGEN AT CRYOGENIC. ROOM, AND ELEVATED TEMPERATURES. NASA-CR-124394 1976.

[318] Pei C, Zeng W, Yuan H. A damage evolution model based on micro-structural characteristics for an additive manufactured superalloy under monotonic and cyclic loading conditions. Int J Fatigue 2020;131:105279. https://doi.org/10.1016/j.ijfatigue.2019.105279.

[319] Puydebois S, Oudriss A, Bernard P, Briottet L, Feaugas X. Hydrogen effect on the fatigue behavior of LBM Inconel 718. MATEC Web Conf 2018;165:1–8. https://doi.org/10.1051/matecconf/201816502010.

[320] Vesely EJ, Bhat BN, McPherson WB, Grethlein CE. Reproducibility and Repeatability of Tensile and Low-Cycle Fatigue Properties in Propulsion Grade Hydrogen. Proc 5th Intl Conf Eff Hydrog Behav Mater 1994:363–374.

[321] Oriani RA. The Physical and Metallurgical Aspects of Hydrogen in Metals. ICCF4, Fourth Int. Conf. Cold Fusion, 1993.

[322] Poletaev GM, Zorya I V., Novoselova D V., Starostenkov MD. Molecular dynamics simulation of hydrogen atom diffusion in crystal lattice of fcc metals. Int J Mater Res 2017;108:785–90. https://doi.org/10.3139/146.111556.

[323] Tiesinga E, Mohr PJ, Newell DB, Taylor BN. CODATA Recommended Values of the Fundamental Physical Constants: 2018. J Phys Chem Ref Data 2021;50:7537. https://doi.org/10.1063/5.0064853.

[324] Prohaska T, Irrgeher J, Benefield J, Böhlke JK, Chesson LA, Coplen TB, et al. Standard atomic weights of the elements 2021 (IUPAC Technical Report). Pure Appl Chem 2022;94:573–600. https://doi.org/10.1515/pac-2019-0603.

[325] von Hartrott P, Schlesinger M, Uhlig R, Jedamski J. Fatigue Life Prediction of Ni-Base Thermal Solar Reciver Tubes 2010:1112–9.

[326] Seifert T, Maier G, Uihlein A, Lang KH, Riedel H. Mechanism-based thermomechanical fatigue life prediction of cast iron. Part II: Comparison of model predictions with experiments. Int J Fatigue 2010;32:1368–77. https://doi.org/10.1016/j.ijfatigue.2010.02.005.

[327] ASME. ASME B31.12 Hydrogen Piping and Pipelines 2011;2011.

Figures

Figure 1.1: Hydrogen embrittlement index ($RAH2/RAHe$ or $\sigma NTS, H2/\sigma NTS, He$) as a function of the yield strength for various metallic materials (690 bar helium or hydrogen) and Alloy 718 (350 bar helium or hydrogen). For Alloy 718, 3 different heat treatment conditions are considered for rolled bars, forgings, thick plates, welds and heat-affected zones, respectively. Data of the various metallic materials was taken from [12] and data of Alloy 718 from [13]. 2

Figure 2.1: Schematic representation of the increase in strength due to precipitates. Depending on the particle size r, coherent particles are either cut or bowed. The maximum increase in strength results for the critical particle radius $rcrit$. 6

Figure 2.2: Time temperature transformation curve for Alloy 718 with commercial heat treatment of solution annealing (954 °C – 1 h) and two step age hardening (718 °C – 8h, 621 °C – 8 h) adopted from [10]. 7

Figure 2.3: Schematic illustration of additive manufacturing using the laser powder bed fusion (LPBF) process. Metal powder is applied to the build platform using a roller and selectively melted by a focused laser beam. This process enables the component to be constructed layer by layer. Once completed, any loose powder is removed from the finished component. 8

Figure 2.4: Low cycle fatigue (LCF) and thermo-mechanical fatigue (TMF) data of alloy 718 with data from Voese et al. [112] obtained for different temperatures. 10

Figure 2.5: Crack loading modes: Mode I (opening), Mode II (sliding) and Mode III (tearing). 11

Figure 2.6: Illustration of a semi-circular crack in a semi-infinite medium, adopted from [49], where σ is the applied stress, a the crack length and λ the angle of the crack front. 12

Figure 2.7: Definition of the crack tip opening displacement ($CTOD$), adopted from Ref. [124]. 15

Figure 2.8: Example for the dependence between logarithmic crack growth per cycle $log(da/dN)$ and the logarithmic stress intensity factor $\log(\Delta K)$ with classification into three regimes. I. Threshold region, II. Stable crack growth region, where Pari's law accounts and III. Instable crack growth. 16

Figure 2.9: Illustration of the hydrogen compressibility factor as a function of pressure and temperature, with data from reference [162]. 21

Figure 2.10: Hydrogen transport steps from gas phase to the dissolved state in the metal lattice and the diffusion to regions of high stress, such as crack tips and inclusions. 23

Figure 2.11: Schematic illustration of the energy levels in the metal lattice and at hydrogen traps: $E_{t,b}$ trap binding energy, $E_{t,a}$ trap activation energy, E_s saddle point energy and $E_{l,d}$ activation energy of hydrogen diffusion in the normal lattice. 27

Figure 2.12: Illustration of the hydrogen enhanced decohesion (HEDE) theory showing separation of metal atoms by tensile stress. Bonding forces are weakened by (a) hydrogen atoms in the metals lattice in front of the crack tip at highest hydrostatic stresses, (b) absorbed hydrogen at crack tip and (c) hydrogen between inclusions and metal lattice, adopted from [201]..... 30

Figure 2.13: Dependence of the hydrogen environment embrittlement (HEE) index for threshold stress intensity factor ratio $KITH\ /KIC$ and RA ratio on temperature for Alloy 718, tested in a 345 bar hydrogen atmosphere [166], reproduced from [237]..... 32

Figure 2.14: Reduction of threshold stress intensity Kth with increasing hydrogen pressure for alloy 718 and 903 [208], reproduced from [238]..... 33

Figure 2.15: Dependence of the reduction of area (RA) and the elongation to failure (εf) on the strain rate for Alloy 718 in a 345 bar hydrogen atmosphere. Reproduced with data from [242]..... 33

Figure 2.16: Fracture surfaces after slow strain rate tensile test of hydrogen free sample with dimples indicating ductile fracture (a) and electro-chemical pre-charged sample with cleavage morphologies indicating brittle fracture (b) [243] © copyright 2002, reprinted by permission of Informa UK Limited, trading as Taylor & Francis Group, https://www.tandfonline.com..... 35

Figure 2.17: Slow strain rate tensile test of 168 h electrochemical pre-charged specimen to a diffusible hydrogen content of 32.8 wppm [244] (licensed under CC BY-NC-ND). Picture (a) shows the fracture surface of the specimen, dominated by transgranular brittle fracture (b) shows the magnification of a brittle area flat facets and transgranular steps, (c) shows a region with many flat facets and (d) a magnification of such a flat facet, where slip bands can be seen on that surface..... 35

Figure 3.1: Hydrogen charging setup: Samples can be introduced to the sample chamber for hydrogen charging. The chamber can be flushed and pressurized with hydrogen gas up to 200 bar. The pressure can be measured by a manometer (as shown in Figure 3.1) or a pressure transducer to record the pressure. The sample chamber can be heated up to 400 °C with a heating cord and a temperature controller..... 39

Figure 3.2: Illustration of the gas permeation test setup with quadrupole mass spectrometer (QMS), turbomolecular pump (TMP) and ion getter pump (IGP) [249] (licensed under CC BY)..... 41

Figure 3.3: Geometries of conventional specimen (CS) and hollow specimen (HS)..... 43

Figure 3.4: Geometries of conventional and hollow low cycle fatigue specimens..... 43

Figure 3.5: Illustration of 5 % stress drop failure criterion for hardening and then continuous softening material as is the case for the investigated alloy 718. 44

Figure 3.6: Illustration of the abrasive flow machining (AFM) process. An abrasive media is pumped through the workpiece from both sides..... 46

Figure 3.7: High pressure hydrogen autoclave test system at Fraunhofer IWM (a), drawing of autoclave with sample, load cell and pull rod (b) and autoclave system at Fraunhofer LBF [272] (c)..... 47

Figure 3.8: Visualization of the specimen clamping and hydrogen charging setup for slow strain rate tensile tests and low cycle fatigue tests on hollow specimens [273]. The specimen is connected with tubes to a pressure gauge and valves, which can be pressurized with hydrogen gas. The specimen is mounted to the fixtures of the pull rods. An extensometer is clipped on the specimen to measure the elongation. 48

Figure 3.9: Liquid nitrogen test setup (-196 °C) on servo-electric central spindle testing machine W+B LFMZ 100 kN for tensile and LCF experiments in a liquid nitrogen bath (left). CAD drawing of the test chamber with liquid nitrogen level sensor, specimen clamping, and hydrogen supply [274]. 49

Figure 3.10: Test setup with temperature chamber (-100 °C to 200 °C) on servo-electric central spindle testing machine W+B LFMZ 100 kN for tensile and LCF experiments. Overview of testing machine (left) and detail view of the temperature chamber (right). The specimen with clamping is placed in the chamber and is temperature-controlled. The gas supply with pressure gauge and valves is outside of the chamber. 50

Figure 3.11: Test set up with induction heating (up to 1000 °C) on servo hydraulic multipurpose fatigue test system W+B LFV 250 kN. A water cooled induction coil is used to heat the specimen. Three thermocouples are used to regulate and control the temperature. An extensometer with ceramic sticks is used to withstand the high temperature. The clamping is cooled with water. 51

Figure 4.1: Micrographs taken by light microscope (a,c,d,f) and SEM (BSE detector) (b,e) of Alloy 718 wrought (a-c) and SLM (d-e) [273]. Wrought material with titanium nitrides (TiN), niobium carbides (NbC) and δ-phase precipitates. SLM material with pores, δ-phase precipitates, γ'- or γ''-phase precipitates and a checkered pattern in the transversal cross section (f), indicated by white dashed lines. 53

Figure 4.2: Light microscope images of the outer surface (lapped) and the inner hole (drilled, honed, abrasive flow machined (AFM), electrical discharge machined (EDM) and reamed) with the corresponding roughness Ra and Rz. 54

Figure 4.3: EBSD maps (image quality and inverse pole figure) of sections of the lapped outer surface and along the holes, prepared by drilling, honing, reaming, abrasive flow machining (AFM), electrical discharge machining (EDM) and electrochemical machining (ECM). The relevant surface is for all pictures at the right side. 56

Figure 5.1: Hydrogen concentration in a plane sheet of thickness 5 mm after hydrogen diffusion from both sides for Alloy 718 at 20 °C and 350 °C. 60

Figure 5.2: Hydrogen concentration measurements after different charging times for Alloy 718 wrought (cylindrical specimens with $d = 6.25$ mm and $l = 7mm$) and SLM (cubic specimens with $l = 5\,mm$). Hydrogen charging was conducted at 350 °C and 100 bar hydrogen gas pressure. 60

Figure 5.3: Hydrogen measurements of Alloy 718 SLM after different desorption times at room temperature in lab air (20 °C) and in liquid nitrogen (-196 °C). 61

Figure 5.4: Example of a deuterium gas permeation measurement. Ion currents of D_2, N_2 and O_2 were measured by mass spectrometry. D_2 inlet started when the desired temperature was reached and the D_2 ion current had dropped to a minimum..... 62

Figure 5.5: Determination of the diffusion coefficient of deuterium in alloy 718 by time lag method.....63
Figure 5.6: Gas permeation through membrane of Alloy 718 SLM. Fit with Arrhenius type relationship ($R2 = 0.98$).....63
Figure 5.7: a) Hydrogen desorption curves of Alloy 718 wrought at heating rates of 3, 6 and 10 K/min. b) Example of the fit with Gaussian distribution to the curve obtained at a heating rate of 3 K/min.....64
Figure 5.8: Plot of $\ln\phi Tp2$ vs. $1Tp$ for the three peaks of each TDS measurements of Alloy 718 wrought with the heating rates 3 K/min, 6 K/min and 10 K/min, respectively.....65
Figure 5.9: Hydrogen permeation (left) and diffusion (right) as a function of temperature from literature for alloy 718 in different conditions in black [36,189,247,248] and additive manufactured alloy 718 in red [36,244,280]. The average line found for different conditions of alloy 718 and published in [231] is plotted in green. 66
Figure 5.10: Hydrogen solubility as a function of temperature calculated from permeability and diffusivity data, shown in Figure 5.9, and measured points from this study for Alloy 718 wrought and SLM charged at 350 °C in 10 MPa and from Ogawa et al. charged at 270 °C in 0.7 MPa, 11 MPa and 100 MPa hydrogen atmosphere [279]. The average line found for different conditions of alloy 718 and published in [231] is plotted in green. 67
Figure 5.11: Energie diagram of lattice diffusion El,d activation energy, dislocation activation Ed,a and dislocation binding Ed,b energies, carbide activation Ec,a and carbide binding Ec,b energies and grain boundary activation Egb,a and grain boundary binding Egb,b energies, ...69
Figure 6.1: Reduction of area for slow strain rate tensile tests over the technical strain rates of X60 pipeline steel. Experiments were conducted on hollow specimens in air and with 100 bar inner hydrogen pressure. Amended published in Reference [296].....72
Figure 6.2: Light microscope images of the fracture surfaces of the hollow specimens tested in air and with 100 bar hydrogen at different crosshead speeds. The corresponding technical strain rates are indicated. 73
Figure 6.3: Reduction of area depending on oxygen content for different numbers of flushing cycles n and on gas quality. Amended published in Reference [296]. 74
Figure 6.4: Slow strain rate tensile tests on Alloy 718 wrought with conventional and hollow specimen. Hydrogen charging in-situ with 10 to 200 bar and hydrogen pre-charging at 350°C and 100 bar hydrogen pressure for 10 days [273]. ..75
Figure 6.5: Slow strain rate tensile tests on Alloy 718 SLM in as-build and heat treated condition (solution annealing at 980 °C for 1 hour, air cooling, and precipitation heat treating at 720 °C for 8 hours and 620 °C for 8 hours). ..75
Figure 6.6: Slow strain rate tensile tests on Alloy 718 SLM with conventional and hollow specimen. Hydrogen charging in-situ with 10 and 100 bar [273].....76
Figure 6.7: Fracture surfaces of conventional specimens of Alloy 718 wrought: Reference specimen tested in air (a, b), pre-charged specimen (c, d) specimen tested in 200 bar hydrogen atmosphere. Blue arrows indicate flat surfaces and red arrows indicate secondary cracks [273].....77

Figure 6.8: Fracture surfaces of hollow specimen of Alloy 718 wrought: Reference specimen tested in air (a, b), specimen tested with 150 bar inner nitrogen pressure (c, d) and specimen tested with 200 bar inner hydrogen pressure. Blue arrows indicate flat surfaces and red arrows indicate secondary cracks [273]. 78

Figure 6.9: Fracture surfaces of Alloy 718 SLM: Conventional reference specimen tested in air (a, b), conventional specimen tested in 100 bar hydrogen atmosphere (c, d) and hollow specimen tested with 100 bar inner hydrogen pressure. Blue arrows indicate flat surfaces and red arrows indicate secondary cracks [273]. 79

Figure 6.10: EBSD (a, e) and KAM maps (b, f) of cracks in hollow specimens appearing at the borehole, for specimens tested in air and with 200 bar internal hydrogen pressure, respectively. Macrographs of the failed specimen (c, g) and illustration of crack growth (d, h) [273]. 80

Figure 6.11: Elongation to failure (a) and reduction of area (b) over hydrogen pressure for conventional specimens (CS) and hollow specimens (HS) (Fit with exponential growth function with time constant parameter ($y = A1 * exp(x/t1) + y0$) [273]. 82

Figure 6.12: Comparison of the reduction of area of conventional specimens (CS) and hollow specimens (HS) from this work with data from Michler et al. for austenitic steels [28]. The arrow indicates increasing hydrogen pressure of the experiments..... 82

Figure 6.13: Illustration of the different failure mechanisms taking place in conventional specimens (CS) and hollow specimens (HS) when in contact with a hydrogen atmosphere or pre-charged with hydrogen. Voids are represented by blue circles, shear fractures are depicted by blue lines in a 45° direction, and hydrogen-assisted cracks are shown in red [273]. 84

Figure 6.14: The multi axial stresses in the spatial directions tangential (σt), axial (σa) and radial (σr) in a hollow specimen for an internal pressure of 100 bar. Adopted from Reference [273]. 85

Figure 6.15: Hydrogen embrittlement indices relative elongation to failure $R\varepsilon f = \varepsilon f, H2/\varepsilon f, Air$ and relative reduction of area $RRA = RAH2/RAAir$ of Alloy 718 wrought and SLM, tested at 10 bar and 100 bar hydrogen pressure with conventional specimens (CS) and hollow specimens (HS) [273]..... 86

Figure 6.16: Low cycle fatigue experiments on conventional specimens (CS) of Alloy 718 wrought in the initial state for reference and in the hydrogen pre-charged state. ($R = -1$, $f = 0.1\ Hz$). Cycles to failure Nf are reduced by about 55 % for hydrogen pre-charged samples..... 87

Figure 6.17: Fracture surface images, taken by SEM, of a conventional specimen tested in air (a-c) and pre-charged at 350 °C and 100 bar hydrogen pressure for 10 days (d-f). ($R = -1$, $\Delta\varepsilon t = 1.24\ \%$ $f = 0.1\ Hz$, $T = 20\ °C$). The fracture surface of the air sample shows crack initiation from several points and ductile crack growth with striations. The pre-charged sample shows a single initiation point and flat facets with slip bands, indicating more brittle crack growth. Adapted from [305]. 88

Figure 6.18: Low cycle fatigue experiments on conventional specimens (CS) and hollow specimens (HS) of Alloy 718 wrought in air, 10 bar nitrogen atmosphere and 50 bar nitrogen inner pressure. ($R = -1$, $f = 0.1\,Hz$, $T = 20°C$). While nitrogen pressure shows no influence on fatigue life, hollow specimens show about 33 % reduced cycles to failure Nf compared to conventional specimens. The sample tested in the autoclave at highest load must be excluded as it buckled. 89

Figure 6.19: Low cycle fatigue experiments on conventional specimens (CS) and hollow specimens (HS) of Alloy 718 SLM in air. ($R = -1$, $f = 0.1\,Hz$, $T = 20°C$). Hollow and conventional specimens show about the same cycles to failure Nf. 90

Figure 6.20: Low cycle fatigue experiments on conventional specimens (CS) and hollow specimens (HS) of Alloy 718 wrought in the autoclave at a hydrogen pressure of 50 bar. ($R = -1$, $f = 0.1\,Hz$, $T = 20°C$). Both, CS and HS show about 60 % reduced cycles to failure Nf und hydrogen atmosphere. Samples tested at highest load must be excluded as they buckled. 91

Figure 6.21: Low cycle fatigue experiments on hollow specimens (HS) of Alloy 718 wrought with 50 bar and 100 bar inner hydrogen pressure. ($R = -1$, $f = 0.1\,Hz$, $T = 20°C$). Reference lines of experiments tested in air and in the autoclave of HS and CS are plotted for comparison. 2 % strain range experiments fall on the reference line of hollow specimens tested in the autoclave. At 3 % the 50 bar experiments show more and the 100 bar experiments less cycles to failure Nf than the reference line. At 1.1 % the 50 bar and 100 bar fall on the reference line of experiments in air. 92

Figure 6.22: Fracture surface images, taken by SEM, of hollow specimens, tested in autoclave (a-c) and tested with inner hydrogen pressure (d-f) at 50 bar ($R = -1$, $f = 0.1\,Hz$, $T = 20\,°C$). White arrows indicate locations of crack initiation. For 1 % strain range, cracks initiated on the outer surface. For the experiments conducted with only inner pressure this means that the crack was not in contact with hydrogen. At 2 % and 3 % cracks initiated at the inner hole, which was in contact with hydrogen for both types of experiments... 93

Figure 6.23: Low cycle fatigue experiments of hollow specimens (HS) of Alloy 718 wrought with the inner hole manufactured by electrical discharge machining and abrasive flow machining. Experiments were conducted in ambient air and with 50 bar inner hydrogen pressure ($R = -1$, $f = 0.1\,Hz$, $T = 20°C$). Fatigue life Nf in air falls between reference tests on CS and drilled HS. With 50 bar inner hydrogen pressure, Nf is reduced by about -60 % for all tested strain ranges, as it was observed by tests in the hydrogen autoclave..... 94

Figure 6.24: Low cycle fatigue life of hollow specimen tested with 100 bar hydrogen pressure at different test frequencies compared to experiment in air (tested at $f = 0.1\,Hz$). ($R = -1$, $\Delta\varepsilon t = 2\,\%$, $T = 20°C$). With decreasing test frequency, the cycles to failure Nf of experiments with inner hydrogen pressure decrease. 95

Figure 6.25: Stress strain hystereses of low cycle fatigue experiments at half cycles to failure with a strain range of $\Delta\varepsilon t = 2\,\%$ in air and with 100 bar inner hydrogen pressure at test frequencies from 0.001 Hz to 1 Hz. ($R = -1$, $\Delta\varepsilon t = 2\,\%$, $T = 20°C$). Hystereses measured in hydrogen fall on the hysteresis measured in air. Only the hysteresis for the experiment at 1 Hz slightly deviates (blue line). 96

Figure 6.26: Fracture surface images, taken by SEM, of hollow specimens, tested at 0.001 Hz (a-c) and 1 Hz (d-f) with 100 bar hydrogen pressure ($R = -1, \Delta\varepsilon t = 2\ \%$, $T = 20\ °C$). While the fracture surface of the 1 Hz experiment shows striations and only few flat facets around the borehole, as indicated by blue arrows, the specimen tested at 0.001 Hz exhibits many flat facets even at the circumference. 97

Figure 6.27: Low cycle fatigue life of hollow specimen tested with different pressures between 10 bar and 250 bar of nitrogen (0 bar = air) and the same pressures of hydrogen. ($f = 0.1\ Hz, R = -1, \Delta\varepsilon t = 2\ \%$). Cycles to failure Nf are not significantly influenced by nitrogen pressure as the linear trendline shows. With increasing hydrogen pressure Nf decreases with a relationship of $Nf = g * ph$. 98

Figure 6.28: Low cycle fatigue life in cycles to failure Nf of hollow specimen tested in air (N_2 for temperatures below 20 °C) or with 100 bar hydrogen internal pressure at different temperatures between -100 °C and 600 °C and test frequencies between 0.001 Hz and 1 Hz. ($R = -1$, $\Delta\varepsilon t = 2\ \%$). Lines are drawn for experiments in air and experiments with hydrogen at 0.1 Hz to guide the eye. The relationships of fatigue life and temperature, as well as other influencing factors are modeled in Chapter 6.4.8. The reduction in Nf is greatest in the range of 20-200 °C and at slow test frequencies. At low temperatures ($< -100\ °C$) and high temperatures ($> 400\ °C$), Nf under hydrogen influence approaches that in air again. 99

Figure 6.29: Fracture surface images, taken by SEM, of hollow specimens, tested at -100 °C, 20 °C, 400 °C and 600 °C in air. ($R = -1$, $\Delta\varepsilon t = 2\ \%$, $f = 0.1\ Hz$). Orange arrows indicate open grain boundaries. A change is visible from fracture surfaces with striations up to 400 °C to a fracture surface containing open grain boundaries at 600 °C..... 100

Figure 6.30: Fracture surface images, taken by SEM, of hollow specimens, tested at -100 °C, 20 °C, 400 °C and 600 °C with 100 bar inner hydrogen pressure. ($R = -1$, $\Delta\varepsilon t = 2\ \%$, $f = 0.1\ Hz$, $pH2 = 100\ bar$). Red arrows indicate secondary cracks, blue arrows indicate flat facets and orange arrows indicate open grain boundaries for the crack area exposed to air. At -100 °C the fracture surface is dominated by striations. At 20 °C and 400 °C flat facets are visible. At 400 °C open grain boundaries can be observed at the cracks that initiated from the outer surface, which was exposed to air during experiment. 101

Figure 6.31: Low cycle fatigue experiments on conventional specimens (CS) and hollow specimens (HS) of Alloy 718 SLM in build direction (0°) in air, with 10 bar and 100 bar inner hydrogen pressure ($R = -1$, $f = 0.1\ Hz$, $T = 20°C$). Fatigue life is slightly reduced at 10 bar and significantly at 100 bar hydrogen pressure for 2 % and 3 % strain range. No hydrogen effect is observed at $\Delta\varepsilon t = 1.1\ \%$. Adapted from [18]..... 102

Figure 6.32: Low cycle fatigue experiments on hollow specimens of Alloy 718 SLM, printed in 0° and 90° to building direction, tested in air at ambient pressure with and without 10 bar inner hydrogen pressure ($R = -1, f = 0.1\ Hz, T = 20°C$). Fatigue life was significantly lower for the 90° printed specimens in both, air and hydrogen atmosphere. The effect of 10 bar hydrogen pressure was comparable between both orientations. Adapted from [18]. 103

Figure 6.33: Low cycle fatigue experiments on hollow specimens (HS) of Alloy 718 SLM in air at 20 °C and in a liquid nitrogen bath at -196 °C with and without 10 bar inner hydrogen pressure ($R = -1$, $f = 0.1\ Hz$). At low temperature the slope of the fit line changed, leading to lower fatigue life at high load and higher fatigue life at low load. The effect of 10 bar hydrogen was negligible at -196 °C. Adapted from [18]. 104

Figure 6.34: Finite element model of conventional and hollow specimens of alloy 718 wrought under cyclic load ($\Delta\varepsilon t = 3\%$) with evaluation of the equivalent plastic strain (PEEQ) for cycle 1, 5 and 10. Maximum PEEQ is increased about 4 % on the inner surface of the HS. 106

Figure 6.35: Fracture surface of a conventional specimen tested in 50 bar hydrogen atmosphere in the autoclave with crack initiation from the outer surface (a) and hollow specimen tested with 100 bar hydrogen inner pressure with crack initiation from the inner surface (b). Illustration of a single crack initiating from the outer surface of a conventional specimen (c) and from the inner hole surface of a hollow specimen (d). Due to the different curvature of the surface where the crack initiates, the fracture area of a crack of 1 mm length differs significantly for CS (1.46 mm²) and HS (1.91 mm²). 108

Figure 6.36: Microstructural characteristics in Alloy 718: a) Light micrograph of the etched Alloy 718 wrought in undeformed state with twin boundaries (TB) and Niobium carbide (NbC), b) etched micrograph of reference specimen after LCF test with dislocation slip bands (DSBs), TB and cross slip (CS), c) SEM-EBSD image of a specimen after 50 bar H_2 LCF test, taken at the main crack showing DSBs and fracture along DSBs (visible as flat facet), d) SEM micrograph of a hydrogen pre-charged specimen, taken at the main crack with voids nucleating at DSBs, fracture surface images taken with SEM of e) a 50 bar H_2 LCF and f) a pre-charged LCF specimen showing flat facets with DSBs. 113

Figure 7.1: Illustration of the hydrogen concentration CL and the dislocation occupation $\theta D(CL)$ ahead of a crack tip for any cycle at any time. 117

Figure 7.2: Iterative process to calculate the crack growth increment ΔaH affected by hydrogen and the cycles to failure Nf for a crack of length $a0 = 17.5\ \mu m$ to reach the critical length $af = 1\ mm$. 119

Figure 7.3: Dependence of dislocation occupancy and diffusion coefficient on temperature. (Calculated for $p = 100\ bar\ H2$ and the material properties of Table 7.2). 120

Figure 7.4: Determination of the crack propagation affected by hydrogen. Starting with the initial value $\Delta aAir$, the crack propagation is determined taking the average trap occupancy in front of the crack tip into account in an iterative process until a relative deviation from the last iteration step smaller than 0.001 % is reached (final value ΔaH). Illustration for cycle 200 of a modeled crack at $T = 20\ °C$, $p = 100\ bar\ H2$, $f = 0.1\ Hz$ and $\Delta\varepsilon t = 2\ \%$. 121

Figure 7.5: Illustration of the average trap occupancy θd for each cycle of simulated experiments at different temperatures ($T = -100\ to\ 600\ °C$, $p = 100\ bar\ H2$, $f = 0.1\ Hz$ and $\Delta\varepsilon t = 2\ \%$). 121

Figure 7.6: Example for the evaluation of the material parameters elastic modulus E, cyclic hardening exponent n' and cyclic yield stress σcy from the cycle at half cycles to failure ($Nf/2$). 122

Figure 7.7: Determination of the temperature-dependent elastic modulus E, the cyclic hardening exponent n' and the cyclic yield stress σcy based on low cycle fatigue experiments. The material properties were evaluated at half cycles to failure, see Table 7.1..... 123

Figure 7.8: Fitting of $Nf, sim = bdn'ZD/\sigma cy\ B$ considering only reference tests in air and with nitrogen inner pressure up to 400 °C. (Blue < 20 °C, black = 20 °C, orange = 200 °C, red = 400 °C)..... 125

Figure 7.9: Comparison of experimental results (points for air and crosses for hydrogen) and prediction by the ZD, H model (solid line for air and dashed lines for hydrogen) for the temperature range from -100 °C to 600 °C and frequency range from 0.001 Hz to 1 Hz ($R = -1$, $\Delta\varepsilon t = 2\ \%$). The model without oxygen diffusion at elevated temperature is represented with a dotted line. The model can very well represent the mechanisms that influence the hydrogen effect on fatigue life across the entire temperature and frequency range. Almost all experimental data points fall within the shaded scatter bands of factor 1.3..... 126

Figure 7.10: Comparison of experimental results and prediction by the ZD, H model (dashed lines) for different pressures of hydrogen and nitrogen. ($T = 20\ °C$, $f = 0.1\ Hz$, $R = -1$, $\Delta\varepsilon t = 2\ \%$). With increasing hydrogen pressure, the cycles to failure Nf decrease as shown by experiments and model..... 127

Figure 7.11: Comparison of experimental results and prediction by the ZD, H model for different frequencies at 100 bar hydrogen pressure ($T = 20\ °C, p = 100\ bar$, $R = -1$, $\Delta\varepsilon t = 2\ \%$). At high frequencies $> 100\ Hz$, the model predicts little hydrogen degradation. In the tested range from 0.001 Hz to 1 Hz cycles to failure Nf from experiments and predicted by the model are in good agreement. At very low frequency of $f < 0.0000001\ Hz$ the model predicts that a maximum hydrogen degradation is approaching..... 128

Figure 7.12: Presentation of experimental results of HS and CS tested in air, 50 bar and 100 bar hydrogen pressure (crosses and triangles) and prediction with the hydrogen damage parameter ZD, H and $\alpha = 35$ for air and 100 bar hydrogen pressure (dashed lines) for different strain ranges $\Delta\varepsilon t$ and frequencies f ($T = 20\ °C$, $R = -1$). No hydrogen degradation of fatigue life Nf below $\Delta\varepsilon t = 0.008$. Hydrogen degradation increases with increasing strain range $\Delta\varepsilon t$ and decreasing frequency..... 129

Figure 7.13: Presentation of experimental results of HS and CS tested in air, 50 bar and 100 bar hydrogen pressure (crosses and triangles) and prediction with the hydrogen damage parameter $ZD, H*$ and $\alpha *= 12000\ m2/J$ for air and 100 bar hydrogen pressure (dashed lines) for different strain ranges $\Delta\varepsilon t$ and frequencies f ($T = 20\ °C$, $R = -1$). No hydrogen degradation of fatigue life Nf below $\Delta\varepsilon t = 0.008$. Hydrogen degradation increases with increasing strain range $\Delta\varepsilon t$ and decreasing frequency..... 130

Figure 7.14: Comparison of fatigue life predictions with $ZD, H*$ for different parameters of binding energy at dislocations Eb, d and parameter $\alpha *$ (dashed lines) and experiments (circles and crosses). Predictions for the upper value of $Eb, d = 19.3\ kJ/mol$ and $\alpha *= 3500\ m2/J$ (left) and the lower value of $Eb, d = 7.7\ kJ/mol$ and $\alpha *= 500$ (right) show similar curves..... 133

Figure 8.1: Developed manufacturing process for the hole of hollow specimens: 1) electrical discharge start hole eroding for a quick machining of a thin hole, 2) electrical discharge wire cutting for a straight and precise hole, 3) abrasive flow machining to remove the erosion layer in the hole and to reach a surface roughness of $Ra = 0.05\ \mu m$. 136

Figure 8.2: Illustration of the effects of temperature, pressure, frequency and strain range on hydrogen distribution around a crack tip, trapping at dislocations and formation of dislocations leading to hydrogen enhanced crack growth. ... 141

Figure 8.3: Simulated ($ZD, H*$ with $\alpha *= 12000\ m2/J$) versus experimental fatigue life Nf of CS and HS in air, nitrogen and hydrogen atmosphere for $p = 0 - 250\ bar$, $T =$ -100 $- 600\ °C$, $f = 0.001 - 1\ Hz$ and $\Delta\varepsilon t = 1.1 - 3$ %. The model can predict the fatigue life for all conditions very well within a scatter band of factor 2 ($R^2 = 0.89$). 145

Tables

Table 2.1: Hydrogen permeation parameters for Alloy 718 [189]. 25
Table 3.1: Chemical composition of Alloy 718 wrought from material certificate and of Alloy 718 SLM measured by energy dispersive X-ray spectroscopy (EDX) (in weight %). Limit values according to ASTM B637-12. 38
Table 7.1: Material parameters evaluated at half cycles to failure (Nf/2) from low cycle fatigue tests (Experiments with almost closed hysteresis were not evaluated). 123
Table 7.2: Parameters of the crack growth model. 130

Publications

1. Wackermann K, Ebling F, Michler T, Schweizer F, Oesterlin H. Design, Usage And Safety Aspects For Tubular Specimens For Materials Qualification With Pressurised Hydrogen. J Eng Integr Soc 2025:12–7.

2. Ebling F, Michler T. Permeability, solubility and diffusivity of hydrogen in alloy 718. Materwiss Werksttech 2025;56:575–80. https://doi.org/10.1002/mawe.202400192.

3. Ebling F, Bratsch P, Wagner S, Pundt A, Preußner J, Oesterlin H, et al. Assessing hydrogen embrittlement of alloy 718: Hollow and conventional tensile tests. Eng Fract Mech 2025;319:111028. https://doi.org/10.1016/j.engfracmech.2025.111028.

4. Ebling F. Effects of Temperature , Pressure and Frequency on Low Cycle Fatigue of Alloy 718 under Gaseous Hydrogen. Proc. 5th Int. Conf. Met. Hydrog., 2025.

5. Ebling F, Oesterlin H, Wackermann K. Mechanism-Based LCF Lifetime Assessment Under the Influence of Hydrogen. Vol. 5A Mater. Fabr., American Society of Mechanical Engineers; 2025, p. 1–7. https://doi.org/10.1115/PVP2025-151456.

6. Michler T, Ebling F, Fischer C, Oeser S, Wackermann K. Tensile testing in high pressure gaseous hydrogen using conventional and tubular specimens: Ferritic steels. Int J Hydrogen Energy 2024;70:262–75. https://doi.org/10.1016/j.ijhydene.2024.05.238.

7. Ebling F, Oesterlin H, Wackermann K. Effect of pressurised Hydrogen on Low Cycle Fatigue Life of Inconel 718:Modelling and Testing. Fatigue 2024, 2024.

8. Michler T, Freitas T, Oesterlin H, Fischer C, Wackermann K, Ebling F. Tensile testing in high pressure gaseous hydrogen using conventional and tubular specimens: Austenitic stainless steels. Int J Hydrogen Energy 2023;48:25609–18. https://doi.org/10.1016/j.ijhydene.2023.03.248.

9. Michler T, Ebling F, Oesterlin H, Fischer C, Wackermann K. Comparison of tensile properties of X60 pipeline steel tested in high pressure gaseous hydrogen using tubular and conventional specimen. Int J Hydrogen Energy 2022;47:34676–88. https://doi.org/10.1016/j.ijhydene.2022.07.211.

10. Ebling F, Wackermann K. Gaseous Hydrogen Charging and Fatigue Testing on IN718. Vol. 4B Mater. Fabr., vol. 4- B, American Society of Mechanical Engineers; 2022, p. 1–5. https://doi.org/10.1115/PVP2022-84184.

11. Ebling F, Reichenbacher A, Oesterlin H, Wackermann K. Hohlprobentechnik zur Werkstoffcharakterisierung im Ermüdungsversuch unter Druckwasserstoffeinfluss. Tagung Werkstoffprüfung 2022, 2022.

12. Ebling F, Oesterlin H, Wackermann K, Primus D, Rehme O. Hydrogen effects on low cycle fatigue of IN718 at RT and 77K using the tubular specimen technique. Proc Fourth Int Conf Met Hydrog 2022:10.

13. Ebling F, Klitschke S, Wackermann K, Preußner J. The Effect of Hydrogen on Failure of Complex Phase Steel under Different Multiaxial Stress States. Metals (Basel) 2022;12:1705. https://doi.org/10.3390/met12101705.

14. Michler T, Ebling F, Ergebnisse D. Einfluss von Hochdruckwasserstoff auf die Zugversuchseigenschaften von ausgewählten Druckbehälter- und Pipelinestählen. Tagung Werkstoffprüfung 2021, 2021.

15. Michler T, Wackermann K, Ebling F, Oesterlin H. Comparison of Tensile Test Results in High Pressure Gaseous Hydrogen Using Conventional and Tubular Specimens. Vol. 4 Mater. Fabr., vol. 4, American Society of Mechanical Engineers; 2021, p. 1–6. https://doi.org/10.1115/PVP2021-61138.

16. Ebling F, Antty I, Wackermann K. Investigation of Hydrogen Embrittlement at RT and 77K using the Tubular Specimen Technique. MaterialsWeek2021 2021:79108.

Statement on the use of AI tools

During preparation of this work, artificial intelligence (AI) based systems were used in accordance with the KIT guidelines on the use of generative AI. The large language models GPT-4, GPT-5 and DeepL were used exclusively for translations into English and to improve readability. The development of the content, the methodology, and the data analysis were carried out entirely independently. All suggestions generated by the AI were critically reviewed for technical accuracy, compared with the original text and adjusted where necessary. Full responsibility is assumed for the content of the work.